2000

Analysis and modelling of weld metal mechanical properties in flux cored arc welded steels

Hai-En Tsuei
University of Wollongong

ANALYSIS AND MODELLING OF WELD METAL MECHANICAL PROPERTIES IN FLUX CORED ARC WELDED STEELS

A thesis submitted in fulfilment of the requirements
for the award of the degree of

Doctor of Philosophy

from

THE UNIVERSITY OF WOLLONGONG

by

HAI-EN TSUEI

(M. ENG.)

Department of Materials Engineering

2000

DECLARATION

The work presented in this thesis is, to the best of my knowledge and belief, original except as acknowledged. I hereby declare that this thesis contains no material which has been submitted to any other university or institution for a high degree.

.....

Hai-En Tsuei

ABSTRACT

The effect of varying welding conditions on multipass weld metal has been investigated in all-weld test plates produced by flux cored arc (FCA) welding. The principal welding conditions varied for the test samples in the current research program were heat input (between approximately 1 and 2.5 kJ/mm), welding technique (stringer or weave beads), shielding gas, welding position (flat or vertical) and consumable type.

Mechanical testing of weld metal included tensile testing and Charpy-vee-notch impact tests over a range of temperatures from -60 °C to 40 °C. The tensile testing results showed that yield and tensile strength generally decreased with increasing heat input and that the changes were of the order of 100 MPa. Impact properties showed more varied behaviour depending on consumable type.

The effect of varying welding conditions on some less commonly studied microstructural factors has also been investigated, such as proportions of reheated and double-reheated regions and mean free path (MFP) in various distinctive microstructural zones. Using the simplifying assumption that the structural gradient in the heat affected zone (HAZ) of reheated weld metal can be characterized in terms of three regions: the grain coarsened, GC; grain refined, GR and intercritical, IC heat affected regions; a second overlapping weld bead creates double-reheated weld metal structures which can be defined in terms of 9 sub-zones: GC-GC, GC-GR, GC-IC, GR-GC, GR-GR, GR-IC, IC-GC, IC-GR, IC-IC. Linear and areal measurement techniques have been used on cross-sections of seventeen test plates to determine the volume fractions of solidified weld metal (SW), GC, GR and IC sub-zones of the reheated weld

metal and the double-reheated zone. The hardness variation in the sub-zones and the influence of welding conditions has also been investigated in the present research.

The mean free path was determined for SW, GC, GR and IC regions and the overall average mean free path of ferrite in each weld was also calculated to provide a characteristic length of the totality of the structural microconstituents in the weld metal. Strong relationships were found between mean free path and heat input and also with the strength of the weld metal. In contrast, toughness correlated poorly with overall mean free path.

Impact toughness is one of the most important mechanical properties of welds. Assessment and understanding of the impact properties of welds is central to the avoidance of catastrophic failure of welded steel structures. Neural networks analysis has been used for the purpose of assessing which factors are beneficial to the low temperature impact properties of steel welds in order to obtain practical guidance as to how impact properties might be improved in FCA welds.

Four major data fields were involved in the training of the neural networks: chemical composition, microstructure, non-metallic inclusions and welding condition. The back-propagation algorithm was used for the analysis. Sensitivity analysis of the neural network model revealed that the characteristics of the non-metallic inclusion distribution exerted only a small direct influence on toughness. In contrast, chemical composition and microstructure were indicated to be very important. In particular the toughness is predicted to increase with increasing % acicular ferrite and % reaustenitised region and these factors in turn are sensitive to the selected FCAW process and the welding conditions.

ACKNOWLEDGEMENTS

The experience, expertise and support of a number of people and organizations have been instrumental in bringing this thesis to completion. With this in mind, I would like to sincerely thank the following people and organzations for their help during the term of the project.

Professor Druce Dunne, as my supervisor, offered his wise expert guidance, patient assistance, and constant encouragement during the entire project. I would not be able to present this work without his academic help.

The Government of R. O. C. for the award of the scholarship which allowed this research to be conducted.

Dr. Huijun Li for his helpful discussions and suggestions and acting as co-supervisor during Druce's absence.

The support of the CRC for Materials Welding and Joining and particularly the contribution of Dr. Ian French and Dr. Otto Schumann of CSIRO Division of Manufacturing Science and Technology in provision of the welded samples and invaluable analysis and testing.

Dr. J. Zhu for his aid in analysis of non-metallic inclusions.

The staff of the Dept. of Materials Engineering, in particular, G. Tillman for his help in constructing various pieces of apparatus and Mrs. R. Cambareri and Mrs. J. Mestre for their assistance with official matters.

Finally, I wish to dedicate this thesis to my wife and my parents, without their love and support, this thesis would have been so much harder to complete.

INTRODUCTION

Arc welding processes using continuous wire electrodes and auxiliary gas shielding, such as flux cored arc (FCA) welding, are becoming increasingly dominant because of the productivity and versatility offered. Such processes are often used for multi-pass welding of structural steels in circumstances where the mechanical properties of the welds are critical.

In order to assure the quality of welds, factors determining quality have to be taken into consideration as have possible defects and their prevention in the planning stage. Due to the complex processes involved during welding, regression analysis is mainly performed, in which the most significant factors are considered with respect to one particular aim in one single equation. Although such approaches may give useful results, they are not able to describe effects on a mechanistic basis. In contrast to this procedure, there are complex physical models which take into account governing mechanisms and the sequential effect on the desired property.

Physical modelling of welding is a rapidly emerging field of research in which analysis, in conjunction with appropriate experimental studies, is used to make predictions of microstructural and property changes in welds. However, due to the extremely complex nature of the weld metal transformations, many aspects in these microstructures are still unclear. As indicated by Bhadeshia and Svensson (1993) progress in the modelling of mechanical properties has been very slow, especially for mathematically based models. For instance, Buchmayr (1995a) has pointed out that there is no physical model to predict the acicular ferrite, although it is known to be very important with respect to toughness behaviour. There is growing evidence that mechanical and microstructural inhomogeneity of the type associated with multipass welds leads to scatter in

mechanical properties, especially for toughness (Bhadeshia and Svensson 1993). It is obvious that the prediction of property-determining parameters is very important although a physically based prediction of the effects on the toughness behaviour is not yet feasible. In other words, although many problems can be solved by numerical models, the problem of toughness is still not able to be solved in a physically correct way.

For quantitative assessments both empirical-based regression equations or physical models have been used in the past. However, in recent years, other alternatives have developed, such as neural networks. Neural networks are human attempts to simulate and understand what goes on in nervous systems, with the hope of capturing some of the power of these biological systems. Neural networks are basically non-parametric and their flexibility makes them capable of discovering more complex relationships in data than traditional regression models. Neural networks have been reported to be very effective in analyzing weldability of power plant steels (Cool et al. 1996), the effect of carbon content on hot strength of steels (Kong et al. 1998) and impact toughness of submerged arc and manual metal arc welds (Bhadeshia et al. 1995). Therefore, developing a neural network model of FCA welding is a potentially valuable way to examine the diversity of factors which might influence impact toughness.

However, to develop a neural network model, the first step is to characterise the input variables. Beside the well-established influences of chemical compositions and proportions of microconstituents, other factors in the field of microstructure should also be investigated, such as volume fraction of reaustenitised region, volume fraction of double-reheated zone, and the microstructural mean free path. Much basic research has been conducted to gain detailed understanding of microstructural phenomena, but

somewhat less emphasis has been given to the study and quantification of microstructural sub-zones produced by overlapping welds and the extent of reaustenitisation of the solidification structure. As the HAZ consists of many sub-zones, the overall mechanical properties of the weld metal are determined by the combination of the properties of all of the different sub-zones (Li et al. 1998). The mean free path (MFP or mean linear intercept "grain size") is also being examined as a suitable variable for correlation with CVN (Charpy-vee-notch) value and also with tensile strength because MFP is a useful index of structural refinement.

CONTENTS

PART A LITERATURE REVIEW

CHAPTER 1

WELDING

1.1 Introduction

1.1.1 Welding processes

In recent years, welding has assumed an even greater role in the fabrication of steel (Metals Handbook 1983). The objective of welding is to produce a joint in which the valuable properties of the material being joined are properly utilized. Many methods of joining one metal to another have been developed, and the ease and cost of making the joint and the capabilities and characteristics of the completed joint vary widely.

Electric welding effectively began with the discovery of the carbon arc in 1881, but the major step of using mineral coated rods is attributed to Kjellberg in 1907 (Yeomans 1994). There were three landmark discoveries: oxy-acetylene gas welding by Le Chatelier, resistance welding by Thompson and carbon electrode arc welding by Bernados (Milner and Apps 1968). The distinguishing features of various processes and their attributes and limitations have been reviewed in the Welding Handbook (1987, 1991), and by Norrish (1992) , Stout (1987) and Houldcroft (1977).

A source of energy of sufficient intensity must be provided to melt both the base plate surfaces and any additional metal needed to fill the joint. The possible sources of energy include: mechanical, thermochemical, electrical resistance, electric arc, and radiation. The hot metal must be protected from the atmosphere during melting and solidification. This also can be achieved by various means such as vacuum, inert gas, gas, flux, and mechanical protection. The various combinations of these energy sources and protective methods are shown in Table 1.1 (Houldcroft 1977). In structural applications, the most common processes encountered are the arc processes and these methods are discussed in the following section.

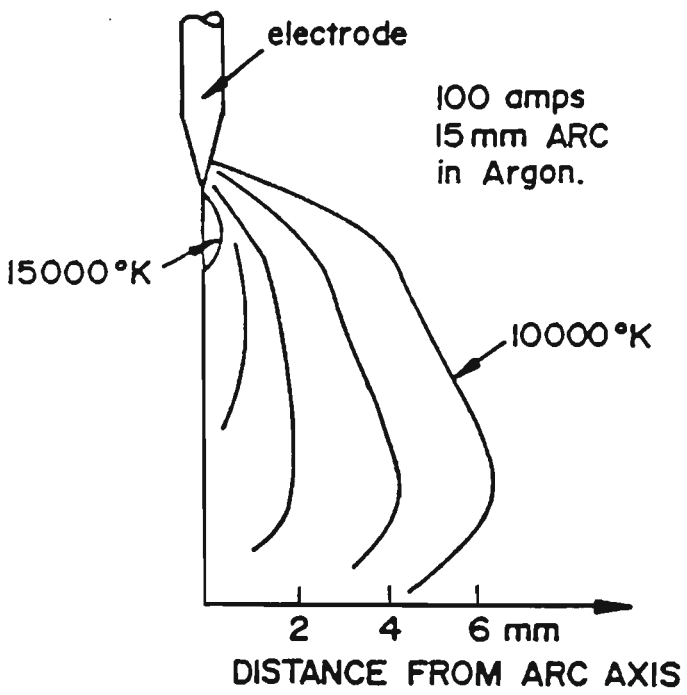

Figure 1.1: Temperature distribution in an arc during welding (After Yeomans 1994).

Table 1.1: Classification of welding processes (After Houldcroft 1977).

Energy Source	Shielding Method					
	Vacuum	Inert Gas	Gas	Flux	None	Mechanical Exclusion
Mechnical	Explosive				Explosive	Friction Ultrasonic
Thermo-chemical		Plasma	Atomic hydrogen	Gas Forge Thermit		Pressure butt
Electrical Resistance				Electro-slag	H.f. induction H.f. resistance Flash butt Projection	Induction butt Spot seam Resistance butt
Electric Arc		Inert-gas metal-arc Inert-gas tungsten-arc	CO_2 metal arc Gas metal arc Flux-cored arc	Covered electrode Submerged-arc	Bare wire Spark-discharge Stud Percussion Carbon-arc	
Radiation	Electron-beam				Laser	
None	Cold-pressure	Thermo-compression bonding				Hot-pressure Cold-pressure

1.1.2 Arc welding

Arc welding is a large and diversified group of welding processes that use a very intense electric arc as the heat source to melt and join metals with or without the use of pressure or filler metal.

The arc itself is a complex mixture of molecules, atoms, ions and electrons derived from the material of the electrodes and the surrounding atmosphere. The proportions of these species depend on such factors as the degree of dissociation of molecules and of ionization of atoms, both of which are temperature dependent. The temperature distribution in the arc varies both radially and longitudinally as shown in Figure 1.1.

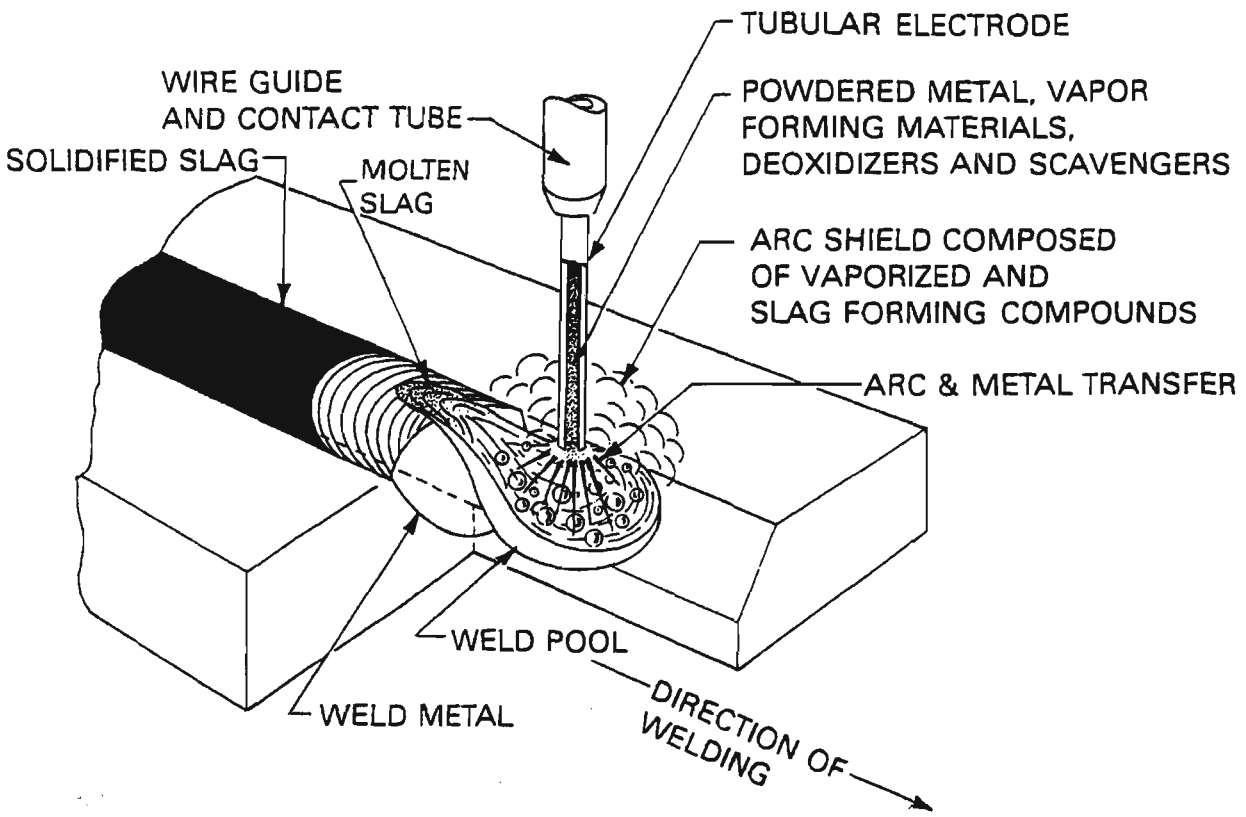

Figure 1.2 (a): Self-shielded flux cored arc welding (After Welding Handbook 1991).

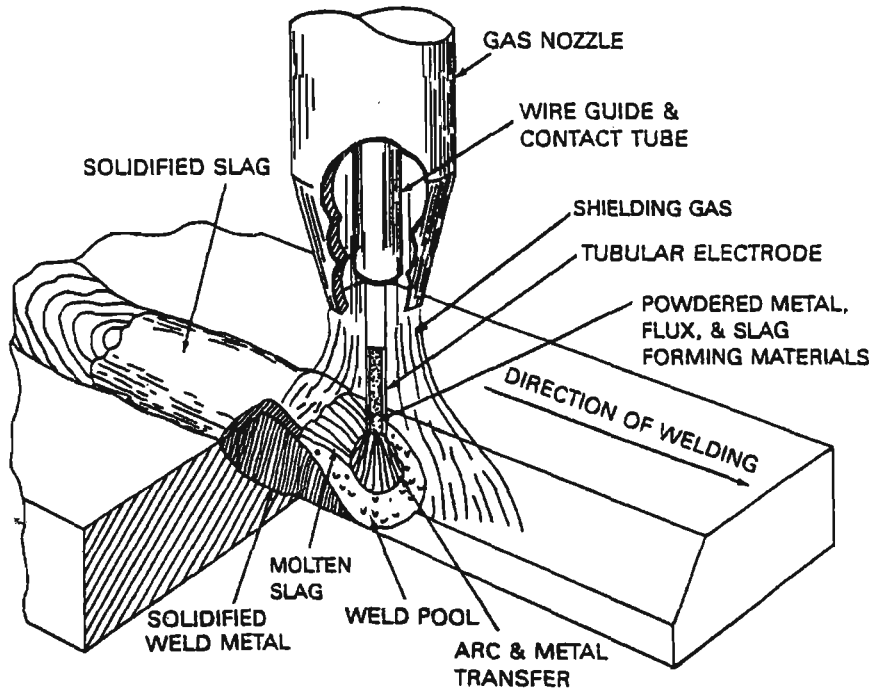

Figure 1.2 (b): Gas shielded flux cored arc welding (After Welding Handbook 1991).

The welding arc is struck between the workpiece and the tip of a current carrying electrode which can be either a consumable wire or a nonconsumable carbon or tungsten rod. The electrode is manually or mechanically moved along the joint, or it remains stationary while the workpiece is moved. When a nonconsumable electrode is used, filler metal can be supplied by a separate wire if needed. A consumable electrode, however, will be designed not only to conduct the current that sustains the arc but also to melt and supply filler metal to the joint. It may also produce a slag covering to protect the hot weld metal from oxidation.

1.1.3 FCA welding

Flux cored arc (FCA) welding has become, in recent years, an important tool in steel fabrication. High deposition rates, all-position capabilities and availability in a wide selection of C-Mn and low alloy grades have made this process attractive. Further more, flux cored arc (FCA) welding is gradually replacing submerged arc welding (SAW) (Metals Handbook 1983). FCAW involves the use of a continuous-wire filler metal. The required equipment for this is relatively simple and is considered portable even though it is somewhat more cumbersome compared to SAW equipment. The advantages of the flux cored arc (FCA) welding process have been thoroughly discussed (Heagey and Wodzinski 1991, Sim 1992, Sakai et al. 1992 and Ferree 1992). An indication of the popularity of the FCAW process can be gauged from worldwide usage which exceeded 200,000 t of wire per year in the early nineties (Heagey and Wodzinski 1991).

In FCA welding, an arc is maintained from the tip of the wire which melts so that the filler metal is added to the molten pool. At the same time a slag is formed and air is excluded by gases generated from the decomposition of the flux core (Figure 1.2 (a)).

The shielding can be augmented by separately supplied gas (Figure 1.2 (b)). For closer control of weld metal chemistry particularly H content, gas shielding is commonly employed in FCAW. The shielding gas reduces the requirement for self-shielding by the flux and allows better control of the slag and weld metal compositions. The FCA welding process shares an important common feature with other continuous-wire processes, namely the capability for high productivity through high operator duty cycles, and the inherently high deposition rates associated with the use of high current densities.

Filler metal and flux are introduced simultaneously to the arc zone in the form of continuous tubular wires, include the flux being contained in the hollow core. The flux composition may, in itself, be sufficient to protect the hot weld zone from the oxygen and nitrogen of the atmosphere or, as mentioned above, an auxiliary shielding gas may be necessary. Therefore, two major process variations are offered in FCA welding: self-shielded FCA welding and gas-shielded FCA welding (Figure 1.2 (a) and (b)).

FCA welding processes are usually carried out in a semi-automatic manner by feeding the wire continuously through a current pick-up tube in a hand-guided welding torch. The high current density at the wire tip gives these processes a deep penetrating capability such as is associated with solid wire gas-shielded systems, whilst the presence of slag on the weld pool gives improved weld surface contour. Unlike submerged arc, the weld zone is visible to the operator and loose flux does not have to be supplied and recovered.

Using wires of smaller diameters, these processes can be used for vertical welding as well as in the flat and horizontal positions. The use of flux-cored wires also proves

attractive as a highly productive method for hard surfacing operations, especially under site conditions where the self-shielded capability is most valuable.

Using appropriate consumables and procedures, good control can be maintained over penetration and bead contour and most metal thicknesses can be joined in most joint positions. These processes excel on horizontal-vertical one-pass fillets, the self-shielded consumables being particularly well suited to open air working situations such as occur in site fabrication.

It has been demonstrated that the gas-shielded FCAW process with small diameter electrodes may offer advantages over the shielded metal arc welding and gas metal arc welding processes (Zimmer and Schmerling 1983). Mechanical properties of the deposited weld metal from self-shielding wires are not as good for the gas-shielded process because of the requirements for the flux to contain more gas forming compounds and deoxidants than the gas-shielded wires. The mechanical properties most affected are ductility and impact strength. The major disadvantages of self-shielded FCA welds are the large amount of welding fume produced during welding and the relatively large amount of nitrides (denitrants) in the weld metal.

In operation, self-shielded FCA welding is associated with more fume evolution than is usual with other processes, which is partly due to the relatively high currents used by this process. Since additional concern arises from the specific nature of self-shielded FCA welding fumes, proper industrial health practices should be maintained by ensuring adequate fume extraction and ventilation at the welding station.

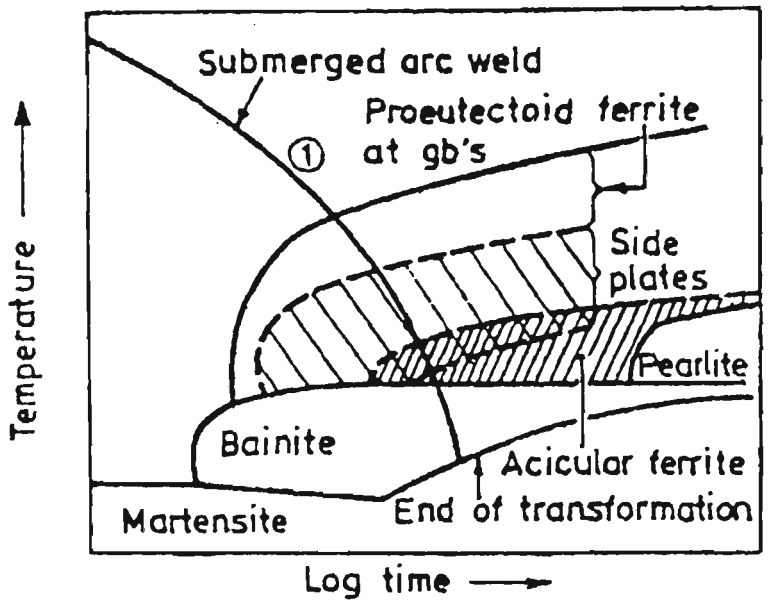

Figure 1.3: Schematic CCT diagram for a steel weld metal (After Easterling 1983).

1.2 Introduction to Multipass Welding

Multipass welds usually provide more benefits than a single pass weld. These benefits include "preheat" from previous weld passes; annealing out of residual stresses due to previous weld thermal cycles; and structural refinement of coarse solidification structures (Easterling 1983, Mercer 1975). A multipass weld metal can be classified in terms of solidified weld metal (SW) and reaustenitised (HAZ) regions. The reaustenitised region generally consists of three sub-zones which are discussed in the following sections.

1.2.1 Solidified weld (SW) region

It has been suggested that solidification of welds progresses from a condition characterized by molten metal turbulence resulting in good mixing of alloying elements (Porter and Easterling 1981). During cooling of the weld metal from its solidification temperature to ambient temperature, additional modifications in microstructure and solute distribution occur (Easterling 1983, Savage 1980).

When several types of transformation product are possible, as with steel, the transformation diagram may appear as in Figure 1.3, which is a continuous-cooling-transformation (CCT) diagram. It is seen from this figure that a number of possible transformation products may appear in a sample at ambient temperature depending upon the cooling rate. Thus, for the cooling curve shown, which corresponds to the cooling of the weld metal, the final structure would consist of a mixture of grain boundary ferrite, side plate ferrite, acicular ferrite, bainite and minor amounts of retained austenite, martensite and pearlite (Abson and Dolby 1978, French 1998).

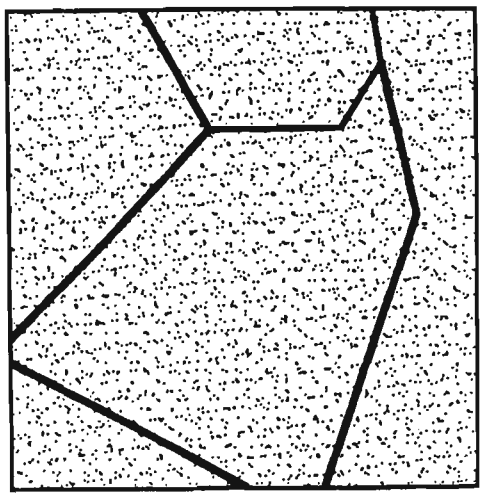

(a)

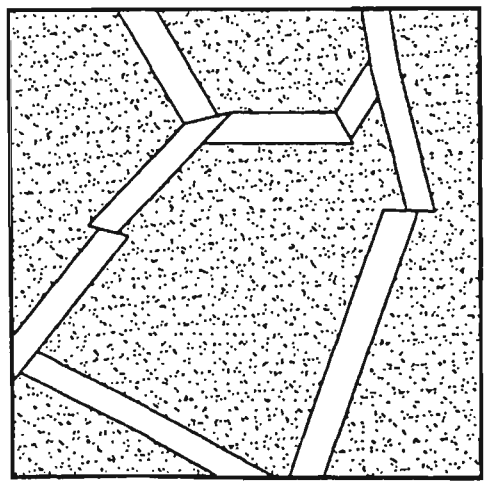

(b)

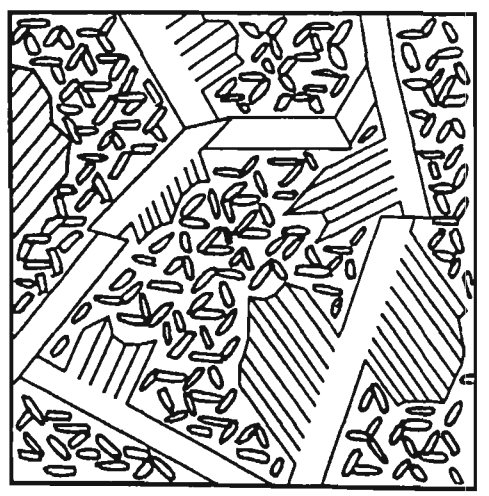

(c)

Figure 1.4: Schematic development of the microstructures in solidified weld metal (SW): (a) The original austenite grains. (b) Formation of grain boundary ferrite (PF(G)). (c) Formation of ferrite with second phase (FS) from PF(G) and acicular ferrite (AF) from within the grains. (After French 1998)

Weld metal for low carbon structural steel generally solidifies as delta-ferrite before undergoing solid state transformations to austenite and ultimately to the ferrite products that are present in the final microstructure. The final ferrite products and their locations with respect to the prior austenite grain boundaries are shown schematically in Figure 1.4. The definitions of these ferrite types and the rules for determining their relative proportions has been established by the International Institute of Welding (1991).

As cooling proceeds the first ferrite type to form nucleates and begins to grow from the prior austenite grain boundaries resulting in grain boundary ferrite (PF(G)). PF(G) is made up of linked grains centred on the prior austenite grain boundaries (see Figure 1.4).

As further cooling takes place, the growth of PF(G) becomes less favoured and a constituent described as ferrite with a second phase (FS), or Widmanstatten ferrite, grows into the austenite grains. FS nucleates from the PF(G) and is made-up of relatively large regions containing only low angle grain boundaries. At the same time as FS is forming from the grain boundaries, another constituent known as acicular ferrite (AF) may be forming within the austenite grains (see Figure 1.4).

1.2.2 Weld thermal cycle (HAZ)

Numerous theoretical analyses of the weld thermal cycle, using a number of simplifying assumptions, have been proposed (Easterling 1983, Alberry et al.1977, Wells 1952), although most generally tend to be modifications to the analysis originally proposed by Rosenthal (Rosenthal 1946, 1935). He assumed the energy of the heat source moves with a constant speed and solutions to the heat flow equations are derived

for a moving point heat source. The thermal energy supplied by the arc is given by the heat input (HI) equation:

$$HI = \eta \frac{V \times I}{S} \tag{1.1}$$

where η is the arc efficiency, V the voltage, I the welding current and S the welding speed. The differential equation of heat flow for the co-ordinates is given in equation 1.2.

$$\lambda\left(\frac{\partial^2 T}{\partial x^2} + \frac{\partial^2 T}{\partial y^2} + \frac{\partial^2 T}{\partial z^2}\right) = \rho c \frac{\partial T}{\partial t} \tag{1.2}$$

where T is temperature, λ is thermal conductivity, ρ is density, c is specific heat and t is time. Different equations can be derived for various assumptions and the introduction of the HI equation. Clark (1985) and Alberry et al. (1983) claimed that the effective welding heat input per unit length could also be used as the independent variable for controlling the dimensions of the weld bead. However, other researchers (Wingrove 1987, Jackson and Goodwin 1948, McGlone 1982, Ahmed and Jarvis 1998) reported that the major welding variables (current, voltage and speed) have individual effects on the output variables (weld bead geometry, dimensions and microstructures) in manual metal arc (MMA), submerged arc (SA) and gas metal arc (GMA) welding.

The HAZ is (usually) referred to regions of the parent metal affected by the severity and extent of the weld thermal cycle and the area heated to a high enough temperature so that changes in the microstructure and properties will be incurred due to the thermal cycle. The metallurgical changes occurring in the HAZ are determined by the nature of the metal, particularly the method by which it has been strengthened and its original

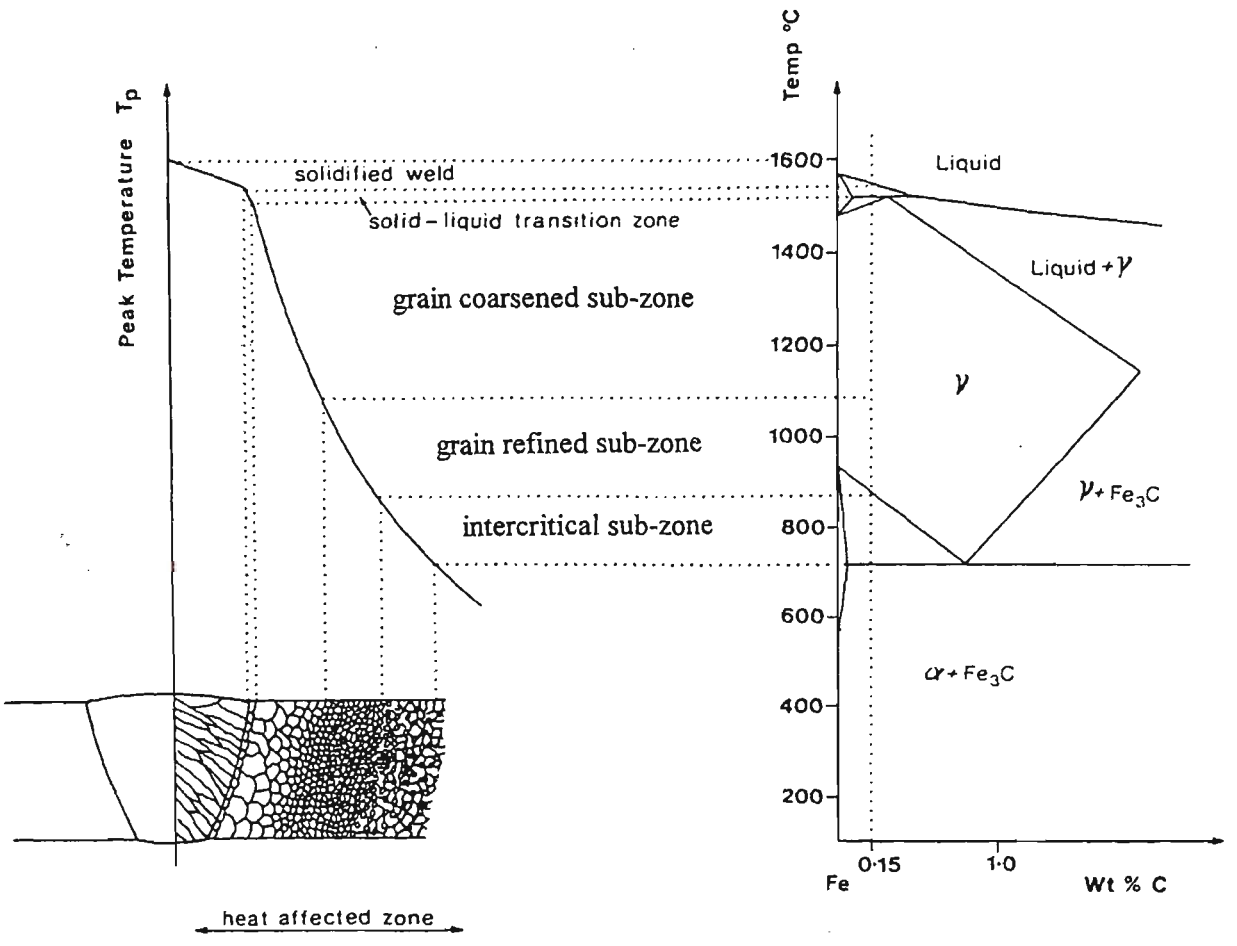

Figure 1.5: A schematic diagram of the various sub-zones of the HAZ approximately corresponding to the alloy C_0 (0.15 wt % C) indicated on the Fe-Fe_3C equilibrium diagram (After Easterling 1983).

microstructure, and the way in which this is affected by the weld thermal cycle (Yeomans 1994).

The HAZ can be conveniently divided into a number of sub-zones depending on the range of temperatures reached during the weld thermal cycle. These sub-zones are illustrated in Figure 1.5 for a low carbon steel (0.15% C).

1.2.3 Grain coarsened (GC) sub-zone

This sub-zone of the HAZ is closest to the fusion boundary (see Figure 1.5) and is heated above about 1100 °C and reaches a temperature of about 1530 °C at the fusion boundary. In the GC sub-zone austenite reforms and undergoes significant grain growth before cooling (Easterling 1983, Thaulow et al. 1987). The rapid grain growth was a result of $\alpha \rightarrow \gamma$ transformation during heating. The metal in this sub-zone is fully austenitized, and because of the high peak temperatures reached very rapid grain coarsening occurs (Rasanen and Tenkula 1972). As the welding heat input is increased, the time of exposure to these high temperatures increases, and as a consequence both the width of this sub-zone and the austenite grain size increase. This sub-zone consists of similar constituents to the solidified weld (SW) region in which PF(G), FS and AF form on cooling (IIW Doc. 835-85 1992). In the GC sub-zone however, the prior austenite grains are generally more equiaxed and smaller. A typical microstructure of GC sub-zone is shown in Figure 1.6 (a).

1.2.4 Grain refined (GR) sub-zone

The metal in this sub-zone is heated above 900 °C but not above about 1100 °C. The reduction in peak temperatures experienced in this sub-zone is only sufficient to reform

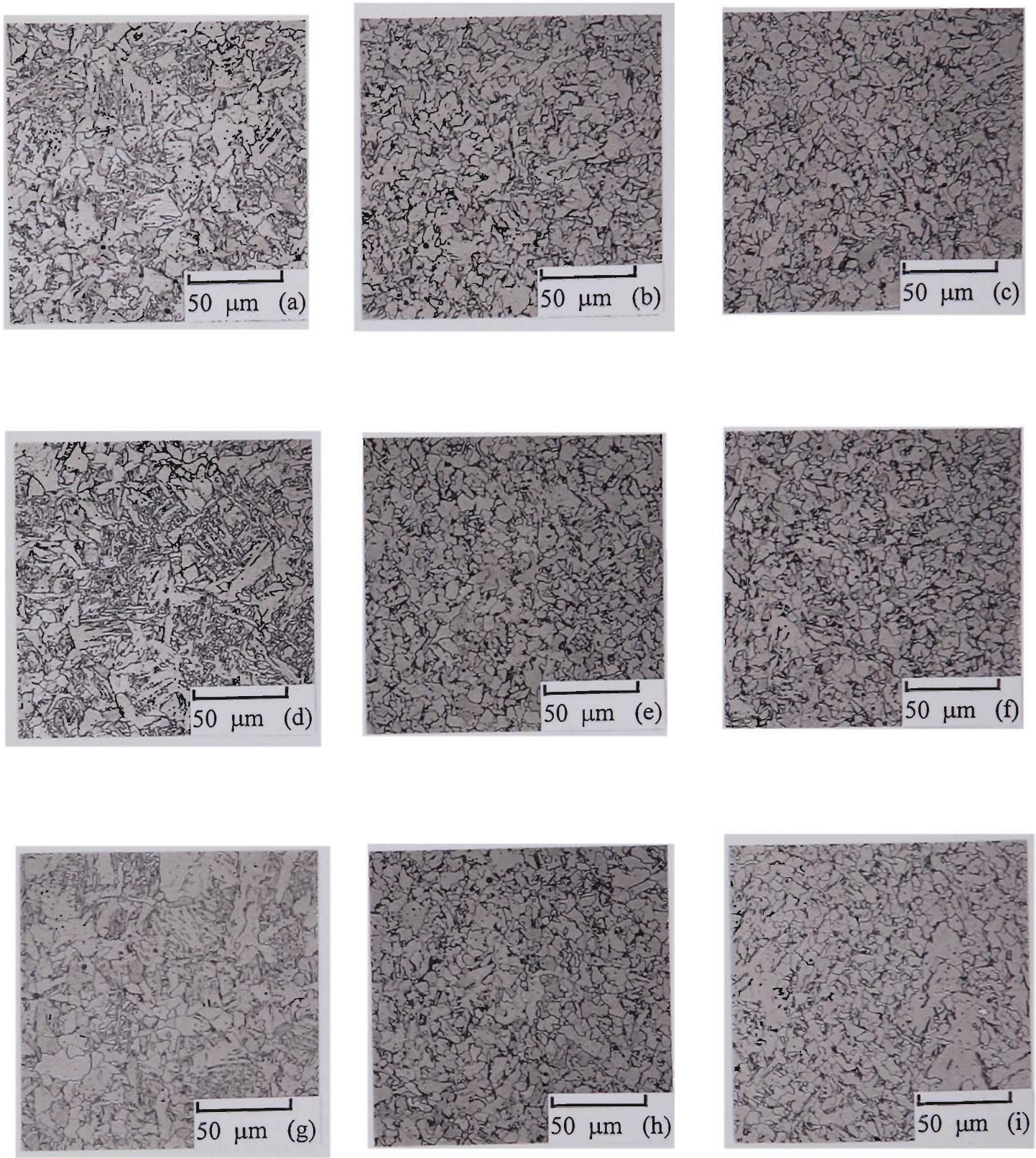

Figure 7.3: The microstructures of the double reheated sub-zones for sample R-3 at 1.44 kJ/mm heat input and CO_2 shielding gas: (a) GC-GC. (b) GC-GR. (c) GC-IC. (d) GR-GC. (e) GR-GR. (f) GR-IC. (g) IC-GC. (h) IC-GR. (i) IC-IC.

the austenite without substantial grain growth and to subsequently form a fine equiaxed ferrite structure. In addition, the carbides and nitrides may not be dissolved completely. On cooling, the fine grained austenite and remaining carbides and nitrides tend to produce a fine grained ferrite plus a second constituent. The second constituent can be pearlite, bainite or martensite-austenite islands depending on the composition of the weld metal and the cooling rate (Easterling 1983). This sub-zone is often stronger and more notch tough than the SW region (Easterling 1983, French 1998). A typical microstructure of a GR sub-zone is shown in Figure 1.6 (b).

1.2.5 Intercritical (IC) sub-zone

The weld metal here is subjected to a short thermal cycle with a peak temperature between the A_{c1} (the temperature at which the transformation of austenite starts) and A_{c3} (the temperature at which the transformation of austenite finishes) range of 727 - 900 °C. In a multipass weld metal, the IC sub-zone is generally the smallest part of the HAZ. The microstructure is partially refined resulting in a slight strengthening (Yeomans 1994). A typical microstructure of an IC sub-zone is shown in Figure 1.6 (c).

CHAPTER 2

MECHANICAL PROPERTIES

The basic aims of welding operations are to produce joints which are fit for their intended purpose at an economically viable overall cost. Fitness for purpose invokes the concept of weld performance and therefore the need to assess the quality of welds to ensure their suitability for some specified application.

For any given composition (and particularly for carbon and carbon-manganese steels), one of the important factors governing mechanical properties of weld metal is the ferrite grain size. However, it must be recognized that a precise correlation between grain size alone and mechanical properties is not possible since these may be influenced by the morphology and distribution of carbides and non-metallic inclusions, the presence of grain boundary precipitates, and other features.

In general, weld metal has higher tensile and yield strength than the equivalent plate material, even when the carbon or alloy content is lower. The hardness of weld metal correlates with ultimate strength in the same way as for wrought steel, and hardness testing is used as a method of controlling weld metal strength. The notch ductility of weld metal, as measured for example by impact testing, depends mainly on composition, microstructure, grain size and inclusion content. Notch ductility is reduced, other things being equal, by the presence of proeutectoid ferrite in the structure, and particularly when it is coarse and block-like in form. Ideally, the weld metal should consist entirely of fine acicular ferrite. The notch ductility is also reduced as the amount of martensite in the structure increases (Lancaster 1993).

The hardness of the HAZ is a measure of the tensile strength of the steel and, for any given alloy type, gives an indication of the degree of embrittlement. For carbon-manganese and some low-alloy high-tensile steels, a hardness of over 350 HV in the

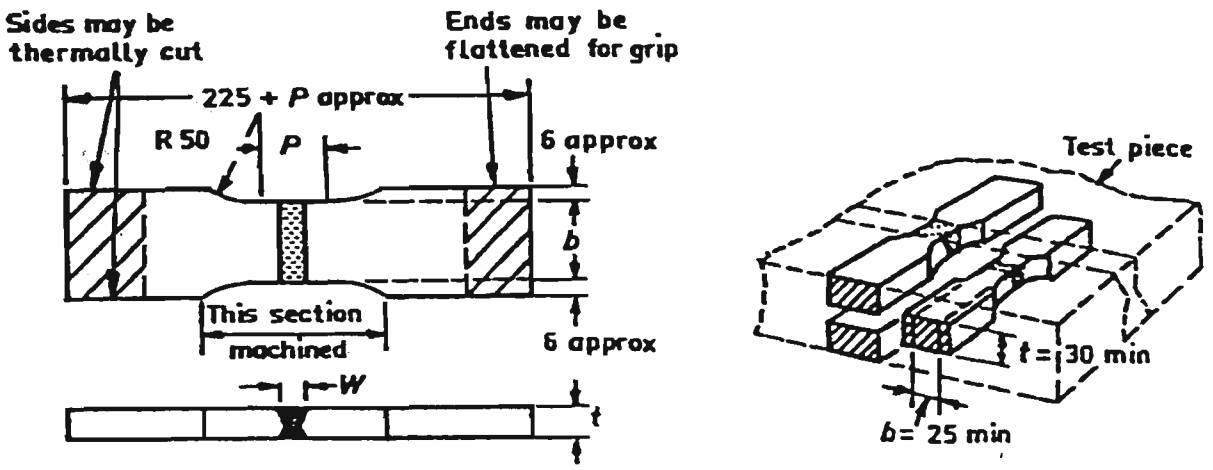

(a) Reduced Section test specimen

(b) Multiple test specimens (t>30 mm)

Figure 2.1: Transverse butt tensile test specimens (After AS 2205).

HAZ would be considered excessive, indicating a susceptibility to cracking (Lancaster 1993). In some cases all the regions of the HAZ (GC, GR and IC sub-zones) are embrittled to some degree as compared to the parent material. However, if the fracture toughness of the parent material is relatively low, the HAZ may have better properties, particularly in the GR sub-zone. The factors affecting HAZ toughness are the nature of the weld thermal cycle, grain coarsening temperature, transformation characteristics, alloy content and non-metallic content (Lancaster 1993).

The testing and assessment of welds is an important aspect of ensuring weld quality. It is also apparent that testing carried out at sufficiently early stages during fabrication (or even during the design phase of a project), can make a valuable contribution to overall cost reduction and indicate where improvements to design are needed. It cannot be over-emphasised that if a particular design of joint causes problems during fabrication, not only will welding costs themselves be increased, but the additional testing needed will also cause costs to escalate.

2.1 Tensile Tests

Tensile testing reveals a number of basic properties of metals of which the Modulus of Elasticity (E) and the yield or proof stress are of fundamental engineering significance (AS 1391).

Two variants of the tension test are in common usage for welds namely:

(1) The transverse butt tensile test to AS 2205.2.1: The transverse butt tensile test, typical geometries of which are shown in Figure 2.1, is taken as a measure of joint

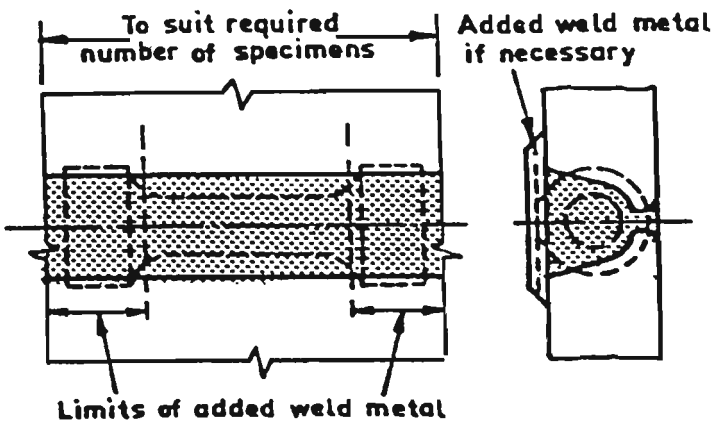

Figure 2.2: All weld metal tensile tensile test specimens (After AS 2205).

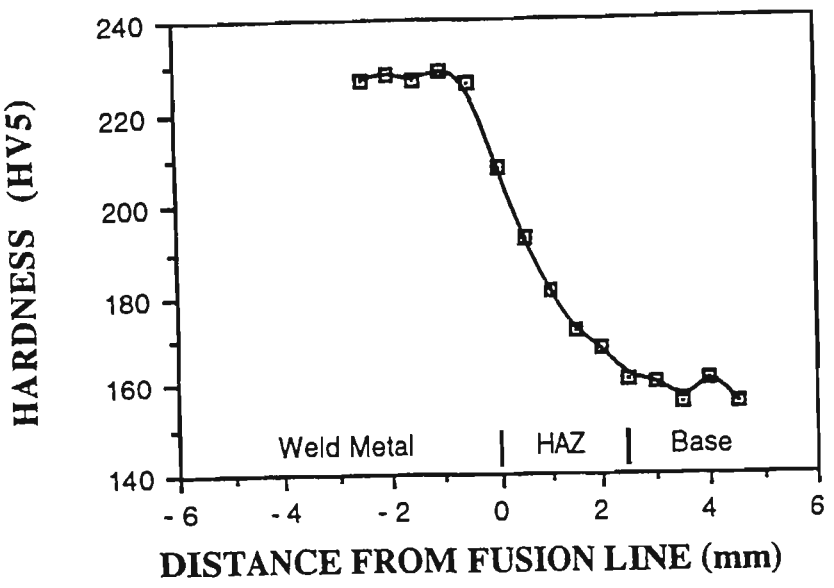

Figure 2.3: Typical hardness traverse across HAZ of C-Mn steel submerged arc welded at 5 kJ/mm heat input (After Pang 1993).

effectiveness in the sense that fracture in the base plate indicates that the weld is at least as strong as the plates being welded.

(2) The all-weld-metal tensile test to AS 2205.2.2: The all-weld-metal tensile test piece (Figure 2.2) is of most significance in consumable development and classification. Manufacture of the sample does require that the weld be made under procedures not usually adopted in practice with consequent variation in the metallurgical state of the deposit due to different thermal history.

2.2 Hardness Tests

Hardness tests are relatively easy to perform and give valuable information on variation of properties in the different regions of welded joints. Hardness depends on the hardenability of the steel. For the HAZ, it also depends on the cooling rate and, to a lesser degree, on the prior austenite grain size. It gives an indication of composition of a steel and microstructural constituents; and serves as the basis for characterising the strength, toughness and hardenability of a steel (Welland 1989). Hardness for HAZ is also regarded as a rough index describing the susceptibility to hydrogen cracking (Yurioka 1990) and correlates reasonably well with implant cracking test results (Karppi 1978, Bryhan 1981, Tanaka et al. 1976).

An example of a hardness traverse across the HAZ is shown in Figure 2.3. Hardness decreases from a maximum at the fusion line to reach a minimum in the base metal, indicating a harder microstructure as a result of a large austenite grain size in the grain coarsened region (GC) near the fusion line. A harder HAZ microstructure is formed at

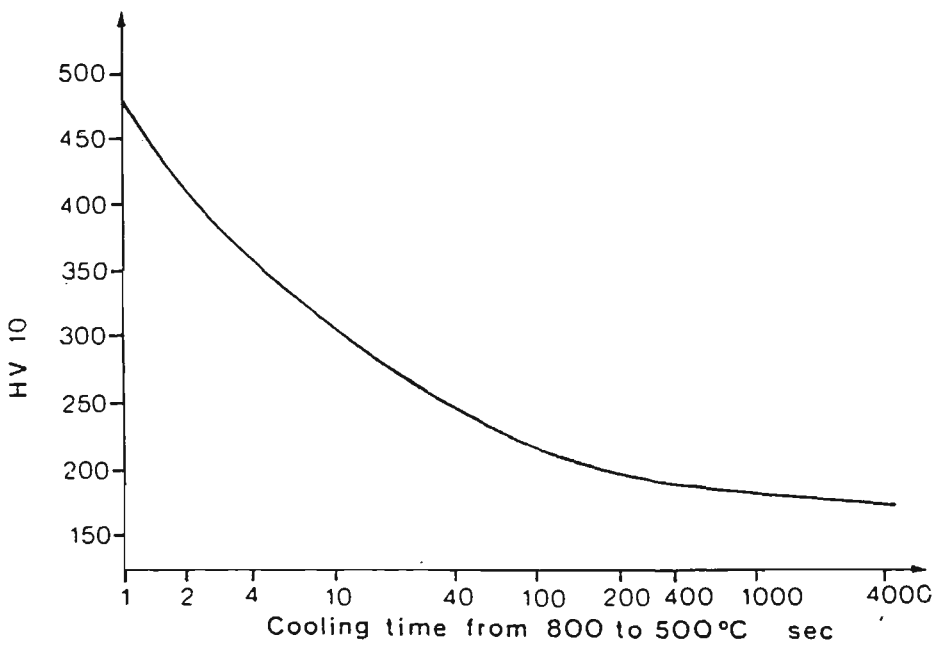

Figure 2.4: Relationship between peak HAZ hardness and cooling time from 800-500°C (Δt_{8-5}) in the HAZ of a medium strength 20 mm C-Mn steel based on several different welding processes (After Inagaki and Sekiguchi 1960).

lower heat input, or faster cooling rate. A relationship between peak HAZ hardness and cooling time $\Delta t_{8\text{-}5}$ is shown in Figure 2.4.

From experimental measurements of the weld thermal cycle it has been found that, for a given welding process, weld geometry and material, the cooling time through the range 800 - 500 °C is constant. The temperature of 800 °C is important in that in most steels it approximately represents the Ar_3 transformation temperature. The use of $\Delta t_{8\text{-}5}$ as descriptive of a given weld has now been widely adopted in welding circles. It is important to note that $\Delta t_{8\text{-}5}$ effectively represents the cooling time for a given heat input, material type, weld geometry, etc. Although it is sometimes more convenient to express the weld cycle in terms of the heat input and plate thickness, $\Delta t_{8\text{-}5}$ is directly proportional to the heat input (Easterling 1983).

Several methods of hardness testing are widely practiced notably Brinell (HB) to AS 1816, Vickers or Diamond Pyramid (VPN, DPN or HV) to AS 1817 and Rockwell (RB or RC) to AS 1815. They differ significantly not only in their suitability for various circumstances, but also in quite fundamental ways and caution is needed in applying the various correlation expressions between the tests.

Hardness depends on the hardenability of the steel, on the cooling rate and, to a lesser degree, on the prior austenite grain size. The hardenability of a steel may be generally correlated with the carbon equivalent (CE). Based on hardness and crack test data, a range of carbon equivalent (CE) formulae have been established (Hart and Harrison 1987). CE formulae have been widely used for assessing hardenability and the risk of cracking in the HAZ of steels for many years. The calculation of a carbon equivalent

level represents an attempt to describe the chemical composition by means of a single number in order to show how changes in composition affect material behaviour. A formula for carbon equivalent (CE) is convenient for assessing the effect of alloying elements on the weldability of steel, particularly of low carbon microalloyed structural steel.

One of the most widely used carbon equivalent formulae is the International Institute of Welding (IIW) formula (1967) based on an early study by Dearden and O'Neill (1940):

$$CE\ (IIW) = C + \frac{Mn}{6} + \frac{Cr + Mo + V}{5} + \frac{Cu + Ni}{15} \qquad (2.1)$$

The element concentrations are expressed in wgt %. This formula is incorporated into a British standard (1974). Ito and Bessyo (1968) proposed a formula which considerably reduced the contribution of elements other than carbon in the calculation. This formula was adopted by the Japanese Welding Engineering Society in 1983 and is given by:

$$Pcm = C + \frac{Si}{30} + \frac{Mn + Cu + Cr}{20} + \frac{Ni}{60} + \frac{Mo}{15} + \frac{V}{10} + 5B \qquad (2.2)$$

Differences between the CE(IIW) and Pcm proposed by Ito and Bessyo may be attributed to differences in the type of steels produced in each period and various formulae have been modified in similar ways (Yurioka et al. 1981, Lorenz et al. 1981, Duren 1985, Ito et al. 1985, Ito et al. 1988, Kihara et al. 1959, Stout et al. 1976, Graville 1976). The purpose of using a CE equation is to restrict the chemistry of welds to assess hardenability and help attain good weldability. Good weldability is ensured by placing a maximum allowable value on hardness which is controlled by keeping the CE

below a critical level. Limiting values of CE were proposed to ensure hardness being kept below 350HV which is generally considered to be the critical value (Bailey 1972). Carbon equivalents may be used to calculate the hardness of the HAZ using a hardness equivalent. A maximum carbon equivalent is often specified for structural steel to minimize the risk of excessive hardenability and/or hydrogen cracking.

The foregoing discussion is based on the hardenability of the base steel. The application of the various CE formulae to the weld metal is less sound because of the very coarse prior austenite grain size, the presence of a large concentration of non-metallic inclusions, compositional heterogeneity and dilution effects. As a result of dilution and weld process variations the CE can only be calculated after welding on the basis of a measured composition.

Hydrogen absorption during welding can lead to various problems that include porosity in the solidified weld metal or cracking in the HAZ (Easterling 1983). The three most important factors that determine the probability of hydrogen-induced embrittlement and cracking of welds are hydrogen content, fracture toughness of the weld metal and HAZ, and the stress to which the joint is exposed as a result of the weld thermal cycle. These factors interact in a complex manner so that a quantitative treatment of the subject is difficult. An element of unpredictability remains about hydrogen-induced cracking of welds, and the problem continues to afflict the fabrication industry in spite of much accumulation of knowledge (Lancaster 1993).

Hydrogen can readily decompose into its atomic state in iron and a very high solubility results. Hydrogen is derived from hydrogenous chemical compounds that are dissociated in the arc column. These compounds are for the most part either hydro-

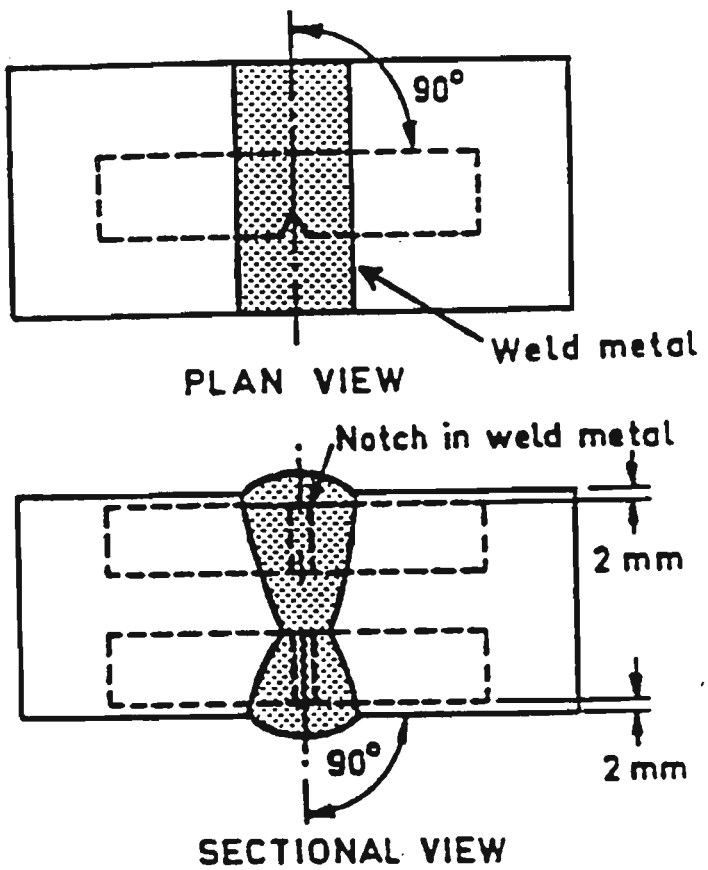

Figure 2.5: Typical locations of Charpy V-notch impact specimens for weld metal (After AS 2205).

carbons or water. In both cases they may be introduced into the arc by contamination of gas lines, electrodes, flux on the workpiece, while water vapour may be drawn in from the air. However, the most important source of hydrogen is electrode coatings or fluxes.

2.3 Toughness Tests

Charpy toughness is defined as the capacity of a material to absorb energy by deforming plastically before fracture. Despite its acknowledged empiricism, this test is still the most widely used method in attempts to control the incidence of catastrophic brittle fracture in service.

The Charpy V-notch impact test and the crack opening displacement test are the two most commonly used experimental techniques when making toughness measurements (AS 1544.2 1989, Verburg 1974). The most widely used technique to evaluate the impact properties or toughness of welds is the Charpy test. This test is believed to rank material toughness in the right order and is particularly useful in quality control testing (deMeester 1988, IIW Doc. 475 1975). The V-notch impact testing of welds is covered by AS 2205.7.1 and some typical locations of the beam specimen and notch is shown in Figure 2.5. This test method of impact testing relates specifically to the behavior of metal when subjected to a single application of a load resulting in multiaxial stresses associated with a notch, coupled with high rates of loading and in some cases over a range of temperatures. For some materials and temperatures, impact tests on notched specimens have been found to predict the likelihood of brittle fracture better than tension tests or other tests used in material specifications (ASTM Standards 1996).

Provided a correlation is available with the performance of a given material grade in service, Charpy test data can be used in a quality control role. However, there are criticisms of the Charpy test. The specific and standardised levels of strain-rate, specimen size and notch geometry used in the test, limits its direct application along for material selection, welding procedure proving, design decision-making and flaw acceptance / rejection decisions (Easterling 1983).

Since the Charpy test is useful for determining variations in fracture resistance throughout welded joints, by suitable location of the notch in various regions of the weld metal and / or the heat-affected-zone of the base plate, this can be of assistance in developing welding procedures to ensure that all regions of the welded joint have optimum resistance to crack initiation (Yeomans 1994).

2.4 Metallurgical factors

Charpy toughness, the most important mechanical property for welds, has not been the focus of basic research designed to rationalize quantitatively as a function of the complex array of variables associated with welding (Bhadeshia et al. 1995). The toughness of a steel depends on many variables, and that of a weld on many more because of the complexity of the welding process.

It is possible to choose a set of variables which should, using experience of welding metallurgy, have an influence on the Charpy toughness, providing the single effect of these can be isolated. These variables are basically divided into four major fields: chemical compositions, microstructures, non-metallic inclusions and welding conditions.

2.4.1 Chemical compositions

2.4.1.1 Oxygen

Oxygen influences welds in both beneficial and harmful ways, e.g. by helping the nucleation of acicular ferrite or contributing to fracture by nucleating cracks (Bhadeshia et al. 1995). Taylor and Farrar (1975), working with submerged arc (SA) weld metals with oxygen contents in the range 300 - 1200 ppm, reported that oxygen had a negative effect on both the Charpy upper shelf toughness and the ductile-brittle transition temperature. Ito and Nakanishi (1976), studying factors affecting impact toughness of SA weld metal, observed that while decreasing oxygen contents greatly improved the impact properties, in some instances, when the oxygen content was below about 200 ppm, there was a deterioration in the toughness. They ascribed this effect to an increase in hardenability of the weld metal due to increased matrix Si and Mn contents, which favored the formation of lath-like or bainitic structures.

Like Ito and Nakanishi (1976), several investigators reported a similar "optimum oxygen effect" on both weld metal microstructures and toughness. Watanabe and Kojima (1980), working with Si-Mn-Mo, Ti and Ti-B weld metals deposited by large current GMAW with various shielding gases, observed that 200-300 ppm oxygen was associated with the lowest transition temperature in the weld metals. Ito et al. (1982), working with the large current GMAW process, observed again that 200-300 ppm weld metal oxygen content was optimum for good toughness. Terashima and Tsuboi (1982), reporting on work carried out to develop SAW consumables for steel plates of tensile strength above 785 MPa, found that at oxygen levels both above and below 300 ppm the toughness deteriorated. Devillers, et al. (1982), working with SA weld metals with

oxygen contents in the range 200-750 ppm, observed that while increasing oxygen levels had a continuously negative effect on the Charpy upper shelf energy, the oxygen content showed an optimum level at 400-500 ppm for the ductile to brittle transition temperature. Lathabai and Stout (1985), working with oxygen contents in the range 350-800 ppm, reported that there was no optimum oxygen level found for FCA weld metals, but a beneficial effect was observed with increasing oxygen level at low heat input (1.6 kJ/mm).

Oxygen appears to have a significant effect on microstructural development and notch toughness of weld metals deposited by different arc welding processes. Some contradictions exist as to the exact mechanism by which oxygen affects the weld metal transformation and the oxygen content that is considered optimum for toughness. As pointed out by Ahlblom (1984) in his detailed review on the effect of oxygen on microstructure and toughness of weld metals, this has to be explained in relation to other factors that affect the weld metal toughness, such as the overall chemical composition and weld thermal cycles.

2.4.1.2 Carbon

The Metals Handbook (1964) states that the most important influence of carbon is connected with hardness, strength and ductility, and its effect on these properties may be varied by heat treatment. Steel can be simply defined as being alloys of iron and carbon. In plain carbon steels, carbon is the controlling element in determining the mechanical properties.

Increasing the carbon content of steel can lead to increased strength, hardness, brittleness and reduced ductility, but it can also lead to inferior weldability (Bain and Paxton 1961, Siebert 1977). Therefore, the carbon content of normal structural steels is limited to a maximum of approximately 0.2 %.

2.4.1.3 Manganese

Manganese is a strong deoxidising element and is used as such in steelmaking. In general, it increases strength and may lead to better ductility and toughness. Manganese is soluble in both α-Fe and γ-Fe and also forms a carbide. As the manganese content is increased the eutectoid carbon content is lowered, occurring at 0.67 % C with the addition of 2.0 % Mn (Desforges et al. 1976, Lula 1986).

Evans (1978), working with MMA welds with manganese content in the range 0.66-1.82 %, reported that increasing manganese refined the acicular ferrite; refined the coarse grains; reduced the grain size of the equiaxed fine grained zone; and the yield and tensile strengths of the deposits were increased by approximately 10 MPa per 0.1% increase of manganese. The optimum impact properties of as welded and stress-relieved deposits were attained at 1.5 % manganese, due to the competitive influence of yield strength and microstructure.

2.4.1.4 Silicon

Like manganese, silicon is also a strong deoxidising element and it has a similar effect on the microstructure (Bhadeshia 1995). Steels with silicon contents up to 0.75 % have increased strengths without any appreciable loss in ductility, simply because the silicon

enters into solution in ferrite and does not form carbides. In their detailed review of alloying elements in steel, Bain and Paxton (1961) pointed out that silicon might induce resiliency and toughness.

2.4.1.5 Sulphur

Sulphur exists in steel chiefly as ferrous sulphide. It reduces ductility and is therefore kept as low as possible. For this purpose, the sulphur content should be less than 0.03 %. The more extensive solidification range of sulphur also makes this element particularly dangerous in connection with hot cracking (Easterling 1983). However, the brittleness caused by sulphur is used to advantage in production of the free cutting steels (Dennis 1963).

Sulphur is also an impurity element which occurs in all commercial steels. Sulphur combines with manganese to form manganese-sulphide non-metallic inclusions. The adverse effect on transverse impact energy values of elongated manganese sulphide stringer inclusions is well known. If present in large amounts as elongated stringers, MnS can adversely effect the toughness (Yeomans 1994).

2.4.1.6 Phosphorus

In general, phosphorus is considered to be one of the most harmful elements found in steel. Its most detrimental effect is on impact resistance (Dennis 1963, Yeomans 1994), and for amounts exceeding 0.1 % it makes the metal brittle under shock loading conditions. However, in spite of the brittleness conferred on the steel, it is of interest to note that phosphorus actually increases the strength and hardness of steel to

approximately the same degree as carbon. Phosphorus also increases resistance to atmospheric corrosion and amounts up to 0.12 % are added to some HSLA steels for the purpose of increasing strength and corrosion resistance.

2.4.1.7 Titanium

Titanium has a strong affinity for oxygen, nitrogen and carbon and it is through these interactions that titanium plays its role as an alloying element in steel. Titanium is used infrequently as a deoxidiser, but its strong nitride and carbide forming tendencies are usefully employed in a number of different types of alloy and low-alloy steels.

Small amounts of strong carbide and nitride forming elements, such as Ti can retard austenite grain growth. Therefore, titanium is added to steels to achieve grain refinement. In addition to grain pinning, these microalloying elements play a useful role in achieving adequate levels of strength and toughness in the steel, as well as in the HAZ of welds. However, in practice, the amount of microalloying elements does not always relate to a finer grain size. This is because the final effect of microalloying elements on restriction of austenite grain growth depends on particle solubility, stability and formation temperature, as well as on the composition of the steel. The particle size is also considered important for pinning austenite grain growth. In general, particles with size less than 0.05μ are effective for grain boundary pinning while those with size of approximately 0.05μ are effective for intragranular ferrite nucleation.

It was demonstrated (McCutcheon et al. 1983, George and Irani 1968, George et al. 1971, Edward et al. 1986, Apps and Andrade 1985, Uwer et al. 1990) that by small additions of Ti, austenite grain size control could be achieved for the reheating cycle

experienced in welding. Because of the marked grain-refining effect of titanium, it might also be expected that the use of this element in small quantities would improve the low temperature impact resistance of steel. However, as was indicated by Comstock (1955), this is not always true.

2.4.1.8 Aluminum

Aluminum is widely used as a deoxidiser during steel making and, in small controlled amounts of about 0.01-0.03 %, for the control of austenite grain size. Aluminium is used as a genuine alloying element in the AISI 7140 nitriding steel, in which the extremely high hardness of the nitrided case is due to the formation of hard, stable aluminum nitride particles (Yeomans 1994).

Aluminum is generally used for the control of austenite grain size in heat treatment of steel but it has little effect on HAZ toughness. However, aluminum in weld metal has a complicated effect on toughness which depends on the amount of oxygen and other elements that are present (Koseki et al. 1997 and Horri et al. 1986).

Evans (1991) reported that for a balanced basic low-hydrogen electrode, of a specific slag base type, the following occurred on increasing from zero the amount of aluminum in the coating: the hardness of as-deposited metal tended, in the main, to increase; the tensile properties of the deposits marginally increased; and optimum notch toughness characteristics were exhibited at the zero aluminum level. Following a decrease in toughness from zero aluminum, a small recovery in toughness was encountered at an aluminum content of 350 ppm.

2.4.1.9 Boron

Boron is added to steel to improve hardenability. Boron treated steels usually have a boron content of 0.0005-0.003 % B. This small amount of boron appears to be the optimum range for enhancing the hardenability effects of other alloying elements and because of this role in steel boron has been described as an alloy intensifier.

Boron can be successfully utilized to improve the toughness of welded joints in Ti-containing steels. Toughness increases with increase in boron content, but decreases when boron content exceeds 15 ppm (Nakano et al. 1986). The improvement in toughness due to boron is considered to result from reduction of free nitrogen, arising from the dissolution of small TiN particles near the fusion line. Boron is considered to fix free nitrogen as BN at an early stage of the weld cooling cycle. Any free boron, however, tends to segregate to the austenite grain boundaries (Yamanaka and Ohmori 1977, Paju et al. 1991) increasing the hardenability. The promotion of intragranular AF formation is considered to be favourable for toughness. However, the enhanced hardenability can promote the formation of hard and brittle constituents or martensite-austenite (M-A) constituents near the grain boundaries (local brittle zones), particularly after intercritical reheating. This kind of structure is reported to be detrimental to toughness (Tomita et al. 1985).

2.4.1.10 Molybdenum

Molybdenum is added to steel chiefly to improve hardness and retain strength at elevated temperatures. A noticeable feature of the addition of molybdenum is the decreased resistance to temper brittleness when the severity of the service conditions

tends to cause brittle features. Therefore, alloy steels containing 0.15-0.30 % Mo show a minimum susceptibility to temper embrittlement (Dennis 1963, Yeomans 1994).

Molybdenum as an alloying element in steel can form a solid solution with the ferrite phase and, depending on the molybdenum and carbon content, can also form a complex carbide. In low carbon steels it is largely in solid solution in the ferrite, while in high carbon steels in the annealed condition it is largely present as carbide. Bain and Paxton (1961) concluded that the principal functions of molybdenum are to: (a) raise austenite coarsening temperature; (b) contribute to deep hardening; (c) raise high temperature strength and creep resistance; and (d) enhance corrosion resistance in stainless steel, especially in chloride solutions.

2.4.1.11 Nitrogen

Nitrogen can be absorbed in the weld pool during arc welding and the saturation level for nitrogen is about equal to the equilibrium solubility at 1 atm pressure. As such air is a particularly unfavorable atmosphere for the arc welding of steel. Nitrogen has a large effect on toughness, as has been well established experimentally (Svensson 1994, Lau et al. 1987, Oldland 1985, Ahlblom et al. 1986, Grong 1988). Nitrogen's detrimental effect is via causing porosity and embrittling the weld deposit. Porosity appears when the nitrogen content exceeds about 0.045%. Nitrogen in the form of FeN has a severely embrittling effect on weld metal. Furthermore, nitrogen in a carbon or carbon-manganese steel may be responsible for strain age embrittlement (Lancaster 1993).

2.4.2 Microstructure

The microstructural characteristics which generally cause a toughness deterioration in the weld metal are as follows: (1) coarse grains (Dolby 1979, Pisarski and Pargeter 1984); (2) upper bainitic structure; (3) martensite-austenite (M-A) constituent (Yoshikawa et al. 1988, Yang et al. 1986); (4) a high proportion of twinned martensite with a relatively high hardness (Uchino 1986, Eichhorn and Pyrasch 1986, Akselsen et al. 1988); (5) age hardening occurring in the slow cooling stage or during post-weld heat treatment (Pang 1993).

In order to explain changes in toughness, many investigators have carried out detailed microstructural analyses with a view to correlating the changes in notch toughness with changes in microstructure in different regions of the weld metal. In solidified weld metal (SW) regions, it is apparent that microstructures consisting predominantly of fine, interlocking laths of ferrite, referred to as acicular ferrite (AF), are the most desirable from a toughness point of view. AF consists of fine interlocking laths of ferrite separated by high angle boundaries and their basket-weave aspect is responsible for the high crack propagation resistance (Lalan et al. 2000, French 1999, French 1998, Liu 1992). In contrast, a structure made up of large proportions of grain boundary ferrite (PF(G)), intragranular polygonal ferrite (PF(I)) and ferrite with second phase (FS) have been found to be detrimental to toughness, because these structures provide preferential easy crack propagation paths, which offer a low resistance during the weld metal cleavage fracture (French 1998, Abson and Pargeter 1986, Grong and Matlock 1986, Farrar and Harrison 1987).

While the above constituents are the main structures present in the SW regions of welds in normal structural steels, minor amounts of microphases can be present, such as retained austenite, martensite, martensite-austenite islands or carbide. It has been claimed that small and isolated regions of microphases do not have a large influence on cleavage resistance (French 1998), but networks of hard islands can have an adverse effect on fracture resistance (Akselsen et al. 1988).

In the reheated region, the GC sub-zone consists of similar constituents to the solidified weld metal (ie PF(G), FS and AF). The resistance to cleavage crack propagation offered by this sub-zone will be similar to, or higher than that offered by solidified weld metal since propagating cracks will at least as frequently encounter grain boundaries. In contrast, the GR sub-zone is highly resistant to cleavage crack propagation, because this sub-zone consists of fine grains separated by high angle boundaries (French 1998).

In general, it appears that the microstructure of solidified weld metal provides the weakest link in determining the impact behaviour of weld metal at low temperature because this is the microstructure that potentially gives the lowest resistance to cleavage crack propagation (French 1998).

2.4.3 Non-metallic inclusions

Non-metallic inclusions in weld metals are the result of chemical reactions which take place during solidification. Most weld metals contain a population of non-metallic inclusions consisting of those products of deoxidation and desulphurisation reactions that have not escaped the weld pool. The volume fraction of inclusions in a weld proposed by Kluken and Grong (1989) is defined as:

$$V_f = \{5\,(O) + 5.4\,(S - 0.003)\}\,10^{-2} \qquad (2.3)$$

where O is oxygen content and S is sulphur content in weight per cent. As sulphur is usually low in modern welds, consequently, oxygen content becomes the major variable. Weld metal oxygen content depends on the welding process, the type of slag system used, flux, consumables, cooling rate and the shielding gas (French 1998, Lathabai and Stout 1985, Kiessling 1989).

Abson et al. (1978) proposed that oxygen contents in the range 200-300 ppm could nucleate, intragranularly, the fine laths of acicular ferrite. The coarse inclusions associated with higher oxygen contents, they proposed, were not efficient as nucleation sites and the few inclusions at lower oxygen levels favored bainitic structures with lower toughness. Ito et al. (1976, 1982) proposed that TiN and oxide non-metallic inclusions nucleated the desirable acicular ferritic structures at the optimum oxygen levels. They concluded, based on dilatometry, that low oxygen contents increased hardenability, producing lower bainitic structures. Lower bainite is relatively tough, while upper bainite is low in toughness. High oxygen decreased hardenability, producing coarse grain boundary ferrite and ferrite with aligned carbides, and that these structures were responsible for the lower toughness.

Cochrane and Kirkwood (1978) suggested that the coarser inclusions associated with higher oxygen contents could pin the austenite grain boundary and serve as nucleation sites for Widmanstatten ferrite at the grain boundaries, leading to the formation of a microstructure consisting of large proportions of ferrite with aligned carbides. Farrar and co-workers (1981, 1982) also proposed that the high volume fraction of oxide-rich

inclusions in high oxygen weld metals affects the austenite to ferrite transformation by pinning the austenite grain boundary-nucleated transformation products, such as grain boundary ferrite and ferrite with aligned carbides. They also observed some evidence of the nucleation of fine, intragranular acicular ferrite on inclusions.

Several investigators have tried to identify the conditions under which non-metallic inclusions can nucleate acicular ferrite in ferritic weld metal. While some have considered TiN to be the nucleating species (Ito and Nakanishi 1976), others think that oxide inclusions are responsible for the nucleation. Some investigators consider oxides of Ti to be essential for the nucleation because of the low lattice disregistry between TiO and ferrite (Watanabe and Kojima 1980, Mori et al. 1981). Aluminum-rich inclusions are favored by others (Bhatti et al. 1984). Still others think that a certain size distribution is essential.

While it is obvious that non-metallic inclusions have some influence on microstructural development, it has also been suggested that they can have a direct influence on toughness, especially in the upper shelf region, because of the role they play in the micro-mechanisms of ductile fracture. Kiessling (1989) found that, in the ductile fracture regime, the toughness of the weld metal can be detrimentally affected by the inclusions, because they are potential sites for void nucleation. Therefore, it was suggested that the toughness of the weld metal will be reduced with an increase in the number and size of the inclusions. Significant numbers of inclusions larger than about 1μm directly influence cleavage fracture resistance because these inclusions can act as initiation points for cleavage cracks (French 1998, Tweed and Knott 1982). Ductile

crack growth will also be promoted by an increased size and decreased separation of inclusions (Chin 1969, Van Stone et al. 1985).

2.4.4 Welding conditions

The weld metal microstructure and properties are affected by changing welding conditions such as heat input, shielding gas, interpass temperature, welding technique and welding position. Although the individual effects of current, voltage and welding speed are relatively unknown, increasing heat input usually results in a coarse structure due to slow cooling. The coarse austenite grains enhance the formation of undesirable microstructures, such as coarse grains and upper bainite. Reducing heat input (fast cooling rate) refines the microstructure, eliminates the formation of these unfavourable structures and consequently improves the toughness (Illin and Razikov 1966, Amano et al. 1986). However, there is a critical heat input value to avoid the formation of twinned martensite which has been reported to cause degradation of toughness (Lebedev et al. 1986). In general, there is an optimum heat input which gives the highest toughness value for the weld metal.

Although increasing heat input is generally believed to be undesirable because of formation of coarse structure, high heat input welding can be used in fabrication, provided the materials can still satisfy the mechanical property requirement, particularly in the weld metal. High productivity (high heat input) welding procedures have been reported to be satisfactory for some steels (Pang et al. 1991, Ahmed and Yellup 1988) for a restricted range of welding conditions. A high heat input can also prevent the formation of susceptible microstructures containing low temperature

transformation products. Thus a high heat input can lead to a reduction in susceptibility to cold cracking.

Shielding gases play an important role in the arc welding process. They have the dual purpose of protecting the arc and weld pool from contamination by air and providing a suitable medium for the stable operation of a sustained low-voltage arc. The toughness of the weld is affected by the interaction of the shielding gas with the base metal and with the filler material.

A mixture of gases is generally required for shielding in order to satisfy the requirements of most material-process combinations. For FCA welding, the generally used shielding gas is a mixture of argon and CO_2. The composition of the shielding gas has a significant effect on the mechanical properties of the weld. A change from pure CO_2 to 75% argon and 25% CO_2 shielding generally increases tensile strength by about 10%, because manganese and silicon strengthen the weld metal (Metals Handbook 1983). These elements also work as deoxidizers. When a more oxidizing shielding gas is used, the manganese and silicon form oxides that evolve from the weld metal, thus lowering strength. However, a pure CO_2 shielding might give a higher arc efficiency than for welds produced by Ar gas mixtures, so that the effective heat input could be higher.

By the selection of welding technique, heat input can also be controlled or minimized. There are two predominant types of welding techniques, stringer and weave beads, which are used in modern welding. The stringer bead is generally preferred because heat input is minimized and welding parameters such as welding speed are very easy to control. However, a high heat input can be achieved by applying the weave bead

technique, if it is needed. If a weave bead technique is required, the weave should not exceed two to three times the electrode diameter (Metals Handbook 1983).

The position of the weld significantly affects the selection of the welding process. For example, welding in the overhead position cannot be accomplished with processes that produce large volumes of molten metal, such as SAW, ESW and SMAW. Among all the welding positions, the horizontal and vertical positions are mostly widely used, because other positions such as overhead joining can be handled by rotating the base metal to a more convenient position. Evans (1981) conducted a detailed study on changing welding position between horizontal and vertical with MMA welding and pointed out that changing welding positions may influence chemical contents, microstructures and consequently, the mechanical properties, because heat flows during welding were different between the flat and the vertical welding positions.

CHAPTER 3

MODELLING OF STRUCTURES AND PROPERTIES OF WELD METAL

In order to assure the quality of welds, factors determining quality have to be taken into consideration as have possible defects and their prevention in the planning stage. Due to the complex processes involved during welding, regression analysis is mainly performed, in which the most significant factors are considered with respect to one particular aim (strength, hardness, toughness etc.) in one single equation. Very often linear multiple regression analysis or polynomial regression is used, without consideration of the relevant mechanistic phenomena. Although such approaches may give useful results, they are not able to describe effects on a mechanistic basis. In contrast to this procedure, there are complex physical models which take into account governing mechanisms and the sequential effect on the desired property.

3.1 Regression Analysis

Welding phenomena have in the past been developed empirically, with some assessment of mechanical properties, and by drawing on accumulated experience. This method has been very successful, as evident in the popularity of the process in many engineering applications. In order to perform quantitative predictions of the effect of influencing parameters, it is usual to use empirical equations which take into account the most significant parameters. Using a large set of experimental data and by multiple regression analysis, predictive equations can be derived. The key element for a successful application is the choice of the parameters without knowledge of the dominant mechanisms involved.

For deriving an empirical equation, first of all, it is necessary to have a well-balanced set of experiments regarding the various influencing factors so that the effect of a single influencing factor (by keeping others constant) can be assessed. If this is not done, a

robust equation type cannot be found, and only linear multiple regression analysis can be carried out. Premises and assumptions made by experimenters are most often based on the results of single-factor experiments. This requires many experiments where no allowance is made for the mutual effect of all the factors. It should also be noted that the application of any regression equation requires the validity range to be taken into account concerning chemical composition, welding parameters etc. Furthermore, it is not surprising that the different empirical equations give quite different results (Buchmayr 1995a, Blodgett 1979).

It has been pointed out by Buchmayr (1995 b) that the predictability of the toughness behaviour is very poor because the synergistic influences and optimum contents of microalloying elements are very difficult to understand and to model physically. However, in order to predict optimum combinations of microalloyed elements, some empirical equations have been derived from experimental investigations (Baumgardt and Strassburger 1985, Evans 1991,Burchmary 1990). Although regression approaches may result in a limited applicability, the vast majority of investigators seem to be satisfied with regression equations which relate, for example, chemical composition to mechanical properties.

The advantages and disadvantages of regression analysis have been summarized by Buchmayr (1995a) in a detailed review. The advantages of empirical equations are as follows: simple to derive; wide applicability, goal-oriented approach, determination of the significance and the effect of the influencing factors; good prediction accuracy. The drawbacks for these equations are: require well-balanced empirical data; just one goal value can be predicted; validity only in a limited parameter range; microstructural causalities are taken into account insufficiently; non-linear influences are seldom

considered. The typical applications for empirical equations are property prediction and process control.

3.2 Physical Modelling

Physical modelling of welding is a rapidly emerging new field of research in which analysis, in conjunction with appropriate experimental studies, is used to make predictions of microstructural and property changes in welds. Although regression analysis has been very useful for the influence of a single parameter, additional problems arise when there are mutual influences between the parameters. In these cases, reliable equations cannot be found and such an approach is not applicable. In order to solve such complex and multiphased problems, more and more researchers now try to simulate dominant processes on a physical basis. This approach allows a correct chaining of various phenomena and their interactions as well as the prediction of the multiple effect on the influencing factors.

3.2.1 Physical modelling for microstructure

Physical models for the development of microstructure have the potential of revealing new phenomena and properties. They can also help identify the controlling variables. The ability to model weld metal microstructure relies on a deep understanding of the phase transformation theory governing the changes which occur as the weld solidifies and cools to ambient temperature. The weld phenomena, which are based on physical fundamentals, are categorized by Buchmayr (1995b) and shown in Table 3.1.

Table 3.1: Weld phenomena which are based on physical fundamentals.

Phenomenon	**Mathematical Component**
Fluid Flow	Navier-Stokes eqn
Heat Conduction	Fourier's Law
Diffusion	Fick's Laws
Heat & Mass Transfer	Convective Transport
Eletrodynamics MHD	Maxwell's eqn
Phase Diagrams	Thermodynamics
Rate Prediction	Kinetics
Stresses / Deform	Constitutive eqns

Considerable progress has been made with the help of these thermodynamic and kinetic theories. Such as much research has been conducted in the modelling of heat and fluid flow in the weld pool (Szekely 1986, Goldak et al. 1986, Lin and Eagar 1986, Matsunawa and Yokoya 1990). Various microstructural constituents in weld microstructures have been the focus of many researchers. Several mechanisms explaining the formation of grain boundary ferrite, ferrite with a second phase and acicular ferrite have been proposed by researchers (Liu and Olson 1986, Ricks et al. 1982, Ferrante and Farrar 1982, Harrison and Farrar 1981, Dowling et al.1986, Kluken et al. 1990). Physical models have also been formulated to describe these evolutions with some success (Buchmayr et al. 1990, Easterling 1990, Vandermeer 1990). In particular, some improved understanding of ferrite formation has been developed by Bhadeshia et al. (1985, 1986, 1989a, 1989b, 1993). The fundamental character of these models fully compensates any losses of precision when compared with regression models, because of the internal physical logic. However, due to the extremely complex nature of the weld metal transformations, many aspects in these microstructures are still unclear. For instance, as pointed out by Buchmayr (1995a) there is no physical model

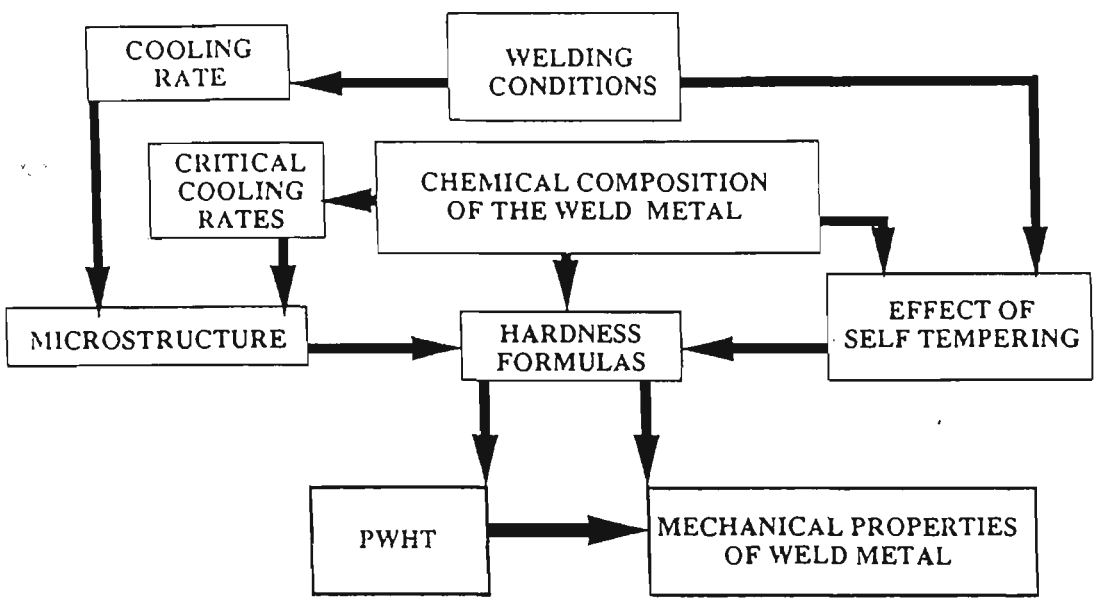

Figure 3.1: Flow chart showing how the mechanical properties of weld metal are determined (After Bourges et al. 1993).

to predict the acicular ferrite, although it is known to be very important with respect to toughness behaviour.

3.2.2 Physical modelling of properties

The progress in the modelling of mechanical properties has been very slow, especially for mathematically based models, as indicated by Bhadeshia and Svensson (1993). Although empirical equations are simple to derive, equations relating chemical composition to the strength are obviously incorrect, since tempering alters the strength without changing the chemistry.

Based on some metallurgical assumptions, Bourges et al. (1993) have established a mathematical system to predict the mechanical properties of the weld metal. The scheme of the application to weld metal properties developed by Bourges et al. (1993) is shown in Figure 3.1. From the knowledge of the austenitisation conditions, they describe the effect of chemical composition in predicting critical rates and transformation temperatures. Consequently, using the knowledge of the microstructure, they predict the mechanical properties through a simple rule of mixing the different formulae obtained for the various microstructures. The required properties of the weld metal can often be described in terms of its microstructure and composition; for example, the prediction of ultimate strength and yield point by taking into account the strengthening effect of elements in solid solution plus the contribution of different structure components. However, this system is mainly focussed on the hardness and tensile properties and Bourges et al. (1993) also stated that it is not possible today to predict completely the Charpy toughness of the weld metal. Other physical models for the prediction of hardness or strength of weld metal have been proposed by many researchers (Sugden and Bhadeshia 1988, Buchmayr et al.1990, Chaillet 1976, Grong

1994). However physical models for the prediction of toughness are only applicable for the HAZ of base materials (Grong 1994, Hrivnak 1995). There is growing evidence that mechanical and microstructural inhomogeneity of the type associated with multipass welds leads to scatter in mechanical properties, especially for toughness (Bhadeshia and Svensson 1993).

It is obvious that the prediction of property-determining parameters is very important although a physically based prediction of the effects on the toughness behaviour is not yet feasible. In other words, although many problems can be solved by numerical models, the problem of toughness is still not able to be solved in a physically correct way. But this is not a draw back from the modelling side; it is caused rather by the lack of physical understanding of toughness. For modelling experts, it is therefore frustrating to admit that the step back to empirical equations provides more useful information (Buchmayr 1995b). This means that empirical equations are the better tools, at least in some ways.

The benefits for mathematical modelling are generally regarded as follows: mechanism-based description of the effect of parameters by coupling of relevant phenomena; leading to improved understanding; and identification of further development potential. However, there are still disadvantages for mathematical modelling such as: long response time; simulation of process kinetics requires adjustment to experimental data; correlation between microstructure and mechanical properties are insufficiently understood. The typical application for mathematical modelling is to act as a tool for research and development.

3.3 Neural Networks

For quantitative assessments either empirical-based regression equations or physical models have been used in the past. These methods demonstrate the effect of influencing factors in order to optimise welding conditions. Their correct use very much depends on the range of application. However, in recent years, there are still other alternatives such as finite element analysis and neural networks. The neural network is an effective and newly developed method which is especially suitable for the assessment of mechanical properties.

In regression analysis, many assumptions must often be made about the data, and sometimes the analysis is limited to a certain number of possible interactions. In contrast, neural networks are basically non-parametric, although in theory a neural network can be thought of as being parametized by its weights. In addition, more aspects can be examined for interaction by a neural network. Their flexibility makes them able to discover more complex relationships in data than traditional regression models which assume a linear dependence of the predicted out variable on the given input variables. Neural networks are able to implement more general and more complex non-linear relationships (Zurada 1992, Hecht-Nielsen 1990, Rojas 1996, Widrow et al. 1998).

The outcome of training is a set of coefficients called weights and a specification of the functions which in combination with the weights relate the input to the output. The training process involves a search for the optimum non-linear relationship between the inputs and the outputs, and is computer intensive. Once the network is trained, estimation of the outputs for any given inputs is very rapid (Cool et al. 1996).

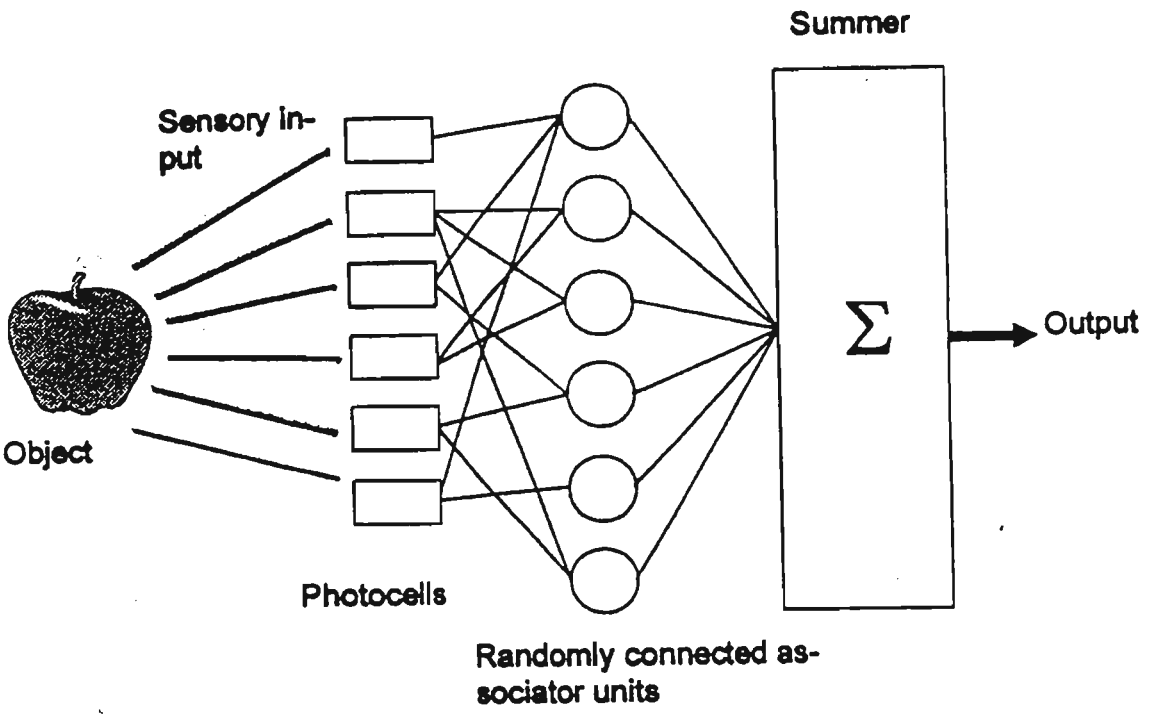

Figure 3.2: Schematic of the perceptron (After Neural Computing 1996).

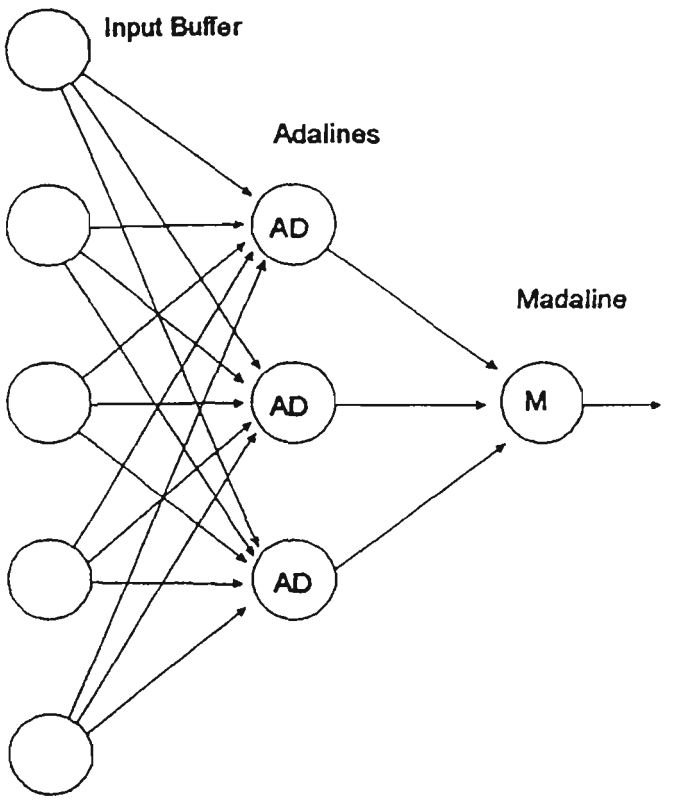

Figure 3.3: Schematic of Madaline network architecture (After Neural Computing 1996).

3.3.1 History of neural computing

In 1943, McCulloch and Pitts (1943) published a watershed paper titled " A logical calculus of ideas imminent in nervous activity." This paper was regarded as a blueprint for "electronic brains". In 1957, Rosenblatt developed an element called "perceptron" which sparked a great amount of research interest in neural computing. The perceptron is a pattern classification system which could identify both abstract and geometric patterns, see Figure 3.2. In 1959, Widrow developed an adaptive linear element, called "adaline" (Adaptive Linear Neuron), based on simple neuron-like elements. The Adaline and a two-layer variant, the "madaline" (Multiple Adaline), see Figure 3.3, were used for a variety of applications. Later, Widrow (1960) used the adaptive linear element algorithm to develop adaptive filters that eliminate echoes on phone lines. This was the first time a neural computing system was applied to a major real world problem.

In the mid-1960s, Minsky and Papert (1969) began work on an in-depth critique of the perceptron. In a published book Perceptrons, they concluded that the perceptron and neural computing were basically not "interesting" subjects to study. This led to a drastic decrease in research on neural computing at the time.

A handful of researchers continued their work in neural computing despite Minsky and Papert's book. One such researcher was Anderson (1972). He devised an extension of the linear associator, called the brain-state-in-a-box (BSB) model. Anderson describes this model: "If we start with an activity pattern inside the box, it receives positive feedback on certain components which have the effect of forcing it outward".

Despite Minsky and Papert's book, Grossberg (1976) spent much of his time devising neurally inspired mechanisms in perception and memory. In his systems, the basic units can take on any real activation value between a minimum and maximum value. The output function is a typical neural computing threshold function - a sigmoid (S-shaped) function. One class of networks he has been studying falls under the title of "Adaptive Resonance Theory".

In 1982, Hopfield (1982) developed a neural computing system called the "Hopfield Model" or "crossbar associative network". Hopfield's model represented neuron operation as a thresholding operation and illustrated memory as an information stored in the interconnections between neuron units. In fact the response mechanism and energy function of his network are a special case of the general class of networks considered by Grossberg (1976).

In 1986, Rumelhart (1986) is credited with the development of the back-propagation network which is probably the most popular network for current applications of neural computing. Many of the applications described in the previous paragraph are based on some form of a back-propagation network. The detailed description of back-propagation networks is given in the "Back-Propagation" section.

Kohonen (1988) developed the principle of competitive learning in which processing elements compete to respond to an input stimulus and the winner adapts itself to respond more strongly to that stimulus. Such learning is unsupervised in that the internal organization of the network is governed only by the input stimuli. The competitive learning paradigm was a result of a general study of self-organizing maps.

The major network types for current applications are listed as follows:

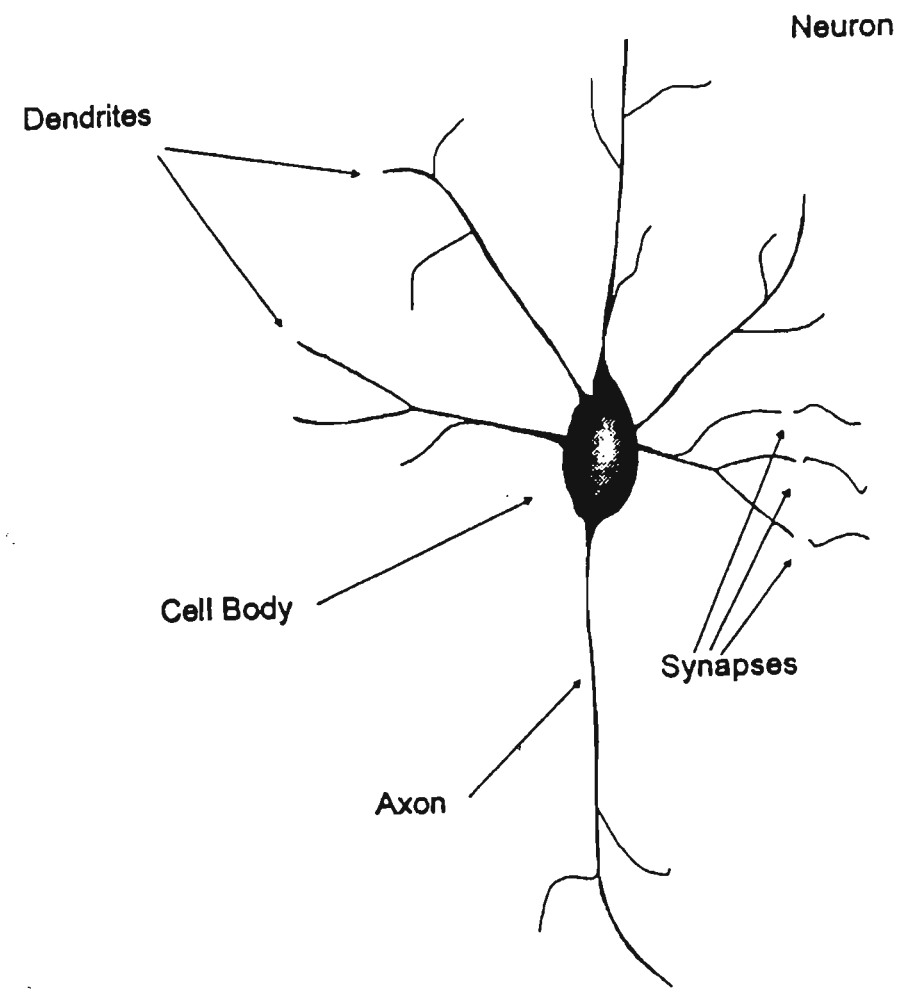

Figure 3.4: The basic structure of a biological neuron (After Neural Computing 1996).

(1) Adaptive resonance theory (ART) (Grossberg 1976).

(2) Back propagation (Rumelhart and McClelland 1986).

(3) General regression (Specht 1991).

(4) Learning vector quantization (LVQ) (DeSieno 1988).

(5) Modular (Jacobs et al. 1991).

(6) Probabilistic (Batchelor 1974).

(7) Radial basis function (Leonard et al. 1992).

(8) Self-organizing maps (SOM) (Kohonen 1988).

3.3.2 Analogy to the brain

The human brain is the most complex computing device known to man. The brain's powerful thinking, remembering, and problem-solving capabilities have inspired many scientists to attempt computer modeling of its operation.

Computers and humans are good at doing different kinds of things. A human is great at recognizing faces, while the most powerful computer can not come close to matching human performance at this task. Conversely, computers are more adept at computational tasks. Traditional computers and humans do excel at such significantly different tasks. Therefore, a suggestion comes in the ways to put together the computer and human nervous systems. A computer usually consists of one processor operating alone, executing instructions written by a programmer one at a time. Human nervous systems consist of billions of brain cells (neurons), richly interconnected to each other, doing relatively simple computations without the benefit of a programmer.

The neuron is the fundamental cellular unit of the nervous system and, in particular, the brain. As shown in Figure 3.4, each neuron is a simple microprocessing unit which

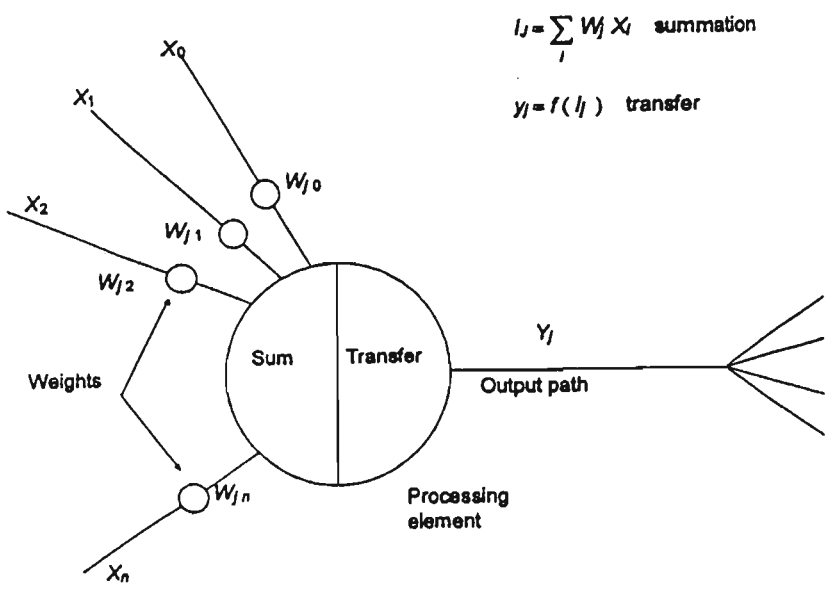

Figure 3.5: The input and output functions of a processing element (After Neural Computing 1996).

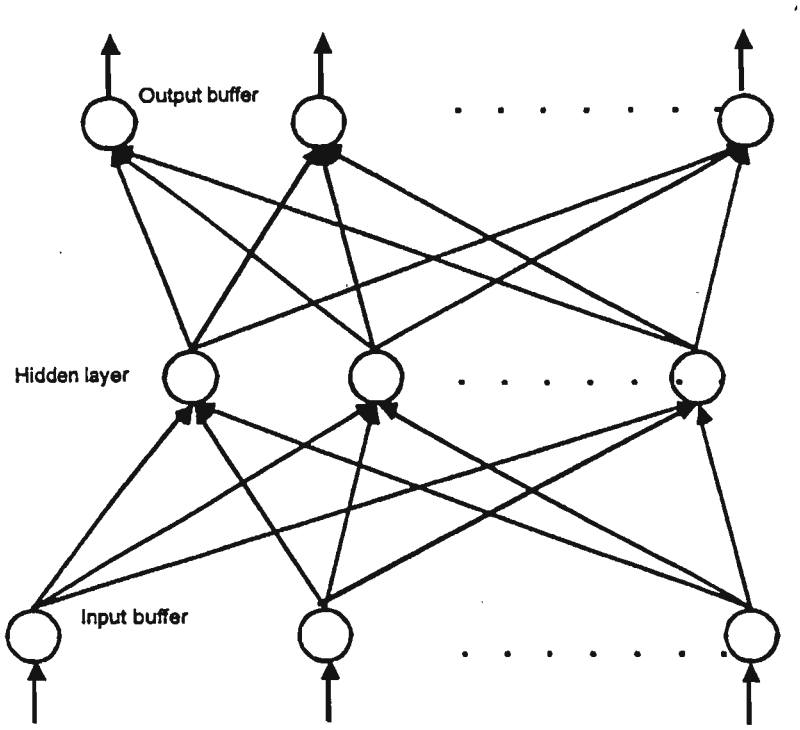

Figure 3.6: A simple neural network architecture (After Neural Computing 1996).

receives and combines signals from many other neurons through input processes (structures) called dendrites. If the combined signal is strong enough, it activates the firing of the neuron, which produces an output signal; the path of the output signal is along a component of a cell called the axon. This simple transfer of information is chemical in nature, but it has electrical side effects which we can measure.

The brain consists of tens of billions of neurons densely interconnected. The axon (output path) of a neuron splits up and connects to dendrites (input paths) of other neurons through a junction referred to as a synapse. The transmission across this junction is chemical in nature and the amount of signal transferred depends on the amount of chemicals (neuro-transmitters) released by the axon and received by the dendrites. This synaptic efficiency (or "strength") is what is modified when the brain learns. The synapse combined with the processing of information in the neuron form the basic memory mechanism of the brain.

Neural networks are human attempts to simulate and understand what goes on in nervous systems, with the hope of capturing some of the power of these biological systems (Zurada 1992, Aleksander and Morton 1995, Rojas 1996).

3.3.3 Basic structure of a neural network

In an artificial neural network, the unit analogous to the biological neuron is referred to as a processing element (PE), see Figure 3.5. The combined input is then modified by a transfer function which only passes information if the combined activity level reaches a certain level. The output path of a processing element can be connected to input paths of other processing elements through connection weights.

A neural network consists of many processing elements joined together in the above manner. Processing elements are usually organized into groups called layers. A typical network consists of a sequence of layers with full or random connections between successive layers. Sometimes PEs are connected to PEs in their own layer. Each PE processes the input it receives via these connections, and provides a continuous analog value to other PEs via its outgoing connections. There are typically two layers with connections to the outside world; an input buffer, an output buffer and hidden layers (Figure 3.6).

3.3.4 Network operation

Traditional programming techniques require that someone create an algorithm. However, it is very difficult to create an algorithm for many real world problems. In contrast to being programmed, neural networks are trained (learn) by means of feeding representative examples to the networks. There are two main phases in the operation of a network - Learning and Recall.

Learning is the process of adapting or modifying the connection weights in response to stimuli being presented at the input buffer and optionally the output buffer. A stimulus presented at the output buffer corresponds to a desired response to a given input. In such a case the learning is referred to as "supervised learning". If no desired output is shown, the learning is called unsupervised learning. Whatever kind of learning is used, an essential characteristic of any network is its learning rule. The learning rule specifies how weights adapt in response to a learning example. Once the learning is completed, recall refers to how the network processes a stimulus presented at its input buffer and creates a response at the output buffer. Therefore, a recall is often an integral part of the learning process.

3.3.5 The back-propagation networks

Among all the supervised learning algorithms, back-propagation is the most wildly used neural network (Cun 1988). Back-propagation is a technique for solving the problem of hard learning as characterised by Minsky and Papert (1969). Rumelhart and McClelland (1986) are credited with invention of the back-propagation method, while Parker (1985) introduced a similar algorithm about the same time.

Hard learning problems occur in nets that are required to map a well-defined set of inputs into a well-defined set of outputs. They can generally be solved by the introduction of hidden units. Back-propagation is the prescription originally suggested by Rumelhart and McClelland (1986) for dealing with the training of these hidden units.

If the output of a neural network is in error, criteria are required to determine which processing element or inter-connection to adjust. Back-propagation provides these criteria by assuming that all processing elements and connections contribute to an erroneous response. Responsibility for the error is affixed by propagating the output error backward through the connections to the previous layer. This process is repeated until the input layer is reached. The name "back-propagation" derives from this method of distributing the blame for errors.

3.3.6 Applications

Neural computing provides an approach which is closer to human perception and recognition than traditional computing. In situations where input is noisy or incomplete, a neural network can still produce reasonable results. Examples of applications that have met with some success using neural networks are: process control, robotics;

classification; pattern recognition on an assembly line; noise filtering; weather forecasting; determination of satellite orientation by star identification; signal analysis and processing; jet engine diagnostic systems; voice recognition; sonar interpretation; machine vision; and converting English text to phonemes (Neural Computing 1996, Using NeuralWorks 1996).

Fusion welding is very important in the fabrication of engineering structures. One of the most important requirements for such structures is that they should be able to resist brittle fracture. The weld deposits therefore have to be tough, with a great deal of energy being absorbed by the metal during the process of fracture. One test used to characterise toughness is the Charpy test. The Charpy test is empirical in that the data cannot be used directly in engineering design. It is nevertheless a useful quality control test which is specified widely in international standards, and in the ranking of samples in research and development experiments.

The toughness of a steel depends on many variables, and that of weld on many more because of the complexity of the welding process. The usual modeling is to correlate the results against chosen variables using linear regression analysis (Akelsen and Grong 1992). These methods are known to be severely limited in their application (Bhadeshia et al. 1995). In normal regression methods, the analysis begins with the prior choice of a relationship (usually linear) between the output and input variables. A neural network is capable of realising a greater variety of non-linear relationships of considerable complexity. The data are presented to the network in the form of input and output parameters, and the optimum non-linear relationship is found. In effect the network tries out many kinds of relationships in its search for an optimum fit. As in regression analysis, the results then consist of a specification of the function, which in

combination with a series of coefficients, relates the inputs to the outputs. The search for the optimum representation can be computer intensive, but once the process is completed (i.e. the network has been trained), the estimation of the outputs is very rapid (Bhadeshia et. al. 1995).

Neural network have been reported to be very effective in analyzing weldability of power plant steels (Cool et al. 1996), the effect of carbon content on hot strength of steels (Kong et al. 1998) and impact toughness of submerged arc and manual metal arc welds (Bhadeshia et al. 1995). Therefore, developing a neural network model of FCA welding is a good way to examine the diversity of factors which might exert an influence on impact toughness. It is known from experience, and from the concepts of fracture mechanics, that certain variables are more important than others in their effect on toughness. The purpose of the present work was to investigate whether an artificial neural network can be trained to predict weld toughness as a non-linear function of these variables, and whether the patterns that emerge from the work emulate metallurgical experience.

PART B EXPERIMENTAL INVESTIGATION

CHAPTER 4

EXPERIMENTAL DETAILS

4.1 Welding

4.1.1 Materials

C-Mn structural steel of 250 MPa minimum yield (Grade 250 to AS 3678, 1990) was adopted as a base material and welding was conducted by CSIRO Division of Manufactory Technology in Adelaide using commercial boron containing microalloyed rutile flux-cored (RB); metal cored (MC) and rutile flux-cored (R) wires of 1.2 mm diameter. As indicated by the classification in Table 4.1, the wires are designated E71T-1 and E70C-3 by the American Welding Society (1979). Table 4.2 gives the nominal compositions of the base metal and the nominal compositions of consumables are given in Table 4.3.

Table 4.1: Consumable classification.

Wire Types	AWS (1979) Classification	AS (1990) Classification
B Containing Rutile Flux-cored (RB) Wire	E71T-1	ETP-GMp-W503ACM1H10
Metal-cored (MC) Wire	E70C-3	ETP-GMn-W5502ACM1H5
Rutile Flux-cored (R) Wire	E71T-1	ETP-GMp-W502ACM1H10

Table 4.2: Nominal composition of base material.

wt %	C	Mn	Si	S	P	B	Cr	Ni	Al	Cu
Base Material	.16	.81	.25	.012	.019	<.001	.015	.023	.029	.01

Table 4.3: Nominal compositions of consumables.

wt %	C	Mn	Si	S	P	B
B Containing Rutile Flux-cored (RB) Wire	.05	.87	.32	.013	.014	.0048
Metal-cored (MC) Wire	.06	1.38	.59	.019	.019	-
Rutile Flux-cored (R) Wire	.03	1.43	.71	.008	.016	-

4.1.2 Joint geometry

The joint geometry for test plates was in accordance with the AWS specification (1979). Plates of 20 mm thickness and 100 mm minimum width were set-up with a 45° included angle, no land and a 12 mm root gap preparation. A steel backing plate of 10 × 25 mm was used.

4.1.3 Welding variables

The welding variables investigated were heat input, use of stringer-bead and weave-bead techniques, welding position and, to a limited extent, shielding gas. Gross heat input was varied over the range 1 to 2.5 kJ/mm for each wire. Stringer-bead techniques were used for heat inputs up to approximately 2 kJ/mm but difficulties were experienced in achieving sound welds at higher heat inputs using this technique. As a result, a weave-bead technique was used for the nominal 2.5 kJ/mm welds. In all instances the welding current (190-300A) and voltage (24-31V) values, while being within the recommended ranges for the consumable, were chosen to be optimum for the particular situation.

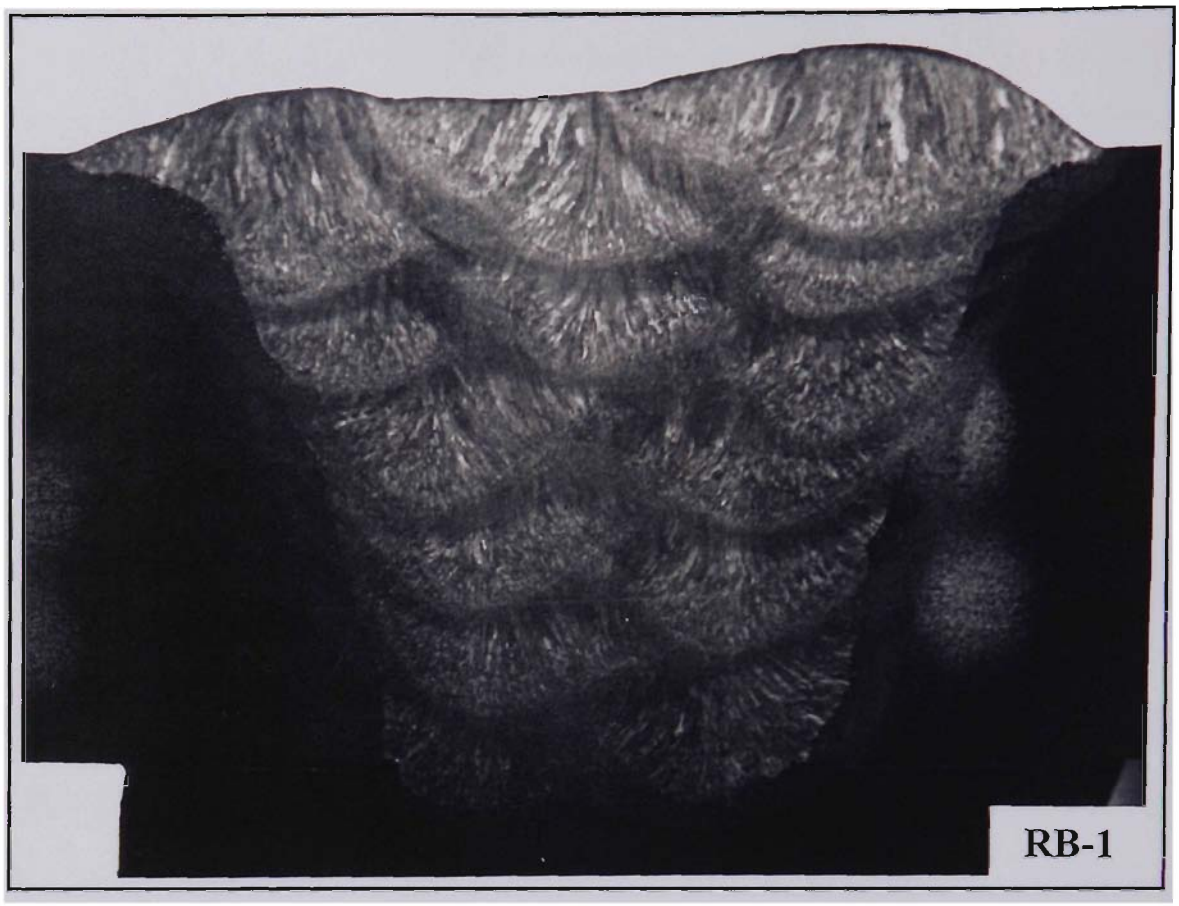

Figure 4.1: Macrostructures of samples for different consumables and welding conditions. Approximately ×4

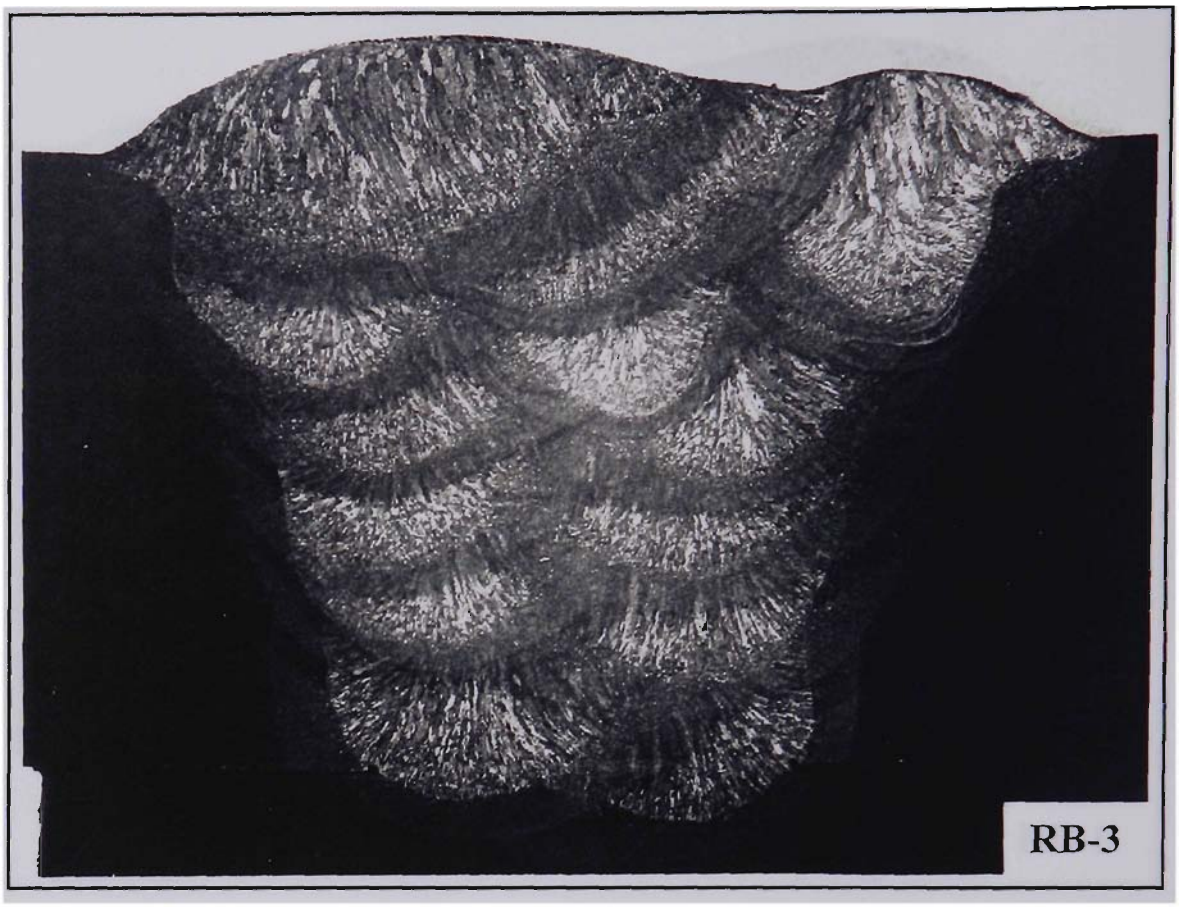

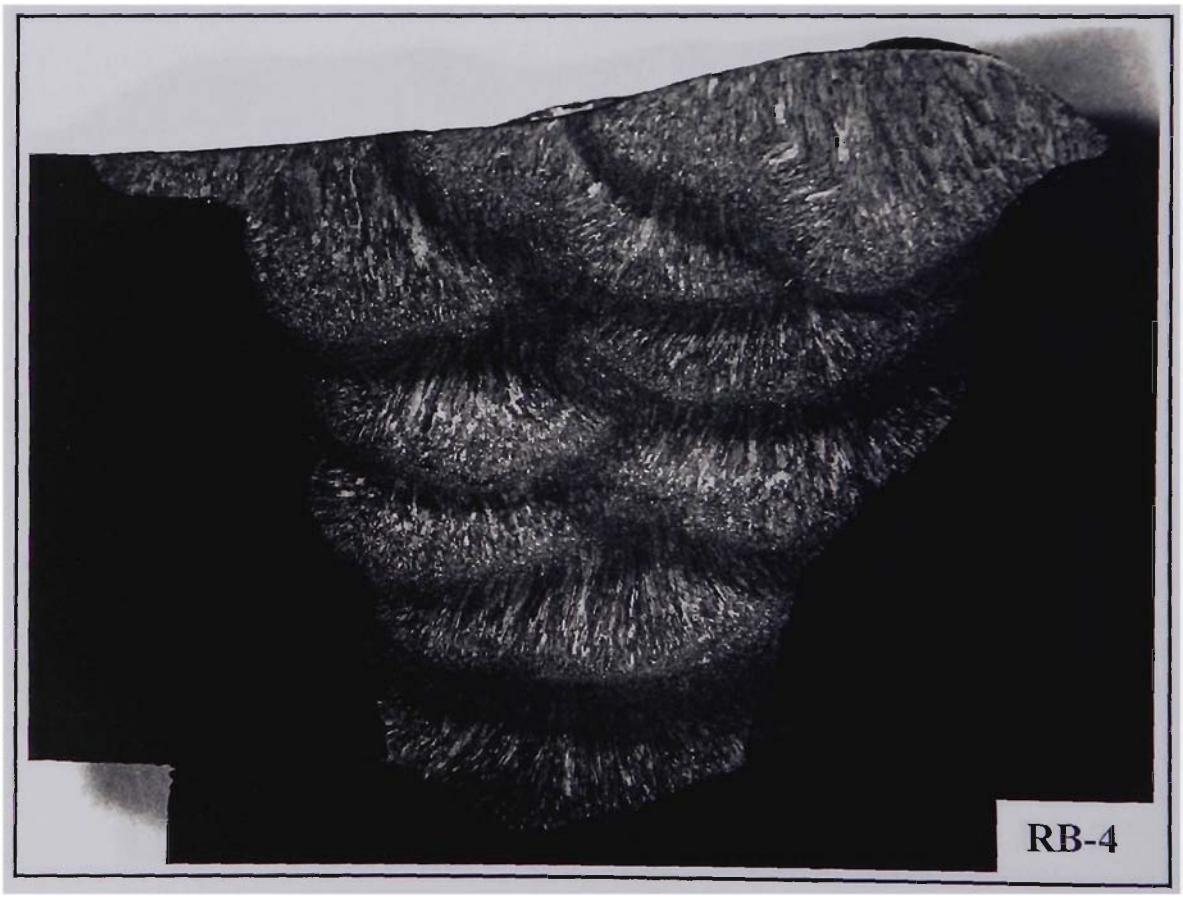

Figure 4.1: (Continued) Macrostructures of samples for different consumables and welding conditions. Approximately ×4

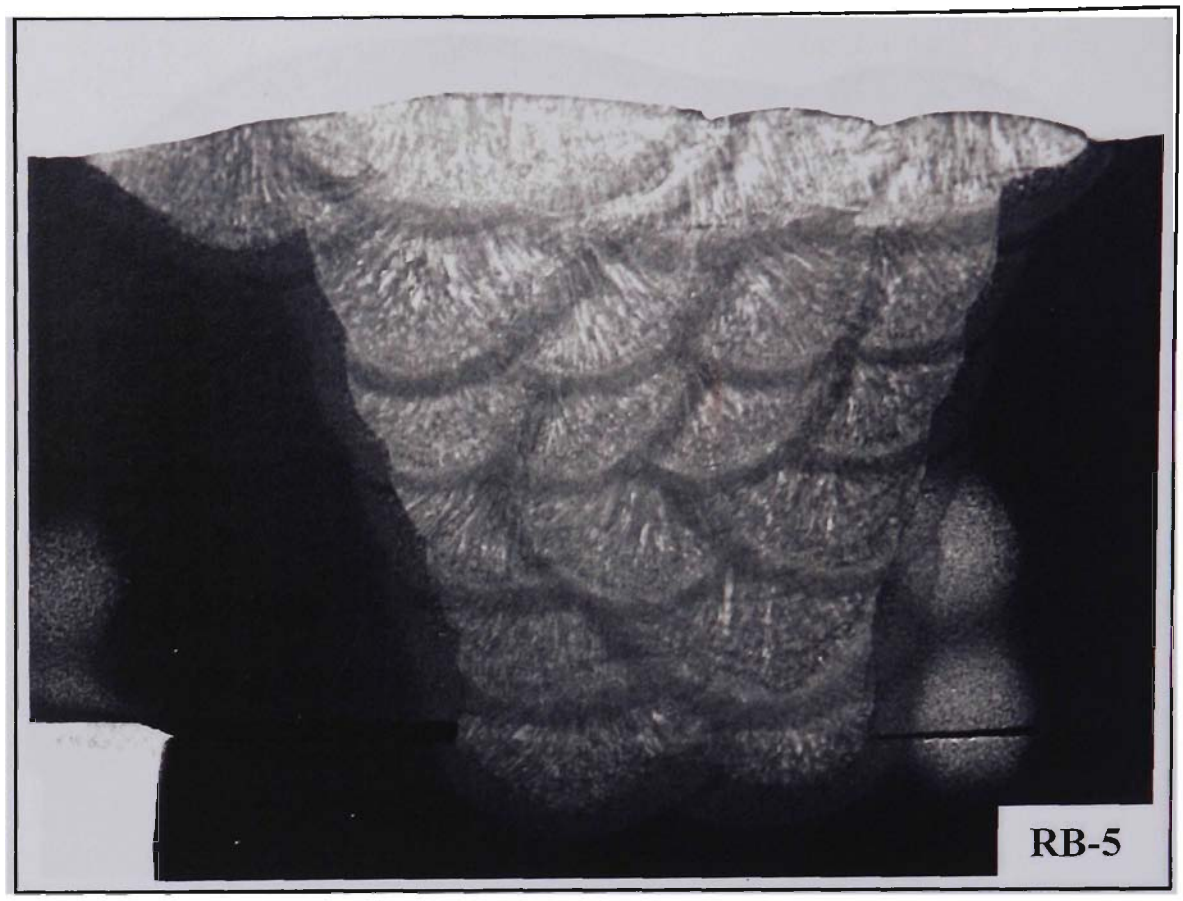

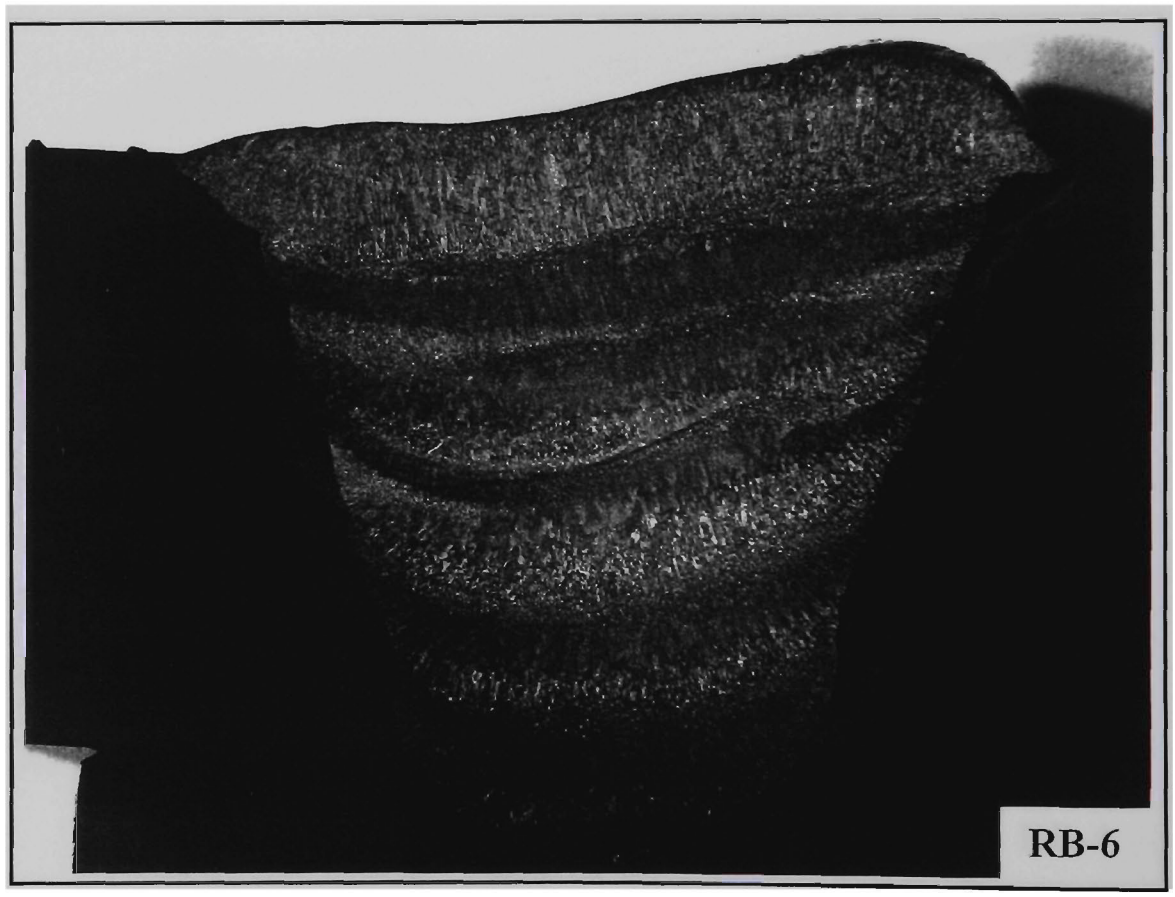

Figure 4.1: (Continued) Macrostructures of samples for different consumables and welding conditions. Approximately ×4

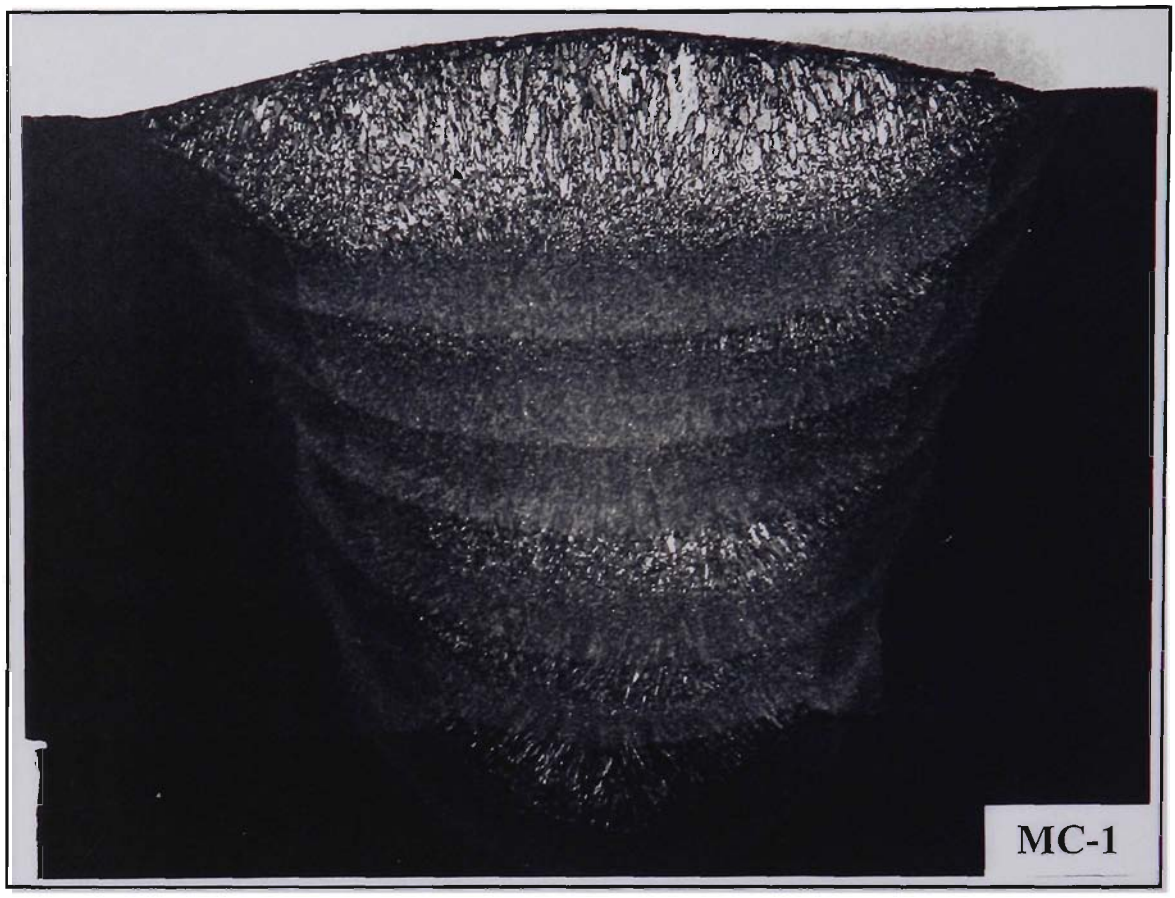

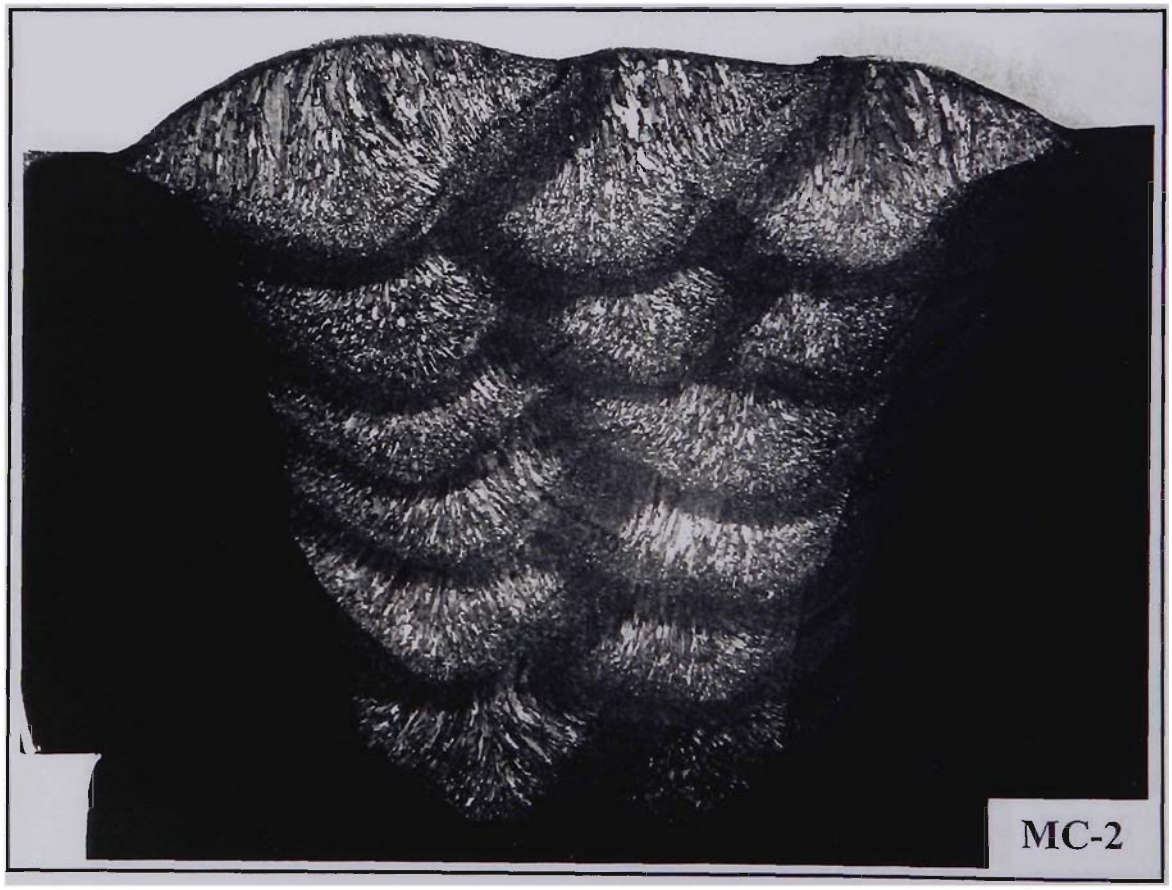

Figure 4.1: (Continued) Macrostructures of samples for different consumables and welding conditions. Approximately ×4

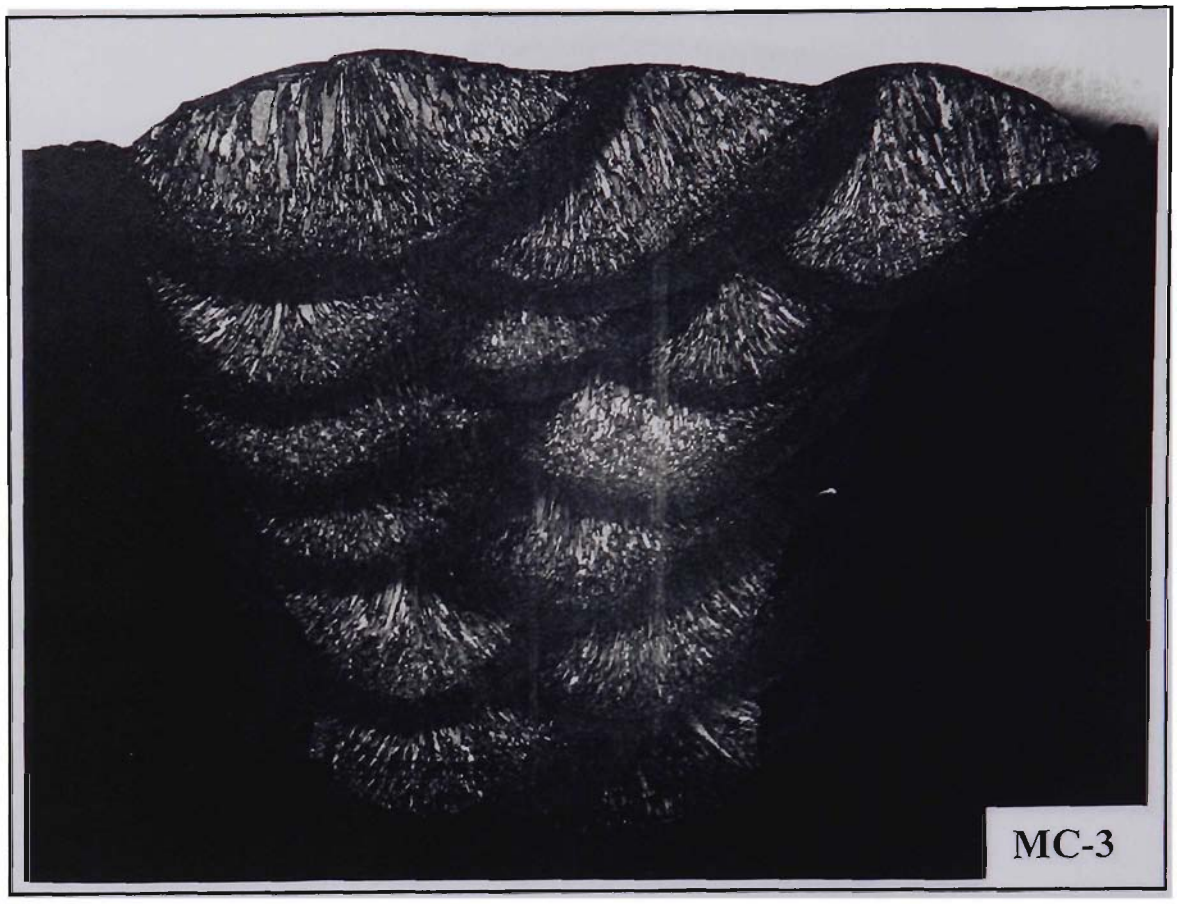

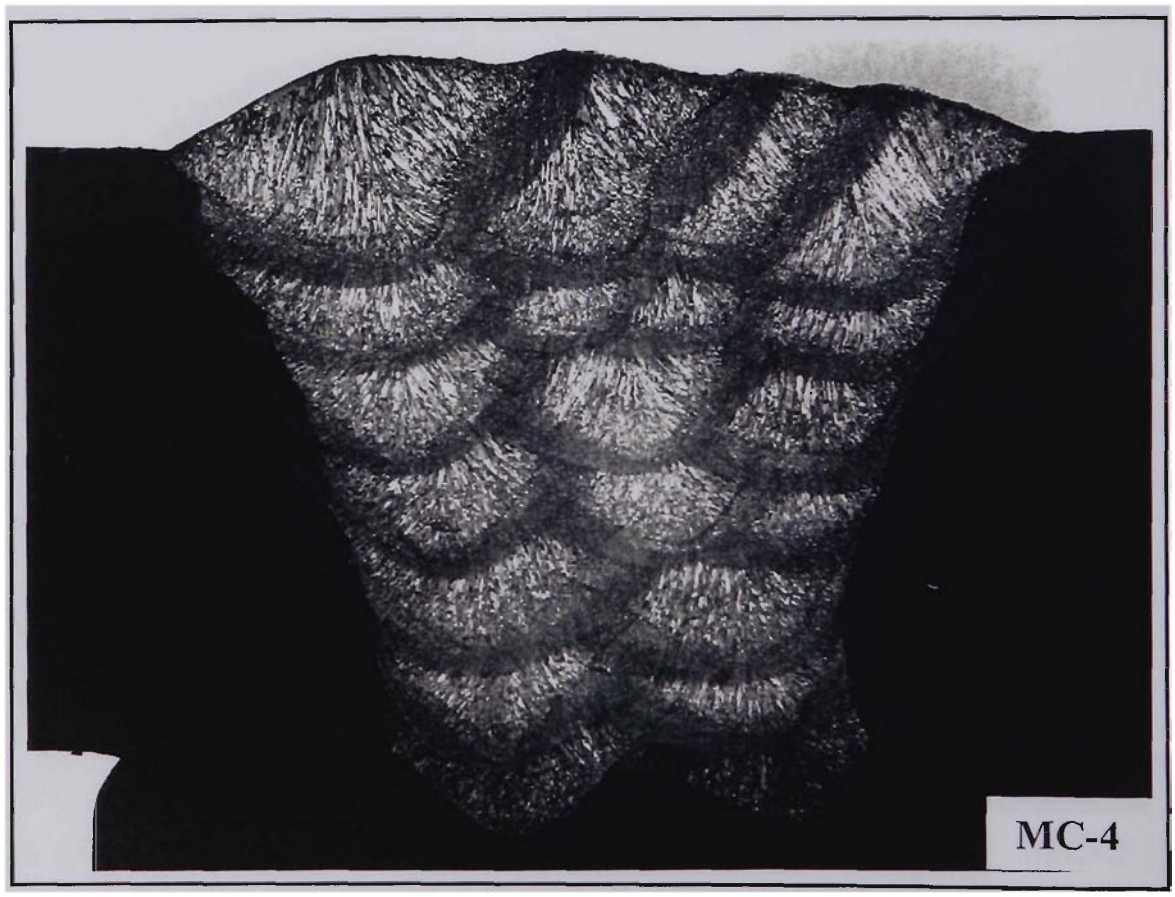

Figure 4.1: (Continued) Macrostructures of samples for different consumables and welding conditions. Approximately ×4

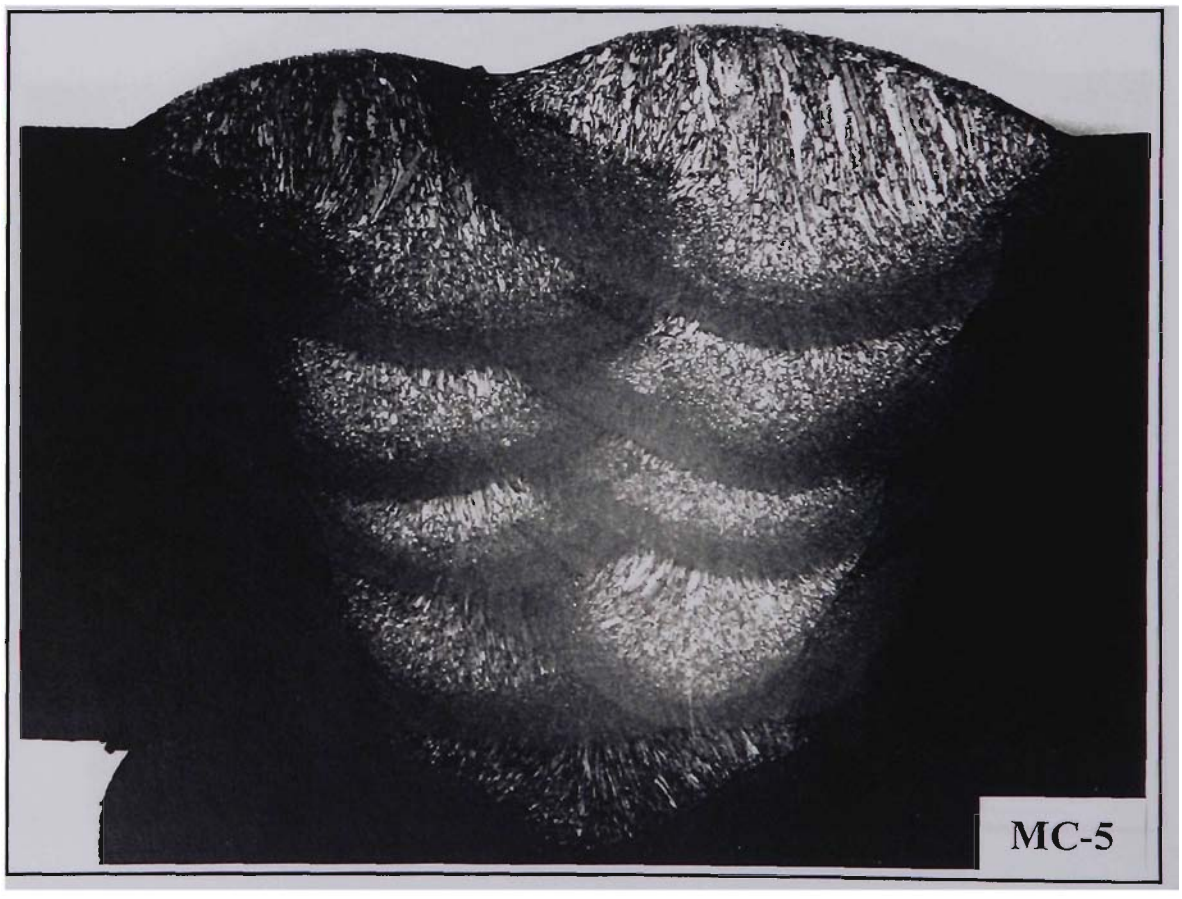

Figure 4.1: (Continued) Macrostructures of samples for different consumables and welding conditions. Approximately ×4

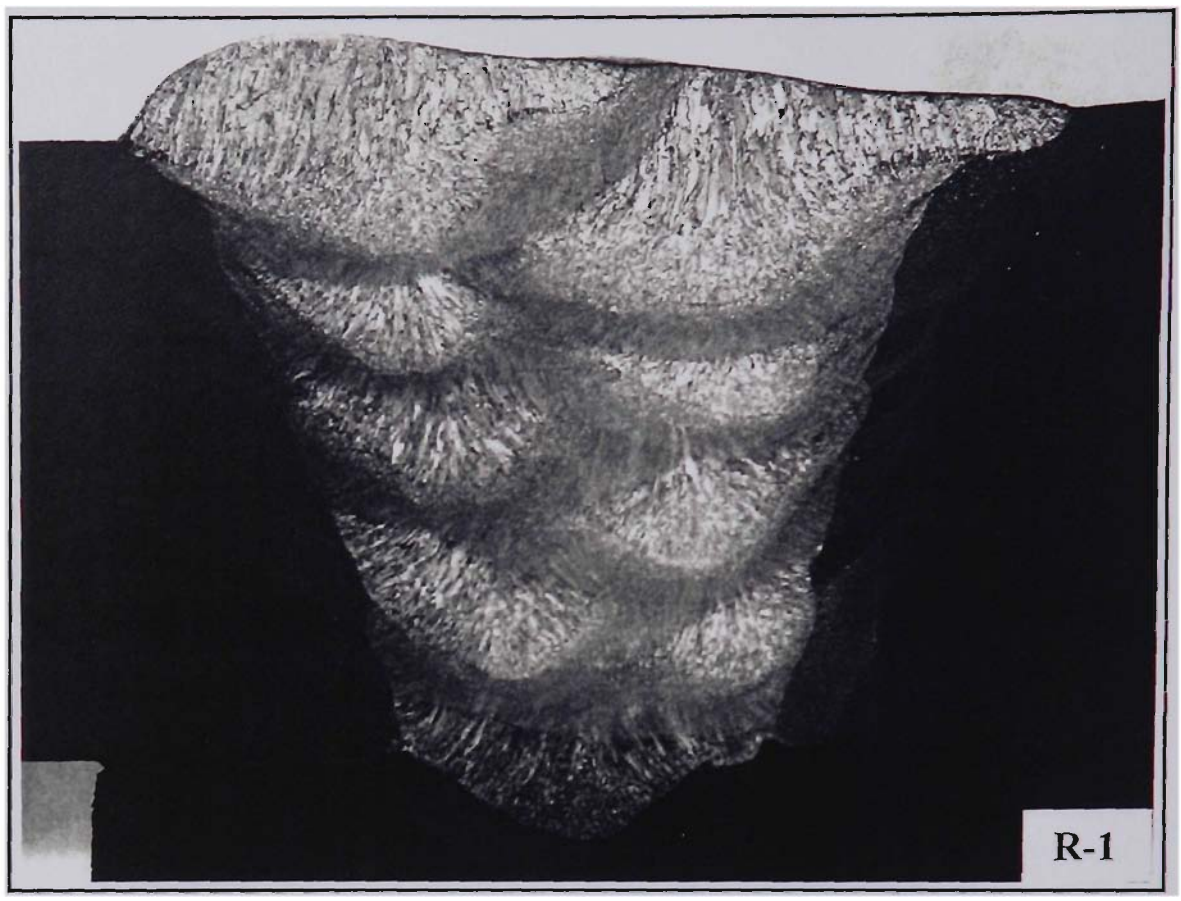

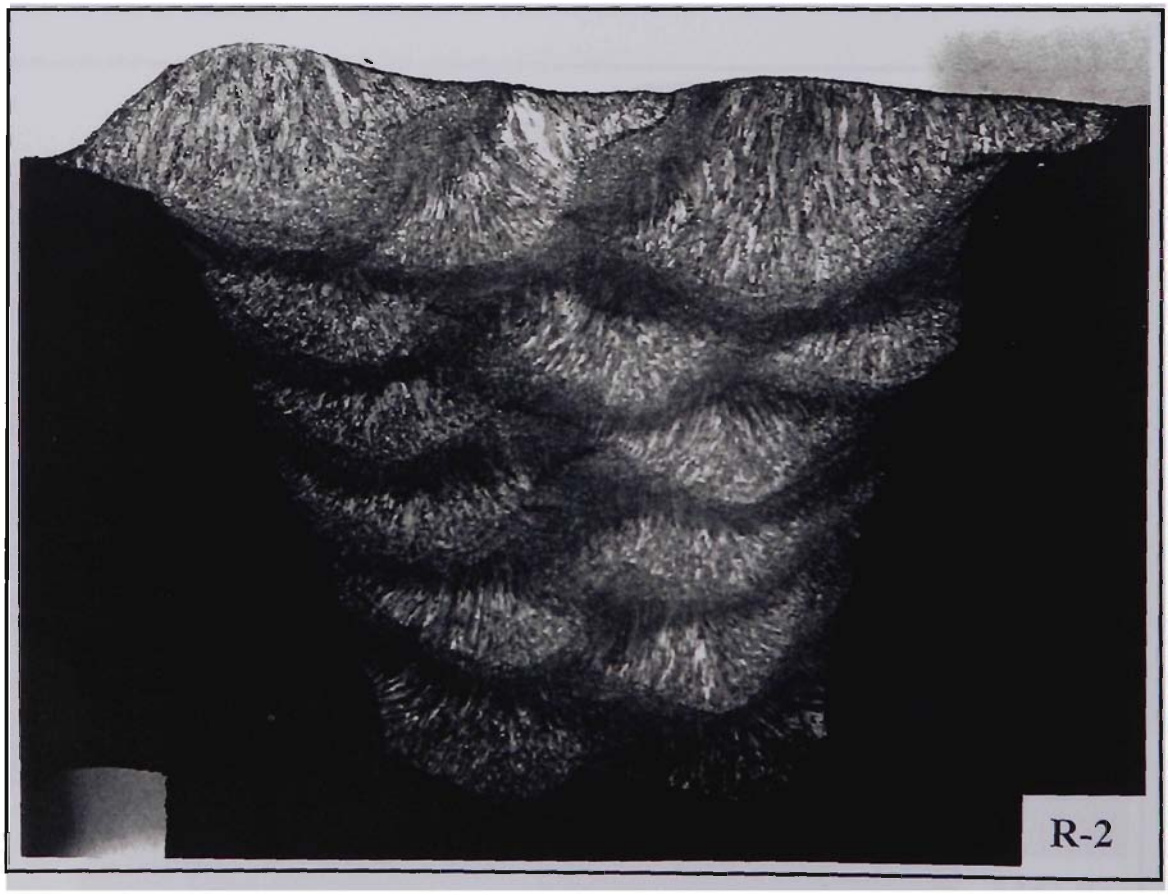

Figure 4.1: (Continued) Macrostructures of samples for different consumables and welding conditions. Approximately ×4

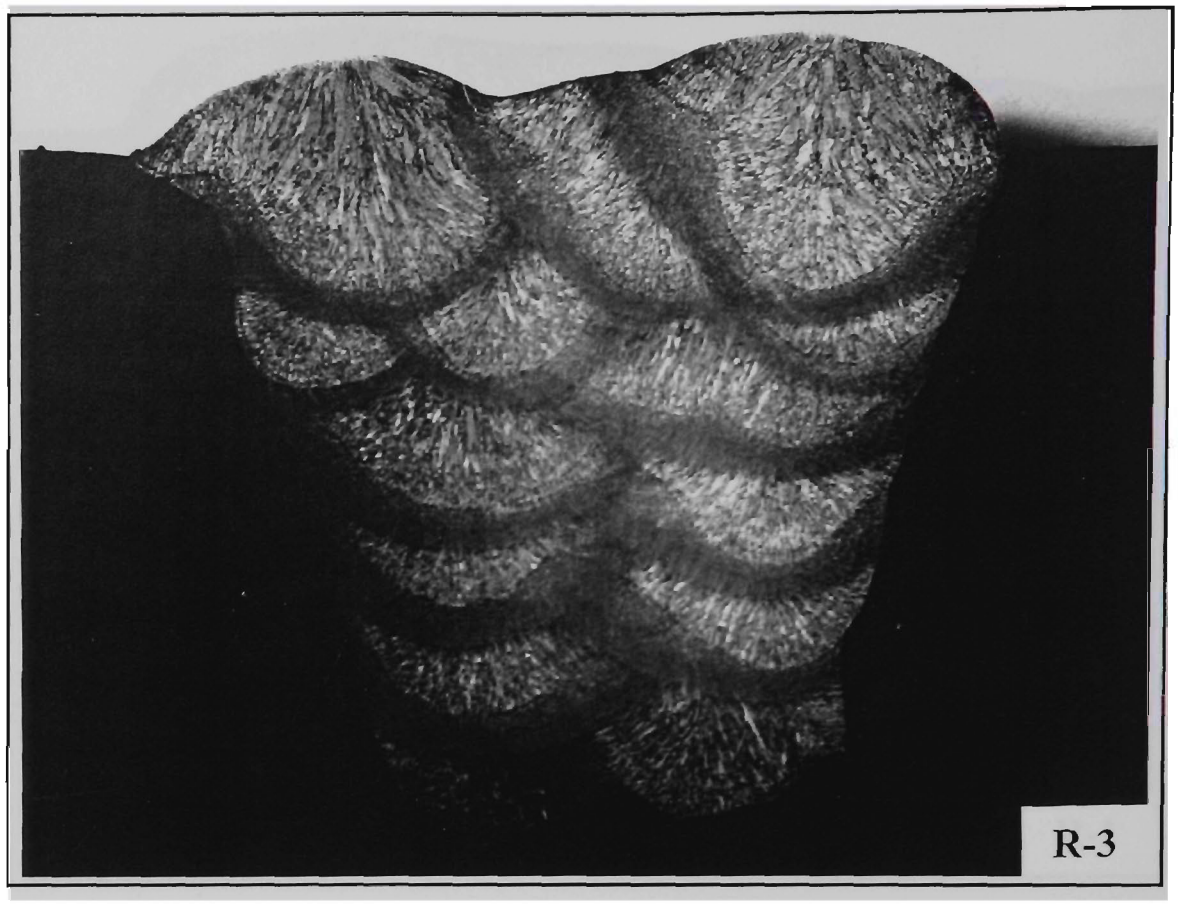

Figure 4.1: (Continued) Macrostructures of samples for different consumables and welding conditions. Approximately ×4

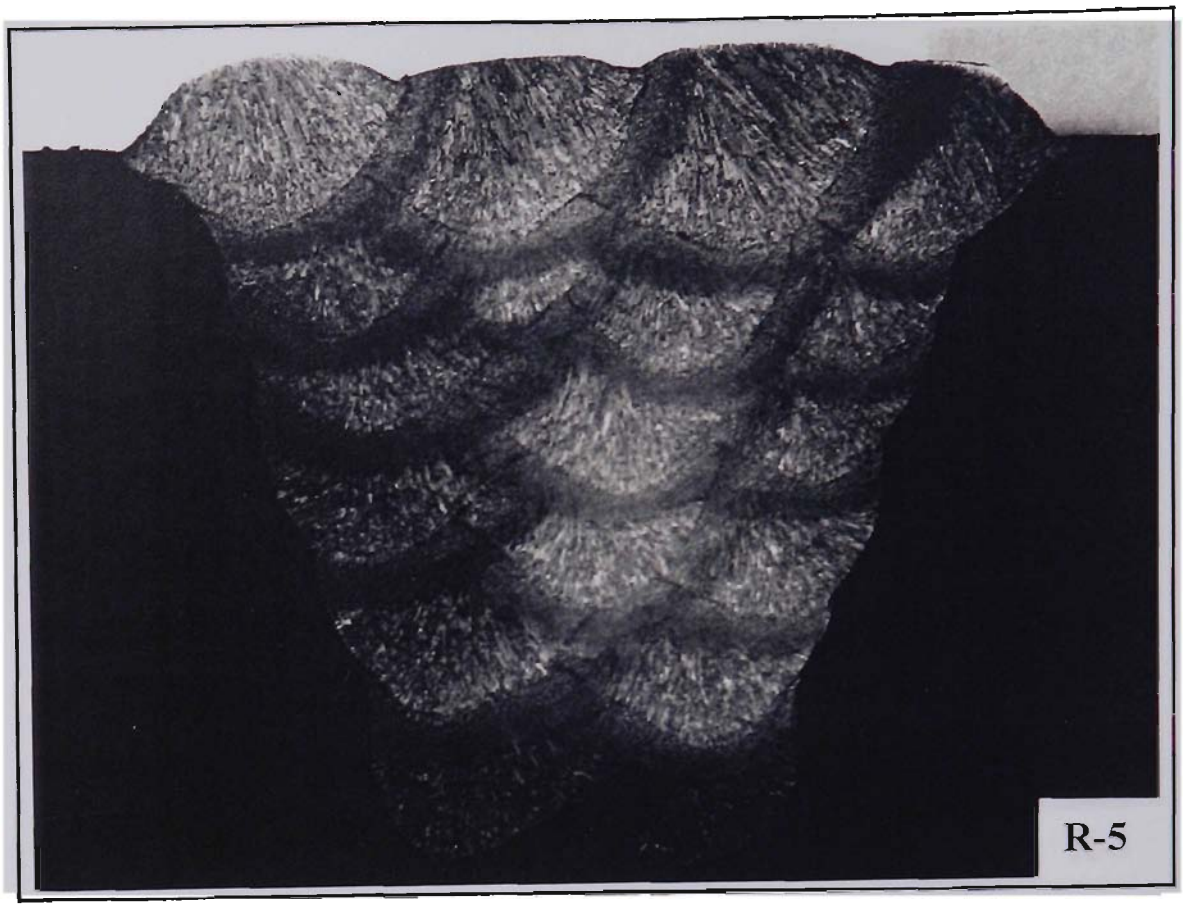

Figure 4.1: (Continued) Macrostructures of samples for different consumables and welding conditions. Approximately ×4

Only the two rutile-flux (RB and R) wires were tested in other than the flat (1G) welding position since the metal-cored (MC) wires are essentially only used for downhand welding. The rutile-flux wires were used to produce vertical-up (3G) welds in addition to the 1G welds.

The predominant shielding gases used were argon-rich mixtures. In line with recommendations, an Ar-25% CO_2 mixture was used with the rutile-flux wires while an Ar-16% CO_2 -2.5% O_2 mixture was used with the metal-cored wire. However, for all wires one test weld, at approximately 1.5 kJ/mm heat input, was made using CO_2 gas shielding, to gain an indication of the influence of shielding gas.

The emphasis in all of these welding trials was that the variables should be kept within ranges over which the consumables would be used in practical applications. A standard, transformer-rectifier, gas-metal-arc-welding power supply was used for all trials. This was achieved by having all welding done by an experienced welder using semi-automatic (i.e. hand held) techniques. An interpass temperature of 150° C was maintained in all cases. Full details of welding conditions are given in Table 4.4. The macrostructures of the 17 welds listed in Table 4.4 are given in Figure 4.1, which shows transverse sections through each of the welded samples. These sections show the considerable differences in run placement and proportions of reaustenitised and unreaustenitised regions resulting from the changes in heat input and welding technique.

Table 4.4: Welding sample code and welding conditions

Wire Classification	Sample Code	Welding Technique	Welding Position	Heat Input (kJ/mm)	Shielding Gas	Number of passes
B Containing Rutile Flux-cored Wire (E71T-1) (RB)	RB1	Stringer	Flat, Butt 1G	1.51	Ar-25%CO2	14
	RB2	Stringer	Flat, Butt 1G	0.87	Ar-25%CO2	24
	RB3	Stringer	Flat, Butt 1G	1.61	CO2	14
	RB4	Stringer	Flat, Butt 1G	2.14	Ar-25%CO2	9
	RB5	Stringer	Vertical, Up 3G	1.20	Ar-25%CO2	20
	RB6	Weave	Vertical, Up 3G	2.44	Ar-25%CO2	
Metal-cored Wire (E70C-3) (MC)	MC1	Weave	Flat, Butt 1G	2.58	Ar-16%CO2-2.5%O2	
	MC2	Stringer	Flat, Butt 1G	1.58	Ar-16%CO2-2.5%O2	14
	MC3	Stringer	Flat, Butt 1G	1.66	CO2	14
	MC4	Stringer	Flat, Butt 1G	0.99	Ar-16%CO2-2.5%O2	20
	MC5	Stringer	Flat, Butt 1G	1.99	Ar-16%CO2-2.5%O2	9
Rutile Flux-cored Wire (E71T-1) (R)	R1	Stringer	Flat, Butt 1G	1.99	Ar-25%CO2	9
	R2	Stringer	Flat, Butt 1G	1.43	Ar-25%CO2	14
	R3	Stringer	Flat, Butt 1G	1.44	CO2	14
	R4	Stringer	Flat, Butt 1G	1.00	Ar-25%CO2	19
	R5	Stringer	Vertical, Up 3G	1.06	Ar-25%CO2	18
	R6	Weave	Vertical, Up 3G	2.51	Ar-25%CO2	

4.2 Weld Metal Chemical Compositions

The weld metal chemical compositions determined using an optical emission spectrometer and a Leco analyzer are given in Table 4.5. Table 4.5 also gives the carbon equivalent (Pcm) values which were calculated according to the Ito-Besseyo equation (see Equation 2.2) for C wt.% < 0.18.

Table 4.5: The weld metal chemical compositions.

wt%	C	Mn	Si	S	P	Ti	Al	B	Mo	O	N	Pcm	CE (IIW)
RB1	.08	1.14	.45	.013	.014	.055	.004	.0116	.01	.073	.0130	.211	.272
RB2	.08	1.14	.42	.010	.015	.063	.004	.0074	.01	.073	.0130	.189	.272
RB3	.06	.94	.34	.014	.015	.050	.004	.0067	.01	.071	.0110	.153	.219
RB4	.08	1.10	.42	.010	.016	.065	.005	.0071	.01	.069	.0130	.185	.265
RB5	.08	1.15	.47	.015	.015	.069	.004	.0086	.01	.073	.0060	.197	.274
RB6	.09	1.14	.47	.012	.012	.066	.006	.0089	.01	.070	.0120	.208	.282
MC1	.06	1.41	.61	.011	.015	.018	.007	<.0005	.02	.110	.0045	.155	.299
MC2	.06	1.50	.66	.011	.014	.018	.005	<.0005	.02	.124	.0074	.161	.314
MC3	.05	1.23	.51	.011	.013	.011	.005	<.0005	.01	.107	.0072	.132	.257
MC4	.06	1.48	.64	.011	.014	.019	.006	<.0005	.02	.121	.0060	.159	.311
MC5	.06	1.43	.63	.011	.014	.015	.004	<.0005	.02	.117	.0054	.156	.302
R1	.09	1.34	.59	.013	.013	.045	.002	<.0005	.02	.070	.0050	.181	.317
R2	.09	1.33	.58	.012	.011	.049	.002	<.0005	.01	.074	.0047	.179	.314
R3	.08	1.24	.53	.013	.012	.056	.004	<.0005	.01	.079	.0083	.163	.289
R4	.09	1.40	.62	.013	.012	.060	.002	<.0005	.02	.079	.0055	.185	.327
R5	.08	1.29	.55	.012	.012	.052	.006	<.0005	.01	.083	.0040	.166	.297
R6	.09	1.41	.62	.011	.014	.055	.002	<.0005	.02	.081	.0047	.185	329

4.3 Weld Metal Mechanical Properties

The impact and tensile tests outlined below were conducted by CSIRO (Adelaide Laboratory) whilst the tests described in 4.3.3 and 4.4 - 4.8 were conducted in the current experimental program.

4.3.1 Charpy impact tests

Standard Charpy V notch (CVN) specimens with 10 × 10 mm section were made as specified in AWS (1979). Specimens were extracted from the central region of the welds and transverse to the weld with their centre-line corresponding to that of the weld and with the notch central in the weld metal and perpendicular to the plate surface. The notch therefore passed through regions of solidified and reheated weld metal. These transverse weld Charpy specimens were tested at +20, 0, -20 and -40 °C and where necessary at +40 and -60 °C. The average absorbed energy was determined from three tests at each temperature to obtain the transition curve.

4.3.2 Tensile tests

All-weld tensile tests were conducted according to AS2205.2.2. Specimens were extracted from the central region of the welds and machined to 10 mm in diameter according to the AWS (1979) specification. Four basic properties were measured: yield strength, tensile strength, elongation and reduction in area.

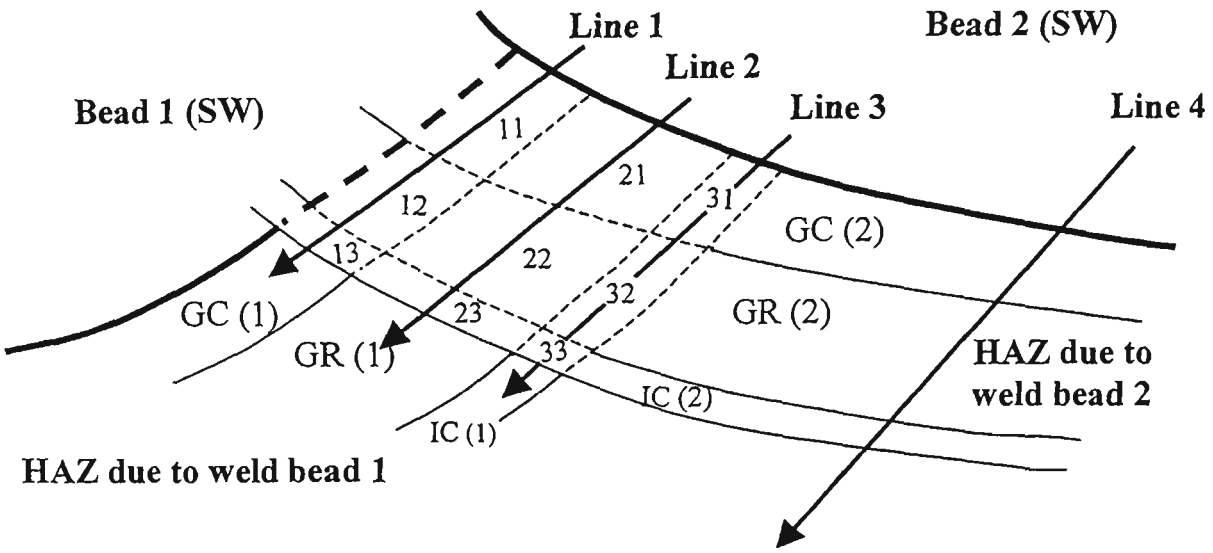

Figure 4.2: Schematic drawing of the double-reheated sub-zones of the weld metal.

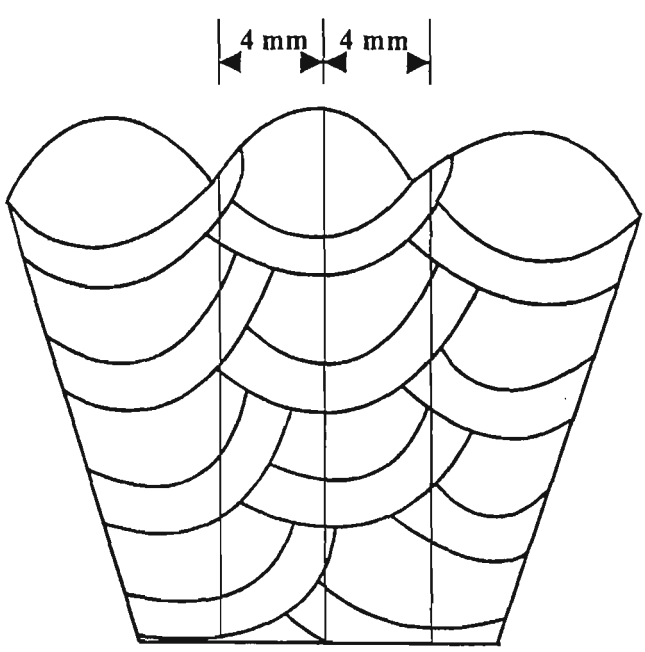

Figure 4.3: The selected test lines for linear measurement.

4.3.3 Microhardness tests

The singly reheated HAZ basically consists of three sub-zones: the grain coarsened (GC); the grain refined (GR) and the intercritical (IC) sub-zones. In the second overlapping region, the HAZ becomes more complicated because overlapping weld beads create double-reheated weld metal structures which consist of 9 sub-zones: GC-GC, GC-GR, GC-IC, GR-GC, GR-GR, GR-IC, IC-GC, IC-GR, IC-IC. Using the numbering system 1 for GC, 2 for GR and 3 for IC the 9 sub-zone array can be represented by a 3×3 matrix of 2 digit elements with the first number representing the 1st pass sub-zone and the second number representing the 2nd weld pass sub-zone. Unmodified as welded regions are referred to by the code SW (solidified weld metal).

$$\begin{aligned} 1 &= GC \\ 2 &= GR \\ 3 &= IC \end{aligned} \qquad \begin{pmatrix} 1,1 & 1,2 & 1,3 \\ 2,1 & 2,2 & 2,3 \\ 3,1 & 3,2 & 3,3 \end{pmatrix}$$

The first row corresponds to the sub-zones traversed by line 1 in Figure 4.2; the second, corresponds to line 2 and the third, line 3. Line 4 traverses the singly reheated HAZ.

Figure 4.2 is a schematic drawing of the double-reheated sub-zones of the weld metal. Microhardness measurements in these double-reheated sub-zones were determined along lines 1-3 and the singly reheated sub-zones were analysed using line 4 in Figure 4.2. A Leco Vickers microhardness test machine was used with a load of 100g to determine the hardness of these sub-zones. The double-reheated region used for the hardness tests was chosen from the central region of the weld metal.

Vander Voort (1984) has suggested that one should always use the highest possible load in any test, because small measurement errors in small indentations will produce

large hardness deviations. However, as the area of each sub-zone in the double-reheated region is very small, especially for the IC-IC sub-zone, a 100g load was chosen as the most suitable load and a minimum distance (centre to centre) between two indentations of 0.12mm was selected. The hardness of each sub-zone is reported as the mean value of the total number of tests in that region along the selected test line.

4.4 Point Counting

Transverse sections of the welds were polished and etched with 2.5 % nital and point counting metallograghy was carried out according to the scheme proposed by the International Institute of Welding (Pargeter and Dolby 1984). The point counting analysis was carried out in the mid-section of the sample corresponding to the location of the CVN specimen. This was done because in multipass welds the solidified weld metal may be influenced significantly by the additional thermal cycles induced during the deposition of subsequent layers (Reed and Bhadeshia 1994). Therefore the final layer, where point counting metallography is usually carried out, will have a different microstructure from modified weld metal in the center of the weldment thus the local mechanical properties will differ. The main constituents measured in the microstructure assessment were, in IIW terminology (IIW Doc. 835-85), acicular ferrite (AF), grain boundary ferrite (PF(G)), intragranular polygonal ferrite (PF(I)), ferrite with a second phase (FS) and ferrite-carbide aggregate (FC). One thousand points were counted at a magnification of 500× for each weld.

4.5 Linear Measurements

Before commencing linear measurement, three vertical ink lines were drawn on each sample from the top bead to the original surface of the backing plate. As shown in

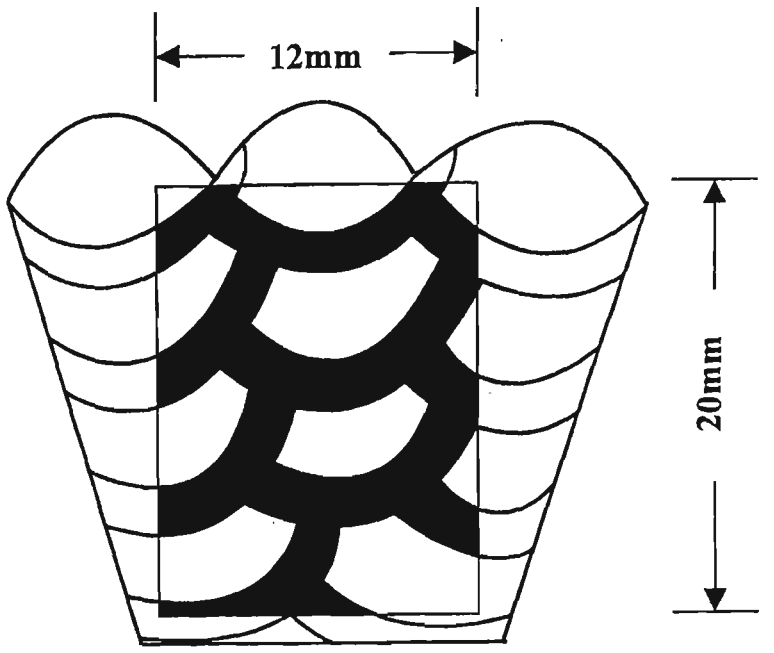

Figure 4.4: The test area for areal measurement.

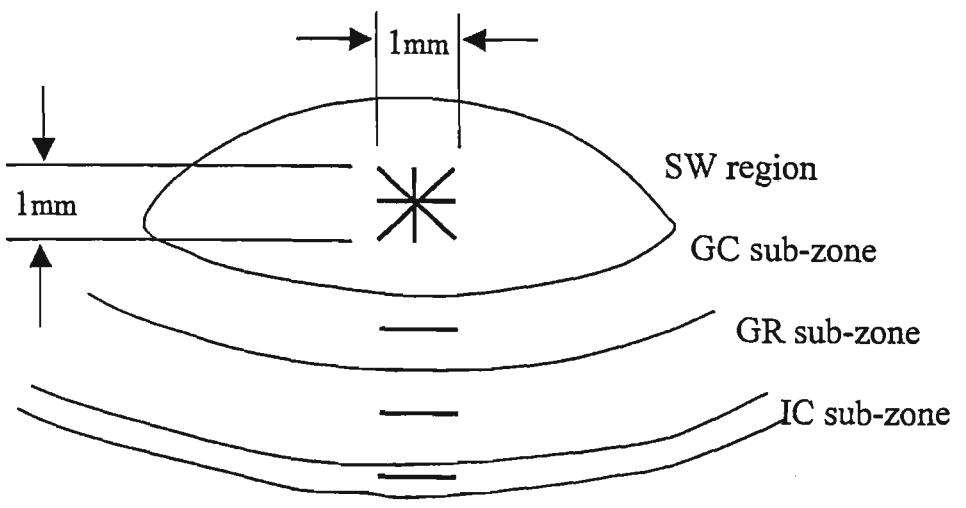

Figure 4.5: The selected test lines for mean free path measurement.

Figure 4.3, the central line was defined first at the geometrical centre of the weld metal and the other two lines were drawn parallel and at a distance of 4mm from the central line. By using an optical microscope with a filar eyepiece, the different weld regions along these three lines could easily be identified. These regions included solidified weld metal (SW); grain coarsened (GC); grain refined (GR); and intercritical (IC) regions. Through linear measurement, the average volume fractions of SW, GC, GR and IC could be obtained.

4.6 Areal Measurements

Areal measurement of each sample was carried out on an image analysis based system with a video camera and the NIH software package. Because of the resolution limit of the imaging system, only two different regions in the weld metal could be clearly discerned, the reaustenitised (HAZ) region and the unreaustenitised (solidified weld metal) region. The test area was based on the geometrical centre of the weld metal and a rectangular area 20 mm long and 12 mm wide was selected (Figure 4.4). The central region sampled by both linear and areal analysis was the region from which all-weld tensile and Charpy test pieces were taken for mechanical property characterisation (Schumann and French 1995). The volume fractions of reaustenitised and unreaustenitised regions were obtained by monitoring 80000 pixels.

4.7 Mean Free Path Measurements

The measurement of MFP for each sample was carried out on a colour image analysis based system with an optical microscope, a video camera and Video Pro 32 software package. The test lines chosen were based on the geometrical centre of each sub-zone located in the central region of the weld metal.

Figure 4.5 shows the selected test lines for the measurement of MFP. For the SW region, four lines crossing at 45° to one another and within a 1mm × 1mm square were selected. An average MFP value was estimated despite the presence of the existing of columnar grains with a smaller size in the thickness direction compared to the perpendicular direction. $\bar{L}_{SW}$ was obtained through the mean value of the measurements along these four test lines. The selected lines for measurement of the GC, GR and IC sub-zones were based on the mid-section of each sub-zone, and a single test line of length 1mm was used, see Figure 4.5.

The mean free path $\bar{L}$ is defined as

$$\bar{L} = \frac{L}{N} \tag{4.1}$$

where N is the number of ferrite grain boundaries intercepted by the selected test line and L is the length of the test line. A weighted MFP for weld region i, $\bar{L}_i^w$, was derived from the volume fraction of each sub-zone f_i and each value of MFP ($\bar{L}i$):

$$\bar{L}_i^w = \bar{L}i \times f_i \tag{4.2}$$

The overall MFP of the weld, $\bar{L}_o^w$ was calculated from the sum of the weighted MFP values:

$$\bar{L}_o^w = \sum_i \bar{L}_i^w \tag{4.3}$$

Since four distinct sub-zones were used to characterise the weld metal (Figure 4.5): SW, GC, GR and IC; $\bar{L}_o^w$ can be represented as

$$\bar{L}_{o}^{w} = \bar{L}_{SW}^{w} + \bar{L}_{GC}^{w} + \bar{L}_{GR}^{w} + \bar{L}_{IC}^{w} \quad (4.4)$$

4.8 Non-metallic Inclusion Distributions

Scanning electron microscopic (SEM) examination of non-metallic inclusions was carried out using a Leica S440 microscope under an accelerating voltage of 10 kV. The magnification of the SEM images was 5000×. The existence of non-metallic inclusions was further confirmed by the secondary electron signal. The qualitative standardless EDS method and X-ray line profile analysis were used to determine composition and effective element distributions in the non-metallic inclusions and matrix in weld zone. A thin window X-ray detector was used for light elements such as oxygen and carbon.

To determine size distributions of non-metallic inclusions, the software for image analysis software NIH Image 1.58 was used. More than five hundred inclusions were included in the SEM images used for the analysis of each sample. The important inclusion characteristics including the arithmetic mean two and three dimensional particle diameters, $\overline{D_a}$ and $\overline{D_v}$, the number of particles per unit area N_a, the number of particles per unit volume N_v, the volume fraction V_v, the average particle surface area per unit volume S_v, the mean particle centre to centre volumetric spacing λ_v were accordingly computed from the following basic stereometric relationships (Ashby and Ebeling 1966, Underwood 1970, Kluken et al. 1988):

$$\overline{D_v} / \overline{D_a} = \pi / 2 \quad (4.5)$$

$$N_v = \frac{6V_v}{\pi(\overline{D_v})^3} \quad (4.6)$$

$$N_a = N_v \, \overline{D_v} \quad (4.7)$$

$$\lambda_v = 0.554 \left(\frac{1}{N_v}\right)^{\frac{1}{3}} \tag{4.8}$$

$$S_v = \pi N_v (\overline{D_v})^2 \tag{4.9}$$

CHAPTER 5

MECHANICAL PROPERTIES AND MICROSTRUCTURES

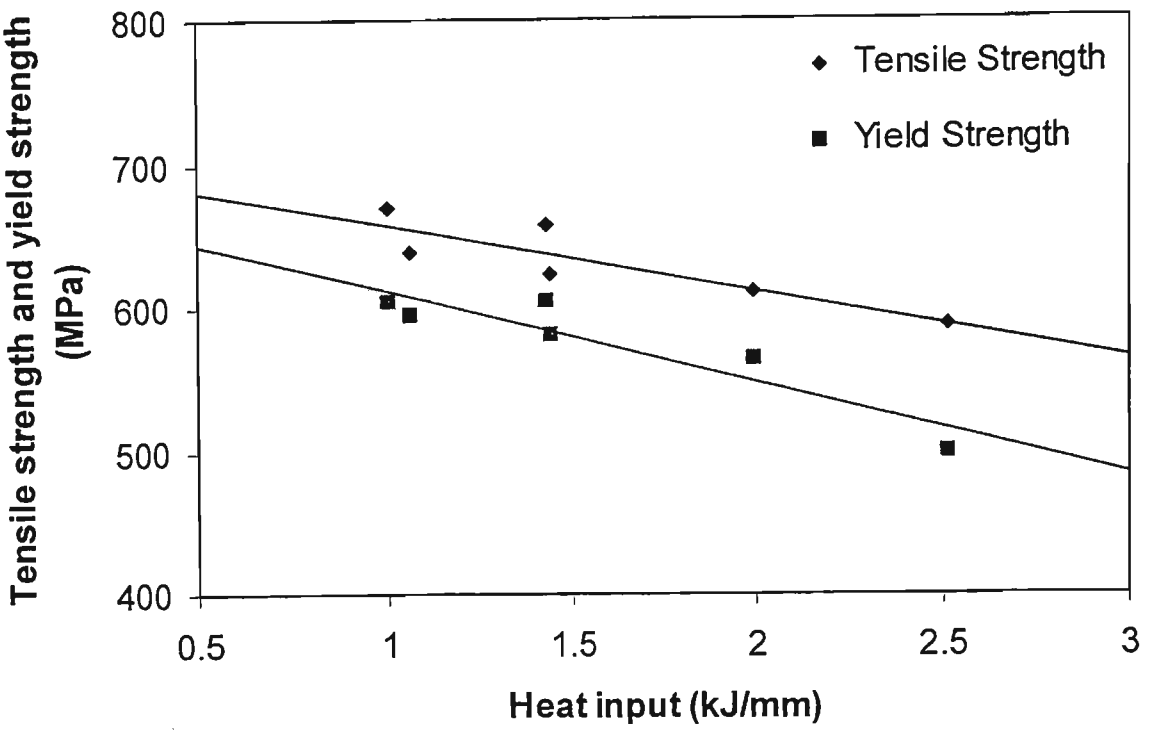

Figure 5.1a: Variation of tensile strength and yield strength with heat input for rutile flux-cored (R) samples.

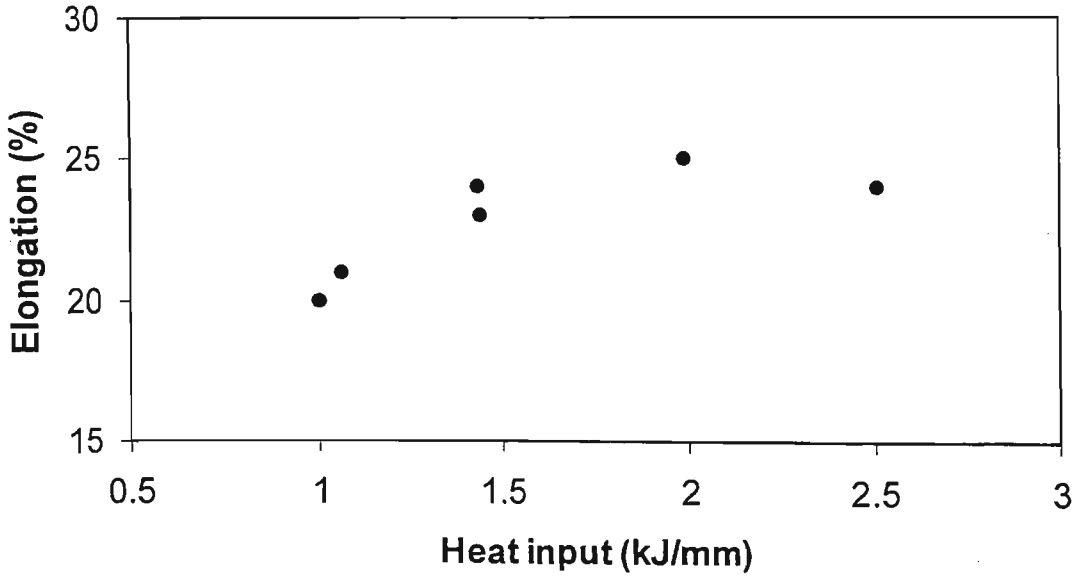

Figure 5.1b: Variation of elongation with heat input for rutile flux-cored (R) samples.

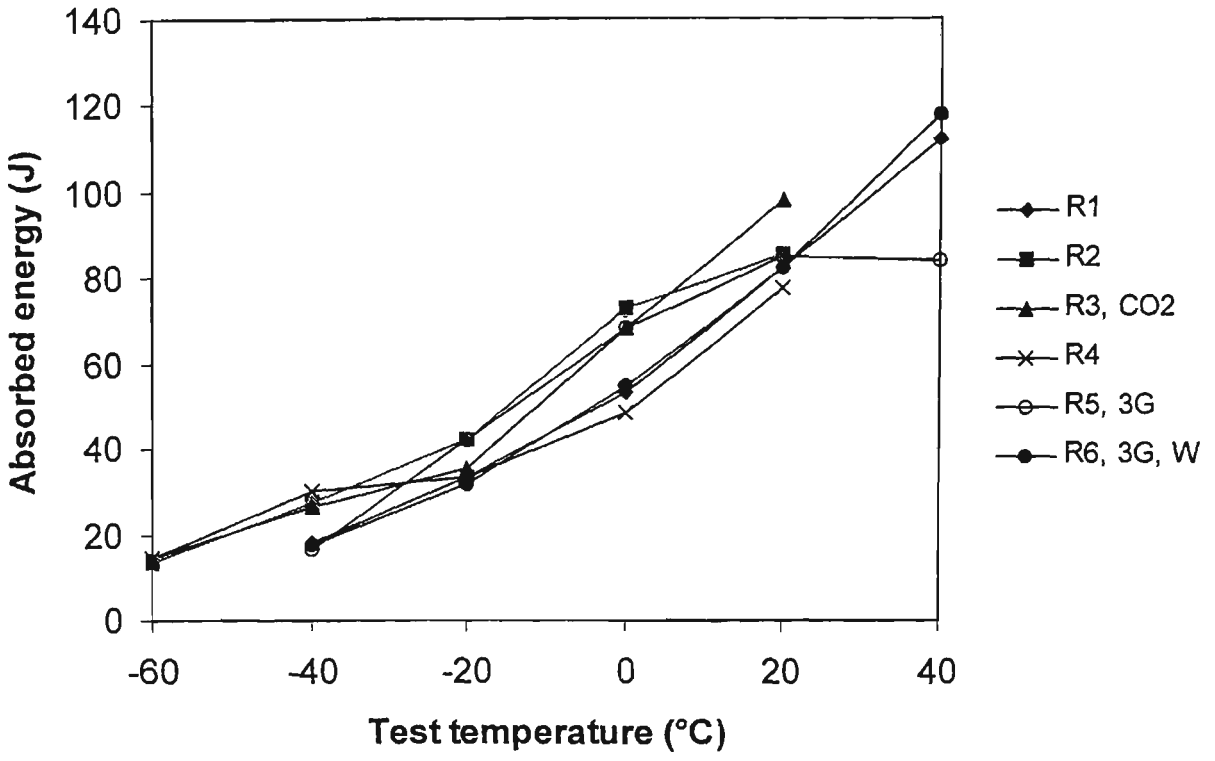

Figure 5.2: Variation of mean CVN energy with temperature for rutile flux-cored (R) samples.

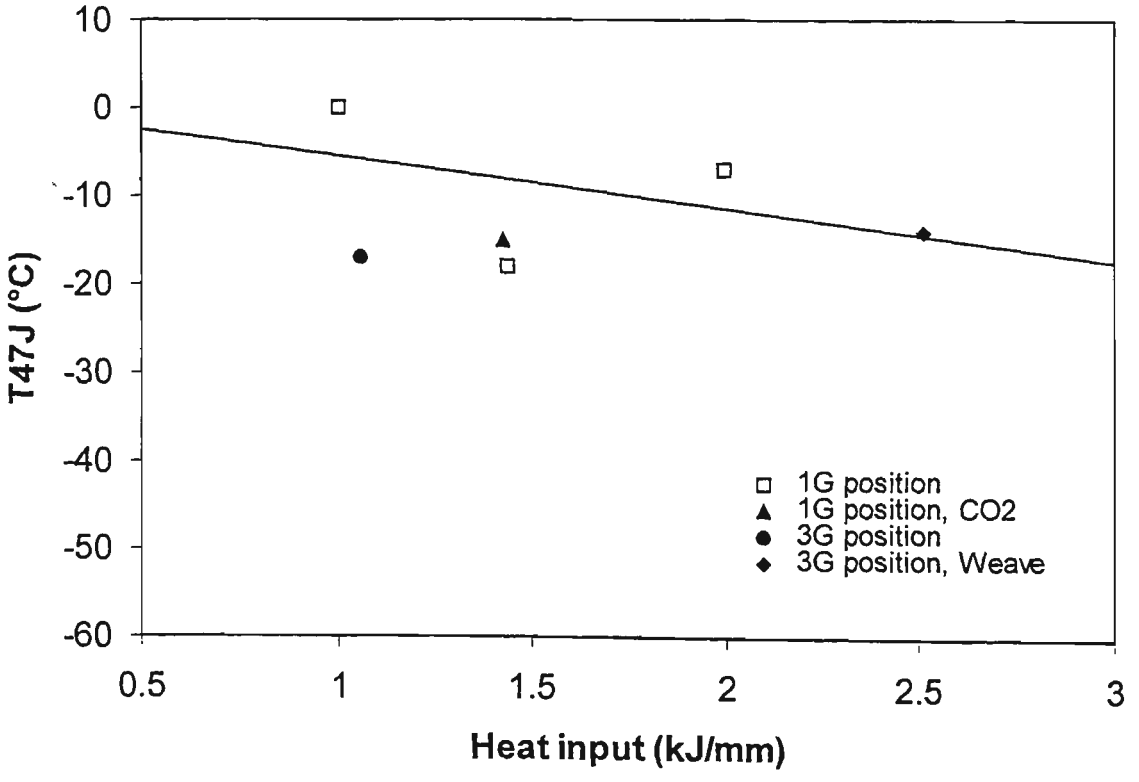

Figure 5.3: Relationship between T47J and heat input for rutile flux-cored (R) samples.

5.1 Introduction

The mechanical properties of the weld metal are determined by the microstructures of the as solidified and reheated regions, including the non-metallic inclusion size distribution and dispersion throughout the weld bead. The microstructure is determined by the weld metal composition and the welding conditions: including heat input, weld pass sequence and interpass temperatures which collectively determine the thermal cycle. The effect of heat input on tensile properties and toughness is assessed in this Chapter. The effect of non-metallic inclusions on nucleation of acicular ferrite (AF) is also analysed, together with the effect of AF content on toughness.

5.2 Results

5.2.1 Rutile flux-cored (R) wire

Figure 5.1 shows the variation of weld metal yield strength, tensile strength and elongation as a function of heat input for the rutile flux-cored welds listed in Table 4.4. Both yield and tensile strength appeared to decrease slightly with increase in heat input. Elongation was generally 23% to 25% except for the 3G position weld at 1.1 kJ/mm which gave 21%. These strength properties appear to be more sensitive to heat input than to the other variables examined such as welding technique, position or shielding gas (see Table 4.4 for details).

The variation of mean CVN value with temperature, over the range -60 to +40 °C, for weld metal from each of the test samples detailed in Table 4.4 is shown in Figure 5.2. These curves suggest that only slight differences exist between the impact properties of these welds. In order that these impact results can be more readily compared the

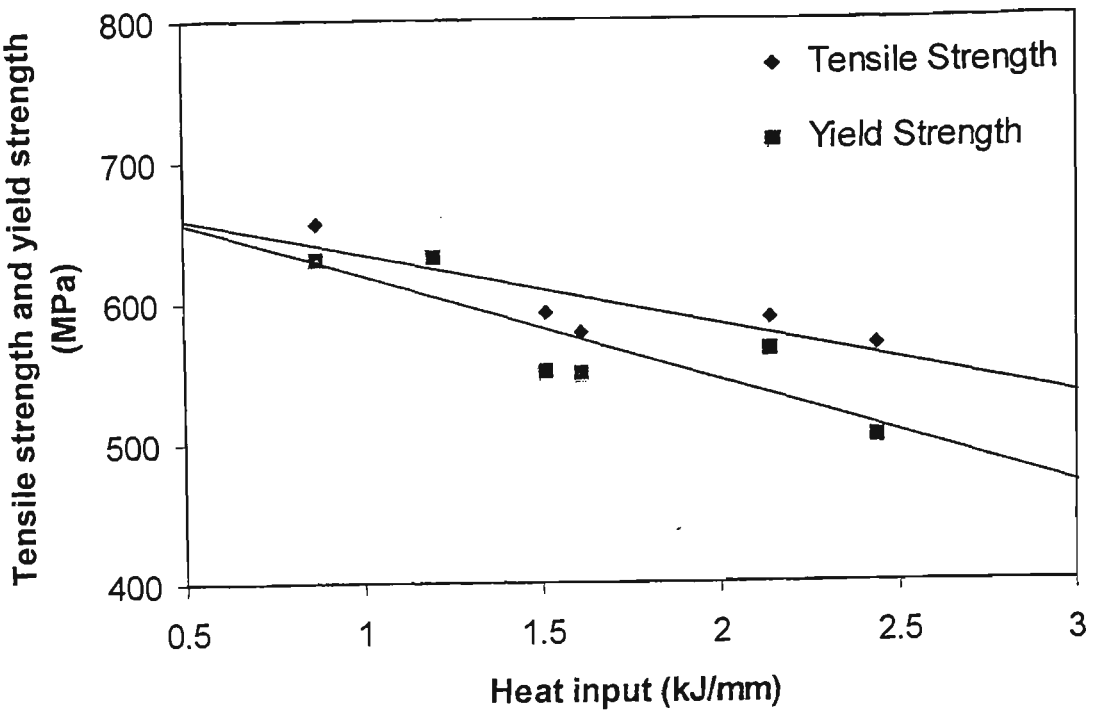

Figure 5.4a: Variation of tensile strength and yield strength with heat input for B containing rutile flux-cored (RB) samples.

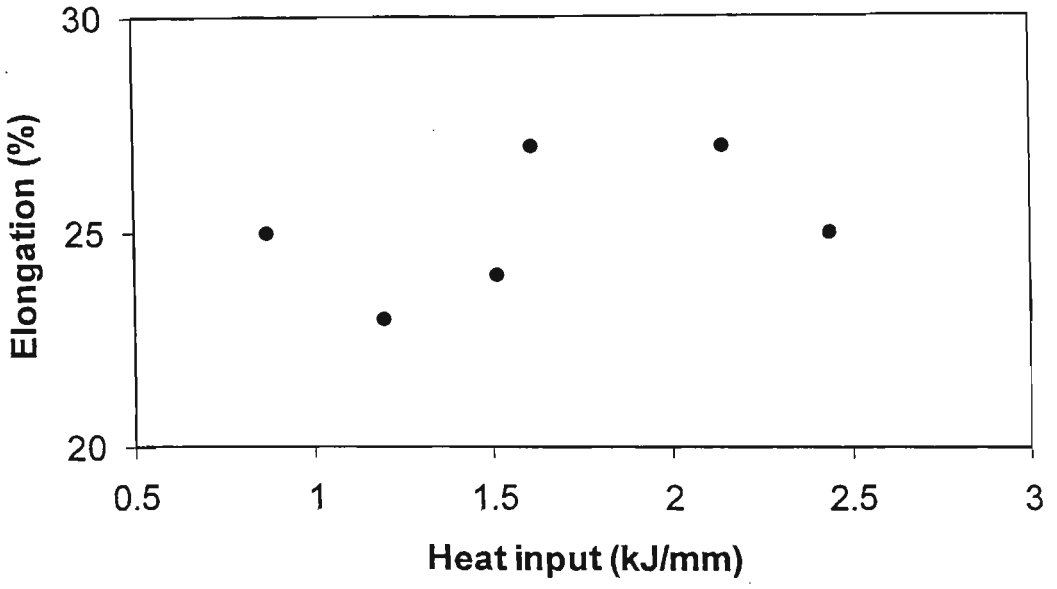

Figure 5.4b: Variation of elongation with heat input for B containing rutile flux-cored (RB) samples.

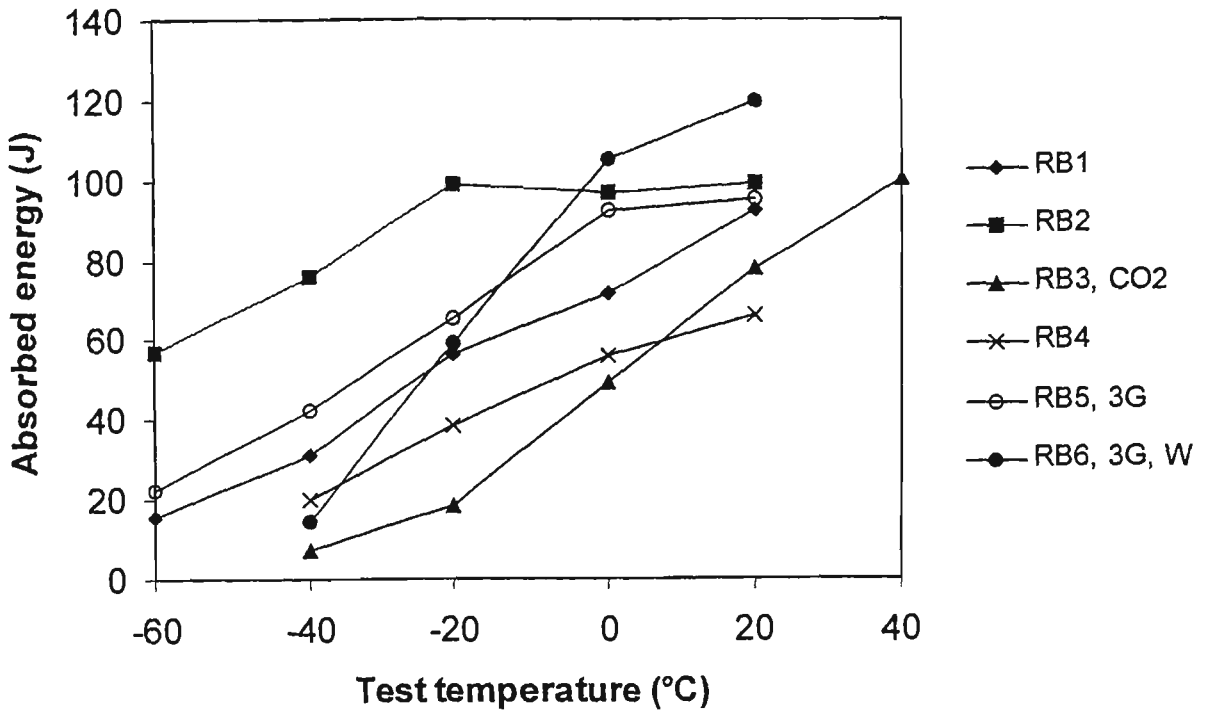

Figure 5.5: Variation of mean CVN energy with temperature for B containing rutile flux-cored (RB) samples.

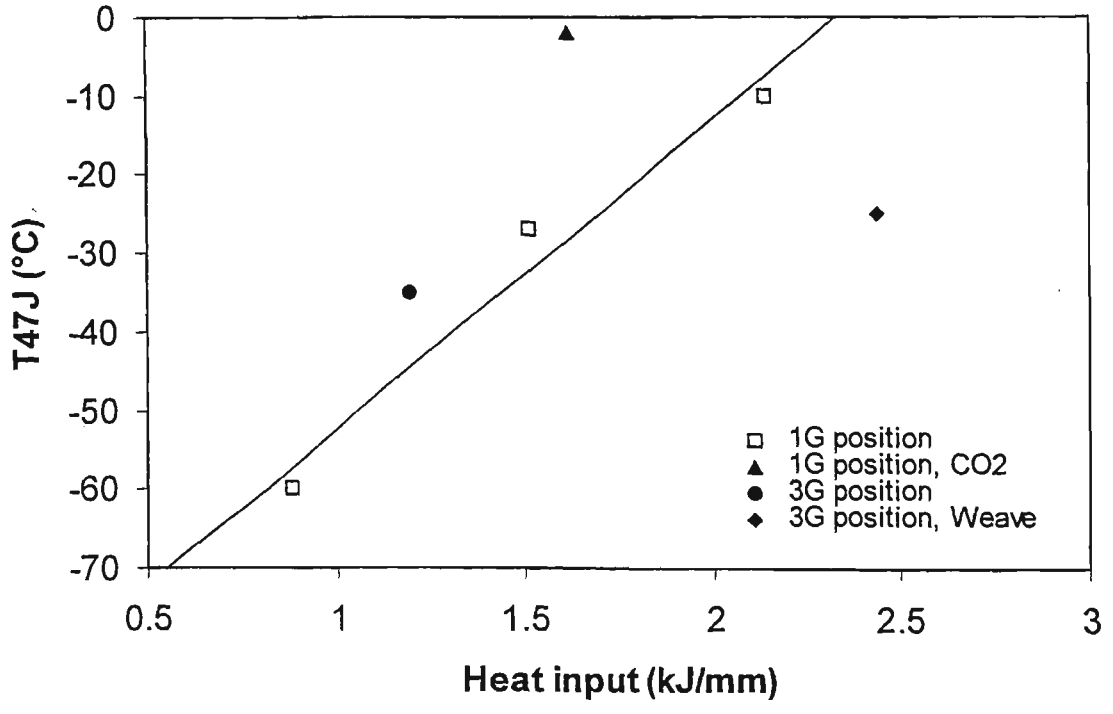

Figure 5.6: Relationship between T_{47J} and heat input for B containing rutile flux-cored (RB) samples.

temperature which corresponds to 47J impact energy was found for each case using the data of Figure 5.2. The basis for using this T_{47J} value is that many welding classification schemes (Lloyds Register 1995, American Bureau of Shipping 1995) specify that the mean CVN impact energy must exceed 47J at a particular temperature.

The resulting T_{47J} values for the R samples are shown in Figure 5.3. This figure shows that all of the T_{47J} values obtained are between 0 and -18 °C so that this consumable meets the Grade 2 (AS 2203-1 1990, Lloyds Register 1995) impact level over the entire range of conditions used. This figure also confirms that the impact properties are insensitive to the welding conditions for R samples. The highest T_{47J} value occurred at the lowest heat input (1 kJ/mm). The T_{47J} values for the 3G position welds were virtually independent of welding conditions and the use of CO_2 shielding gas appeared to have no strong influence.

5.2.2 B containing rutile flux-cored (RB) wire

The tensile test results for the RB samples are plotted in Figure 5.4a. The tensile strength and particularly the yield strength values decreased with heat input. Elongation values showed no systematic change with heat input. The use of CO_2 shielding gas, or a weave rather than a stringer bead technique did not appear to exert a significant effect on strength. All of the tensile strength and elongation values obtained were within the ranges specified in AS 2203-1 (1990) for a W50 consumable.

The variation of mean CVN value with temperature for weld metal from the various test samples is shown in Figure 5.5. In this case there is considerable variation in impact behaviour between the samples. In general the lower heat input, Ar-25% CO_2 shielded welds appear to have the best impact values, particularly at lower

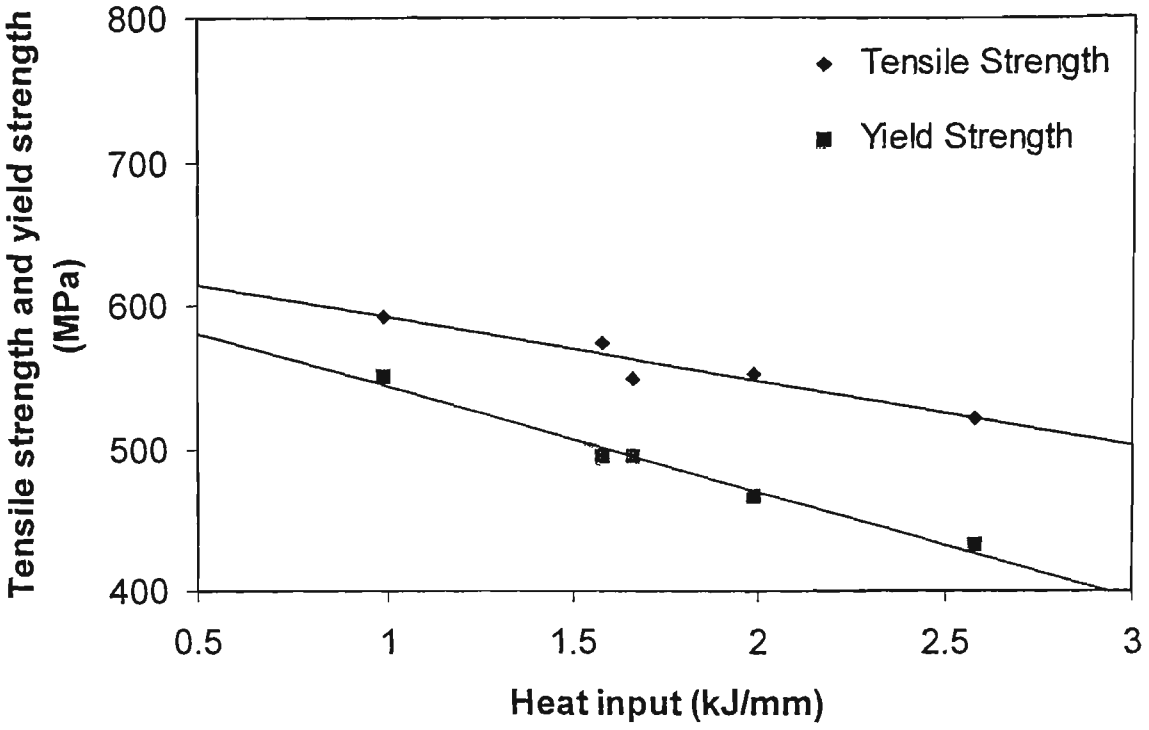

Figure 5.7a: Variation of tensile strength and yield strength with heat input for metal-cored (MC) samples.

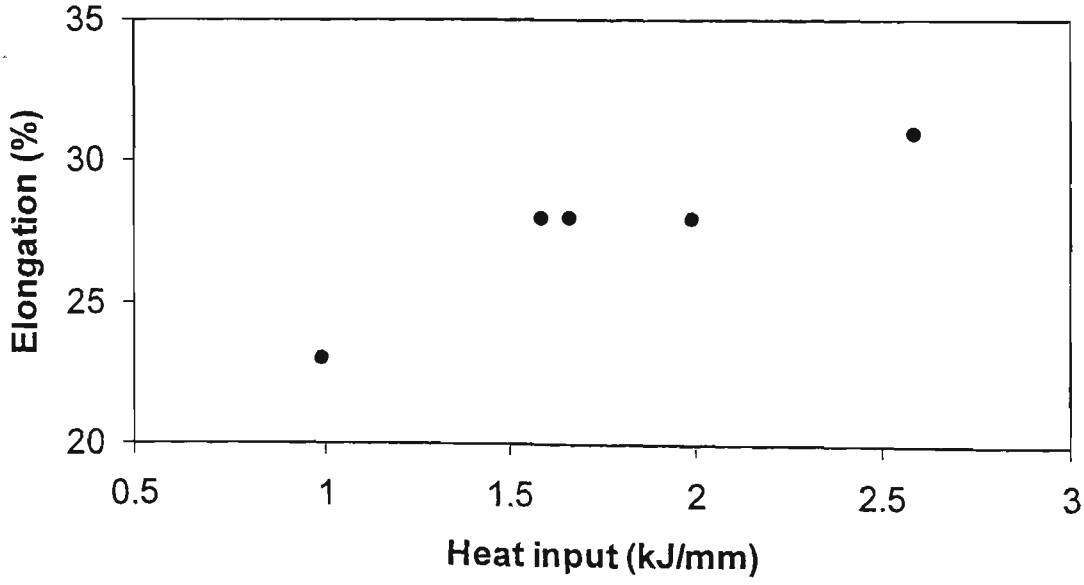

Figure 5.7b: Variation of elongation with heat input for metal-cored (MC) samples.

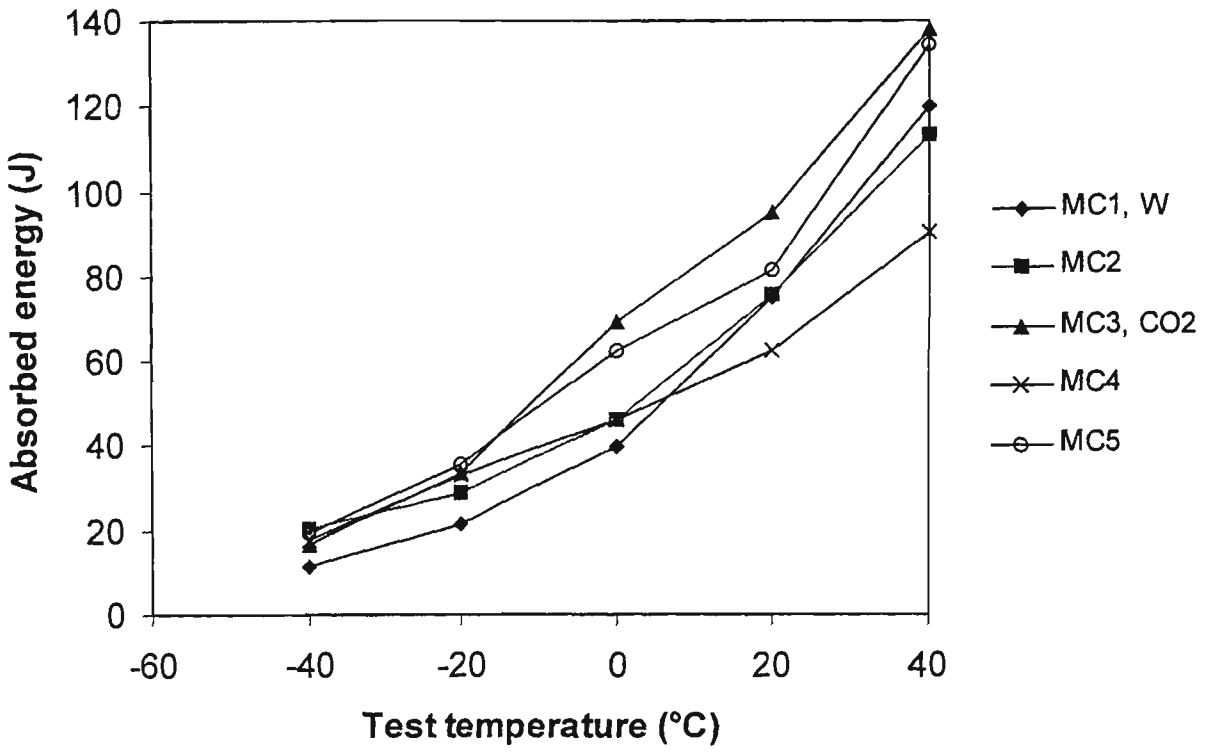

Figure 5.8: Variation of mean CVN energy with temperature for metal-cored (MC) samples.

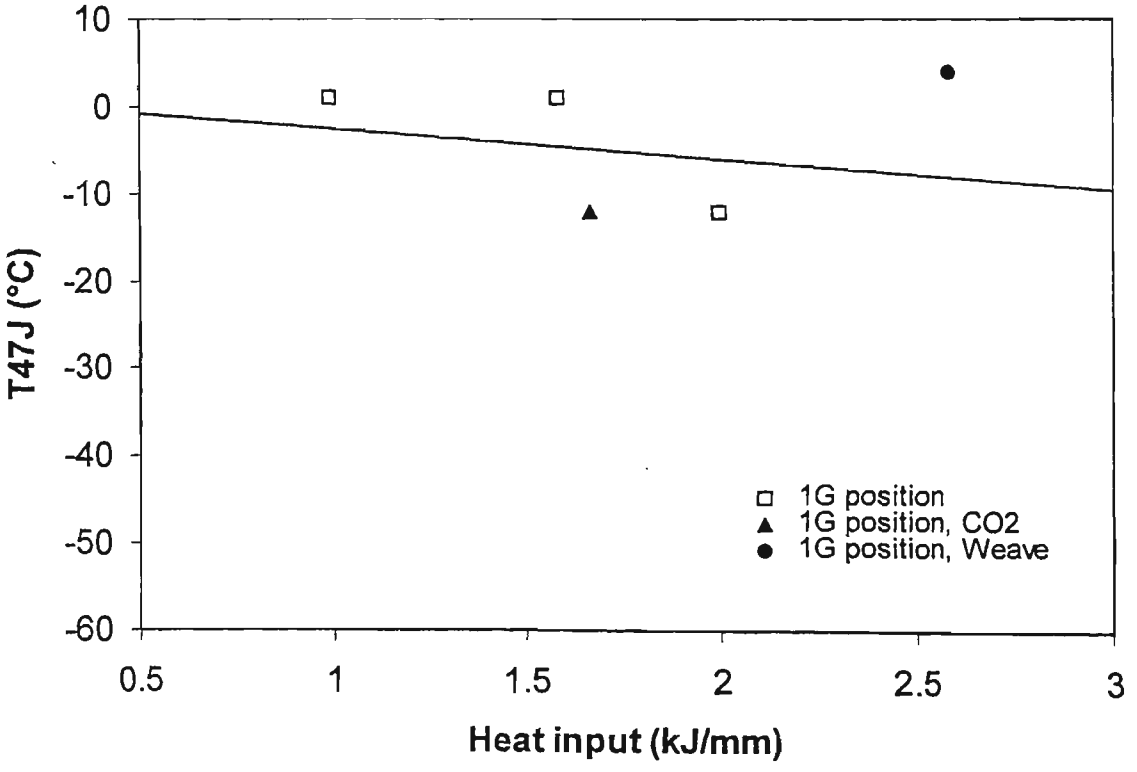

Figure 5.9: Relationship between T_{47J} and heat input for metal-cored (MC) samples.

temperatures. A plot of the variation of T_{47J} value with welding conditions for the welds from the RB wire is shown in Figure 5.6. This shows that the impact properties of welds made in the 1G position were heat input dependent as the T_{47J} values varied between -60 and -10 °C as heat input varied from 0.9 to 2.1 kJ/mm. The T_{47J} value for the weld made with CO_2 shielding, at -2 °C, was considerably higher than for any other weld. The impact properties of the 3G position welds were less heat input dependent than the 1G welds as T_{47J} only varied from -35 to -25 °C for heat inputs of 1.2 and 2.4 kJ/mm respectively.

5.2.3 Metal-cored (MC) wire

The variation of weld metal tensile properties with heat input for the MC samples is shown in Figure 5.7. Again yield and tensile strength can be seen to generally decrease with increasing heat input. These variations are approximately linear with heat input and appear to be not greatly influenced by the use of CO_2 shielding. The elongation values were mostly high and appeared to be independent of welding conditions. The exception was the lowest heat input test-plate which had significantly lower elongation. All of the strength and elongation values obtained meet the requirements of the W50 classification in AS 2203-1 (1990).

Figure 5.8 shows the variation of mean CVN impact value with temperature for the various test-plates. This data indicate that while considerable spread in CVN values is present at higher temperatures, most of the results are closely grouped at temperatures lower than about -10 °C. Only the highest heat input weld metal (MC-1) appears to differ significantly from the others at low temperature with this sample giving lower

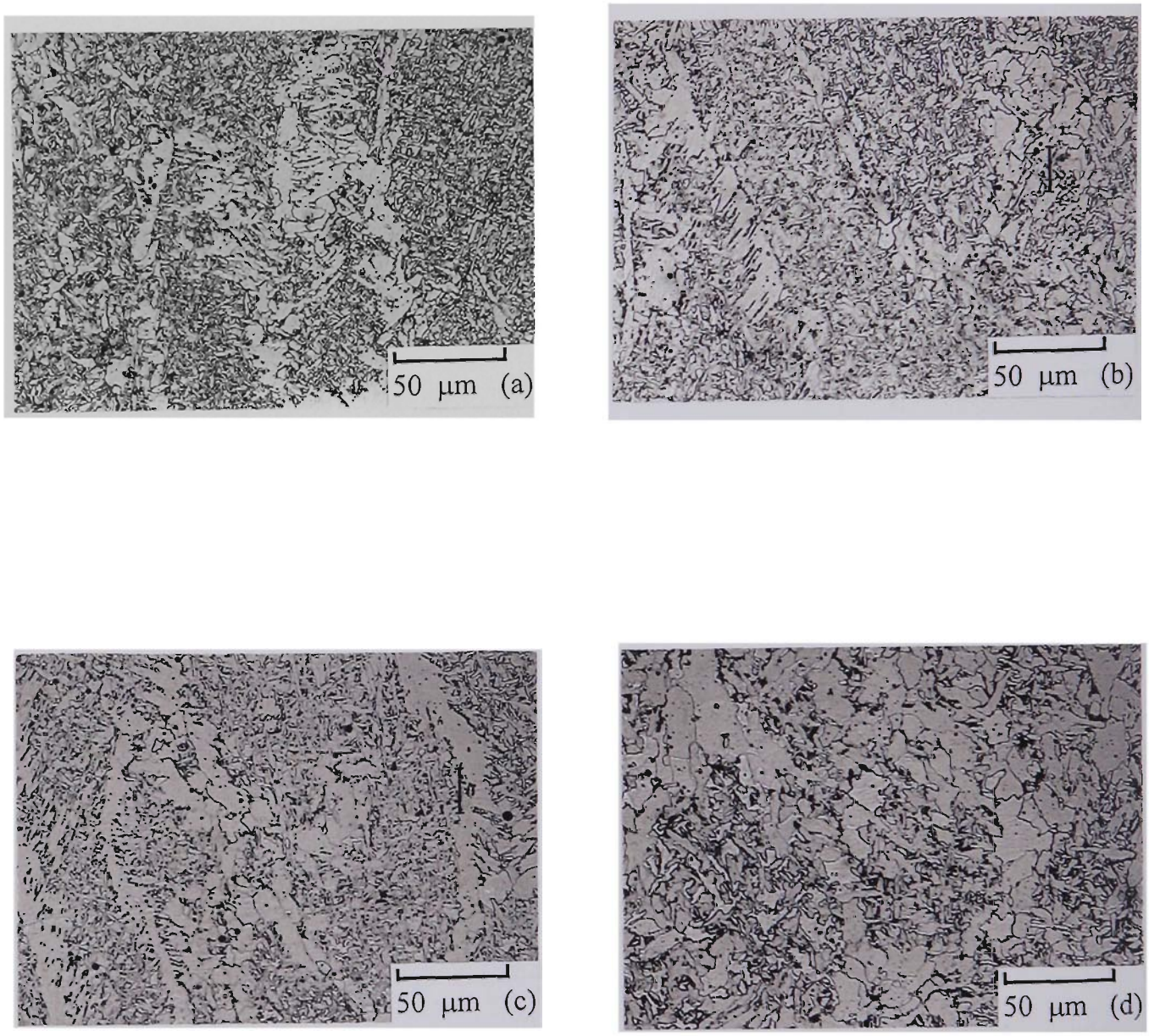

Figure 5.10: The microstructures of the SW regions for the B containing rutile flux-cored (RB) welded samples at the heat inputs: (a) 0.87 kJ/mm. (b) 1.51 kJ/mm. (c) 2.14 kJ/mm. (d) 2.44 kJ/mm (weave).

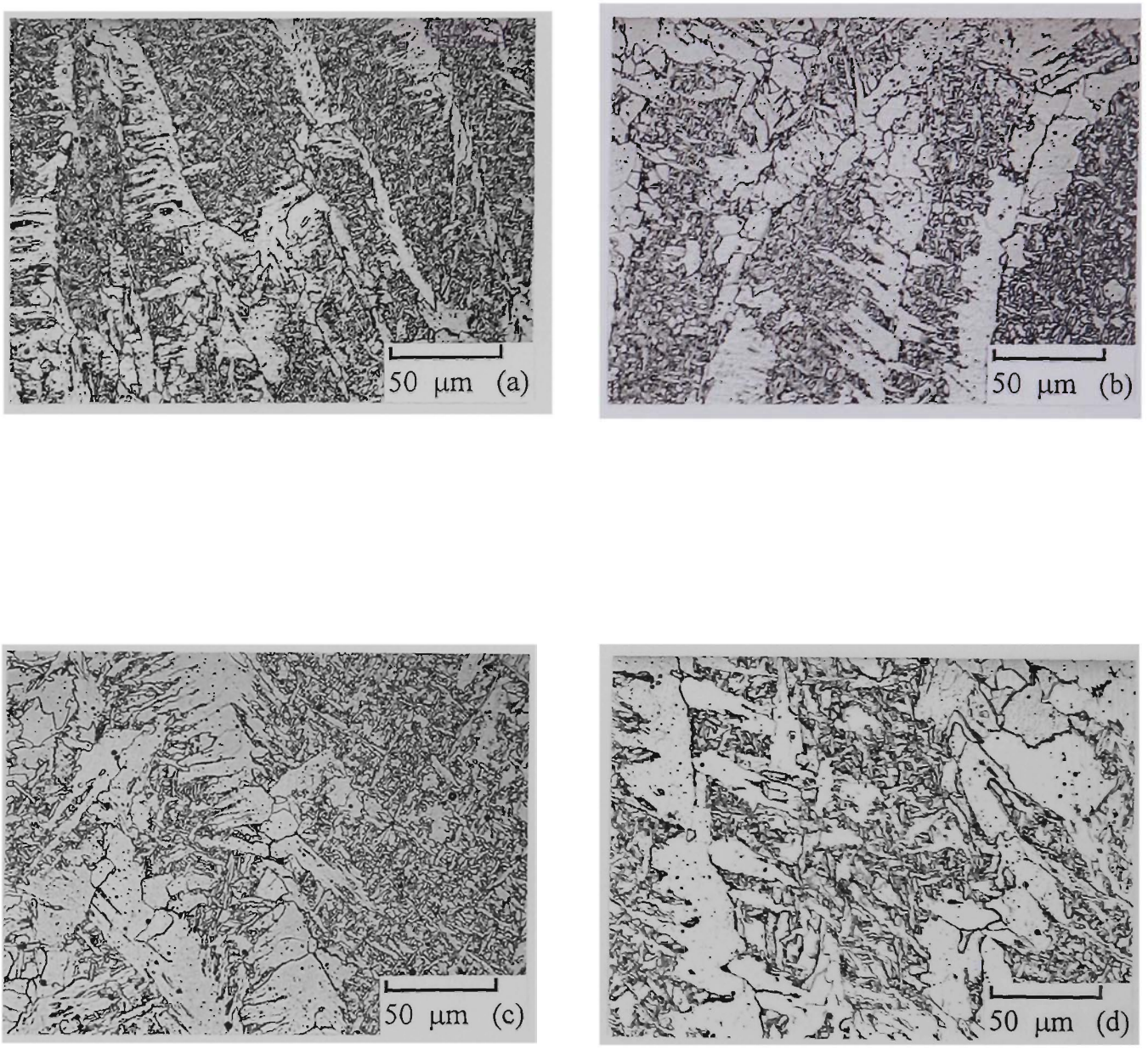

Figure 5.11: The microstructures of the SW regions for the metal-cored (MC) welded samples at the heat inputs: (a) 0.99 kJ/mm. (b) 1.66 kJ/mm (CO_2 shielding). (c) 1.99 kJ/mm. (d) 2.58 kJ/mm (weave).

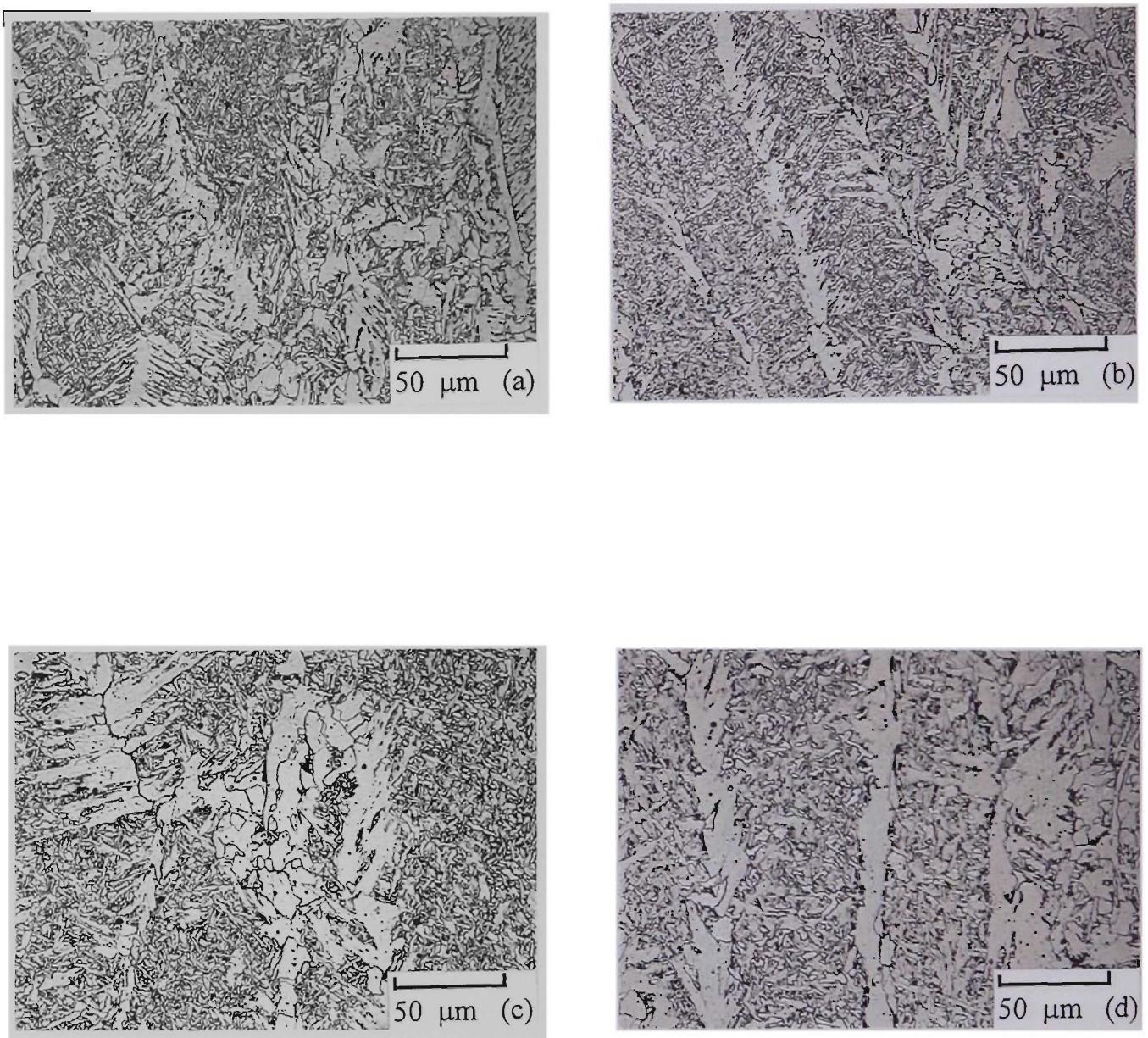

Figure 5.12: The microstructures of the SW regions for the rutile flux-cored (R) welded samples at the heat inputs: (a) 1.06 kJ/mm. (b) 1.43 kJ/mm. (c) 1.99 kJ/mm. (d) 2.51 kJ/mm (weave).

CVN values. The resulting variation in T47J with heat input is shown in Figure 5.9. The T47J values varied between 4 and -12 °C for heat inputs from 0.99 to 2.58 kJ/mm.

5.2.4 Quantitative metallography

Figures 5.10 to 5.12 reveal the predominantly columnar microstructure typical of unreaustenitised regions from the central portion of welds made at approximately 1kJ/mm, 1.5 kJ/mm (CO_2 shielding), 2 kJ/mm and 2.5 kJ/mm (using a weave technique) with the different wires. In general, the microstructures of all wires contain regions of AF, PF(I), PF(G) and FS. However, the proportion of acicular ferrite (AF) appears higher for the RB welds, particularly for the low heat input welds.

Table 5.1: Quantitative analysis of microconstituents for solidified weld metal.

Wire Classification	Heat Input (kJ/mm)	Area Percentage (%)			
		AF	PF(G)	PF(I)	FS
B Containing Rutile Flux-cored Wire (E71T-1) (RB)	0.87	71.6	12.3	14.4	1.8
	1.51	60.6	26.6	9.1	3.7
	2.14	54.3	32.4	8.0	5.3
	1.61	46.7	32.3	8.7	12.0
	1.20	58.8	22.8	9.0	9.2
	2.44	39.9	45.8	5.9	8.4
Metal-cored Wire (E70C-3) (MC)	0.99	33	41	12	14
	1.58	36	31	17	15
	1.66	36	42	11	11
	1.99	31	44	15	10
	2.58	20	2	72	6
Rutile Flux-cored Wire (E71T-1) (R)	1.00	45.8	26.9	10.6	16.7
	1.43	39.9	32.0	7.7	20.4
	1.99	37.5	30.5	15.7	16.3
	1.44	40.2	32.0	8.0	19.8
	1.06	43.2	28.8	10.1	17.9
	2.51	21.2	29.3	40.3	9.2

The results of the point counting for all wires are given in Table 5.1 and Figure 5.13. All of the welds made with stringer technique, including that with CO_2 shielding,

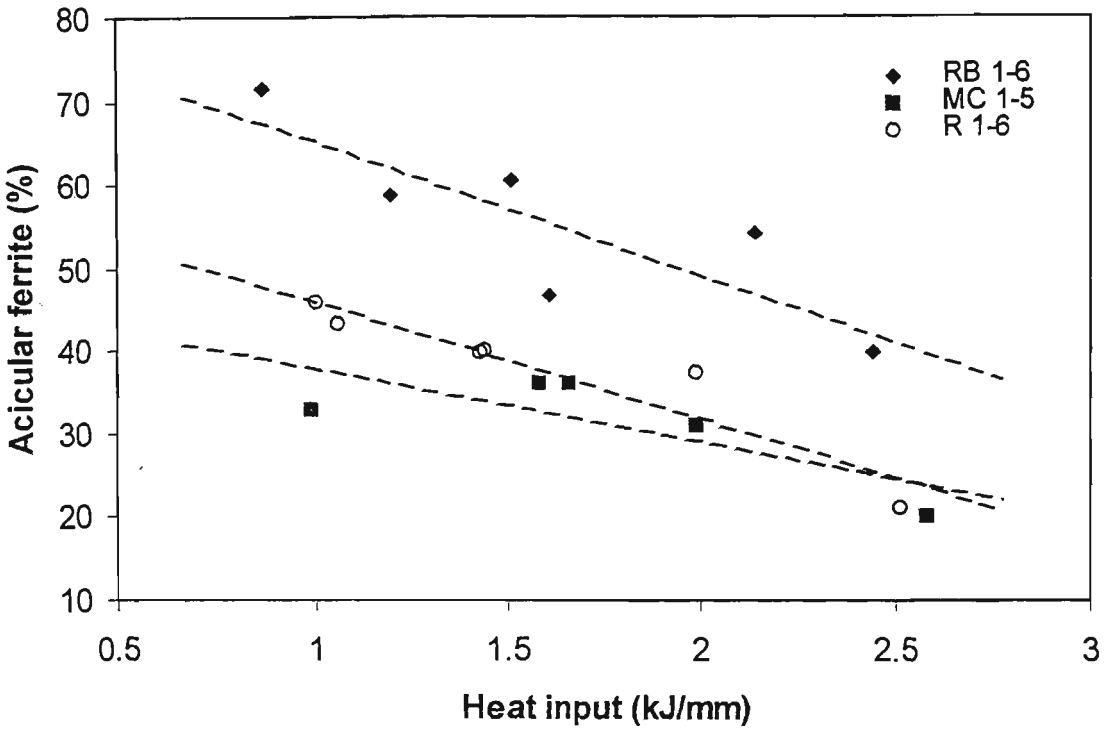

Figure 5.13: Variation of % acicular ferrite in SW regions with heat input.

contained similar proportions of the micro-constituents for R and MC samples. In all cases AF consisted of approximately 40 vol, % for R samples and 30 vol, % for MC samples, whereas PF(G) was about 30 vol, % for R samples and 40 vol, % for MC samples. The percentage of PF(I) was about 10% for both wires. The welds made with a weave-bead technique at 2.5 kJ/mm contained less AF (about 20%) but a higher level of PF(I). It should be noted that Table 5.1 applies to the proportion of constituents in solidified weld metal (SW) only. The overall volume percentages of AF, PF(G), PF(I) and FS will be lower as the percentages in Table 5.1 should be weighted in terms of the volume fraction of SW. However, the total volume fractions will be increased slightly by contributions from the reaustenitised region. For example, AF occurs both in the SW and GC regions of the weld.

The welds made with the RB wire contained a generally higher proportion of AF (Figure 5.13). For welds made with a stringer-bead technique and Ar-CO_2 shielding, the proportion of AF decreased with heat input while the proportions of PF(G) and FS increased. The amount of PF(I) was similar for most welds made with RB and R wires except for those with the lowest heat inputs and the weave-bead technique weld. For RB samples, the weld made with CO_2 shielding contained a significantly lower proportion of AF and higher levels of PF(G) and FS than the Ar-CO_2 shielded weld at similar heat input but a slightly contrary tendency was shown for R and MC samples. However, the lowest AF proportion was contained in the weave-bead technique weld at approximately 2.5 kJ/mm for all three wires.

5.2.5 Compositions of non-metallic inclusions

The non-metallic inclusions in the weld metals were globular in shape. Four types of globular non-metallic inclusions were distinguished in SEM images: (a) large dark

particles (1 to 3 μm), (b) fine dark particles (0.05 to 0.25 μm), (c) medium contrast particles (0.3 to 0.6 μm), and (d) large light and dark particles (2 to 5 μm). The compositions of the type (a) and (b) inclusions are given in Table 5.2.

Table 5.2: The mean weight compositions (wt %) of type (a) (large) and type (b) (small) non-metallic inclusions determined by a qualitative EDS method.

Types	Type (a) (large) particles							Type (b) (small) particles						
Composi -tions	Al	Si	Mn	Fe	S	Ti	O	Al	Si	Mn	Fe	S	Ti	O
BR wire	2.4	2.7	10.1	25.1	0.27	8.7	50.7	1.0	1.0	3.7	56.9	0.2	2.4	34.8
MC wire	3.0	7.3	14.0	20.8	0.3	1.0	53.5	1.4	3.6	6.3	47.5	0.2	0.5	40.4
R wire	2.1	4.8	13.9	13.3	0.2	10.9	54.9	0.8	2.3	5.7	51.7	0.7	2.1	36.8

Although type (a) and (b) particles existed in all three welds, the compositions of the particles varied both within a single weld and for the different weld metal types (Table 5.2). Therefore, the compositions listed in Table 5.2 are only approximate and the high Fe concentrations, particularly for the small particles, suggest that the electron beam sampled matrix material surrounding the particle. However, the compositions are useful in revealing the dominant inclusion elements and the ratios of these elements.

For RB weld metal, the large particles were characterised by high Mn, Ti and O levels indicating that the dominant oxide species are MnO and TiO, consistent with the overall weld metal compositions (Table 4.5). Assuming that Ti preferentially combines with N, Ti present in excess of the stoichiometric composition for TiN, will form TiO. Unreacted oxygen will then preferentially form SiO_2 and especially MnO, because of the high concentration of Mn (Bhadeshia et al. 1993). Al_2O_3 and SiO_2 are minor oxides associated with the TiO and MnO. The presence of S also suggests a small amount of

MnS is present. The small particles (type (b)) have similar ratios of the main constituent elements so the same species of oxide are indicated. In the RB welds the relatively high Ti contents are expected to prevent BN formation, leaving the B as solute atoms which can diffuse to and limit ferrite formation at prior γ grain boundaries. The reduced effectiveness of B at higher heat inputs in forming acicular ferrite may be related to BC formation at lower cooling rates and reduced inhibition of grain boundary nucleation.

The MC weldments were low in Ti (Table 4.5) and thus the type (a) and (b) particles show SiO_2 and MnO as the main oxide inclusions. MnS is also likely to be present. The rutile weld metal (R) has a Ti level well in excess of stoichiometric composition for TiN (10 : 1 compared to 3.4 : 1) and thus TiO is expected to be prominent in the inclusions. In addition, relatively high Mn and Si levels in the large and small inclusions indicate the presence of MnO and SiO_2.

The type (c) inclusions were only observed in the MC weld metals and EDS analysis indicated that they were relatively high in Si, Mn and Al, consistent with the weld metal analysis (Table 4.5), which shows a slightly higher Al level than the RB and R welds and much lower Ti content. The Mn and particularly the O contents were also higher than for the other two weld metals.

On the other hand, type (d) (mixed) inclusions were not observed in the MC weld metal. EDS analysis indicated that the darker constituent contained S whereas the lighter constituent did not. Both regions contained Ti and some Mn, but the darker constituent was leaner in O, Al and Si. It is inferred that the darker constituent consists of mixed oxide-sulphide, based mainly on Ti and Mn; whereas the lighter constituent contains Si, Ti, Mn and Al oxides.

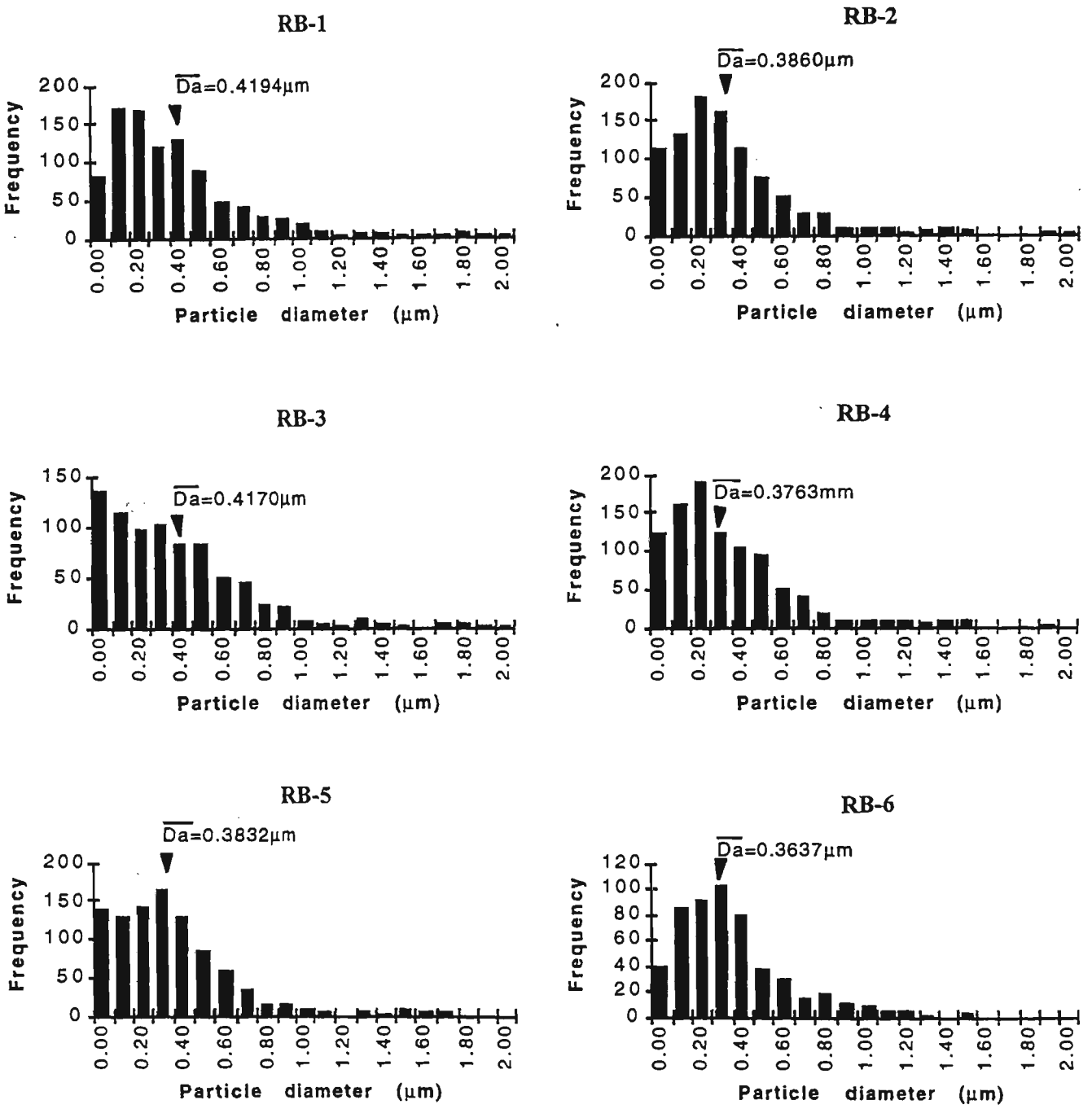

Figure 5.14: Size distributions of non-metallic inclusions for B containing rutile flux-cored (RB) samples The arrows indicate the arithmetic mean two dimensional particle diameters.

5.2.6 Inclusion parameters

It was found that the non-metallic inclusion distributions and sizes were non-uniform. The results from the determination of the non-metallic inclusions size distributions for each of the RB samples are presented graphically in Figure 5.14, based on the measurement of nearly 1000 particles in each case. These measurements were carried out at a SEM accelerating voltage of 10 kV, using a magnification of 5K. The histogram curves in Figure 5.14 were not normal and symmetrical.

Table 5.3: The important characteristics of non-metallic inclusions.

Sample Code	$V_V = A_A$ (%)	$\overline{D_a}$ (μm)	$\overline{D_v}$ (μm)	N_a ($1/\mu m^2$)	N_v ($1/\mu m^3$)	S_v (μm^{-1})	λ_v (μm)	F≥1.5μm (%)
RB-1	0.8092	0.4194	0.6587	0.03561	0.05407	0.0737	1.4651	1.81
RB-2	0.6354	0.3860	0.6063	0.03302	0.05446	0.0629	1.4616	0.76
RB-3	0.6890	0.4170	0.6551	0.03067	0.04681	0.0631	1.5372	1.78
RB-4	0.6120	0.3763	0.5911	0.03346	0.05660	0.0621	1.4429	0.74
RB-5	0.6566	0.3832	0.6019	0.03462	0.05752	0.0655	1.4352	1.71
RB-6	0.7605	0.3637	0.5714	0.04449	0.07787	0.0799	1.2973	0.96
MC-1	1.0353	0.5710	0.8970	0.02457	0.02740	0.0692	1.8377	3.93
MC-2	0.8611	0.3946	0.6198	0.04281	0.06907	0.0834	1.3502	1.53
MC-3	1.1272	0.4825	0.7580	0.03747	0.04944	0.0892	1.5095	3.67
MC-4	0.7721	0.3809	0.5983	0.04119	0.06886	0.0774	1.3516	1.79
MC-5	0.8301	0.4321	0.6788	0.03441	0.05069	0.0734	1.4969	2.12
R-1	0.7503	0.3288	0.5165	0.05373	0.10400	0.0872	1.1781	1.29
R-2	0.9011	0.3661	0.5751	0.05203	0.09048	0.0940	1.2340	0.76
R-3	0.6860	0.3440	0.4775	0.05746	0.12034	0.0862	1.1221	0.69
R-4	0.8921	0.3440	0.5403	0.05836	0.10802	0.0991	1.1633	1.02
R-5	0.7101	0.3216	0.5052	0.05314	0.10518	0.0843	1.1736	1.49
R-6	0.6105	0.3529	0.5542	0.03796	0.06850	0.0661	1.3540	1.30

The important inclusion characteristics are given in Table 5.3. These include the volume fraction of inclusions $V_V (A_A)$; the arithmetic mean two and three dimensional particle diameter, $\overline{D_a}$ and $\overline{D_v}$; the number of particles per unit area N_a; the number of particles per unit volume N_v; the total particle surface area per unit volume S_v; the

mean particle center to center volume spacing λ_v ; and the volume fraction of particles ≥ 1.5 μm.

5.3 Discussion

5.3.1 Chemical compositions of welds

Although the levels of C, Mn, Si, S, P and Mo were similar for the three wires, there were significant differences in Ti, Al, O and N (see Table 4.5). The RB wire contained higher levels of B, Ti and a generally higher N level, whereas the Ti and N levels were lower in the MC wire and the Al and O contents were higher. In addition the Mn and Si contents were generally higher in the MC welds than in the other two types of weld metal. The MC welds showed the highest average values of V_v, $\overline{D_a}$ and F≥1.5μm ie they contained the highest volume fraction of inclusions and the coarsest inclusions. These results are consistent with the weld metal compositions (Table 4.5) which show that the MC welds contained significantly more oxygen than the R and RB welds. Shielding gas appeared to have a larger effect on weld metal composition than the other welding variables investigated, as CO_2 shielding gave lower Mn, and also lower Si and B levels. These observations are consistent with other studies of the influence of shielding gas (Lathhabai and Stout 1985, Ferree 1992).

5.3.2 Quantitative microstructural analysis

The microstructural observations can provide explanations of several of the differences in weld metal mechanical properties among the three wires. A major difference in the unreaustenitised microstructures relates to the proportion of acicular ferrite (AF) present (see Table 5.1). For the R and MC wires, this value was about 40%(± 10%) for

all welding conditions except where a weave bead was used. In this case the lower proportion of AF was accompanied by an increase in PF(I). For the RB wire, the proportion of AF decreased significantly with increasing heat input (Figure 5.13). This decrease was roughly linear for those welds made using a stringer technique and Ar-CO_2 shielding, but the AF proportion was lower than this trend for both the CO_2 shielded weld and a weave-bead technique.

Although SW only comprised a fraction of the total weld metal structure (see Chapter 6), the trends in the proportion of AF showed several correlations with the observed low temperature impact properties. Firstly, the AF proportion was generally higher for the RB wire in line with its better impact properties. Secondly, the AF proportion reflected the heat input dependency of the impact properties for the three wire types in welds made with the stringer technique. With the R and MC wires, for which the toughness values were relatively insensitive to welding conditions, the proportion of AF only decreased with increasing heat input from 46 to 37% for the R wire and 36 to 31% for the MC wire. For the RB wire, for which the toughness values were considerably more sensitive to welding conditions, the proportion of AF decreased significantly with increasing heat input from 72 to 54%.

The fact that the amount of AF in the unreaustenitised regions is generally higher in the RB samples can be attributed to the presence of boron. The addition of a combination of titanium and boron to the weld metal produces a fine acicular microstructure that displays good low temperature toughness (Chen et al. 1993), particularly at high heat input levels (Lathabai and Stout 1985, Koshio et al. 1981). Several authors have reported that the formation of grain boundary nucleated ferrite, PF(G) and FS, can nearly be eliminated by balanced alloying with boron and titanium (Tsuboi and

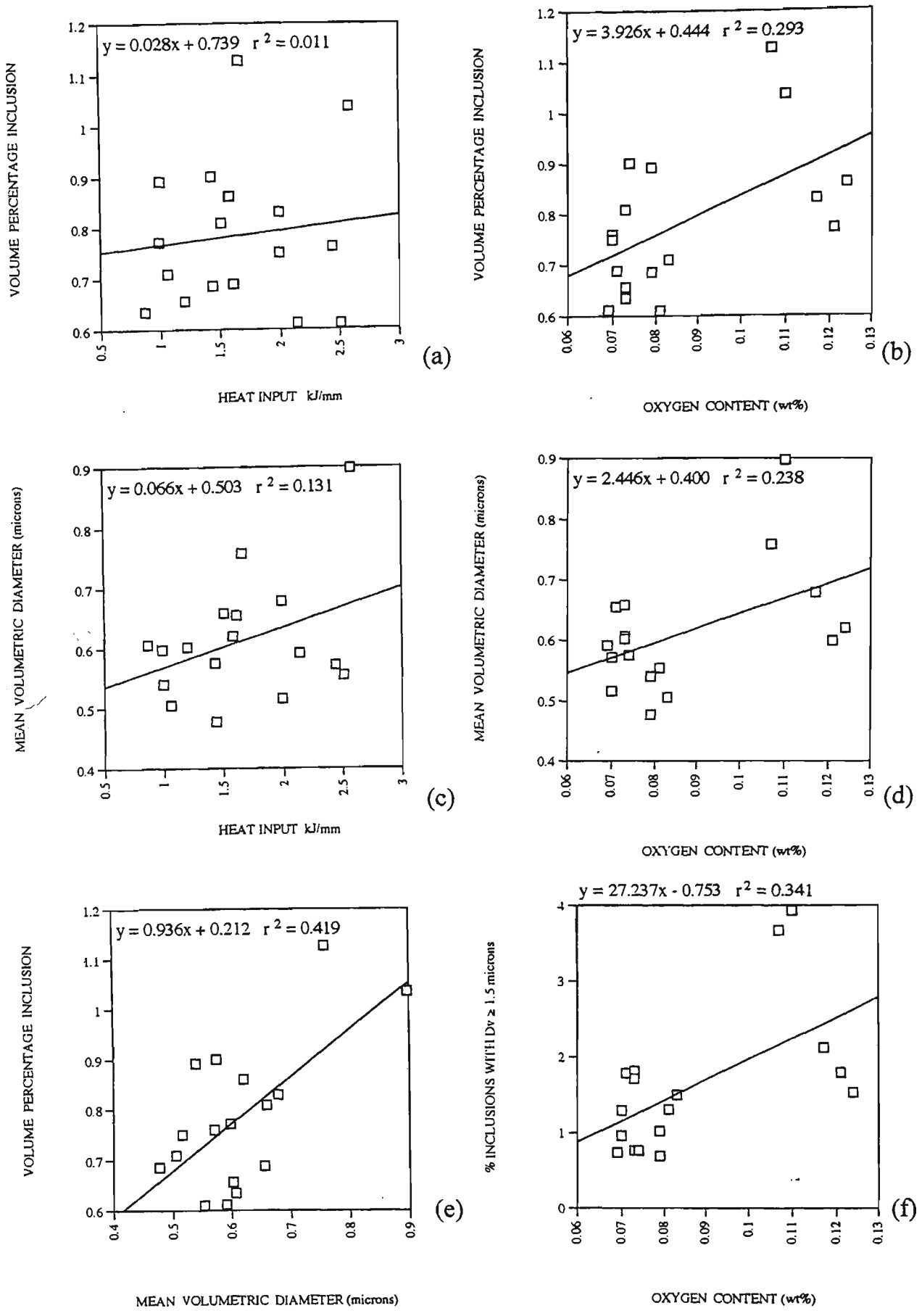

Figure 5.15: Relationships between important inclusion characteristics and heat input/ oxygen content for all welds: (a) V_v versus HI; (b) V_v versus O2; (c) $\overline{D_v}$ versus HI; (d) $\overline{D_v}$ versus O2; (e) $\overline{D_v}$ versus V_v; and (f) F≥1.5μm versus O2.

Terashima 1983, Mori et al. 1982, Watanabe and Kojima 1983, Kohno et al. 1982, Davis et al. 1983, Watanabe et al. 1980). The mechanism for the hardenability contribution of boron is based on the fact that boron segregates extensively to the prior austenite grain boundaries, where it reduces the grain boundary energy (Hondros and Seah 1983). The reduction in grain boundary energy will then increase the energy barrier to nucleation by lowering the surface free energy and therefore suppressing the formation of grain boundary nucleated ferrite and facilitating the intragranular nucleation of AF on oxide inclusions (Widgery 1974). The above effect is reflected in Table 5.1, where it can be seen that the amount of grain boundary nucleated ferrite is lower in the RB samples than in the other samples. The other factor that can influence the amount of AF is the effect of the size and distribution of the non-metallic inclusions on the nucleation of AF which is discussed in the next section.

5.3.3 Trends in inclusion distribution parameters

The inclusion parameters V_v and $\overline{D_v}$ for all weld samples are plotted in Figure 5.15 as a function of heat input and oxygen content. Figure 5.15 (a) shows the volume fraction V_v lies in the range of 0.62-1.13% and essentially there appears to be no correlation with heat input. However, Figure 5.15 (b) with oxygen content shows a weak correlation between V_v and oxygen content. The arithmetic mean volumetric particle diameter $\overline{D_v}$ is in a range of 0.48-0.90 μm and shows no correlation with changing heat input (Figure 5.15 (c)), but appears to weakly correlate with changing oxygen content (Figure 5.15 (d)). A reasonably strong relationship between V_v and $\overline{D_v}$ is shown in Figure 5.15 (e) as expected. The volume fraction of inclusions ≥ 1.5 μm was in a range of 1.81-3.93 % and correlates moderately well with changing oxygen content (Figure 5.15 (f)).

From Figures 5.14 and 5.15, it can be seen that although some inclusion parameters were generally increased with increasing oxygen content (Figure 5.15 (b), (d) and (f)), the distribution and size of non-metallic inclusions (Figure 5.14) and the inclusion parameters (Figure 5.15) show no apparent correlation with heat input. The indication is therefore that weld metal oxygen content is a more important factor in determining the inclusion parameters than heat input. Moreover, the current results show that the low temperature impact properties of the RB samples are significantly degraded with increasing heat input (Figure 5.6). It is therefore inferred that the low temperature impact properties do not correlate with the non-metallic inclusion size and distribution over the range observed for the welding conditions used. However, the non-metallic inclusions can contribute to the intragranular nucleation of AF and thus impart better toughness to the weld metal (Ito and Nakanishi 1976, Abson et al. 1978, Liu et al. 1982). It should also be noted that large or coarse inclusions are often located in the weakest region of the weld (eg centreline of single pass butt welds) and do not contribute to intragranular nucleation of AF (Sugden and Bhadeshia 1988). The proportion of large inclusions was highest for the MC welds but was not increased with increasing heat input in the current case, see Table 5.3.

5.3.4 Tensile properties

A common heat input range of approximately 1 to 2.5 kJ/mm was used for each of the three types of wire. In each case the use of a weave-bead technique was found to be advisable for heat inputs above 2.0 kJ/mm to allow better control of the large weld pools. With the exception of the 3G position samples, which were necessarily made at lower welding current (190 A), all samples were welded with currents of approximately 280 A, and appropriate voltages to obtain optimum metal transfer and bead-shape.

These conditions were chosen because they are close to those which would be used in practice for these wires in situations where high productivity under semi-automated conditions is sought.

The weld metal yield and tensile strengths from the 3 types of wire appeared to depend primarily on heat input with minor effects due to CO2 shielding or positional welding see Figures 5.1, 5.4 and 5.7. In every case, yield and tensile strength tended to decrease with increase in heat input. These decreases are similar for each type of wire with the majority being in the range 70 to 80 MPa for an increase in heat input from 1 to 2.5 kJ/mm. All yield strength values meet the requirements of AS 2203-1 (1990) and AWS (1979). However, the maximum tensile strength of 650 MPa for W50 grade in AS 2203-1 (1990) is exceeded by the welds from R and RB wires at the lowest heat input used (approximately 1 kJ/mm). The elongation values did not, in general, show such a clear trend with heat input. All were above the specified minimum of 22% except for the R wire at approximately 1 kJ/mm heat input.

Approximately linear decreases in tensile and yield strengths with heat input occurred for all wires. Weld metal composition, see Table 4.5, did not show any regular changes with heat input for any of the wire types, so the changes in strengths with heat input do not appear to be related to compositional factors. Also, none of the changes in the proportions of microstructural constituents with heat input, see Table 5.1, can explain the behaviour of the strength levels since the changes in these constituents vary considerably between wire types.

However, a decrease in strength level with heat input is in line with other studies involving variation of tensile properties with heat input (Evans 1982, Smith 1989) and is probably related to increases in grain size which can be expected at the longer

cooling times associated with higher heat input (Evans 1982). Assessment of the effect of the overall scale of the weld metal microstructure is presented in Chapter 8.

5.3.5 Impact properties

As shown by Figures 5.3, 5.6 and 5.9, the variations in weld metal impact value with heat input differ among the various types of wire. The T_{47J} values used to characterise low temperature impact are relatively insensitive to heat input for both the R and the MC wires. The low temperature impact properties however appear sensitive to heat input for the RB wire. The variation in T_{47J} over the heat input range of 0.87 to 2.44 kJ/mm is approximately 60 °C for the RB wire. Although weld metal from RB samples showed an increase in T_{47J} value with heat input, R and MC samples showed a general decrease with heat input. However, considerable scatter was present; the weave-bead technique generally gave low T_{47J} values (particularly for the RB wire); and the CO_2 shielded welds were often associated with high T_{47J} values. In contrast, the MC wire showed T_{47J} values which were largely independent of welding conditions. Only in the case of the RB wire is this sensitivity of low temperature impact properties to heat input large enough to affect the ability of the weld metal to meet requirements. In this instance, Grade 3 (AS 2203-1 1990, Lloyds Register 1995) impact properties were not achieved if the heat input was greater than approximately 1.75 kJ/mm and a stringer bead technique was used.

The impact properties for the R and MC wires welded with CO_2 shielding and weave-bead techniques did not differ from the trend for flat stringer welding. It should be noted, however, that CO_2 shielding was only used at one heat input for each wire. In contrast, the impact properties from the RB wire did appear to be sensitive to both CO_2 shielding and use of a weave-bead technique for vertical welding. The use of CO_2

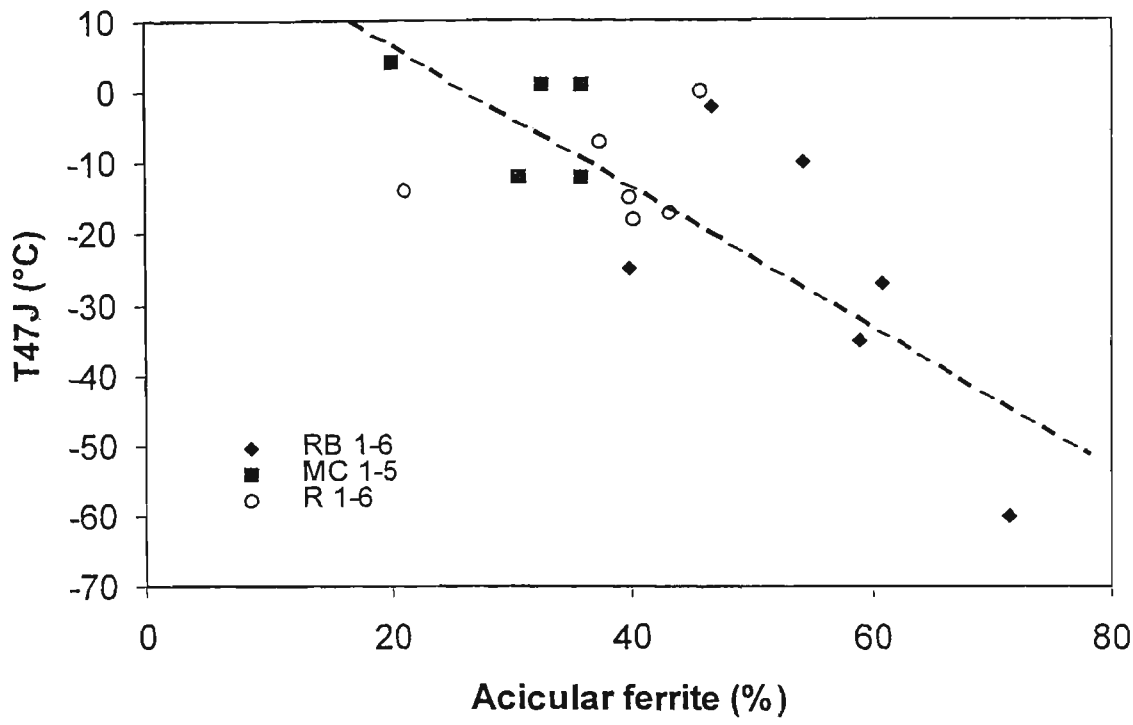

Figure 5.16: Variation of T_{47J} with acicular ferrite (AF) content in solidified weld metal (SW).

shielding resulted in poor impact properties with a high T_{47J} value (see Figure 5.6), while use of a weave-bead technique at high heat input had a beneficial effect on impact properties.

The majority of recent work in the field of weld metal microstructure-mechanical property relationships has emphasised the importance of increasing acicular ferrite content in obtaining optimum low temperature impact properties. Most of this work has been concerned with weld metal from processes other than gas-shielded continuous wires, so it is interesting to check this correlation in the present case. Figure 5.16 is a plot of the T_{47J} values obtained against measured area percent of acicular ferrite (AF). This figure indicates that, for the present data, T_{47J} decreased with increasing AF, especially for the RB samples. It is widely accepted for many welding processes (Abson and Pargeter 1986, Farrar and Harrison 1987, Dolby 1983) that low temperature impact properties of weld metal improve with proportion of AF in unreaustenitised regions. The current results confirm that weld metals from the R, MC and RB wires generally follow this trend.

These results also suggest that, while the proportion of acicular ferrite in unreaustenitised regions is a factor in determining low temperature impact properties of the weld metal, there must be other factors which have an influence in the present circumstances. Possible factors, for which measurements are available, are proportions of the unreaustenitised and reaustenitised material; volume fractions of each HAZ sub-zone and double-reheated sub-zone; overall hardness; mean free path (MFP); weld metal composition; and non-metallic inclusion parameters. The influences of these factors on impact properties are considered in following chapters.

5.4 Conclusions

1. Shielding gas appeared to have a larger effect on weld metal composition than the other variables investigated, as CO2 shielding gave significantly lower Mn, and generally lower Si, C and B levels than Ar gas mixtures.

2. For the R and MC wires, the toughness values were relatively insensitive to welding conditions, and the proportion of AF only decreased with increasing heat input from 46 to 37% for R wire and 36 to 31% for MC wire. With the RB wire, for which the toughness values were considerably more sensitive to welding conditions, the proportion of AF decreased significantly with increasing heat input from 72 to 54%.

3. The non-metallic inclusions in welded metal were globular in shape. Four types of globular non-metallic inclusions could be distinguished in SEM images: (a) large dark particles (1 to 3 μm), (b) fine dark particles (0.05 to 0.25 μm), (c) medium contrast particles (0.3 to 0.6 μm), and (d) large light and dark particles (2 to 5 μm).

4. The large and small dark particles were present in all three weld types and the dominant oxide species was Mn oxide, together with Ti oxide in the two rutile welds (R and RB) and SiO2 in the MC welds. Type (c) particles were confined to the MC welds and consisted of Mn, Si, Al oxides. The mixed particles (d) consisted of Ti, Mn oxides with S concentrated in one constituent and Al, Si and O in the other.

5. The sizes and distributions of the non-metallic inclusion were non-uniform and the MC welds were characterised by the highest volume fraction and coarest particles, consistent with the highest weld metal oxygen content.

6. Although non-metallic inclusions are known to contribute to the intragranular nucleation of AF and thus impart better toughness to the weld metal, the characteristics of the non-metallic inclusions themselves did not show a strong correlation with the low temperature impact properties. Furthermore, the proportion of large inclusions was not increased significantly with high heat input in the current work.

7. Weld metal tensile and yield strengths for all three wires decreased by approximately 70 to 80 MPa when heat input was increased from 1 to 2.5 kJ/mm. The maximum tensile strength allowed in some specifications (AS 2203 1990, Lloyds Register 1995) was exceeded by weld metal from the R and RB wires at the lowest heat input used (approximately 1kJ/mm).

8. Weld metal impact properties for the R and MC wires appeared to be relatively insensitive to the heat input, welding technique and shielding gas used. In contrast, the impact properties of the RB wire were more sensitive to heat input, welding technique and shielding gas. For a stringer-bead technique at heat inputs above 1.75 kJ/mm, the RB wire did not reach the minimum specified impact values (AS 2203 1990, Lloyds Register 1995).

CHAPTER 6

REAUSTENITISED AND UNREAUSTENITISED WELD METAL

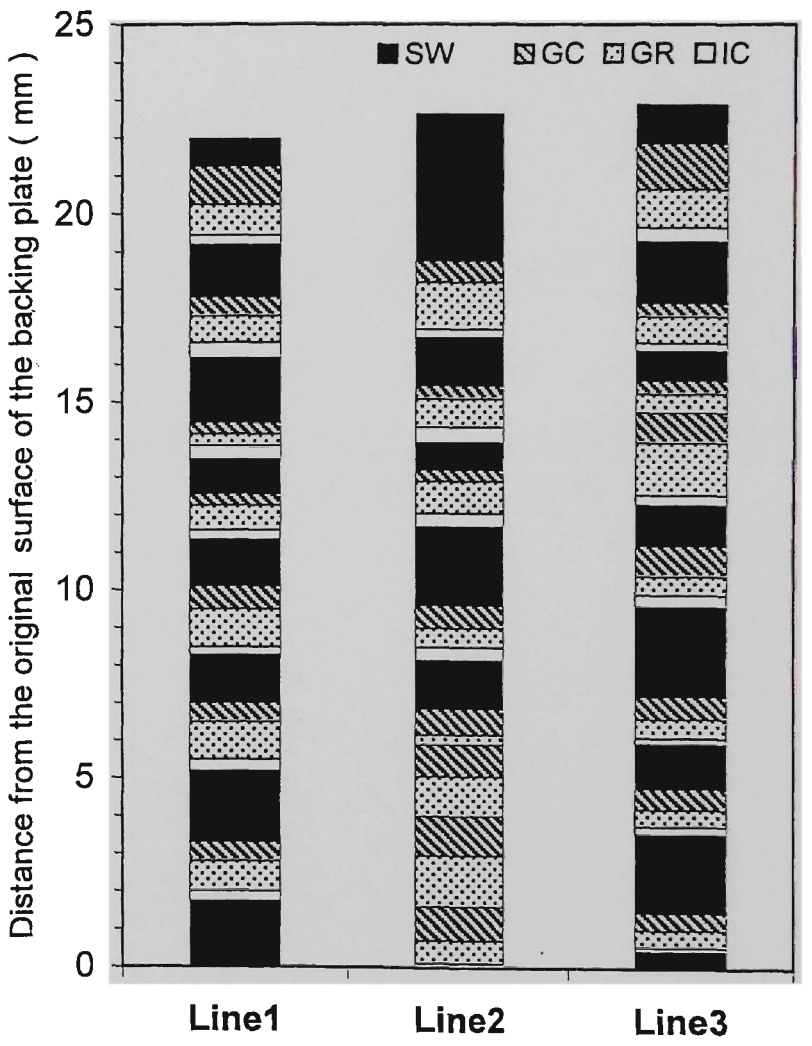

Figure 6.1: The sub-zone distribution along selected test lines for sample RB-2.

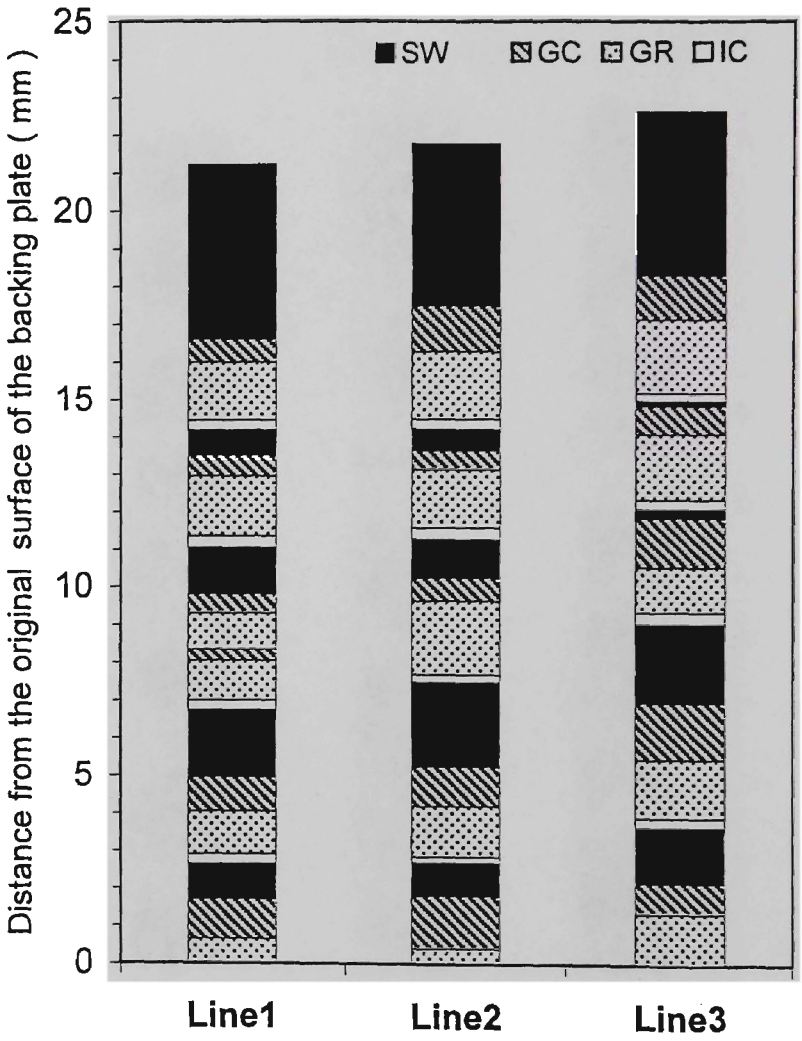

Figure 6.3: The sub-zone distribution along selected test lines for sample RB-6.

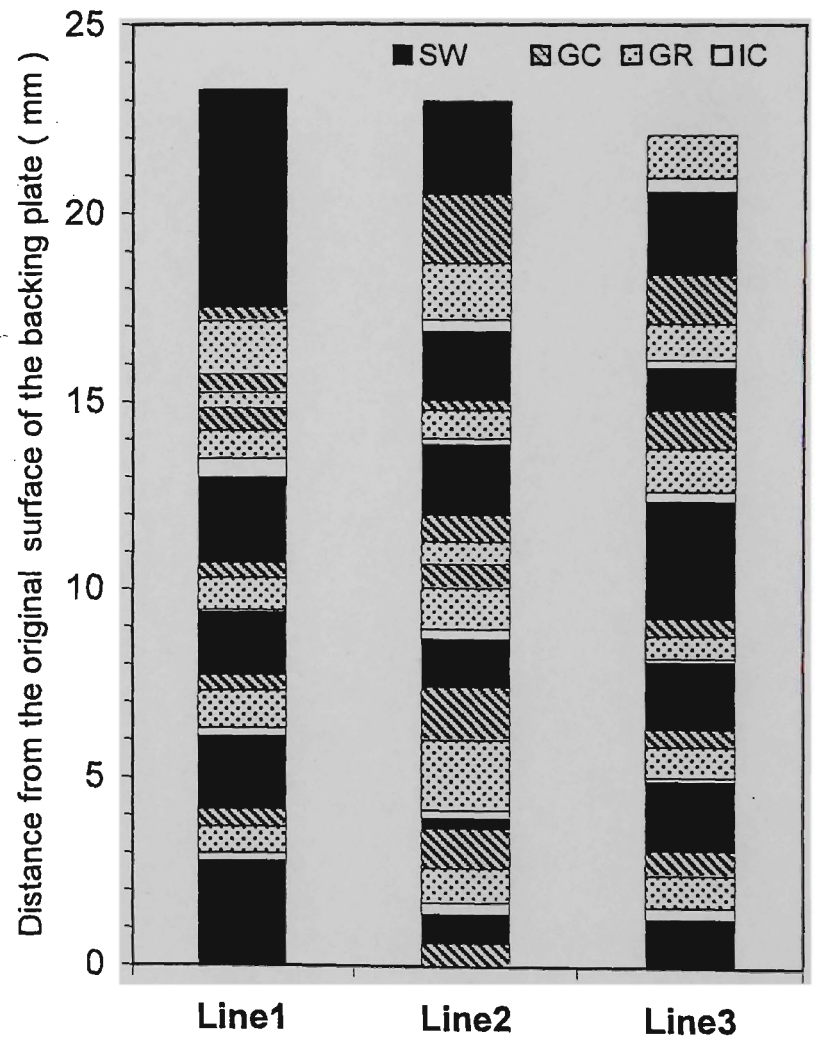

Figure 6.2: The sub-zone distribution along selected test lines for sample RB-3.

6.1 Introduction

There has been recent discussion of the relative importance of reaustenitised and unreaustenitised weld metal in determining mechanical properties of multipass welds. Burget et al. (1988) investigated the effects of differing weld metal microstructures in multi-layer submerged arc welds on the impact and static fracture toughness. They concluded that the toughness properties are lower for unreaustenitised regions compared to reaustenitised regions. On the other hand, Chen et al. (1993) carried out a comparative study on the toughness of specimens from a multi-layer C-Mn steel weld by simulating the various reheating cycles using weld thermal restraint stress and strain cycle simulation. This led to the suggestion that the weakest region for fracture would be the reheated one. Therefore, investigations of the proportion of reaustenitised and unreaustenitised regions and further, the volume fraction of each sub-zone (GC, GR, IC) are useful to improve understanding of the contributions to toughness. Linear and areal measurements have been used for this purpose.

6.2 Results

6.2.1 Volume fractions of reaustenitised and unreaustenitised regions

The typical distribution of different regions of weld metal from the results of linear measurement along three parallel test lines for samples RB2, RB3 and RB6 are shown in Figure 6.1-6.3. These regions included solidified weld metal (SW); grain coarsened (GC); grain refined (GR); and intercritical (IC) regions. These figures illustrate the considerable differences in run placement and proportions of the SW region and the GC, GR and IC HAZ sub-zones resulting from the changes in heat input and welding technique. The volume fractions of reaustenitised and unreaustenitised regions were

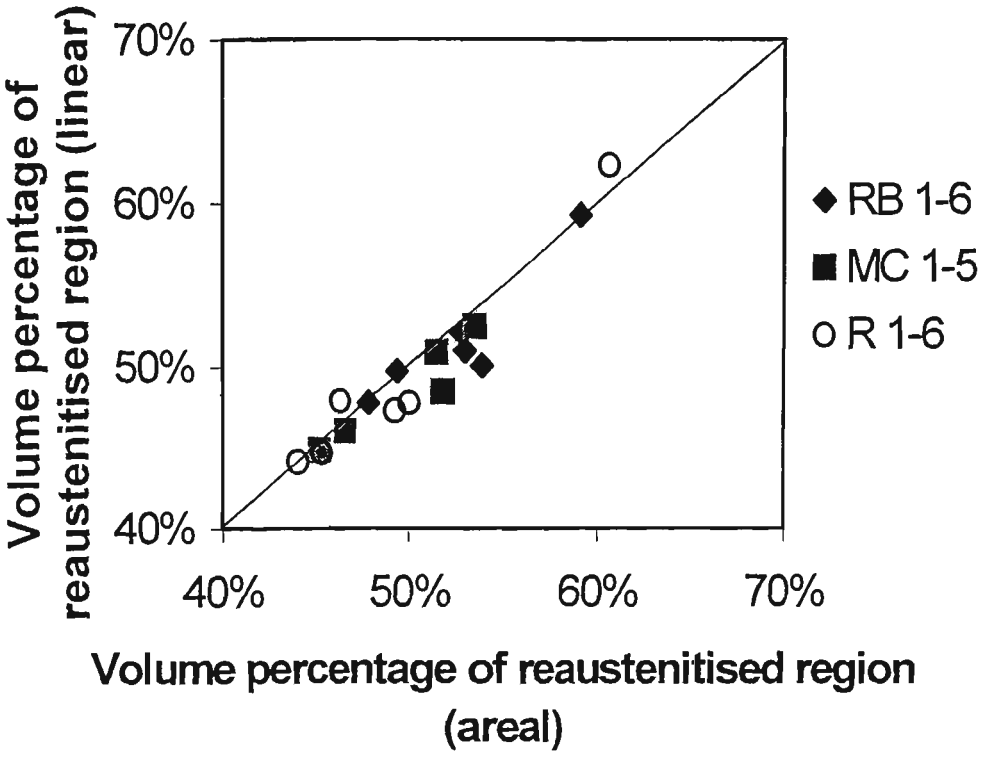

Figure 6.4: Comparison of linear and areal results.

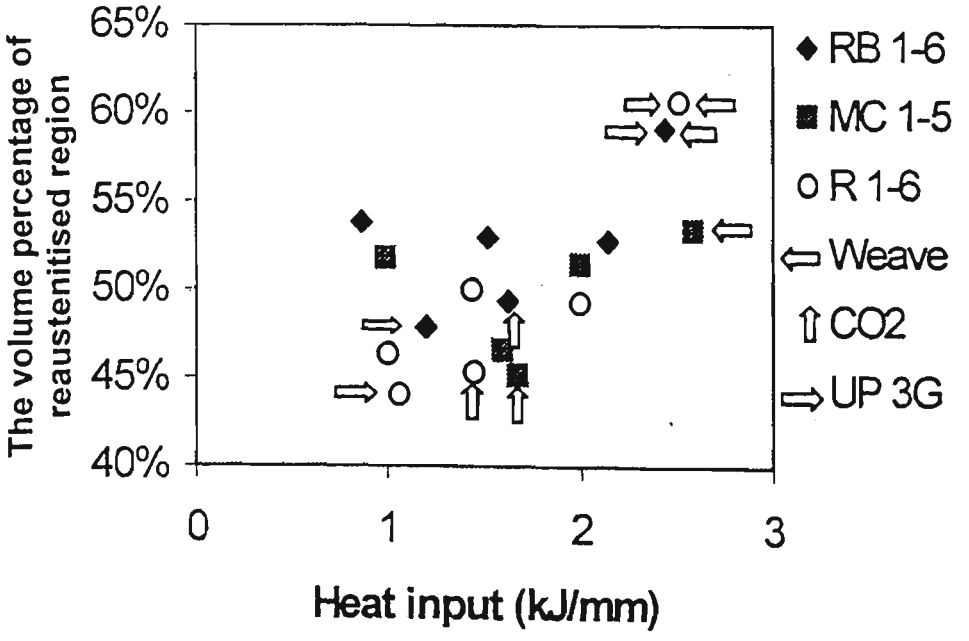

Figure 6.5: The volume percentage of reaustenitised region versus heat input.

obtained from both linear and areal measurements and very similar values appeared in both sets of results. The difference between these two methods is less than 4%. Figure 6.4 indicates that the test area and linear measurement methods give mutually consistent results.

It is well known that the volume fraction of reaustenitised regions in the weld metal is affected systematically by electrode diameter and interpass temperature (Easterling 1983, Evans 1980, 1979): the volume fraction of reaustenitised regions decreases with increasing electrode diameter and increases with interpass temperature. In order to study which other parameters could affect the percentage of reaustenitised structure, the present experiments fixed these two factors.

Figure 6.5 shows the volume fraction of the reaustenitised regions in the weld metal versus heat input for linear measurement. For the flat stringer welds with Ar gas mixtures there was no strong trend in percentage reaustenitised region with increasing heat input. In general, about 50% reaustenitised region was obtained over the heat input range of 0.87 - 2.14 kJ/mm, independent of consumable type. However, all three consumables showed the trend that the volume fraction of reaustenitised region increased with weave welding over the stringer technique.

A slight change in microstructure resulted from the use of 100 % CO_2 as the shielding gas: the volume fraction of the reaustenitised region decreased relative to welds produced using Ar rich shielding gas at a similar heat input. Changing the welding position from horizontal to vertical also decreased the volume fraction of the reaustenitised region.

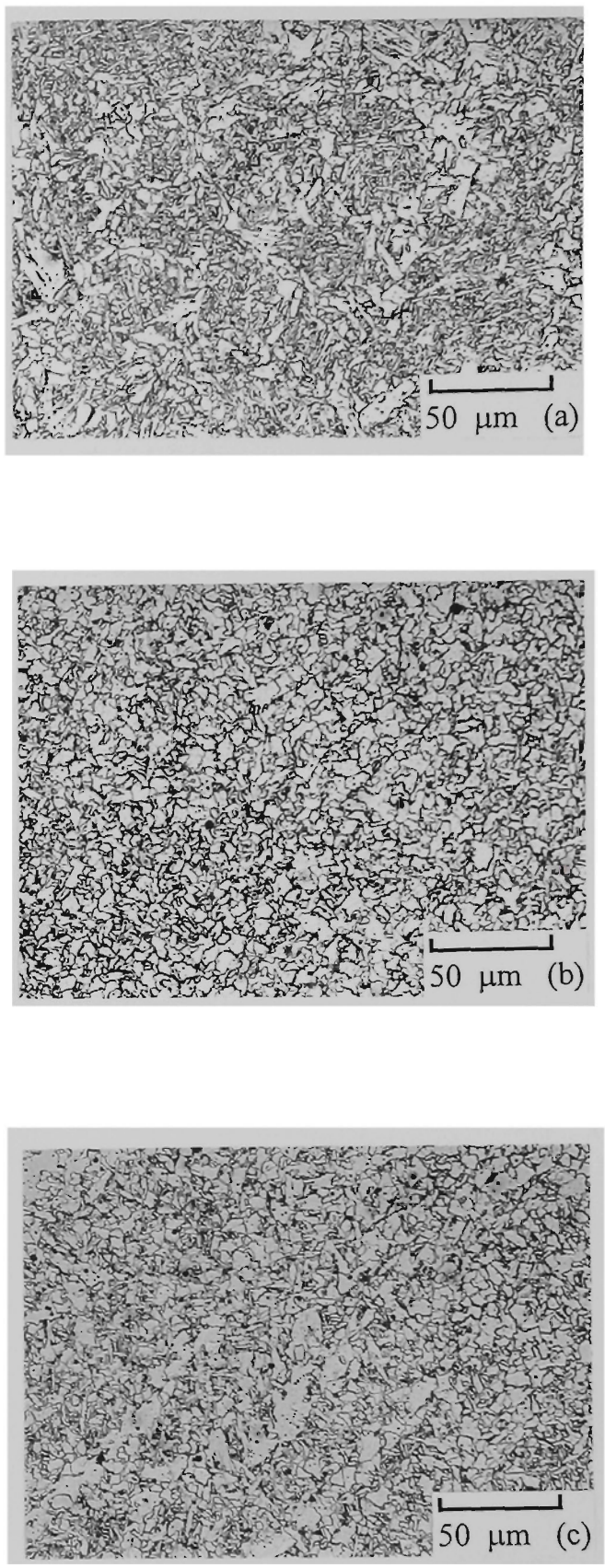

Figure 6.6: The microstructures of each sub-zone in HAZ for sample RB-2 at 0.87 kJ/mm heat input: (a) GC sub-zone. (b) GR sub-zone. (c) IC sub-zone.

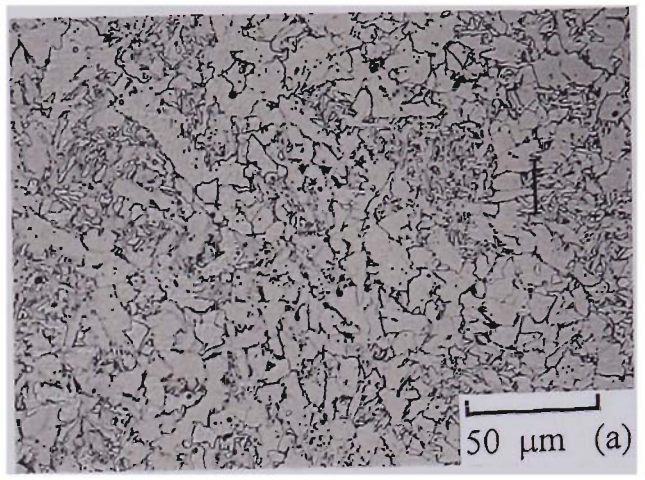

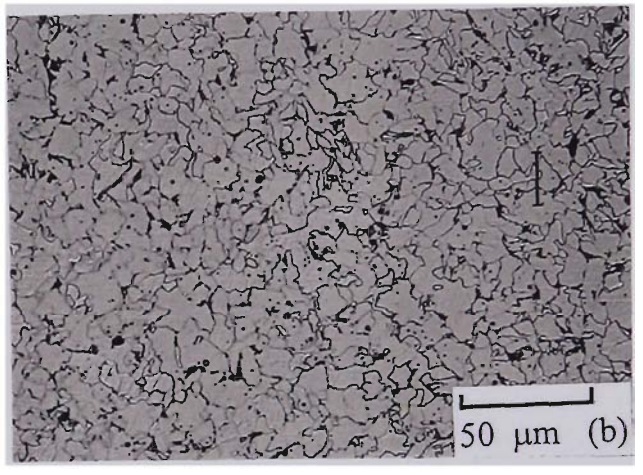

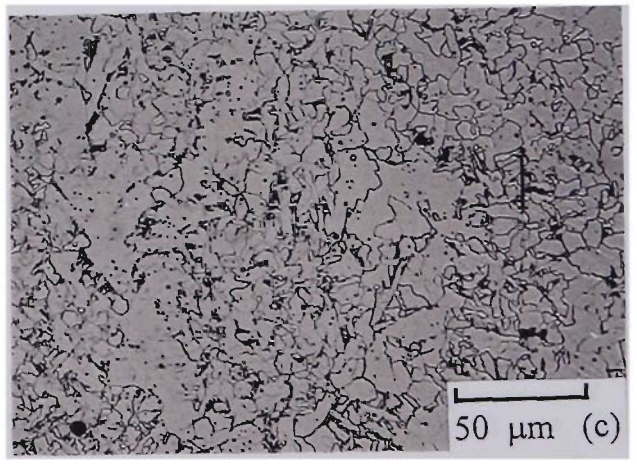

Figure 6.7: The microstructures of each sub-zone in HAZ for sample RB-3 at 1.61 kJ/mm heat input and CO_2 shielding gas: (a) GC sub-zone. (b) GR sub-zone. (c) IC sub-zone.

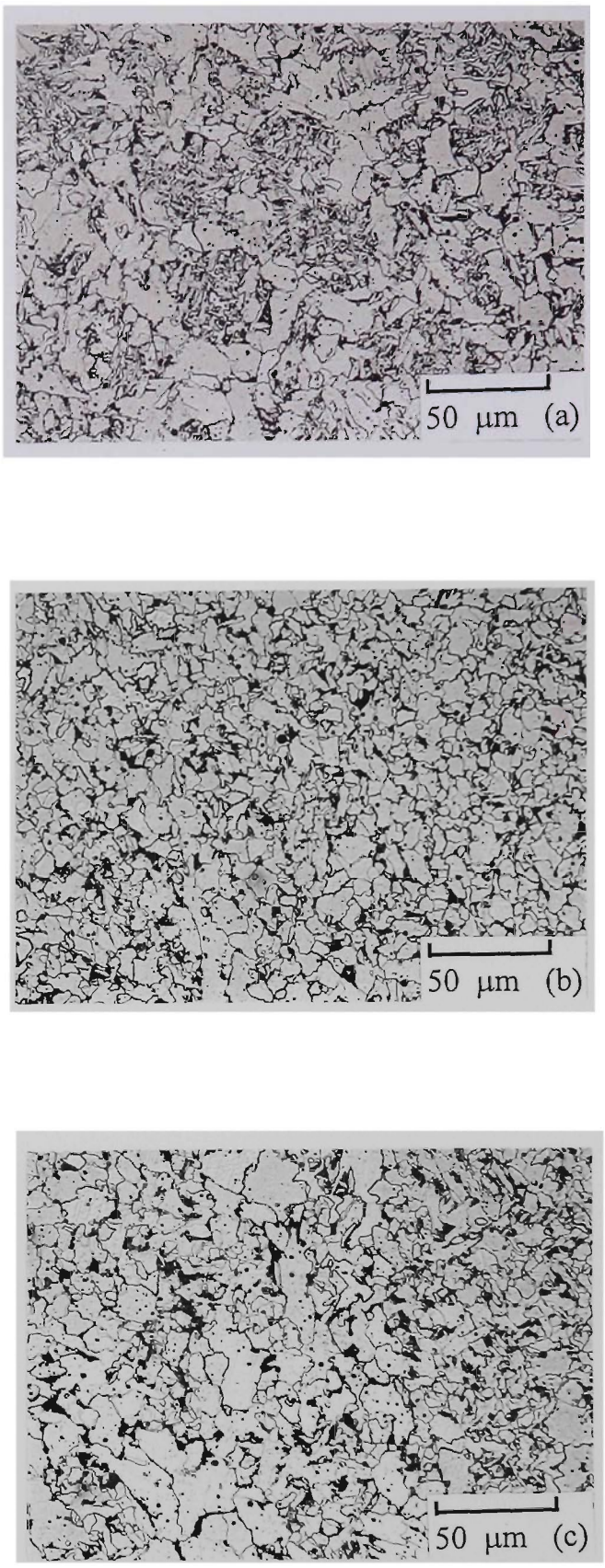

Figure 6.8: The microstructures of each sub-zone in HAZ for sample RB-6 at 2.44 kJ/mm heat input, 3G position and weave-bead technique: (a) GC sub-zone. (b) GR sub-zone. (c) IC sub-zone.

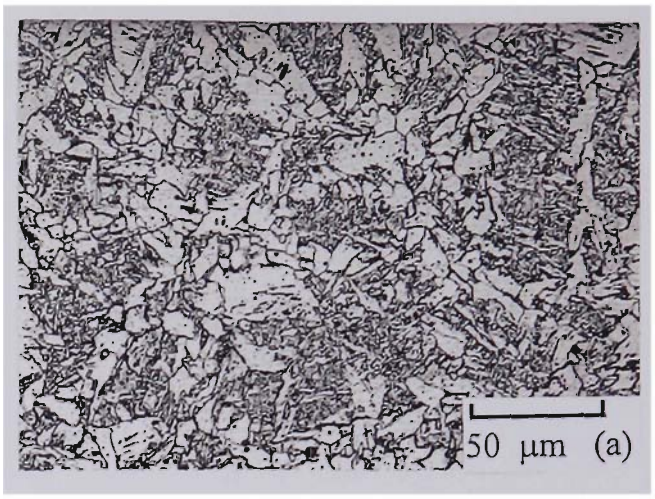

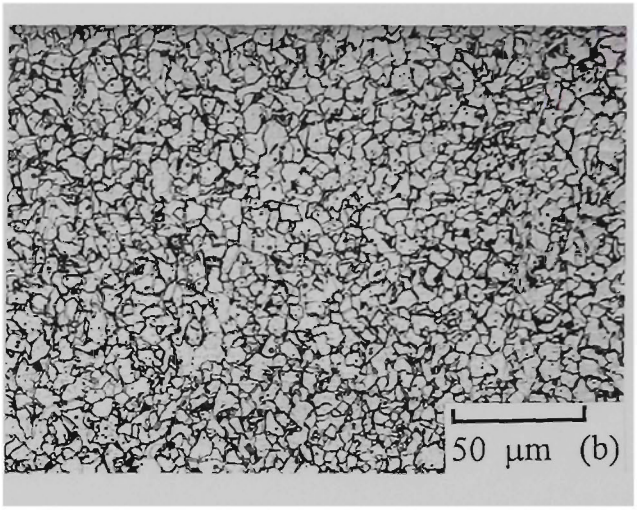

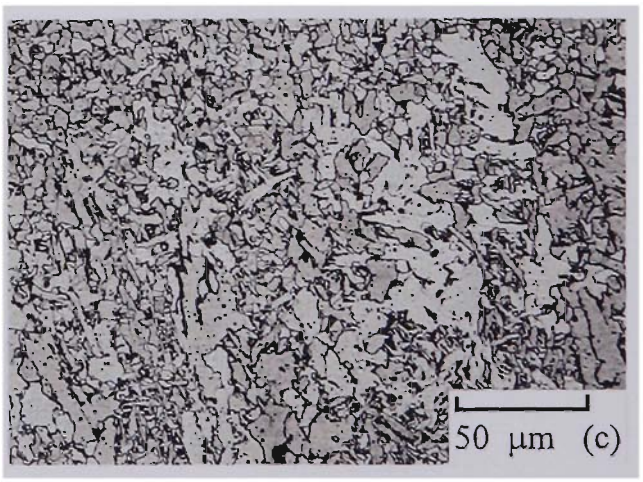

Figure 6.9: The microstructures of each sub-zone in HAZ for sample MC-4 at 0.99 kJ/mm heat input: (a) GC sub-zone. (b) GR sub-zone. (c) IC sub-zone.

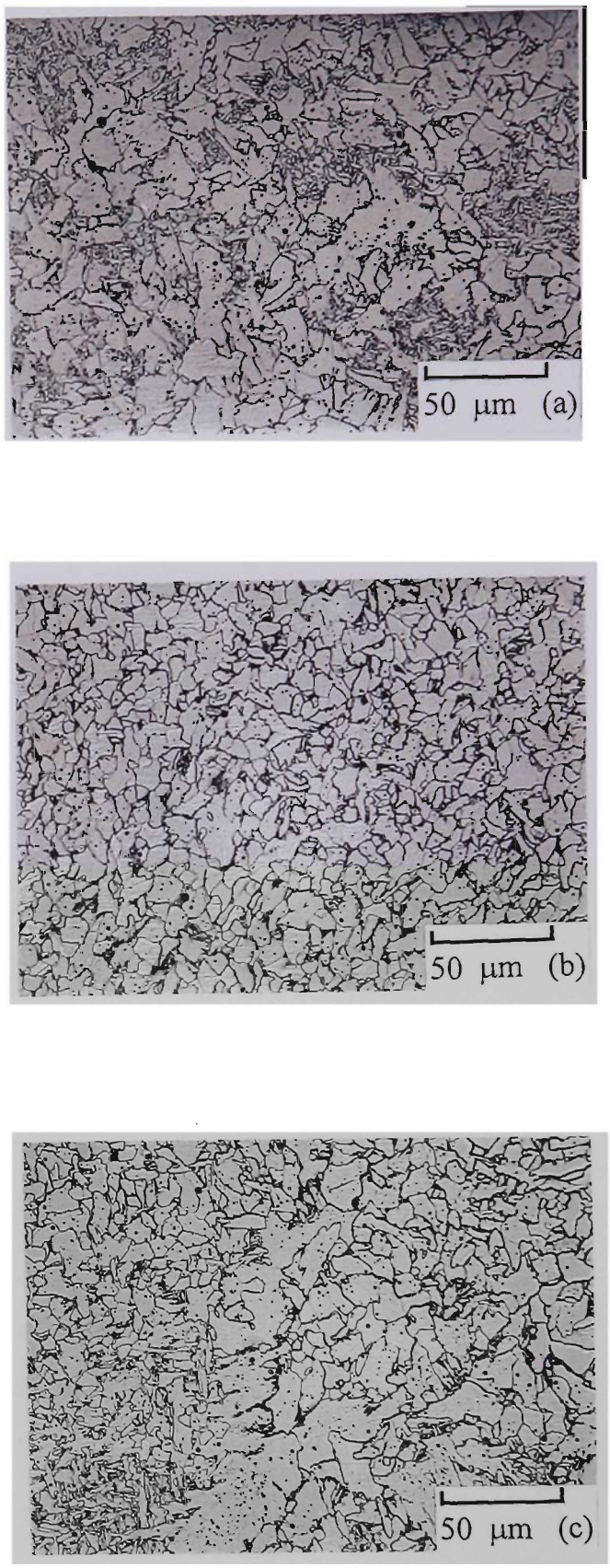

Figure 6.10: The microstructures of each sub-zone in HAZ for sample MC-3 at 1.66 kJ/mm heat input and CO_2 shielding gas: (a) GC sub-zone. (b) GR sub-zone. (c) IC sub-zone.

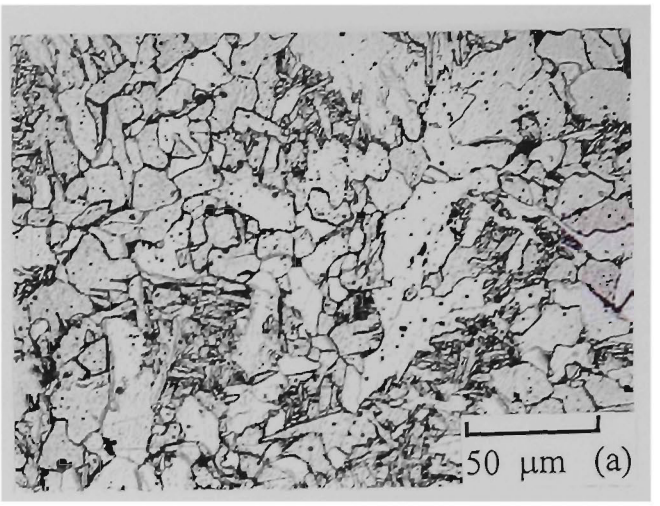

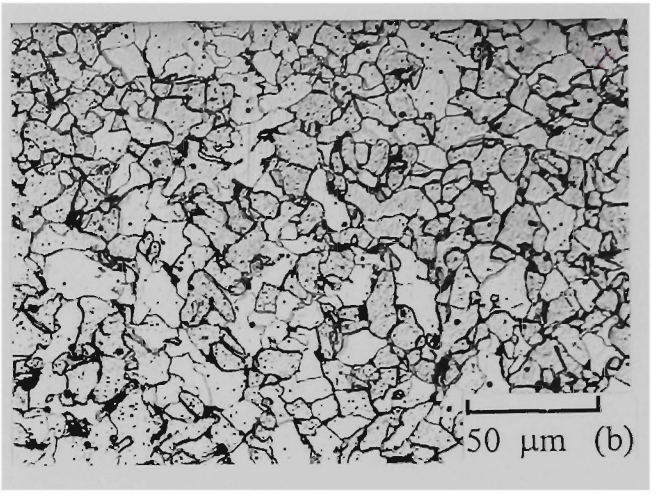

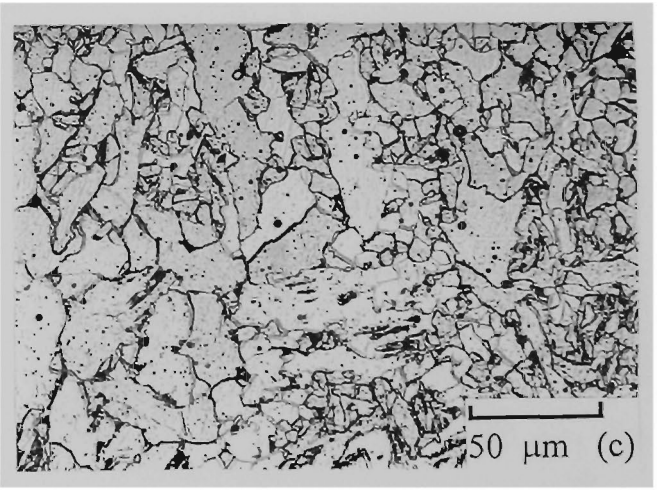

Figure 6.11: The microstructures of each sub-zone in HAZ for sample MC-1 at 2.58 kJ/mm heat input and weave-bead technique: (a) GC sub-zone. (b) GR sub-zone. (c) IC sub-zone.

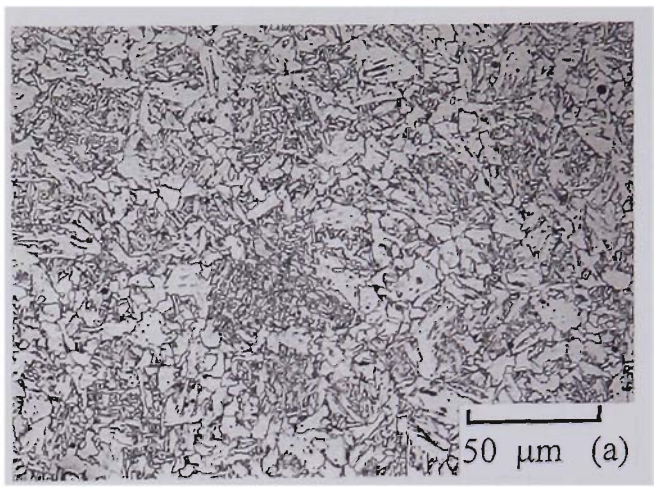

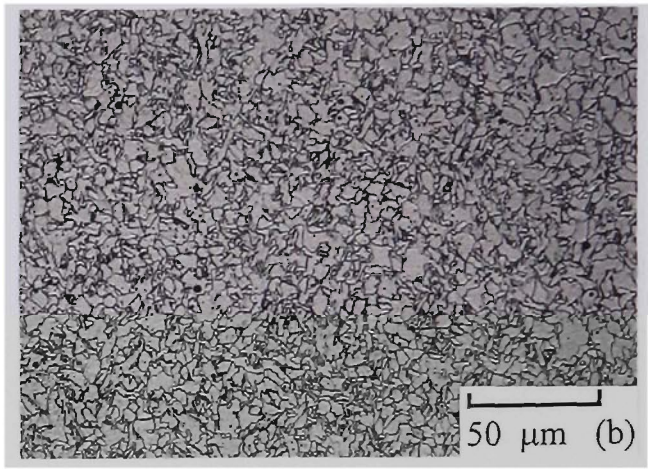

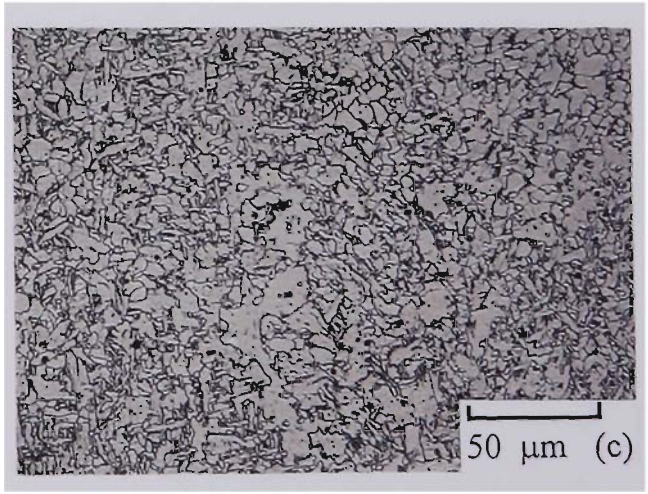

Figure 6.12: The microstructures of each sub-zone in HAZ for sample R-5 at 1.06 kJ/mm heat input and 3G position: (a) GC sub-zone. (b) GR sub-zone. (c) IC sub-zone.

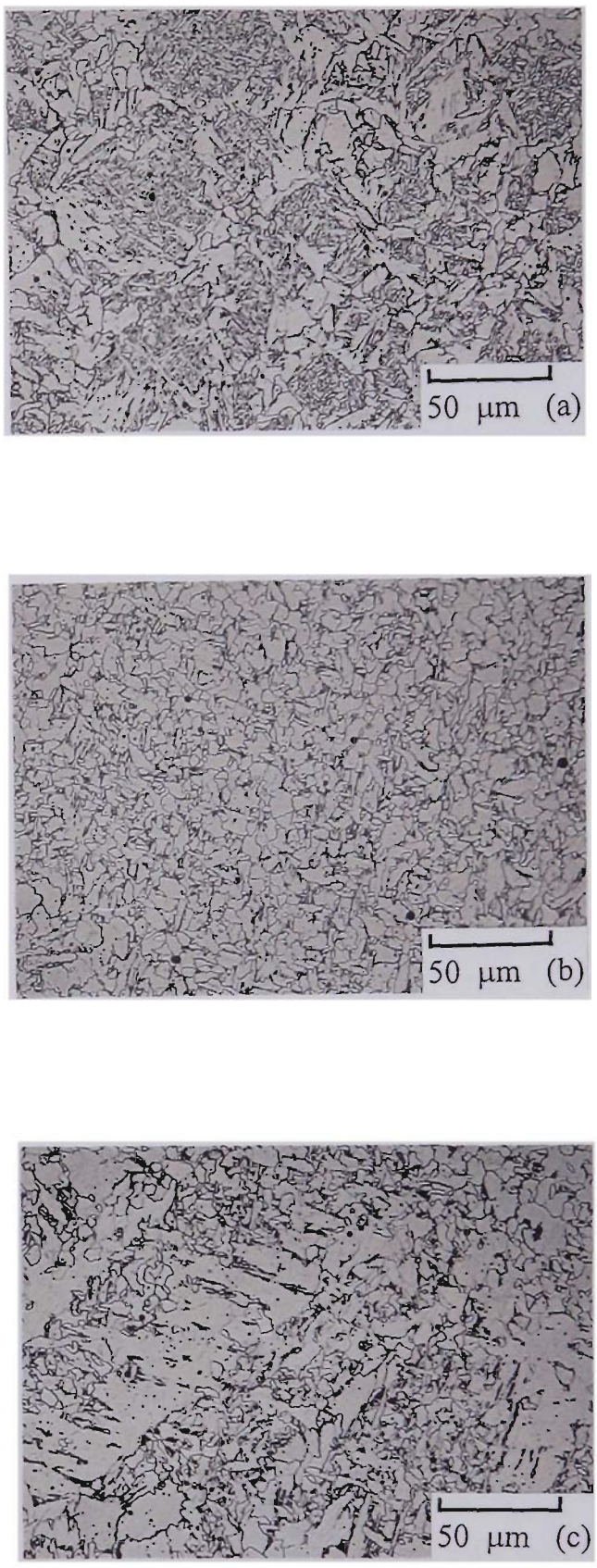

Figure 6.13: The microstructures of each sub-zone in HAZ for sample R-3 at 1.44 kJ/mm heat input and CO_2 shielding gas: (a) GC sub-zone. (b) GR sub-zone. (c) IC sub-zone.

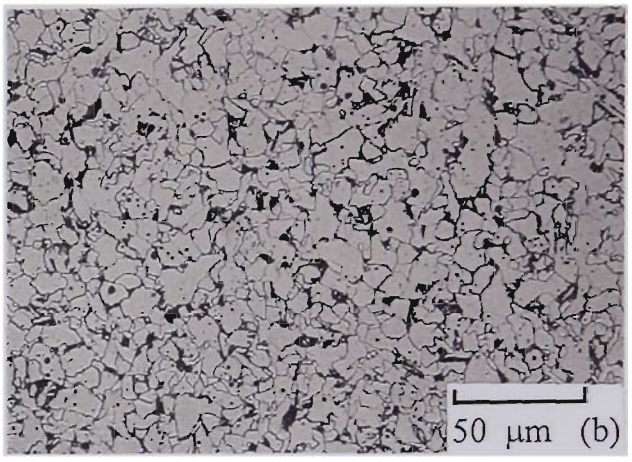

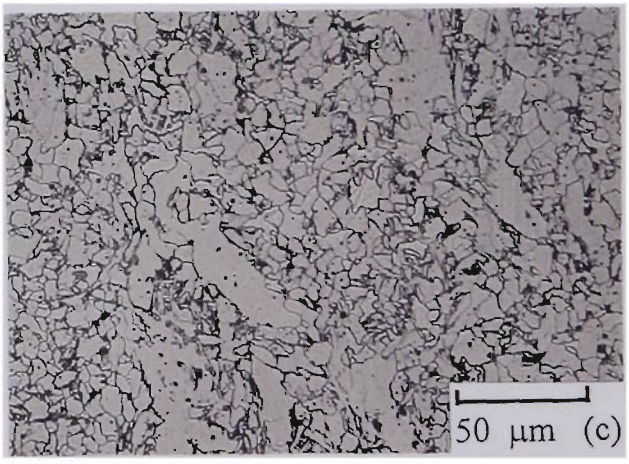

Figure 6.14: The microstructures of each sub-zone in HAZ for sample R-6 at 2.51 kJ/mm heat input and, 3G position and weave-bead technique: (a) GC sub-zone. (b) GR sub-zone. (c) IC sub-zone.

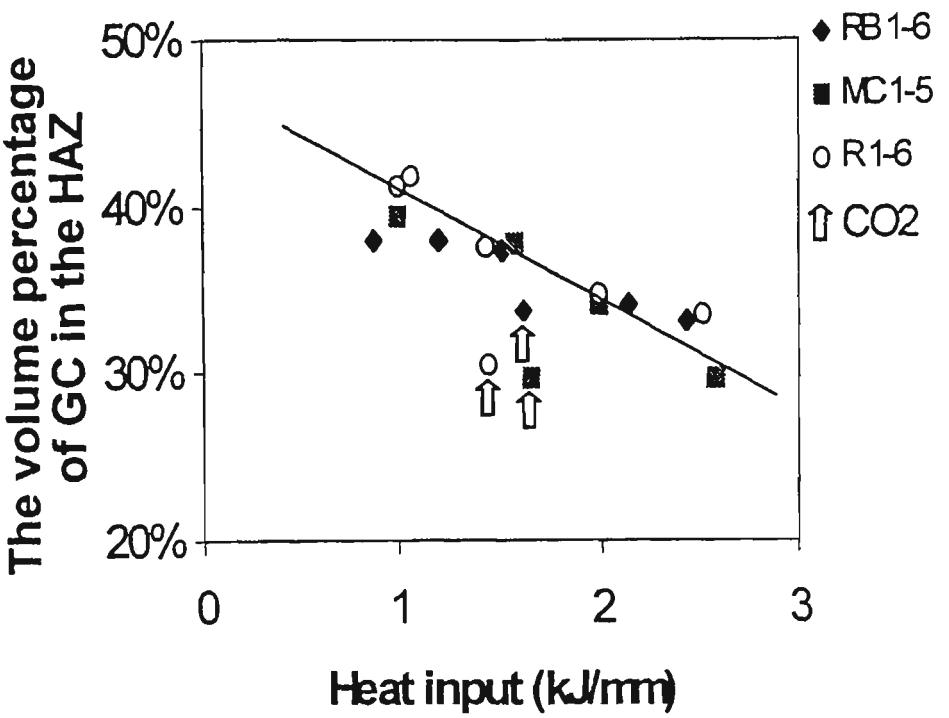

Figure 6.15: Relationship between the volume percentage of grain coarsened (GC) sub-zone in HAZ and the heat input.

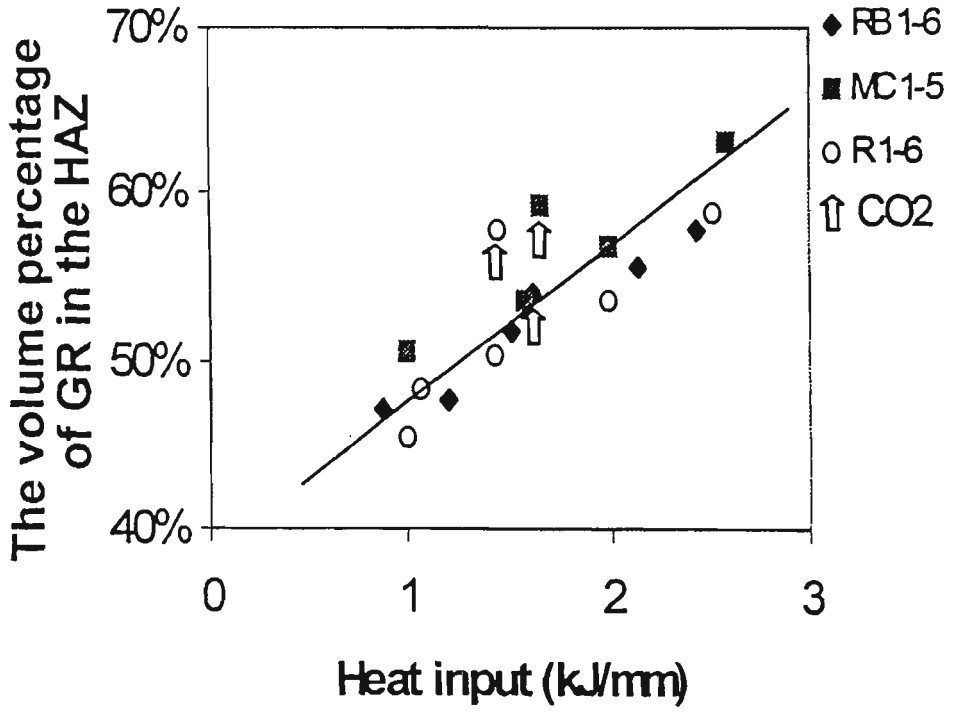

Figure 6.16: Relationship between the volume percentage of grain refined (GR) sub-zone in HAZ and the heat input.

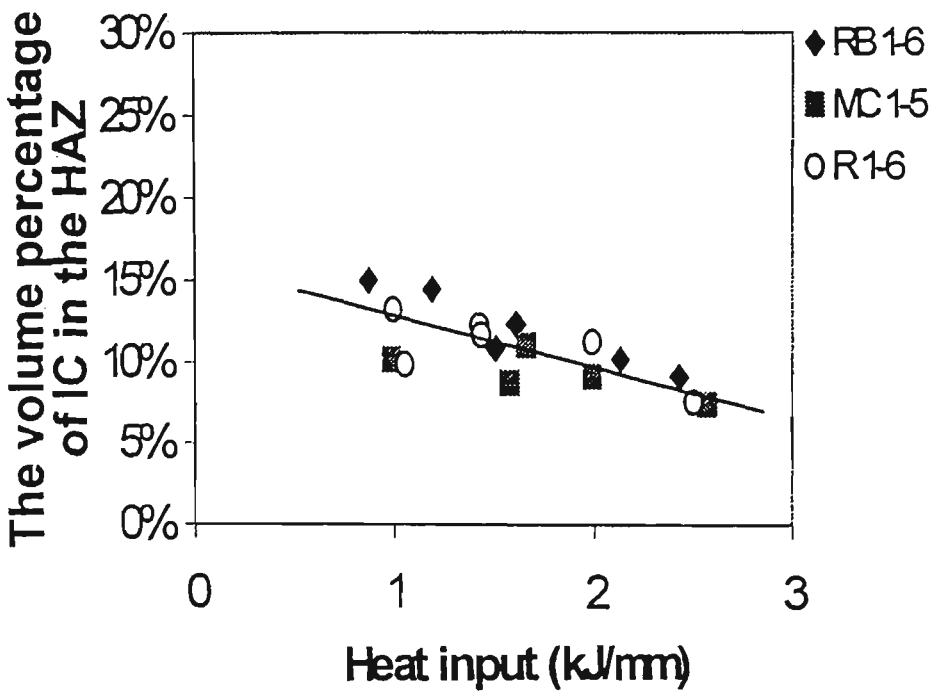

Figure 6.17: Relationship between the volume percentage of intercritical (IC) sub-zone in HAZ and the heat input.

6.2.2 Volume fractions of weld metal sub-zones

The microstructures of GC, GR and IC HAZ sub-zones in weld metal produced at approximately 1.0, 1.5 and 2.5 kJ/mm for each wire are shown in Figures 6.6 - 6.14. These micrographs illustrate the considerable differences in microstructure resulting from the changes in welding conditions such as heat input, shielding gas, welding technique and welding position. Through linear measurement, the average volume fractions of GC; GR; and IC sub-zones were obtained. The volume fractions of the GC and GR sub-zones in the HAZ for each sample are given in Figure 6.15 and Figure 6.16. These figures show that the volume fraction of GC sub-zone decreased linearly with increasing heat input. On the contrary, the volume fraction of GR sub-zone increased linearly with increasing heat input. However, the volume fraction of the GC sub-zone in the HAZ for pure CO_2 shielding gas was found to be decreased relative to Ar-CO_2-(O_2) welds at similar heat inputs (Figure 6.15) and the volume fraction of GR structure was correspondingly increased for CO_2 shielding gas (Figure 6.16).

In the multipass weld metal, the IC region is the smallest part of the HAZ and the change of volume fraction is relatively small with different heat inputs compared to the other two main regions (GC and GR). However, a slightly decreasing trend with increasing heat input could still be observed (Figure 6.17).

6.3 Discussion

6.3.1 Effects of welding technique and welding position

Evans (1980) reported a similar result to the trend in Figure 6.5 for the effect of changing welding techniques on the volume fractions of reaustenitised and unreaustenitised regions. He noted that for fully weaved deposits (4.3 kJ/mm) the heat-affected zones penetrated to such an extent that no columnar structure remained in the mid-section. Therefore, the increase in volume fraction of reaustenitised region with weave welding over the stringer technique observed in the present work is consistent with Evans' results.

Changing the welding position from flat to vertical also decreased the volume fraction of the reaustenitised region. This condition is consistent with results also reported by Evans (1981) who claimed that by using vertical-up welding the bead size was greater, resulting in fewer layers being laid and in a greater proportion of columnar weld metal being retained.

6.3.2 Effects of pure CO_2 shielding

A slight change was observed in the volume fraction of reaustenitised region from the use of 100 % CO_2 as the shielding gas (see Figure 6.5). It is possible that the more highly oxidised weld metals produced using CO_2, with their lower carbon equivalents, are characterized by higher Ac_1 and Ac_3 temperatures, therefore leading to less extensive austenitisation on heating. However, other factors may need to be considered as discussed below.

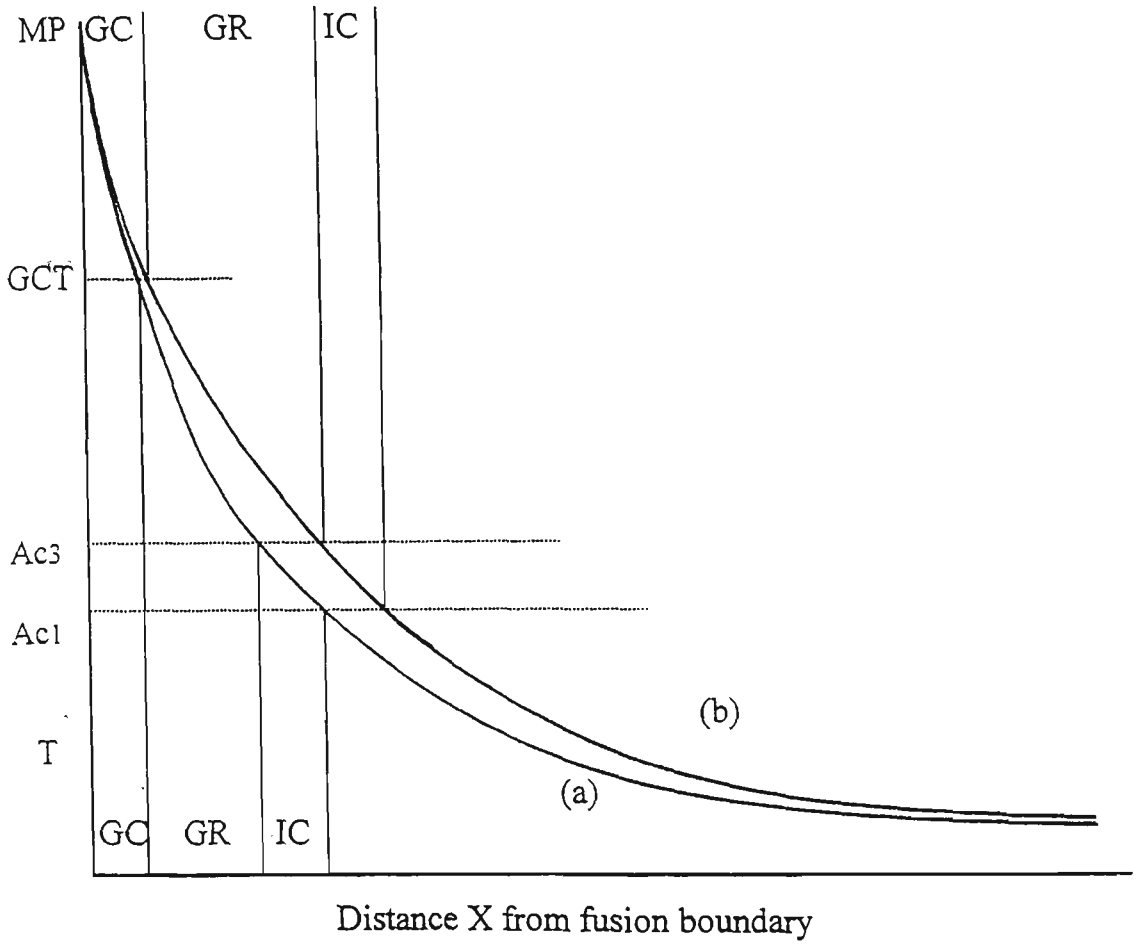

Figure 6.18: Schematic diagram showing maximum peak temperature versus distance X from fusion boundary for (a) lower and (b) higher heat input weld thermal cycles. The relative widths of the GC, GR and IC sub-zones are indicated. The total HAZ width increases for rate (b) but the relative widths of the sub-zones change: the GR sub-zone increases relative to the GC sub-zone for rate (b) compared to rate (a).

In general, for each group of samples, the compositions of the weld metals were largely independent of welding conditions for most elements when the Ar - CO_2 - (O_2) shielding gas was used. There were only slight differences in the C and Mn contents and larger differences in N and B levels (see Table 4.5). However, when pure CO_2 was used as a shielding gas, the Mn and Si recoveries were significantly reduced. Therefore, the CE values are lower.

The volume fraction of the GC sub-zone in the HAZ for pure CO_2 shielding gas was found to be decreased relative to Ar-CO_2-(O_2) welds at similar heat inputs (Figure 6.15). The volume fraction of GR structure was correspondingly increased for CO_2 shielding gas (Figure 6.16). The reason for this effect is probably because CO_2 shielding has a large effect on composition, giving lower Mn and Si levels, and changing the Ac_1 and Ac_3 temperatures (Schumann et al. 1995, Lathabai et al. 1985, Ferree 1992).

Although the Ae_1 and Ae_3 temperatures should be raised slightly in the less highly alloyed weld metal the effect on the Ac_1 and Ac_3 temperatures is less certain, because of modification of the kinetics of transformation of the ferritic as cast microstructure back to austenite. Less alloyed weld metal would be expected to transform more rapidly, thus lowering Ac_1 and Ac_3 compared to higher alloy weld metal for a given heating rate. Hence the overall effect on Ac_1 and Ac_3 of the composition difference between weld metals produced by Ar-CO_2 (O_2) and CO_2 is expected to be small. A much larger effect than composition could arise from differences in the effective heat input. CO_2 shielding gives a higher arc efficiency (0.85 compared to 0.70, Grong 1994) so that the effective heat input would be expected to be higher and the cooling rate lower than for welds produced by Ar gas mixtures. This will have the effect of altering

the relative widths of the GC, GR and IC sub-zones as shown schematically in Figure 6.18.

6.3.3 Effects of cooling rate

In Figure 6.15, the volume fraction of GC sub-zone decreased linearly with increasing heat input. It is considered that the decrease is influenced by cooling rate. Higher heat input produces a slower cooling rate which causes the grain refined region to increase relative to the GC region and, therefore the volume fraction of GC sub-zone in the HAZ decreases with increasing heat input while the volume fraction of GR sub-zone increases (Figure 6.16).

This effect is illustrated by Table 6.1 which shows the linear measurement results for samples RB5 and RB6 with heat inputs of 1.2 and 2.44 kJ/mm, respectively. Both welds were vertical up, but the higher heat input weld was produced by a weave technique. Therefore, the percentage reaustenitised structure is significantly higher for the 2.44 kJ/mm weld. The percentage of GR sub-zone is also higher in the high heat input weld and the percentage of GC sub-zone is correspondingly lower. The GC and GR regions constitute nearly 90 % of the HAZ in multipass weld metal, and some reports (Evans 1980, Reed et al. 1994) only indicate the presence of GC and GR regions.

Table 6.1: Linear measurement results for RB-5 and RB-6.

Heat Input	1.2 kJ/mm	2.44 kJ/mm
Volume Fraction of Reaustenitised Regions	47 %	59 %
GC in HAZ	38 %	33 %
GR in HAZ	47.5 %	58 %
IC in HAZ	14.5 %	9 %

6.4 Conclusions

1. All three groups of test plates followed essentially the same trend in that the volume fraction of reaustenitised region was reduced by the use of 100 % CO_2 as the shielding gas and changing from flat to vertical welding. In contrast, using weave welding increased the volume fraction of the reaustenitised region relative to the stringer welding technique.

2. The volume fraction of grain coarsened (GC) sub-zone in the HAZ decreased linearly with increasing heat input and slower cooling rate. For CO_2 shielding gas the proportion of GC sub-zone in the HAZ decreased relative to welds at a similar heat input using argon containing gas mixtures, because the higher arc efficiency results in a higher effective heat input and a slower cooling rate.

3. The volume fraction of grain refined (GR) sub-zone in the HAZ increased linearly with increasing heat input. Using pure CO_2 as the shielding gas increased the proportion of GR sub-zone in the HAZ, largely because of higher effective heat input and decreased cooling rate.

4. The volume fraction of intercritical (IC) sub-zone in the HAZ decreased slightly in relative terms with increasing heat input.

CHAPTER 7

DOUBLE-REHEATED SUB-ZONES AND WELD METAL HARDNESS

7.1 Introduction

Using the simplifying assumption that the structural gradient in the heat affected zone (HAZ) of reheated weld metal can be characterized in terms of three regions: the grain coarsened (GC); the grain refined (GR) and the intercritical (IC) heat affected regions; a second overlapping weld bead creates double-reheated weld metal structures which can be defined in terms of 9 sub-zones: GC-GC, GC-GR, GC-IC, GR-GC, GR-GR, GR-IC, IC-GC, IC-GR, IC-IC.

Multipass welds usually provide more benefits than single pass welds. These benefits include "preheat" from previous weld passes, annealing out of residual stresses due to previous weld thermal cycles; and structural refinement of coarse solidification structures (Easterling 1983, Mercer 1975). However, the HAZ becomes more complex during multipass welding, since a proportion of the HAZ is reheated by the next and even subsequent welding thermal cycles. As the HAZ consists of many sub-zones, the overall mechanical properties of the weld metal are determined by the combination of the properties of all of the different sub-zones (Li et al. 1998).

Image analysis of multipass welds in 1/2Cr-1/2Mo-1/4V steam pipe has demonstrated that double-reheated zones make up about 50% of the HAZ of the base material (Li et al. 1998). Although several HAZ simulation studies have been reported recently (Liao et al. 1996, Lomozik et al. 1997, Tsuchida etal.1996, Bowers and Letts), little effort has been devoted to the simulation of the weld metal structure and even less emphasis has been given to the study and quantification of double-reheated sub-zones produced by overlapping welds. Therefore, determination of the volume fractions of double-reheated sub-zones is an important step in understanding the evolution of the weld metal structure and its influence on mechanical properties. In order to relate weld mechanical

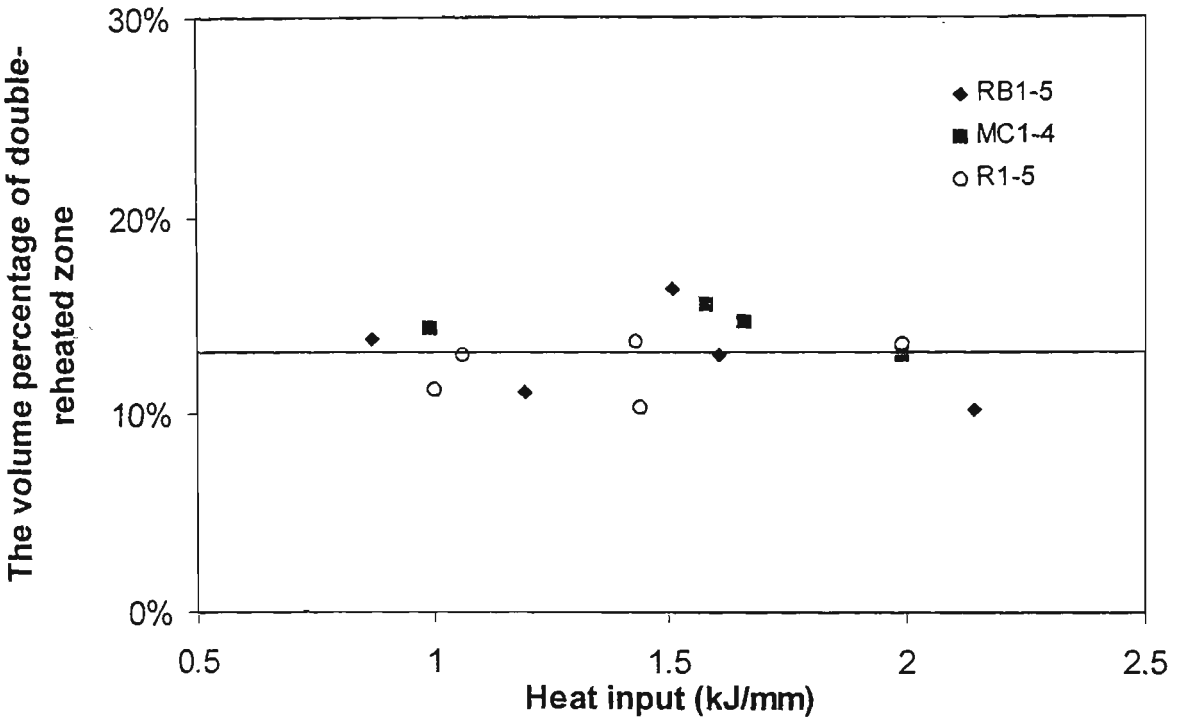

Figure 7.1: The volume percentage of double-reheated zone versus heat input for stringer (1G) and vertical up (3G) welding.

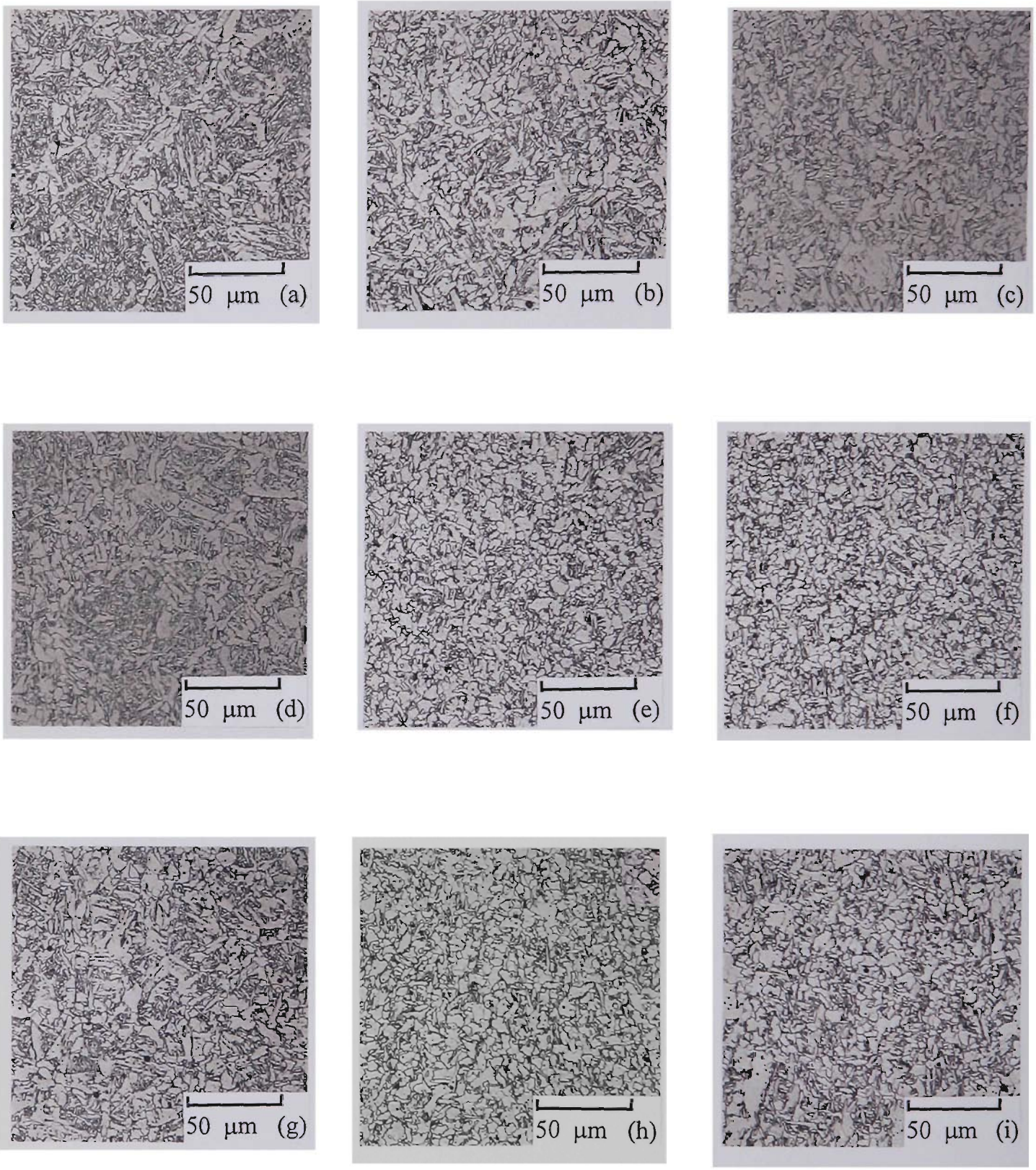

Figure 7.2: The microstructures of the double reheated sub-zones for sample R-5 at 1.06 kJ/mm heat input and 3G position: (a) GC-GC. (b) GC-GR. (c) GC-IC. (d) GR-GC. (e) GR-GR. (f) GR-IC. (g) IC-GC. (h) IC-GR. (i) IC-IC.

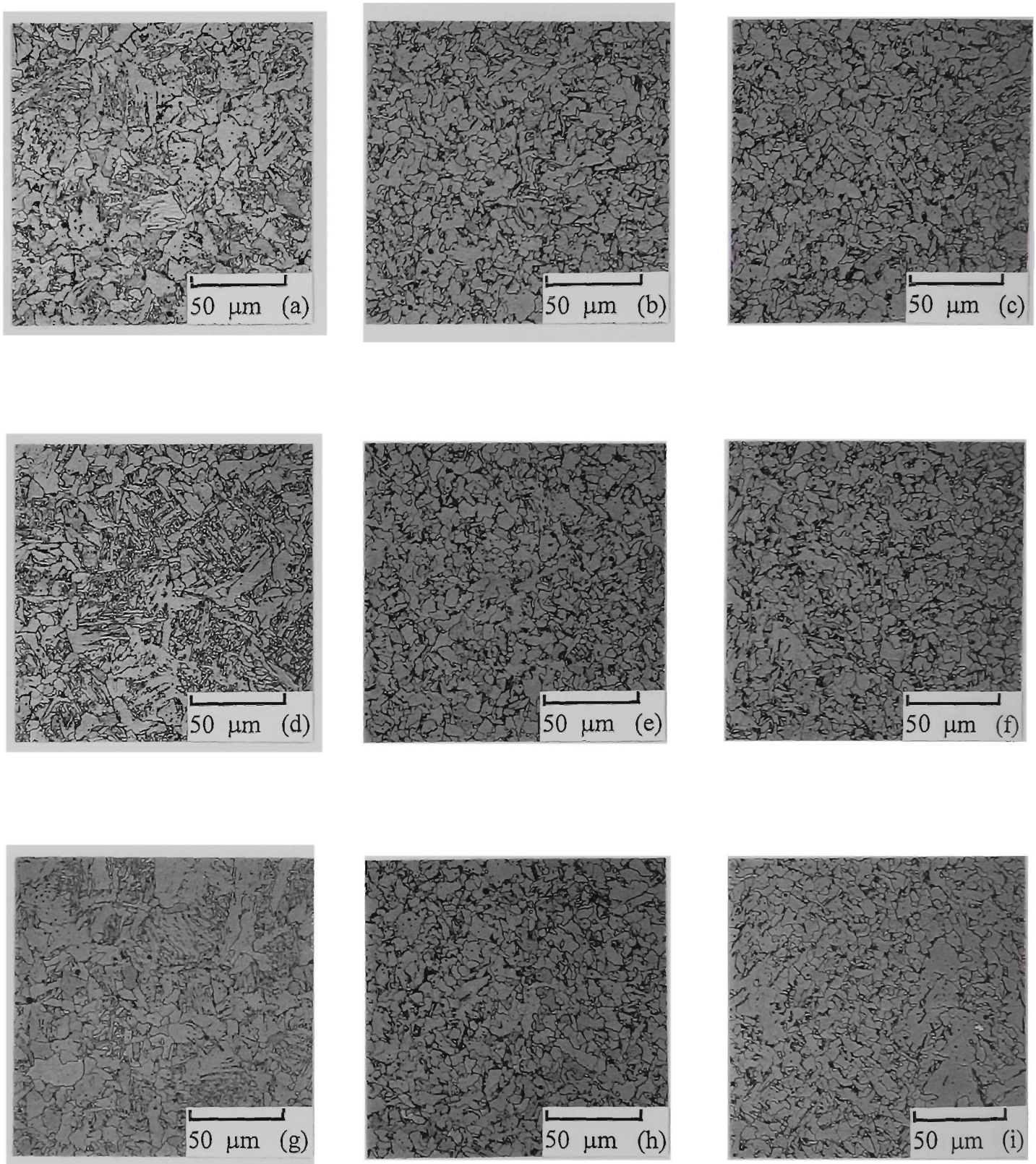

Figure 7.3: The microstructures of the double reheated sub-zones for sample R-3 at 1.44 kJ/mm heat input and CO_2 shielding gas: (a) GC-GC. (b) GC-GR. (c) GC-IC. (d) GR-GC. (e) GR-GR. (f) GR-IC. (g) IC-GC. (h) IC-GR. (i) IC-IC.

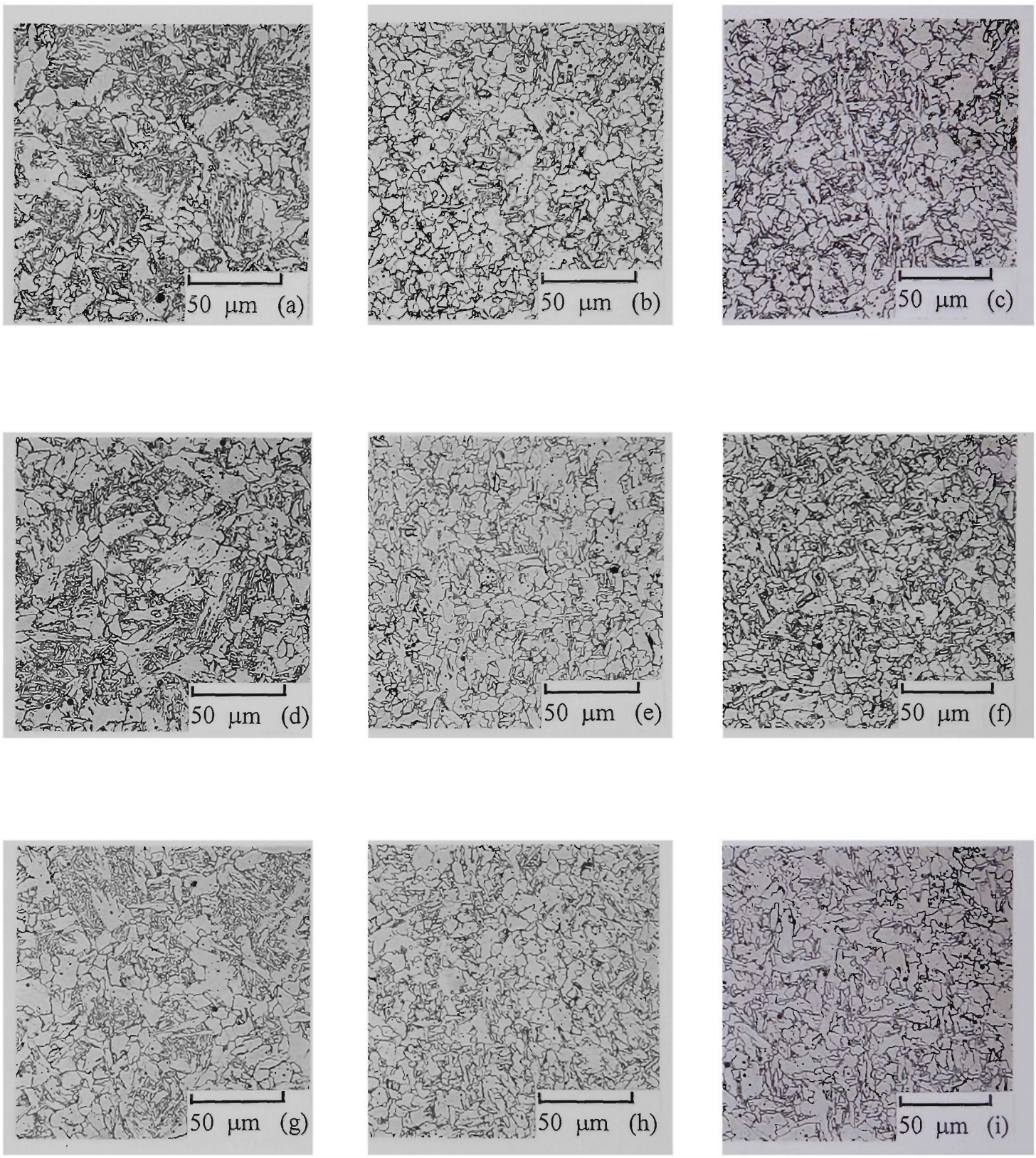

Figure 7.4: The microstructures of the double reheated sub-zones for sample R-1 at 1.99 kJ/mm heat input: (a) GC-GC. (b) GC-GR. (c) GC-IC. (d) GR-GC. (e) GR-GR. (f) GR-IC. (g) IC-GC. (h) IC-GR. (i) IC-IC.

properties to weld metal structure, characterisation of the weld metal sub-zones in multipass flux cored arc (FCA) welds has been undertaken. Investigation of double-reheated regions of the weld metal is useful to improve understanding of the contributions of these sub-zones, together with singly reheated regions and unreheated solidified structure, to the weld metal mechanical properties. Microhardness measurements have been used for this purpose.

7.2 Results

7.2.1 Volume fraction of double-reheated zone

Figure 7.1 shows the volume fraction of the double-reheated region versus heat input. For all three consumable types, there was no strong trend in percentage double-reheated zone with increasing heat input. In general, about 13 % double-reheated zone was obtained over the heat input range of 0.87 - 2.14 kJ/mm. As discussed in Chapter 6, the volume fraction of reaustenitised region in the weld metal is influenced by the welding position and the shielding gas (Tsuei et al. 1998, Evans 1981). In contrast, the volume fraction of the double-reheated region remains relatively unchanged with changes in welding conditions.

7.2.2 Microstructures of the double-reheated zone

The microstructures of the double-reheated sub-zones (GC-GC, GC-GR, GC-IC, GR-GC, GR-GR, GR-IC, IC-GC, IC-GR, IC-IC) for the rutile weld metals made at approximately 1, 1.5 and 2 kJ/mm are shown in Figures 7.2, 7.3 and 7.4. Optical microscopic examination, the microstructures of the double-reheated sub-zones 1,1 , 1,2 , 1,3 , 2,1 , 2,2 , 2,3 , 3,3 (see Figure 4.2) did not reveal marked differences from reheated zones experiencing a single thermal cycle equivalent to the second cycle of the

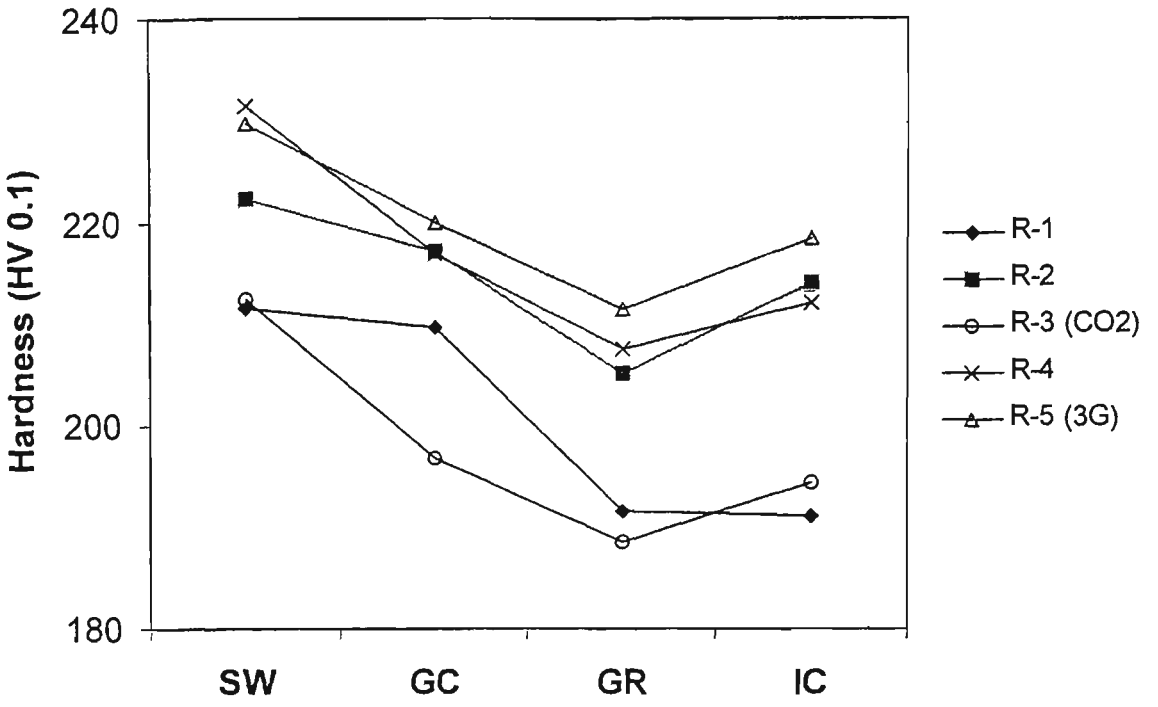

Figure 7.5: The hardness distributions along line 4 for the rutile flux-cored (R) samples.

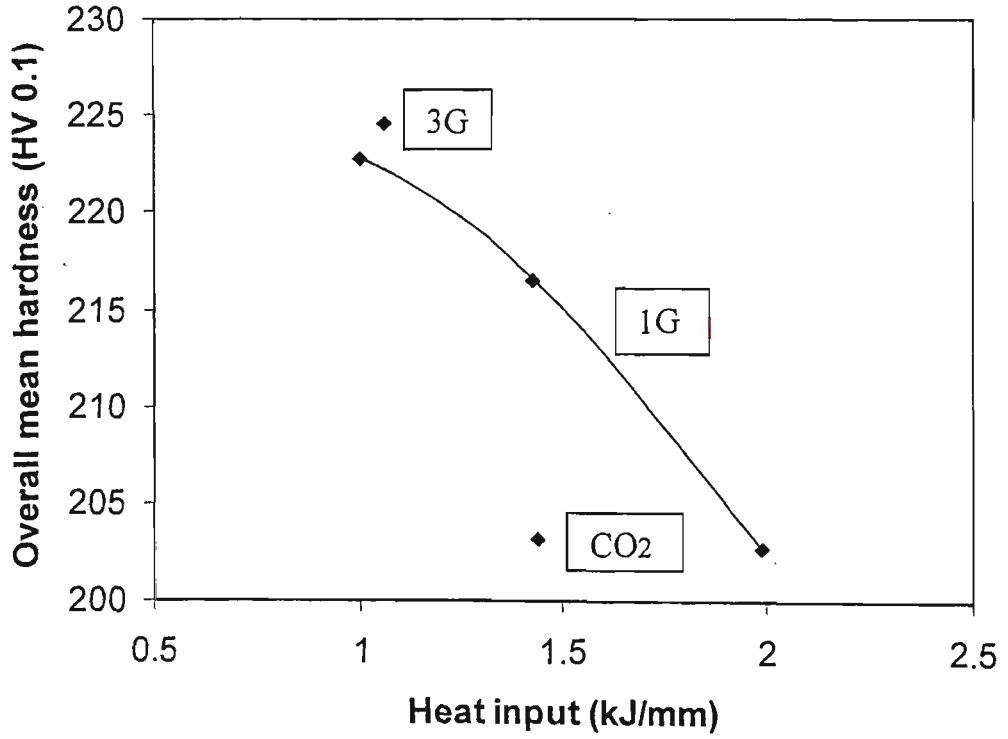

Figure 7.6: Relationship between overall mean hardness ($\overline{H}$) and the heat input for samples R-1 to R-5.

double-reheated zone. There are exceptions for the GC-IC (1,3) and the GR-IC (2,3) sub-zones in that only partial reaustenitisation of the prior structure occurred.

7.2.3 Hardness distribution

The microhardness distributions along line 4 (Figure 4.2) for samples R-1 to R-5 are shown in Figure 7.5. All test samples showed the trend that the SW was the hardest region and the GR was the softest region. The refined grain region showed the minimum hardness because of the equiaxed recrystallized ferrite microstructure. This result is consistent with results reported by Evans (1980a, 1980b) for stringer technique welds and for measurements conducted along the vertical central line of the cross section from the top bead to the bottom, which indicated a wave distribution of hardness.

7.2.4 Weighted mean hardness and overall mean hardness

The relationship between the volume fraction and the hardness for various sub-zones was derived as the weighted hardness contribution (ΔH).

$$\Delta H\,(i) = vf \times \overline{H}\,(i) \tag{7.1}$$

where vf is the volume fraction and $\overline{H}\,(i)$ is the mean hardness of each sub-zone. The overall mean hardness for each sample could be calculated through the combination of each of the weighted hardness contributions:

$$\overline{H} = \Delta H\,(SW) + \Delta H\,(GC) + \Delta H\,(GR) + \Delta H\,(IC) + \sum_{n=1}^{9} \Delta H\,(\text{Double-reheated Sub-zone}) \tag{7.2}$$

The volume fraction and weighted mean hardness of each sub-zone for sample R-2 are given in Table 7.1 based on Equation 7.1. In general, the SW region had the largest weighted hardness contribution because it occupied the largest volume fraction of the weld metal and it had the highest mean hardness. Accordingly, the IC-IC sub-zone had the smallest weighted hardness contribution. The overall mean hardness for samples R-1 to R-5 using Equation 7.2 is plotted in Figure 7.6. In general, higher heat input produced welds with lower hardness and CO_2 shielding also appeared to reduce the overall mean hardness.

Table 7.1: The weighted mean hardness of each sub-zone for sample R-2.

Sub-zone	Volume Fraction (%)	Mean Hardness	Weighted Hardness Contribution
SW	50.0	222.3	111.06
GC	13.6	217.2	29.54
GR	18.3	205.2	37.53
IC	4.4	214.1	9.51
GC-GC	2.2	213.8	4.62
GC-GR	1.9	204.8	3.93
GC-IC	0.4	200.0	0.86
GR-GC	3.4	215.9	7.28
GR-GR	3.5	208.3	7.27
GR-IC	0.7	208.2	1.52
IC-GC	0.6	216.3	1.26
IC-GR	0.9	205.7	1.77
IC-IC	0.2	202.0	0.32

7.3 Discussion

7.3.1 Effects of welding conditions on double-reheated zone

The current results show that the volume fraction of double-reheated zone is insensitive to heat input and other welding conditions (Figure 7.1). This is different from the results reported for base material (Li et al. 1998) in which the total volume fraction of double-reheated and triple-reheated zones increased with increasing heat input. However, the volume fraction of double-reheated zone is likely to closely correlate with the percentage reaustenitised zone and therefore the present result is considered to be reasonable based on Figure 6.5 which showed no strong trend in percentage reaustenitised region with increasing heat input, for 1G and 3G welds.

As discussed in Chapter 6, the use of the weave-bead technique appeared to significantly influence the percentage reaustenitised region. Thus, in this double-reheated zone investigation, the weave welding technique welds were not listed because weaving results in little or no doubly reheated region in the weld metal. Other major welding variables such as electrode diameter and interpass temperature which are well known to change the volume fraction of reaustenitised region systematically (Easterling 1983, Evans 1980a, 1979) were, however, fixed in the present study. Therefore, a roughly constant value of the volume fraction of double-reheated zone is evident in Figure 7.1, indicating independence of consumable type as well as heat input.

7.3.2 Dominant thermal cycle

Figures 7.2, 7.3 and 7.4 show similar microstructures for a double-reheated sub-zone and singly reheated sub-zone with the same thermal as the second cycle of the double-reheated region. Exceptions are the GC-IC (1,3) and GR-IC (2,3) regions. It is inferred

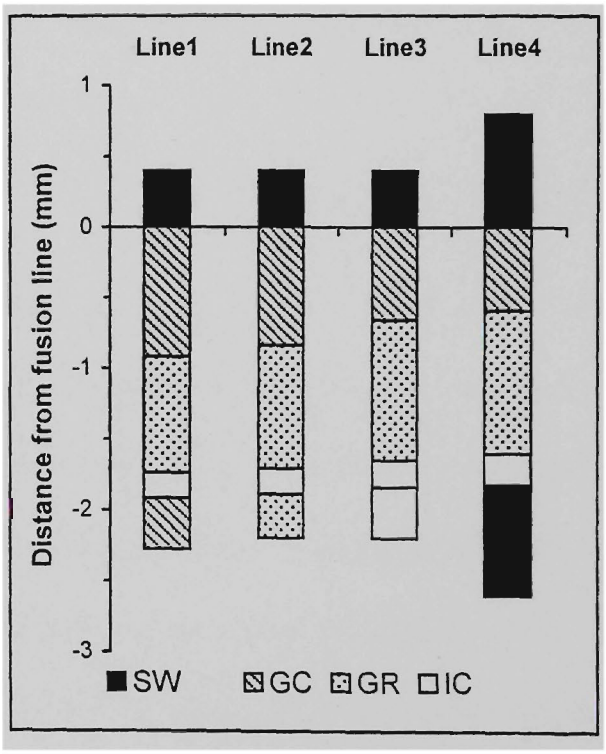

Figure 7.7: The sub-zone distributions for sample R-2 along the 4 lines shown in Figure 4.2.

that the later (second) thermal cycle dominates the microstructure of the doubly reheated sub-zones. These observations confirm previous work which has also shown that the microstructures of double re-heated sub-zones are closely similar to the sub-zones of singly reheated weld regions because the peak temperature of the second pass normally eliminates the previous microstructural features (Li et al. 1998). For the GC-IC and the GR-IC sub-zones partial re-austenitisation of the prior structure occurred. Therefore, unlike other double-reheated sub-zones, microstructural features appeared to be different from those of singly reheated sub-zones.

7.3.3 Effects of second pass thermal cycle on microstructure

The sub-zone strucural distribution along each line in Figure 4.2 is shown in Figure 7.7 for sample R-2 and typical microstructures are shown in Figure 7.2 to Figure 7.4. All samples examined followed a similar trend: line 1 had the highest proportion of GC structure while line 4 had the smallest amount of GC structure. Obviously, different peak temperatures are produced in the first pass in the various sub-zones, and the following pass sees a temperature cycle which differs in the various regions. The second thermal cycle has a marked effect on the volume fraction of doubly reheated sub-zones and the relative amounts of the sub-zones.

7.3.4 Effects of welding conditions on hardness

Figure 7.6 shows that the higher heat input deposit tends to give generally lower hardness values. Varying the heat input varied the thermal cycles experienced by the welds. Higher heat input produces a slower cooling rate. It is considered that the decrease in hardness is due to the slower cooling rate. This result is consistent with results reported by Evans (1980b) and Lathabai (1985).

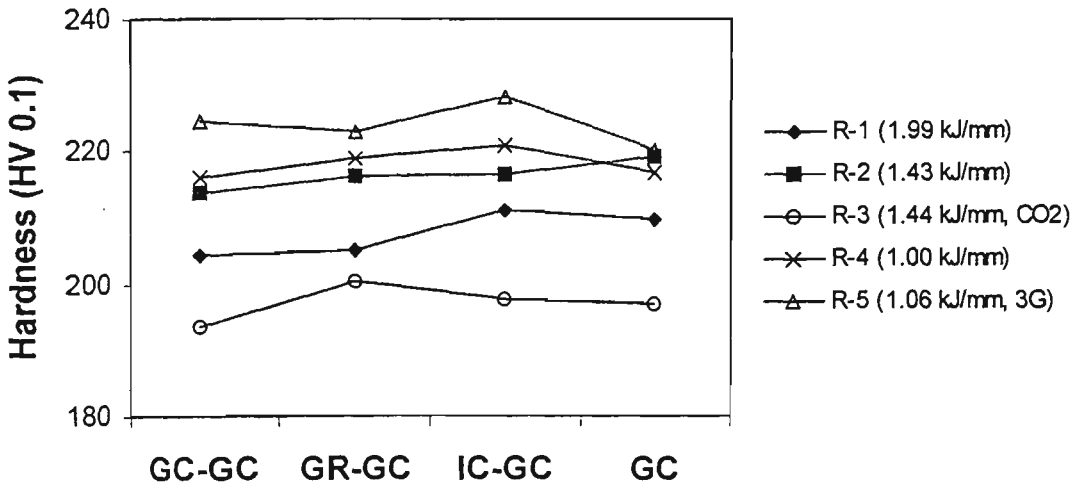

Figure 7.8a: Hardness values for double-reheated sub-zones with the second pass generating a GC sub-zone. Data for a single reheated GC sub-zone are also given.

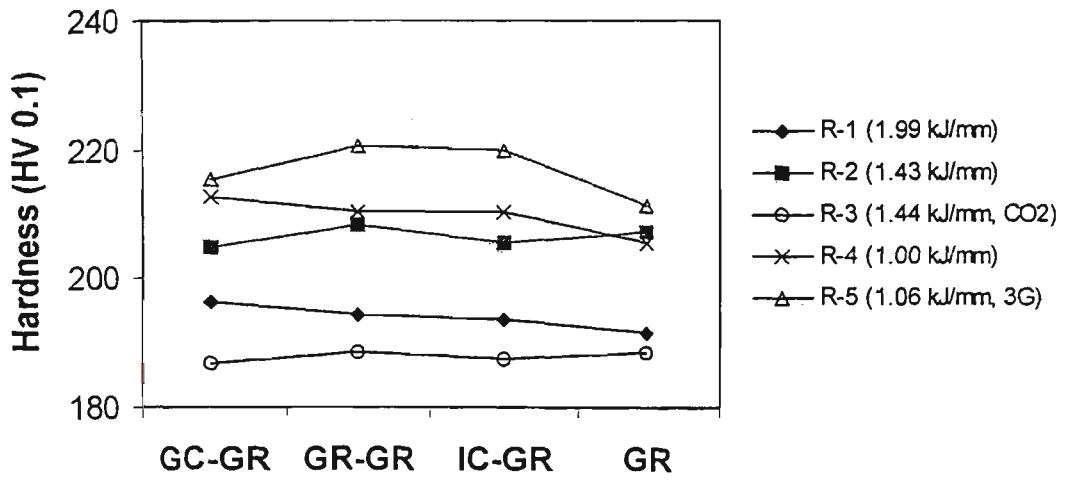

Figure 7.8b: Hardness values for double-reheated sub-zones with the second pass generating a GR sub-zone. Data for a single reheated GR sub-zone are also given.

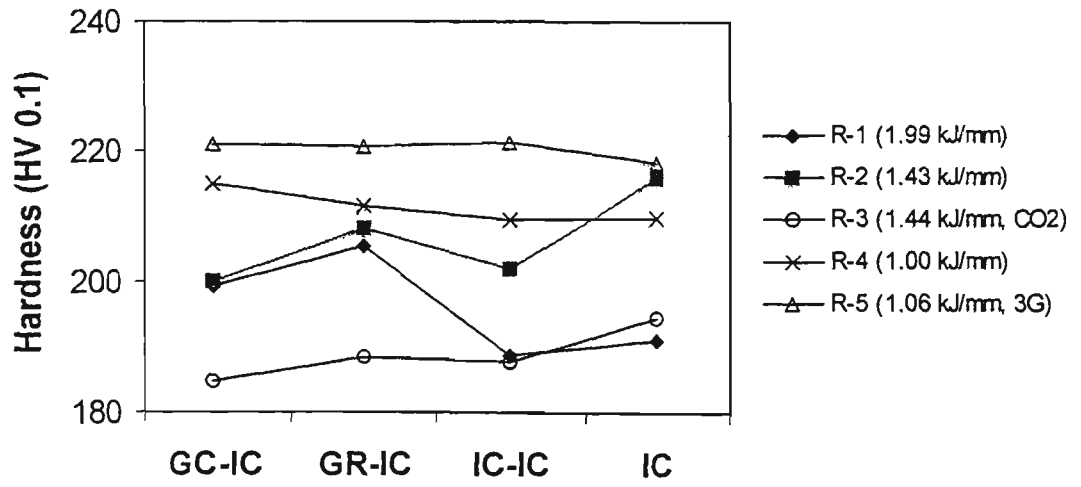

Figure 7.8c: Hardness values for double-reheated sub-zones with the second pass generating a IC sub-zone. Data for a single reheated IC sub-zone are also given.

Carbon is the most important element affecting the hardness and hardenability of the HAZ (Yurioka et al. 1987). Therefore, many authors have successfully correlated the carbon equivalent (CE) and cooling rate to the hardness prediction for the HAZ of the base metal (Yurioka et al. 1987, Beckert and Hoz 1973,Yurioka et al. 1981, Boothby 1985). For the weld metal, the effect of carbon is equally important. Increasing the proportion of CO_2 in the shielding gas tends to give lower carbon content in the weld metal. With 100% CO_2 shielding gas, a lower carbon content was generally produced. With a lower CE level, the hardness decreased correspondingly (Table 4.5 and Figure 7.6). This result showed a good agreement with results reported by Yurioka (1987) and Lathabai (1985).

Changing the welding position from horizontal to vertical has a small effect on hardness. The microstructural examination did not reveal marked differences at similar heat inputs, between the two principal welding positions. However, a slightly higher hardness level for 3G weld is shown in Figure 7.6. This condition is consistent with results reported by Evans (1981) for stringer technique.

7.3.5 Mean hardness of double-reheated sub-zone

The results for mean hardness for each double-reheated sub-zone are shown in Figure 7.8. For a second pass GC sub-zone (GC-GC, GR-GC, IC-GC) and a second pass GR sub-zone (GC-GR, GR-GR, IC-GR), the use of 100% CO_2 as the shielding gas produced sub-zones of lower hardness, with no significant difference between the hardness of the different double reheated sub-zones. This similarity in hardness is consistent with the similarity of the microstructures. The data support the assumption made by Li et al. (1998) that the mechanical properties for double-reheated sub-zones and singly reheated sub-zones are closely similar because of similar microstructural

features. Except for the case of CO_2 welding, the hardnesses of the X-GC (Figure 7.8a) and X-GR (Figure 7.8b) sub-zones were, within each sample of stringer bead welds (1G), similar at the same heat input, with a higher heat input generally giving a lower hardness level. 3G welds were generally harder than 1G welds at the similar heat inputs. This implies faster cooling rate and lower effective heat input is produced for the 3G as opposed to the 1G position. According to Norrish's study (1992), the behavior of metal transfer in Ar-CO_2 arc welding is determined by welding current. In Ar-CO_2 welds where CO_2 is less than 30%, the critical amperage is 210 A (when the wire diameter is 1.2 mm). Short circuit transfer occurs when current is lower than the critical amperage and streaming spray transfer occurs for an amperage higher than the critical. Therefore, the modes of metal transfer for sample R-5 (3G weld, low current of 190 A) are likely to be globular drop and short circuit. In contrast, for sample R-4 (1G weld, high current of 280 A) metal transfer is expected to occur by streaming spray and drop spray. The detailed welding variables are given in Appendix 1.

Less effective heating of the weldment is generally considered to occur for globular drop transfer compared to a streaming spray mode because the transfer mechanism is dominated by gravitational forces. Although electromagnetic forces exist they are not sufficiently developed to influence the droplet detachment at low currents (Norrish 1992). Therefore, the efficiency of a certain energy input should be lower for globular drop mode compared to a streaming spray mode. A more extensive fume is generally produced with a globular drop mode, implying that a higher energy loss occurs in such a metal transfer mode. Therefore, a 3G position (short circuit current and globular drop mode) with lower effective heat input is likely to produce welds with a higher hardness compared to a 1G position.

A contribution to the higher hardness could also arise because of less effective slag cover in 3G welds, due to thinning out and reduced coverage of the weld pool, a greater radiation loss and therefore faster cooling could occur. The above assumptions could be confirmed in future work by using thermocouples to measure the cooling rate for these two major welding positions. Hence the effective heat input can be determined.

As opposed to the X-GC and X-GR sub-zones, no regular trend could be found when the second sub-zone was an IC region (Figure 7.8c). The extremely small area and partially transformed microstructure from each different prior microstructure (GC, GR and IC) made the investigation more complicated. However, comparing the influence of 100% CO_2 shielding and high heat input, the effects were still distinctive in that a lower hardness was obtained. The apparently discontinuous trend of the hardness of the second IC region could be confirmed by a weld metal simulation. Through simulation, a larger uniform area can be produced and a more accurate hardness average can be obtained.

7.4 Conclusions

1. For stringer welds the total volume fraction of the double-reheated zone was largely unaffected by heat input, welding position, shielding gas, composition and the changes in consumable types examined in this investigation.

2. Examination of the microstructures of the double-reheated sub-zones did not reveal marked differences from reheated zones experiencing a single thermal cycle equivalent to the second cycle of the double-reheated sub-zone, except for the GC-IC and GR-IC sub-zones. It is inferred that, in general, the final thermal cycle dominates the final microstructure.

3. The hardness distribution in the double-reheated zone also showed similar trends to that in singly reheated zone. However, the proportion of the grain coarsened region increased relative to grain refined region in the double-reheated zone because of the effects of the second pass thermal cycle.

4. The hardness of each region and each sub-zone in the weld metal decreased with increasing heat input and was reduced for 100% CO_2 shielding gas compared to an Ar rich gas mixture.

5. The influence of welding position (1G versus 3G) on hardness was slight. However, a higher hardness level was measured for the 3G weld, probably because of a lower effective heat input and a faster cooling rate.

6. The weighted mean hardness values were calculated for the SW, the reheated and double-reheated HAZs using the hardness and the volume fractions of the various sub-zones. The overall mean weld metal hardness for 1G welds decreased by about 20 points (HV 0.1) as the heat input was doubled from 1 to 2 kJ/mm.

CHAPTER 8

MEAN FREE PATH

8.1 Introduction

The evolution of microstructure in the weld metal is very complex, and depends on the composition, composition gradients and other variables such as cooling rate and peak temperature (Easterling 1983). Grain size is a widely used index of structural refinement and the mean free path (or mean linear intercept " grain size") correlates directly with the grain boundary surface area per unit volume (Underwood 1970). Although chaotic microstructures such as acicular ferrite are considered to provide improved toughness over regular microstructures such as packets or sheaves of bainitic ferrite, it is more difficult to quantify "chaos" than to measure the mean linear intercept crystal size. Moreover, the presence of fine irregularly shaped structures should be reflected in the value obtained for mean free path.

However, the measurement of ferrite grain size, which is normally considered to be a key factor in determining the strength and toughness (Easterling 1983), is not straight forward for weld metal microstructures because of the structural variability. Some authors have correlated the grain size in the HAZ with the peak temperature and distance from the fusion boundary (Alberry et al. 1977, Ikawa et al. 1977) and others have expressed grain size as a function of composition (George and Irani 1968, Matsuda and Okumura 1978, Porter and Easterling 1981). In the present work, the mean free path (MFP), the mean characteristic distance between ferrite grain boundaries, has been determined as a structural index which takes account of the complexity of the different microstructures in different regions of the weld metal. In these measurements, the distance between boundaries of individual plates was measured, and not the plate / lath packet size which is sometimes used as a mean-free-path for dislocation motion or crack propagation.

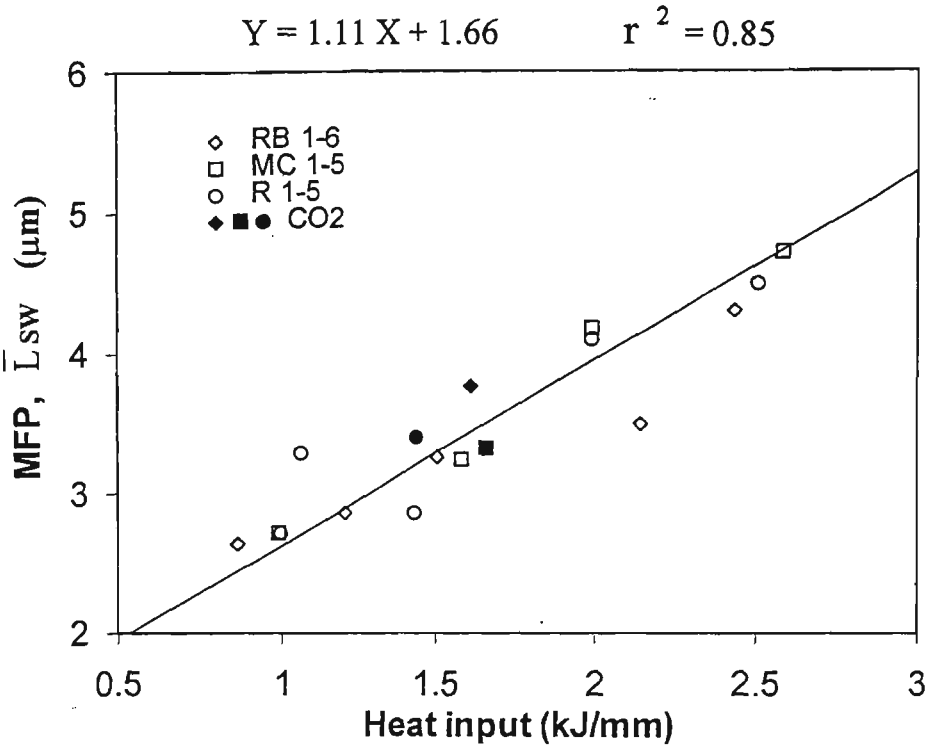

Figure 8.1: Relationship between $\bar{L}_{SW}$ and heat input.

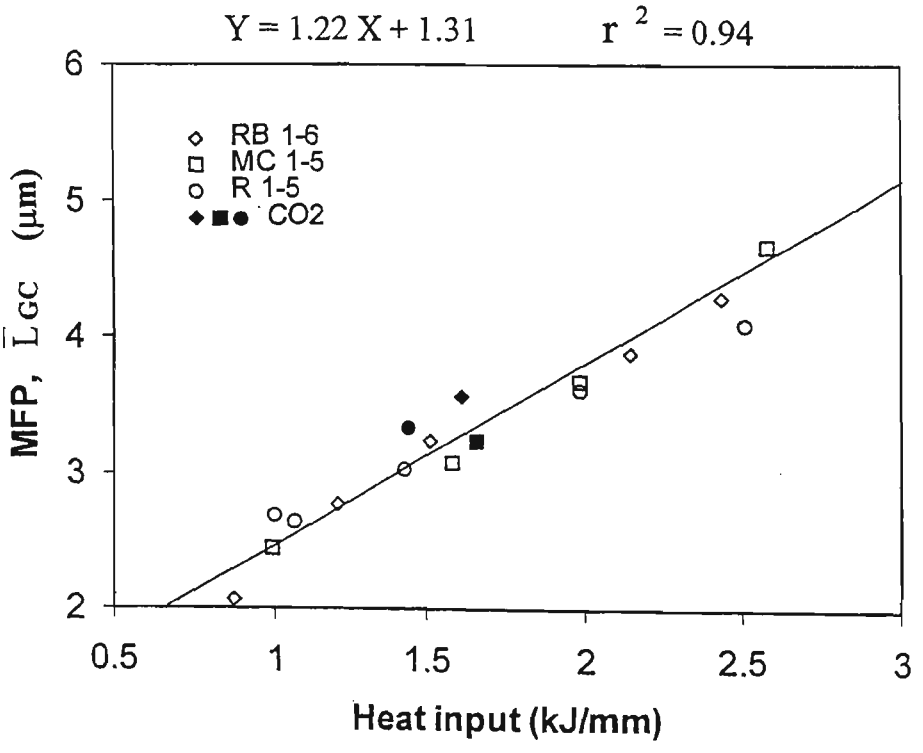

Figure 8.2: Relationship between $\bar{L}_{GC}$ and heat input.

Since one of the main aims of the work was to relate Charpy toughness to weld metal structure, MFP was examined as a suitable variable for correlation with CVN value. A weighted mean characteristic length ($\bar{L}_i^w$) has been derived for each distinct weld metal sub-zone i using the volume fraction and the sub-zone MFP. The sum of the weighted mean MFPs ($\sum_{i=1}^{n} \bar{L}_i^w$) is used to represent the average value for the overall weld metal structure.

8.2 Results

8.2.1 SW region

Figures 5.10 to 5.12 show the predominantly columnar microstructure in the solidified weld metal (SW) regions of all the samples, in the central regions of welds made at approximately 1, 1.5 and 2 kJ/mm (using stringer beads) and 2.5 kJ/mm (using a weave technique). The main constituents in the microstructure were acicular ferrite (AF), grain boundary ferrite (PF(G)), intragranular polygonal ferrite (PF(I)) and ferrite with a second phase (FS). The results for MFP in the SW region are given in Figure 8.1. In general, the MFP values for the SW region ($\bar{L}_{SW}$) increased linearly with increasing heat input and the $\bar{L}_{SW}$ values for CO_2 shielding gas were found to be slightly higher than for Ar-CO_2 welds at similar heat inputs in the RB and R samples.

8.2.2 GC, GR and IC sub-zones in HAZ region

The measurement of MFP for the GC sub-zone ($\bar{L}_{GC}$) is less complicated than SW regions because of the simpler combination of microconstituents of polygonal ferrite and acicular ferrite. In the region of the GC sub-zone close to the boundary of SW, the

ferrite grain size is larger than in regions closer to the boundary of the GR sub-zone. The grain size in the GC region is a function of peak temperature (Underwood 1970, Alberry et al. 1977) which depends on the distance from the heat source. It has also been found that the GC band is wider in double-reheated sub-zones (overlapping HAZs). Therefore, the test line was placed in the mid-section of the GC band in order to obtain an average value. The values of MFP for the GC sub-zone ($\bar{L}_{GC}$) for each sample are given in Figure 8.2. In the weld metal HAZ, $\bar{L}_{GC}$ increased linearly with increasing heat input and for CO2 shielding gas, $\bar{L}_{GC}$ was increased slightly relative to the Ar gas mixture.

The measurement of MFP for the GR sub-zone is straight forward compared to the other regions. This region has a uniform distribution of refined ferrite grains. Since only one ferrite morphology exists in this region (equiaxed ferrite grains), the measurement of $\bar{L}_{GR}$ is considered to be more accurate than in other regions. In the multipass weld metal, the IC sub-zone is the smallest part of the HAZ: partial reaustenitisation takes place in this sub-zone and optical examination reveals that the columnar grains are surrounded by refined ferrite grains. MFP is larger (8.3μm) than for the three other measured sub-zones because of the different combination of microconstituents.

The MFP values for the GR sub-zone ($\bar{L}_{GR}$) are given in Figure 8.3 and the relationship between $\bar{L}_{IC}$ and heat input is illustrated in Figure 8.4. As expected, these figures show that the cooling rate affects MFP in the GR and IC sub-zones: $\bar{L}_{GR}$ and $\bar{L}_{IC}$ increase linearly with increasing heat input.

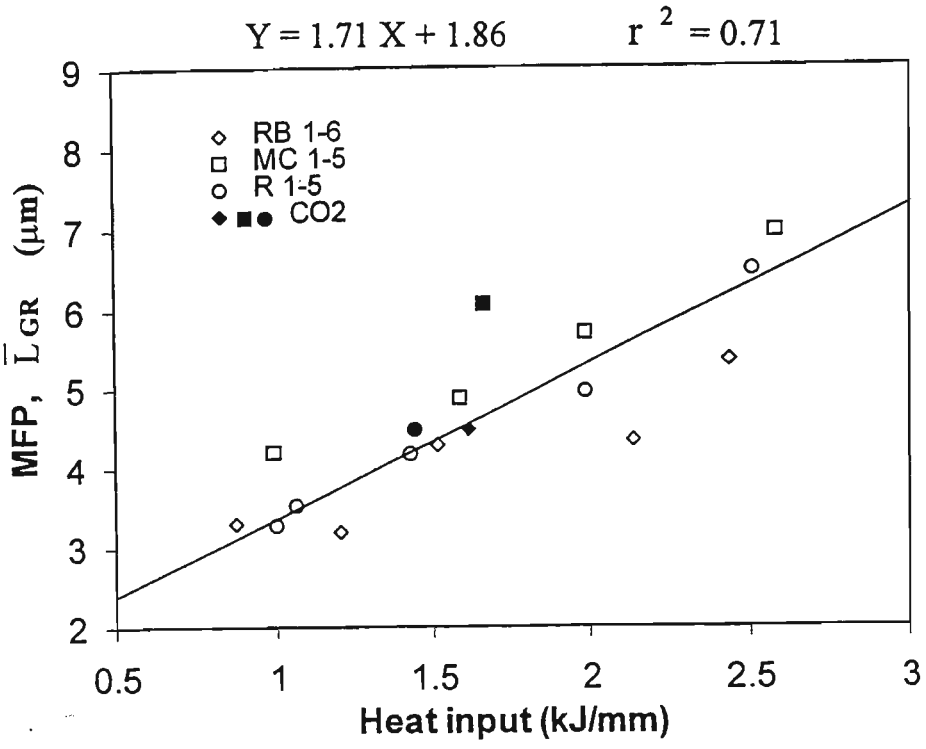

Figure 8.3: Relationship between $\bar{L}_{GR}$ and heat input.

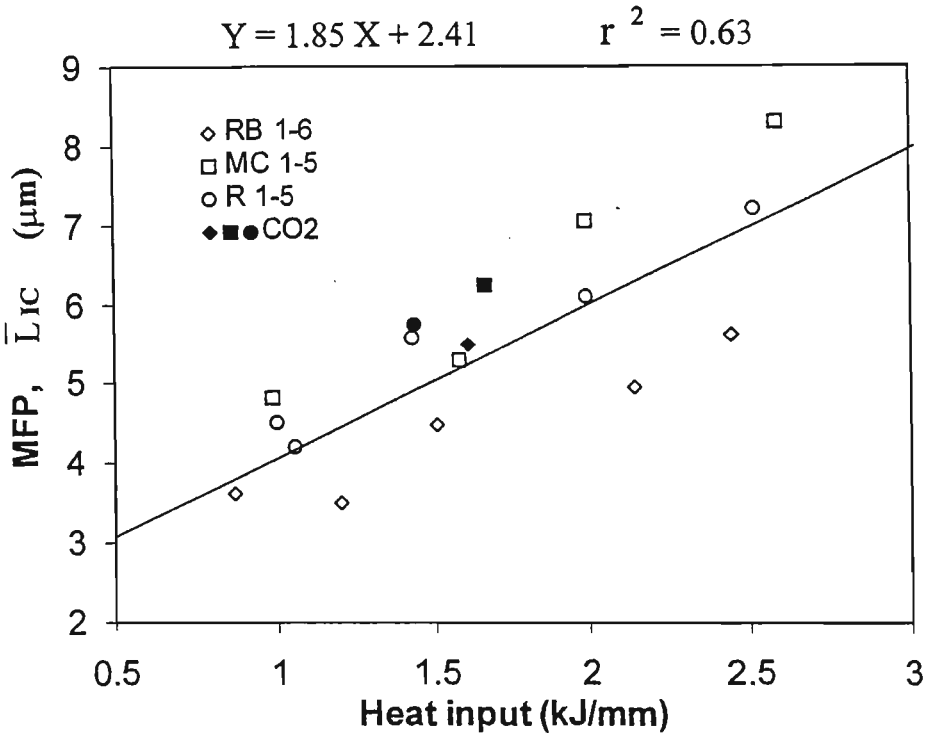

Figure 8.4: Relationship between $\bar{L}_{IC}$ and heat input.

8.3 Discussion

8.3.1 Influences of cooling rate and CO2 shielding

In the SW region, the increased value of $\bar{L}_{SW}$ with increasing heat input is considered to be influenced mainly by cooling rate. Higher heat input produces a lower cooling rate which causes structural coarsening (French and Schumann 1994). Therefore, the mean values for the characteristic length of AF, PF(G), PF(I) and FS became larger. This conclusion has also been reached in a previous study (Zhu et al. 1995) of the correlation between the grain size of AF and various welding conditions. This report indicates that the main correlation is with heat input: the higher the heat input the coarser the grain size of the AF region.

The $\bar{L}_{SW}$ values for CO2 shielding gas was found to be slightly higher than for Ar-CO2 welds at similar heat inputs in the RB and R samples. It is likely that CO2 shielding gives a higher arc efficiency (Grong 1994) so that the effective heat input is higher and the cooling rate lower than for welds produced by Ar gas mixture.

The results for volume fraction of SW are affected by welding technique, CO2 shielding and welding position, as discussed in Chapter 6. Changes in electrode diameter and interpass temperature are also known to influence the volume fraction of the SW region (Easterling 1983, Evans 1980a, 1979), but these factors were kept constant in the present work. The MFP of SW is dominated by heat input and is roughly independent of consumable type, welding position and welding technique.

Figures 8.2, 8.3 and 8.4 indicate that the cooling rate does affect the GC, GR and IC sub-zones in that the MFP of each HAZ sub-zone increased linearly with increasing

heat input, except for samples welded with 100% CO_2 shielding gas. For CO_2 shielding gas, the value of MFP was increased slightly due to the higher effective heat input relative to the Ar gas mixture (Grong 1994). Results for the IC sub-zone clearly show the highest scatter ($r^2 = 0.63$) but the scatter seems to be systematically related to the consumable type. The B containing rutile electrode (RB) showed the lowest values of MFP and the lowest sensitivity to heat input, probably because of relatively high alloy content and Pcm (~ 0.20) which would be expected to retard both reaustenitisation (high Ac_3) and retransformation (low Ar_3) on cooling, as well as restricting ferrite growth.

A slight difference in the relationship between MFP and heat input appeared to be associated with the use of different consumables. For example, the MFP/heat input relationships are approximately linear and the gradients for the $\bar{L}_{GR}$ and $\bar{L}_{IC}$ values for the RB samples are slightly smaller than those of the MC and R samples. It is considered that differences in basic chemical compositions could be the cause for this effect. Table 4.5 shows that the C and N contents are generally high for the RB samples. The MC samples have the lowest C levels and lower N levels than RB, whilst the R samples have similar C levels to RB and much lower N levels. The Mn and Si levels are lower for the RB samples than for the other two consumables. The higher C and N levels for RB are consistent with the kinetics of grain growth reported by Porter and Easterling (1981). They claimed that in most commercial microalloyed steels, the presence of carbide or nitride particles tends to hinder grain growth in the HAZ. In this case the driving force for a migrating boundary is counterbalanced by the increase in boundary area due to its interaction with these particles. Therefore, the increase in mean free path of refined ferrite grains with heat input for the RB samples was smaller than for the other two consumable types.

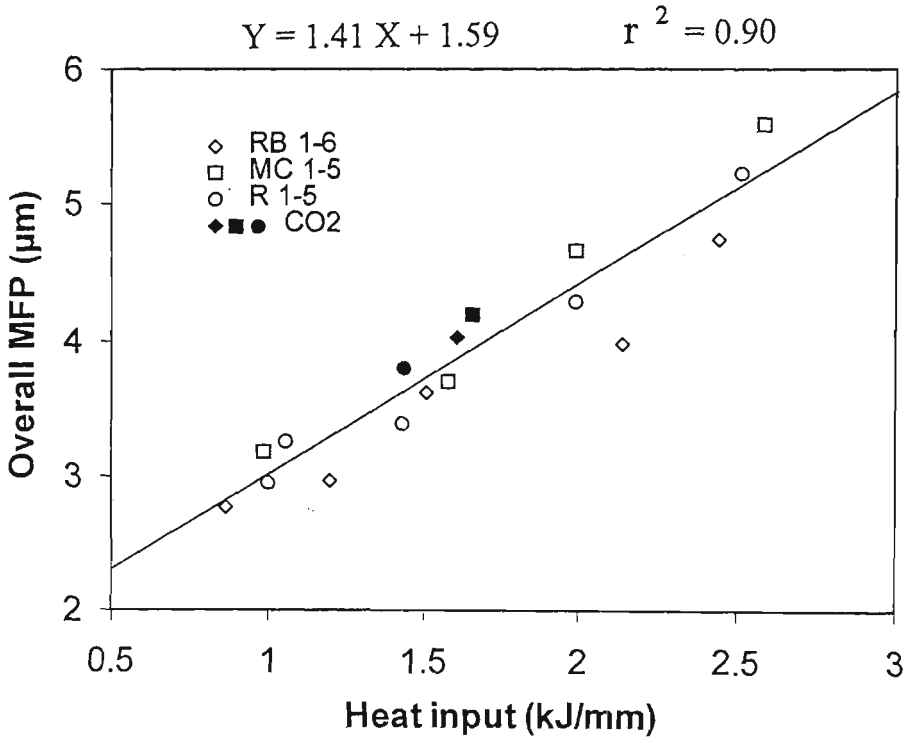

Figure 8.5: Relationship between overall MFP ($\overline{L}_{o}^{w}$) and heat input.

8.3.2 The overall MFP ($\bar{L}_o^w$)

The average MFP ($\bar{L}_o^w$) for each test plate was derived from the combination of each MFP and the volume fractions of the various sub-zones by using equation 4.4. $\bar{L}_o^w$ is an average characteristic length for the overall weld metal microstructure, representing all of the microconstituents AF, PF(G), PF(I), FS and equiaxed ferrite grains in all of the sub-zones (SW, GC, GR and IC). Figure 8.5 shows that $\bar{L}_o^w$ increased linearly with increasing heat input, changing roughly from 3μ to 6μ. The effect of heat input is illustrated in Table 8.1. This Table shows the relative weighted MFP values ($\bar{L}_i^w$) and the overall MFP ($\bar{L}_o^w$) with respect to the highest and lowest heat inputs for each consumable.

Table 8.1: Weighted MFP ($\bar{L}_i^w$) values and overall MFP ($\bar{L}_o^w$).

Sample Code	Heat Input (kJ/mm)	$\bar{L}_{SW}^w$ (μm)	$\bar{L}_{GC}^w$ (μm)	$\bar{L}_{GR}^w$ (μm)	$\bar{L}_{IC}^w$ (μm)	$\bar{L}_o^w$ (μm)
RB2	0.87	1.21	0.42	0.84	0.29	2.77
RB6	2.44	1.76	0.84	1.83	0.30	4.75
MC4	0.99	1.31	0.50	1.10	0.25	3.17
MC1	2.58	2.19	0.74	2.34	0.33	5.60
R4	1.00	1.45	0.51	0.70	0.28	2.94
R6	2.51	1.77	0.83	2.31	0.33	5.24

The use of 100% CO2 shielding gas tended to slightly increase the value of $\bar{L}_o^w$. The increased arc efficiency probably contributes to this effect (Grong 1994), but another factor could be the significantly reduced C, Mn and Si levels (Table 4.5) which allow faster austenite grain growth on reaustenitisation and ferrite growth during cooling. The results also show that there is little correlation between MFP and welding technique or welding position.

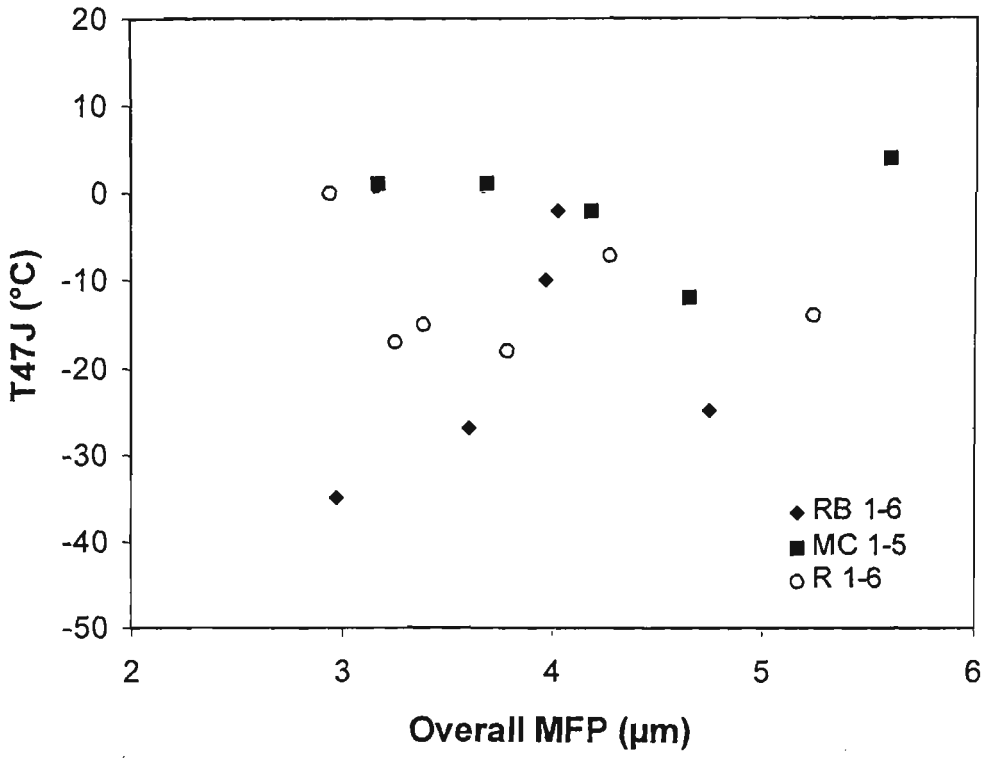

Figure 8.6: Variation of T47J with overall MFP ($\bar{L}_o^w$).

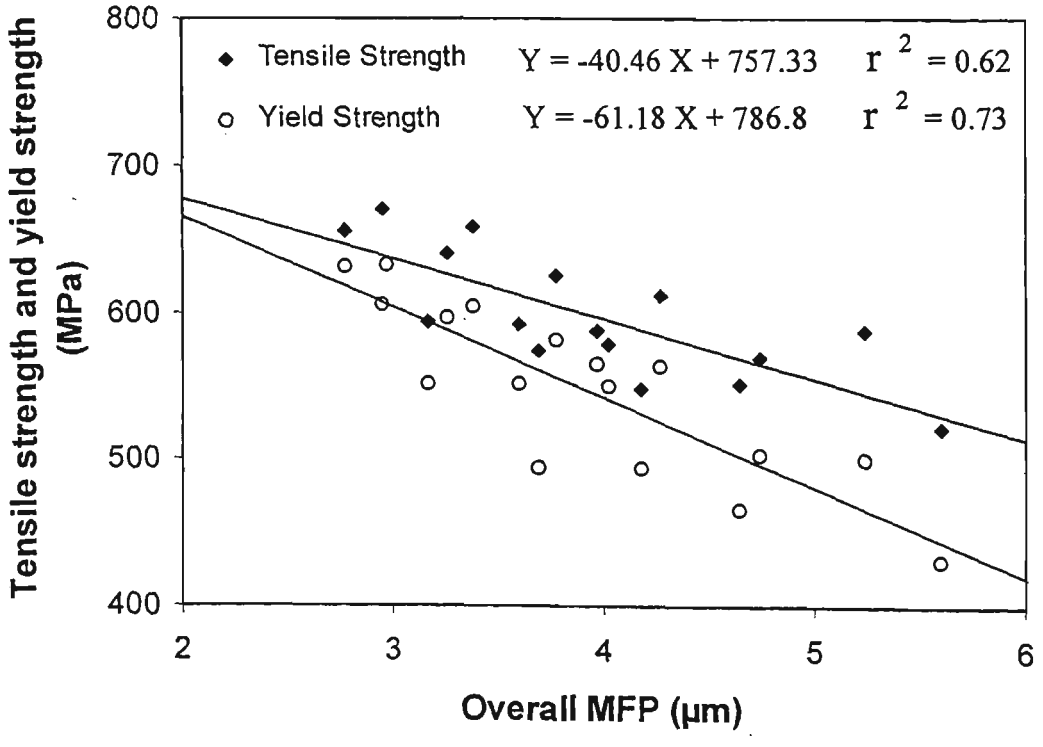

Figure 8.7: Variation of tensile strength and yield strength with overall MFP ($\bar{L}_o^w$).

One of the most interesting results from the analysis is that the grain coarsened reheated zone showed a smaller average MFP than the GR and IC regions. Grain coarsening certainly occurs in relation to the austenite grain size, but the increased hardenability due to grain size plus that imposed by the weld metal composition ensure that fine acicular ferrite forms in the bulk of the austenite grain by nucleation at non-metallic inclusions, more than compensating for the coarser allotriomorphic grain boundary ferrite (see Figures 6.6 to 6.14).

The lower average values of MFP in the grain coarsened zone is consistent with the higher local hardenability leading to a lower transformation temperature range and the formation of finer and more chaotic ferrite crystals in intragranular regions. It is also implied that reaustenitising to an elevated temperature (1200 - 1500°C) does not compromise the efficiency of non-metallic inclusions in re-nucleating acicular ferrite.

Whilst it is recognised that the connectivity of coarse structures may influence impact energy and hydrogen assisted cold cracking by providing low energy crack paths (eg. intergranular fracture), the complexity of the stress systems present in impact loading or because of stress concentration and restraint stresses should generally ensure that the overall structure will be exposed to the fracture path. Therefore, refined structures would be expected to contribute strongly to energy absorption and cracking resistance. However, as shown in Figure 8.6, the relationship between toughness (T47J) and overall MFP ($\bar{L}_o^w$) shows a very high scatter. There was no strong trend in the values of T47J with $\bar{L}_o^w$ for all three consumable types. The influence of mean free path is probably via individual sub-zones of the weld metal. More assessments of overall MFP and the MFP of each sub-zone on impact properties are discussed in the next chapter.

The overall MFP ($\bar{L}_o^w$) shows a better correlation with strength than toughness. Variation of tensile strength and yield strength with overall MFP ($\bar{L}_o^w$) is plotted in Figure 8.7. The weld metal tensile and yield strengths for the 3 types of wire appeared to correlate strongly with $\bar{L}_o^w$, with a larger $\bar{L}_o^w$ leading to a lower strength level. The data support the assumption made by Schumann et al. (1995) that variation of tensile properties with heat input is related to increases in grain size which can be expected at the longer cooling times associated with higher heat input.

8.4 Conclusions

1. An overall mean free path for the ferritic transformation products ($\bar{L}_o^w$) of the weld metal microstructure can be determined from the volume fractions of each sub-zone and the characteristic lengths between grain boundaries in each sub-zone.

2. All three groups of test plates followed essentially the same trend: the mean free path values for the SW, GC, GR and IC weld metal regions increased linearly with increasing heat input due to the decrease in cooling rate which allowed transformation of austenite at a higher temperature to coarser ferritic products.

3. The overall mean free path ($\bar{L}_o^w$) increased linearly with increasing heat input. The IC sub-zone was characterised by the highest value for MFP (8.3μ) while the SW and GC sub-zones generally showed smaller values. Surprisingly, the "grain coarsened" sub-zone showed a lower value of MFP for ferrite than the "grain refined" sub-zone because of transformation to acicular ferrite.

4. A slight change in the value of MFP resulted from the use of 100% CO2 as the shielding gas: the mean free path was slightly larger relative to welds produced using Ar rich shielding gas at a similar heat input.

5. Changes in welding technique between stringer and weave or welding position from horizontal to vertical did not significantly affect the value of mean free path.

6. There was no strong trend in mean free path of the SW and GC sub-zones associated with a change from rutile, to rutile-boron, to metal cored FCA welding consumables, but the consumable type slightly influenced the GR and IC sub-zones because of different contents of weld metal C and N which tend to hinder grain growth in the HAZ.

7. The overall MFP ($\bar{L}_o^w$) shows a better correlation with strength than toughness. While the relationship between toughness (T47J) and $\bar{L}_o^w$ shows a very high scatter, the weld metal tensile and yield strengths appeared to correlate well with $\bar{L}_o^w$, with a larger $\bar{L}_o^w$ leading to a lower strength level.

PART C MODELLING

CHAPTER 9

NEURAL NETWORK ANALYSIS OF TOUGHNESS

9.1 Introduction

The Charpy V-notch (CVN) impact test has been used extensively in mechanical testing of steel products, in research and in procurement specifications for more than four decades. For some materials and temperatures, impact tests on notched specimens have been found to predict the likelihood of brittle fracture better than tension tests or other tests used in material specifications (ASTM Standards 1996). Neural networks have been reported to be very effective in analyzing weldability of power plant steels (Cool et al. 1996), the effect of carbon content on hot strength of steels (Kong et al. 1998) and impact toughness of submerged arc and manual metal arc welds (Bhadeshia et al. 1995). Therefore, developing a neural network model of FCA welding is a potentially valuable way to examine the diversity of factors which might influence impact toughness.

There are many neural network algorithms which can be used to solve a wide diversity of problems. Examples are Adaptive Resonance Theory (ART), Back-propagation, General Regression, Learning Vector Quantization (LVQ), Modular, Probabilistic, Radial Basis Function (RBF), and Self-organizing Maps (SOM). However, among all the supervised learning algorithms, back-propagation is the most widely used neural network system (Cun 1988). Back-propagation is a technique for solving the problem of hard learning that is required to map a well-defined set of inputs into a well-defined set of outputs. Therefore, a back-propagation network algorithm was selected for the analysis of weld metal toughness.

9.2 Input Variables

Using experience of welding metallurgy, there are four major fields which might have influence on the Charpy toughness: chemical composition, microstructure, non-metallic inclusions and welding conditions. These fields are also interactive. All of the work reported here relies on those experimental data which have been collected over several years for the FCAW samples studied in this work. The variables which have been selected for analysis are given in Table 9.1. There are 31 input data fields and 83 examples . The variables for each example included carbon content, manganese content, silicon content, sulphur content, phosphorus content, titanium content, aluminium content, boron content, molybdenum content, oxygen content, volume fraction of reaustenitised region, volume fraction of double-reheated zone, overall mean free path ($\overline{L}_{o}^{w}$), mean free path of solidified weld metal ($\overline{L}_{SW}$), mean free path of grain coarsened sub-zone ($\overline{L}_{GC}$), mean free path of grain refined sub-zone ($\overline{L}_{GR}$), mean free path of intercritical sub-zone ($\overline{L}_{IC}$), volume fraction of acicular ferrite (AF), volume fraction of grain boundary ferrite (PF(G)), volume fraction of intragranular polygonal ferrite (PF(I)), volume fraction of ferrite with a second phase (FS), volume fraction of grain coarsened (GC) sub-zone, volume fraction of grain refined (GR) sub-zone, volume fraction of intercritical (IC) sub-zone, volume fraction of non-metallic inclusions (V_v), arithmetic mean three dimensional particle diameter ($\overline{D_v}$), the number of particles per unit volume (N_v), volume fraction of particle ≥ 1.5 μm ($F \geq 1.5$), overall mean hardness ($\overline{H}$) and test temperature (T).

Table 9.1: Variables selected for impact toughness analysis.

Variables	Range	Mean
Carbon (wt %)	0.05 - 0.09	0.075
Manganese (wt %)	0.94 - 1.50	1.27
Silicon (wt %)	0.32 - 0.66	0.54
Sulphur (wt %)	0.010 - 0.015	0.012
Phosphorus (wt %)	0.011 - 0.016	0.014
Titanium (wt %)	0.011 - 0.069	0.045
Aluminium (wt %)	0.002 - 0.007	0.004
Boron (wt %)	0.0001 - 0.01160	0.0033
Molybdenum (wt %)	0.01 - 0.02	0.014
Oxygen (wt %)	0.069 - 0.124	0.087
Nitrogen (wt %)	0.004 - 0.013	0.0077
Volume fraction of reaustenitised region (%)	44.16 - 62.28	49.83
Volume fraction of double-reheated zone (%)	0 -16.4	10.86
$\bar{L}_o^w$ (μm)	2.77 - 5.24	3.90
$\bar{L}_{sw}$ (μm)	2.63 - 4.71	3.49
$\bar{L}_{GC}$ (μm)	2.07 - 4.67	3.31
$\bar{L}_{GR}$ (μm)	3.20 - 6.95	4.66
$\bar{L}_{IC}$ (μm)	3.50 - 8.30	5.46
Volume fraction of AF (%)	9.3 - 33.2	19.7
Volume fraction of PF(G) (%)	0.9 - 23.0	14.9
Volume fraction of PF(I) (%)	2.45 - 33.40	7.73
Volume fraction of FS (%)	0.9 - 10.8	5.1
Volume fraction of GC sub-zone (%)	13.41 - 20.46	17.92
Volume fraction of GR sub-zone (%)	21.12 -35.74	27.16
Volume fraction of IC sub-zone (%)	3.96 - 8.08	5.44
V_v (%)	0.6105 - 1.1272	0.7846

$\overline{D_v}$ (μm)	0.4775 - 0.8970	0.6121
N_v ($1/\mu m^3$)	0.02740 - 0.10400	0.07114
$F \geq 1.5$ (%)	0.69 - 3.93	1.61
$\overline{H}$	191.5 - 224.6	206.4
Temperature (°C)	-60 to +40	

9.3 Training Data Set and Testing Data Set

Neural networks are built of neurons to simulate and understand what goes on in the nervous systems, with the hope of capturing some of the power of these biological systems of the human brain. In supervised learning networks, such as the back-propagation algorithm, the inputs are presented along with desired outputs during the training phase. The test phase consists of presenting new inputs to the trained model, along with desired outputs, to see how well the trained network performs.

To be most objective, it is the best to make the training and testing set completely separate (no overlap) (Using NeuralWorks 1996). Otherwise, the network might only show how well the network memorized the training data (overfitting). It is important to create a neural network model that will generalize to new input situations. For that reason, the data available are normally broken down into a training set and a testing set. The training and the testing sets might be thought as the "homework" and the "final exam". In the process of doing homework, the basic skills, techniques and relationships are learned. In the final exam, those techniques and skills are tested and scored. The same is true with neural network modelling. The training set is designed to maximize the learning process. The testing set is designed to provide the network with a challenge which represents what it is likely to find in real circumstances.

For best results, it is usually advisable to select the training set in the following way. Firstly, it must be reasonably representative of the entire condition. Secondly, the data are evenly divided between the various outcomes (Using NeuralWorks 1996).

According to the above advice, the database of the experimental examples was divided into two complete data sets. The training data set contained 66 examples and the testing data set contained 17 examples which involved one example for each welded sample. There was no overlap for the two data sets and both data sets have 31 input data fields and 1 desired output data field. Full details of the experimental data are given in Appendix 1.

9.4 Analysis

9.4.1 The generalized delta rule

The aim of the back-propagation learning process is to minimize the global error of the system by modifying the weights and the learning rule is used for specifying how connection weights are changed during the learning process. Many learning rules have been developed to solve back propagation network weight updates (Neural Reference Guide 1996). The delta rule which was developed by Rumelhart, Hinton and Williams (1986) is still a widely used standard one. Therefore, the delta rule was chosen for the current analysis.

The proof of the validity of the back-propagation network is essentially mathematical and relies on a knowledge of differential calculus. Rumelhart et al. (1986) give a detailed mathematical exposition. The learning rules have been specifically related to Hopfield models and Boltzmann machines. The activation of the jth unit for the pth

training example (a_{pj}) is given by taking the sum for all inputs i of the unit multiplied by the appropriate weight w_{ji} and adding to it the value of some threshold u.

$$a_{pj} = \sum_{(\text{for all } i)} w_{ji} o_{pi} + u_j \tag{9.1}$$

where o_{pi} is the actual (computed) output.

$$o_{pj} = f_j(a_{pj}) \tag{9.2}$$

In Equation 9.2, actual output of the jth node and pth input pattern is function f_j of the activation a_{pj}. Feed-forward nets with input units, output units and hidden units are considered, the Rumelhart et al. (1986) prescription is summarized by three statements.

1. For the pth presentation of an input/output pair for training, the change for the weight which joins the jth unit to its ith incoming connection ($\Delta_p w_{ji}$) is proportional to some computed error (e_{pj}) for this jth unit. In mathematical form this can be expressed as:

$$\Delta_p w_{ji} = \beta e_{pj} o_{pi} \tag{9.3}$$

   where o_{pi} is the value of the ith incoming connection and β is a constant (learning coefficient) which determines the rate of learning.

But most of the work of Rumelhart et al. (1986) centres on the way in which the error e_{pj} may be computed even for hidden units. Hence the next two statements.

2. For output units, the error is calculated in a straightforward way based on a knowledge of a desired output for the jth unit, d_{pj}. In fact the error is stated as:

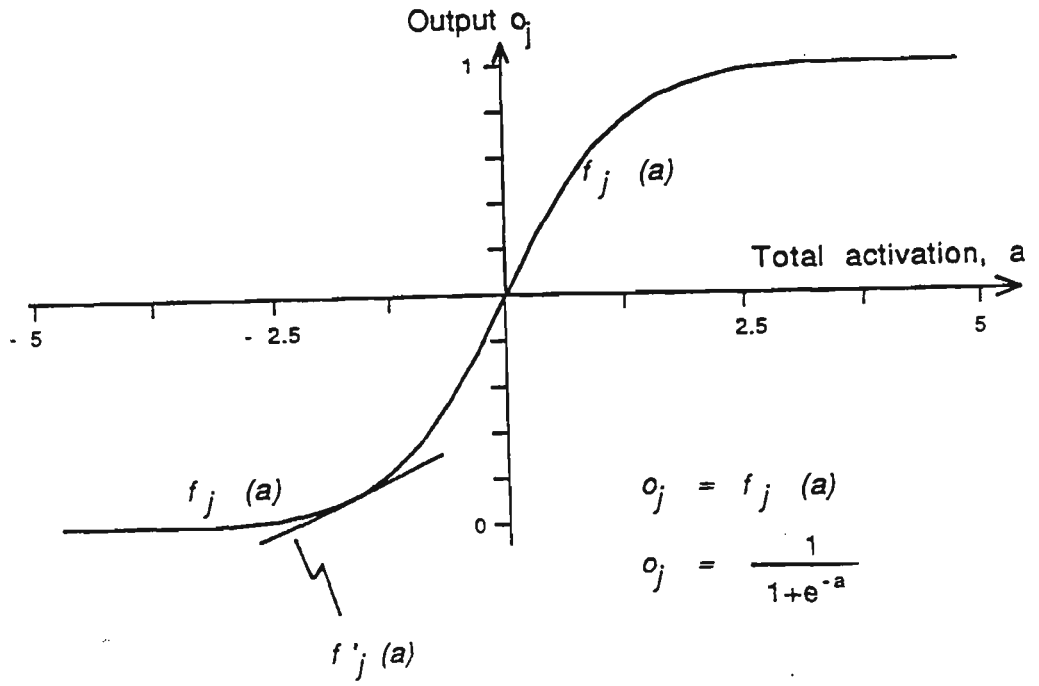

Figure 9.1: Examples of $f_j(a)$ and $f'_j(a)$ (After Aleksander and Morton 1995).

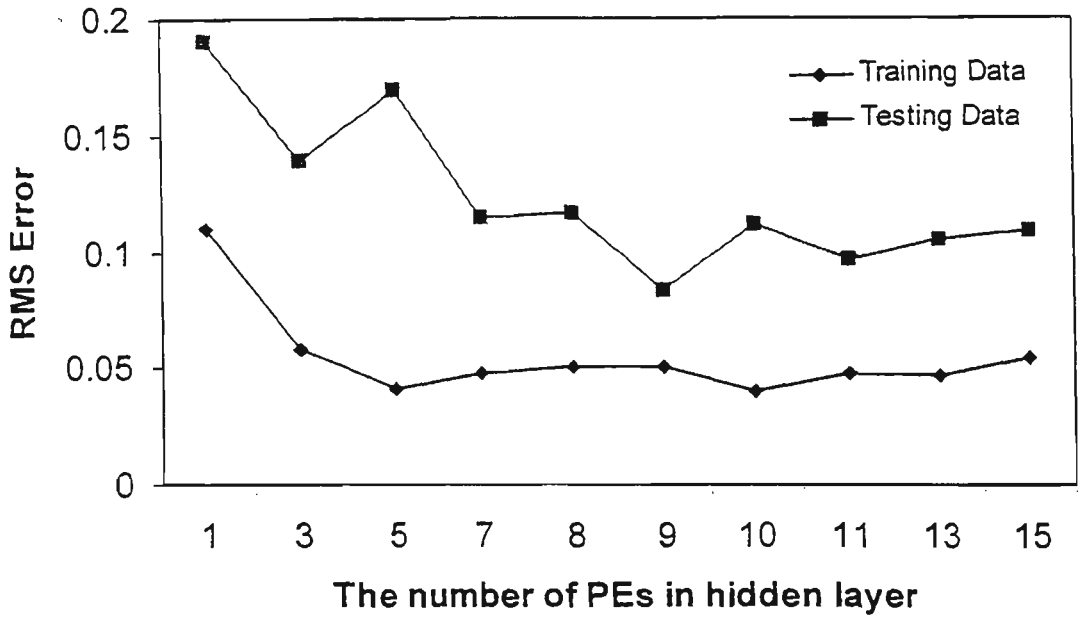

Figure 9.2: Variation in RMS error as function of the number of processing elements (PEs) in the hidden layer.

$$e_{pj} = (d_{pj} - o_{pj}) f'_j(a_{pj}) \qquad (9.4)$$

The term $(d_{pj} - o_{pj})$ clearly indicates that the error is proportional to the difference between the actual output o_{pj} and the desired output d_{pj}. The term $f'_j(a_{pj})$ means the rate of change of o_{pj} with respect to $f_j(a_{pj})$. This last point is illustrated for a particular form of $f_j(a_{pj})$ in Figure 9.1.

Rumelhart et al. (1986) have shown that it is essential that $f'_j(a_{pj})$ be a smoothly increasing function with a_{pj}. In cases such as Figure 9.1 this causes greater weight-changing activity to take place for units where the output is less certain (i.e. close to 0.5, where the slope is steepest) than those in which it is more certain (i.e. close to 0 or 1).

3. If the unit is hidden, and its output is connected to k units, its error is defined as being proportional to the sum of the errors of all the k units as modified by the weights connecting these units. In symbols:

$$e_{pj} = \left(\sum_{(\text{for all } k)} e_{pk} w_{kj} \right) f'_j(a_{pj}) \qquad (9.5)$$

Back-propagation training implies two steps. First is the 'forward' step during which the input is applied and allowed to propagate to the output. The error values of the output units are calculated and compared to the desired output. During the second, 'backward', phase these errors are propagated backwards and weight changes made. To be precise, once the output error has been calculated, the weight changes in the output layer can then be made using (9.4) and (9.3). This fixes the error values for the previous layer. This procedure may be propagated backwards until the weights in the input unit are adjusted. This is then followed by another forward step and a further backward step,

and so on. The work of Rumelhart et al. (1986) shows that an overall output error defined as half the sum of the squares of all the output errors, or in symbols:

$$E_p = 0.5 \sum_{(\text{for all } j)} (d_{pj} - o_{pj})^2 \qquad (9.6)$$

The aim of the back-propagation process is to minimize the overall output error of the system by modifying the weights.

9.4.2 Transfer function

Transfer function is the method of transforming the input and is used for all layers in the network. The transfer function is usually a non-linear function that transfers the internally generated sum for each processing element (PE) to a potential output value. Rumelhart et al. (1986) have suggested an S-shaped function as shown in Figure 9.1 is useful in this sort of work - such as the sigmoid function:

$$o_{pj} = \frac{1}{1 + e^{-a_{pj}}} \qquad (9.7)$$

where

$$a_{pj} = \sum_{(\text{for all } i)} w_{ji} o_{pi} + u_j \qquad (9.1)$$

as seen earlier.

A useful property of this formulation is that $f'_j(a_{pj})$ has a simple form:

$$f'_j(a_{pj}) = o_{pj}(1 - o_{pj}) \qquad (9.8)$$

This simplifies the weight adjustment rules:

for output nodes, (9.4) becomes, $e_{pj} = (d_{pj} - o_{pj})o_{pj}(1 - o_{pj})$ (9.9)

for hidden nodes, (9.5) becomes, $e_{pj} = \left(\sum_{(forallk)} e_{pk}w_{kj}\right) o_{pj}(1 - o_{pj})$ (9.10)

In place of the sigmoid function any smooth function can be used as the transfer function for a processing element in a back-propagation network, such as the hyperbolic tangent function. The hyperbolic tangent (TanH) function is just a bipolar version of the sigmoid function which was used by Rumelhart (1986). The sigmoid function is a smooth version of a {0,1} step function whereas the hyperbolic tangent is a smooth version of a {-1,1} step function.

Hyperbolic tangent is defined by

$$o_{pj} = \frac{e^{a_{pj}} - e^{-a_{pj}}}{e^{a_{pj}} + e^{-a_{pj}}} \quad (9.11)$$

As with the sigmoid function, the derivative of the hyperbolic tangent can also be expressed in terms of itself:

$$f_j'(a_{pj}) = (1 + o_{pj})(1 - o_{pj}) \quad (9.12)$$

Thus with this type of transfer function the error propagation equation is to:

for output nodes, (9.4) becomes, $e_{pj} = (d_{pj} - o_{pj})(1 + o_{pj})(1 - o_{pj})$ (9.13)

for hidden nodes, (9.5) becomes, $e_{pj} = \left(\sum_{(forallk)} e_{pk}w_{kj}\right) (1 + o_{pj})(1 - o_{pj})$ (9.14)

Available transfer functions for back propagation network are sigmoid, hyperbolic tangent, linear and sine. The current network works with TanH because it is

recommended for most real-world back propagation applications (Using NeuralWorks 1996).

9.4.3 Hidden layer

The root mean square (RMS) error is a general index for the performance of the model created by a neural network. The RMS error is measured through all the PEs in the output layer and adds up the squares of the errors between calculated outputs and measured outputs, divided by the number of a certain iteration epoch in the output layer to obtain an average, and then takes the square root of that average. The squaring of the errors gets rid of the sign of the error, but increases the magnitude. The square root removes the magnitude increase of the squaring operation:

$$\text{RMS Error} = \sqrt{\frac{e_1^2 + e_2^2 + e_3^2 + \cdots\cdots + e_n^2}{n}} \tag{9.15}$$

where e is the error between measured and estimated values and n is the number of the iteration epoch. The number of the iteration epoch is set by the number of examples in the training or testing data set in the current neural network. Therefore, n is the number of examples in the training data set or testing data set.

The number of PEs in the hidden layer was adjusted by examining performance on testing data. The RMS errors for different numbers of PEs in the hidden layer are given in Figure 9.2. The result shows that 9 PEs has a very good consistency for both the training data and testing data. Therefore, 9 PEs for the hidden layer were selected to build a reasonable level of complexity to represent the variations in toughness as a function of the input variables. Larger numbers of PEs in the hidden layer did not give significantly lower values of RMS error for the test data. Moreover, the complexity of

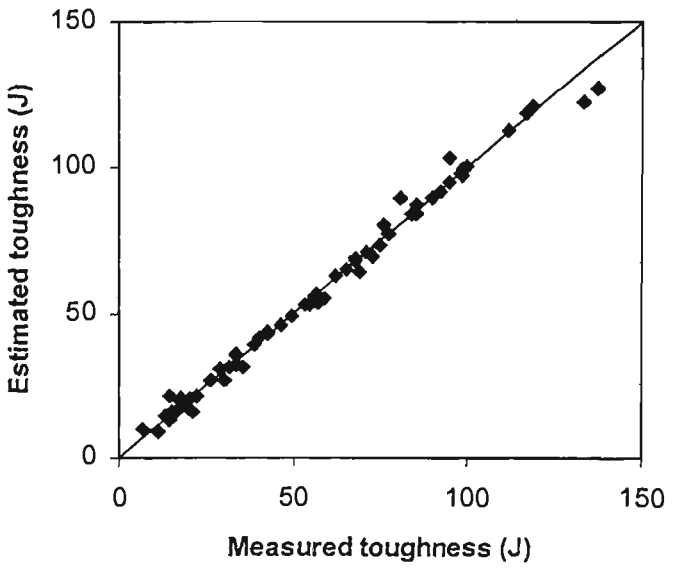

Figure 9.3: Comparison of estimated and measured toughness for training data.

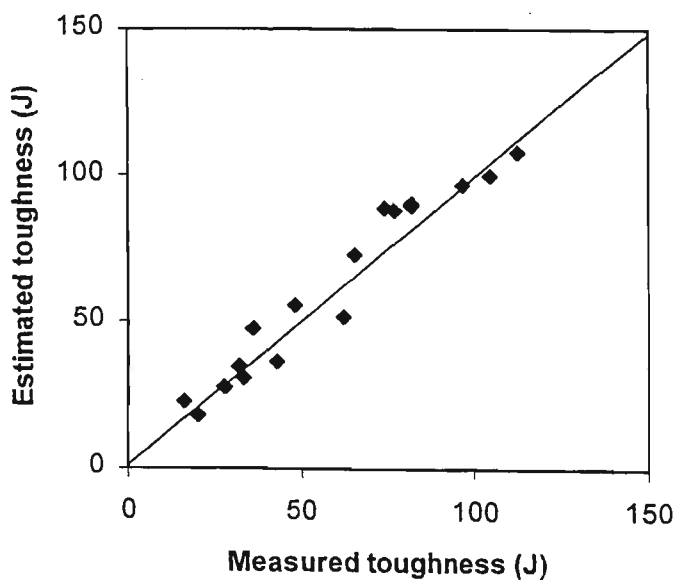

Figure 9.4: Comparison of estimated and measured toughness for testing data.

the model also increases with a large number of PEs. A high degree of complexity may not be justified, and in an extreme case, the model may in a meaningless way attempt to fit the experimental data (Bhadeshia et al. 1995). Generalization is a significant issue in building any model. The opposite of generalization is overfitting. In general, the more complex a model is, the more chance of overfitting (NeuralWorks Predict 1996).

9.4.4 The agreement between training and testing data

The levels of agreement for the training and testing data sets are shown in Figure 9.3 and Figure 9.4. Good predictions occur in both instances. It should be emphasised again that the training data and testing data are two complete data sets (no overlap). That means the testing data were not included in training process which derived the weights for the network. The proof is obvious that the current neural network model does show a good performance in analysis of toughness by using the ranges of the present input variable.

9.5 Sensitivity

In some neural network applications, it is desirable to know which of the inputs has the most effect on the output. Sensitivity analysis calculates, for a given input record, how sensitive any given output field is to fluctuations in the value of any given input field. In other words, sensitivity analysis allows determination of the effect that a small change in an input value will have on the output value, and ranks the input fields according to this sensitivity. In mathematical terms, the output of sensitivity analysis shows a matrix of partial derivatives of output variables with respect to input variables.

Sensitivity analysis can provide good insights into the model. High sensitivity to a particular input that is likely to fluctuate around its current value may lead to

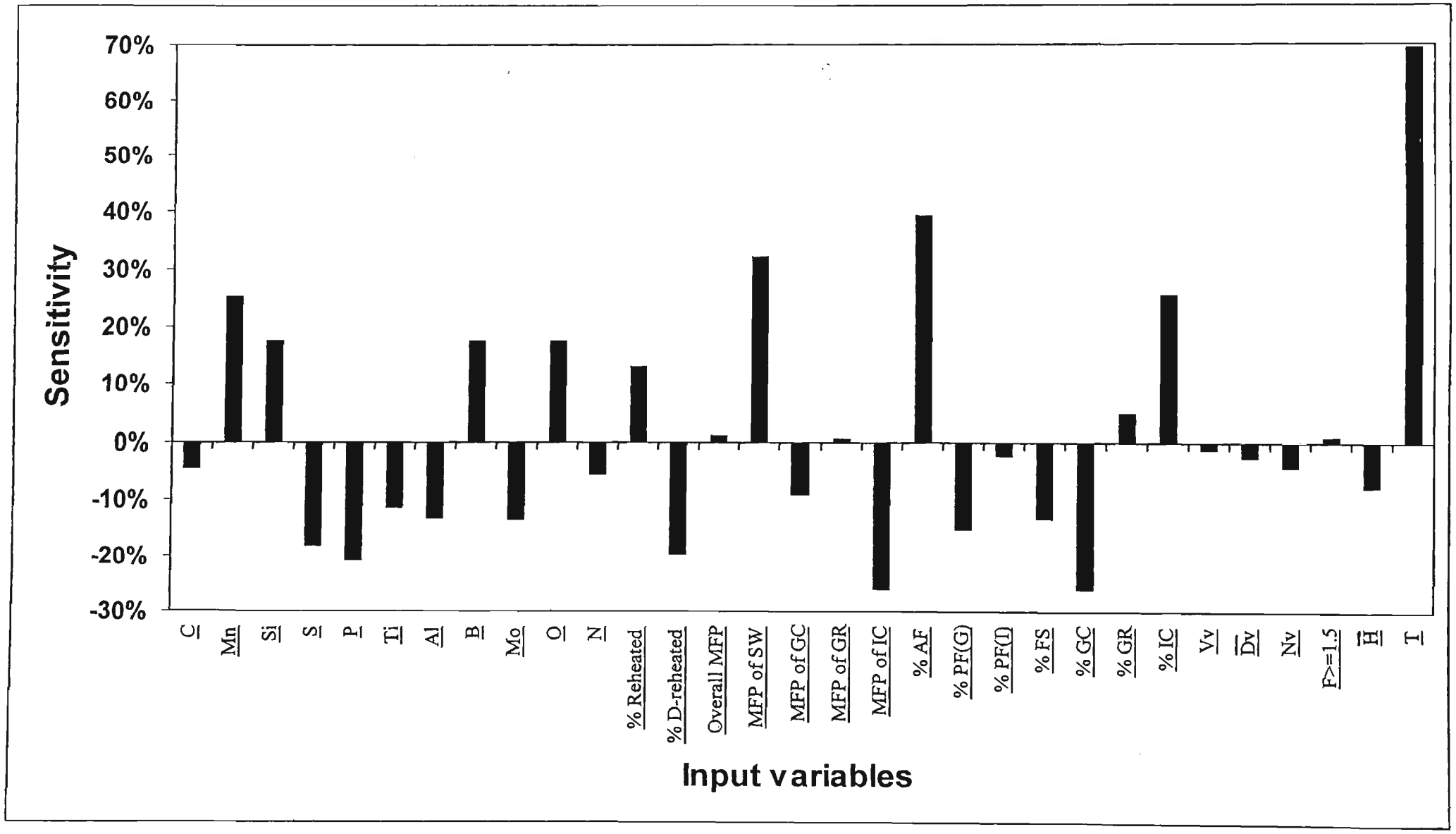

Figure 9.5: Sensitivity analysis of neural network model.

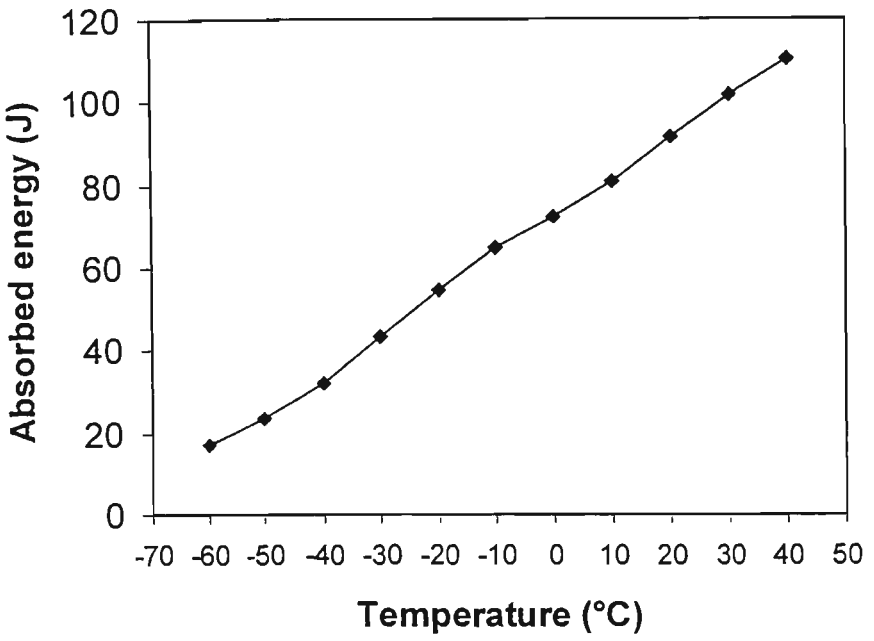

Figure 9.6: Relationship between estimated toughness and test temperature.

questioning of the output. If the input field values can be controlled, sensitivity analysis shows which fields can be changed and which direction should be changed in order to achieve the desired model output.

Nevertheless, the high sensitivity of an individual data may not necessarily be important for application. Sensitivity analysis can also be generated across an entire data set to give an overall indication of the influence of each input fields on the output fields. Therefore an average sensitivity analysis is more meaningful than an individual one. To do so, the input values are varied by a small amount and then determine how much the outputs change as a percentage of the individual input change. Therefore, the average sensitivity (S) of each input variable can be calculated through all input data.

$$S = \frac{S_1 + S_2 \cdots\cdots + S_n}{n} \tag{9.16}$$

where S is the sensitivity for an individual input datum for a certain input variable in the training data set and n is the number of examples in the training data set.

The average sensitivity for each input variable is shown in Figure 9.5. This figure shows that both chemical content and microstructure have very large influences while the direct influence of non-metallic inclusions on impact toughness is very small.

9.6 Discussion

It is obvious at first sight of the sensitivity analysis of the neural network model (Figure 9.5) that test temperature has the most significant effect. Test temperature has been established as the most important factor affecting toughness for a long time. Figure 9.6

shows good consistency with an abundance of experimental results which have established that toughness increases with increased test temperature.

The metallurgical significance of the sensitivity of the selected variables to toughness is discussed below. The discussions are divided into three fields: chemical compositions, microstructures and non-metallic inclusions. In general, each field of input variables is interactive with the others and has its own importance in the influence on impact toughness. Predictions were made on the basis of the mean values of the input variables shown in Table 9.1 and within the range of the experimental data used during training. Some aspects which might take years to study experimentally were examined using the neural network model.

9.6.1 Chemical compositions

The sensitivity analysis of the neural network model (Figure 9.5) shows that over the range studied carbon has a small detrimental effect. Carbon has strong influence on hardness, strength and ductility (Metals Handbook 1964). In general, a higher hardness is usually associated with a higher carbon content. Increasing the carbon content of steel leads to increased strength, hardness, brittleness and reduced ductility and also leads to inferior weldability (Bain and Paxton 1961, Siebert 1977). The contribution of C to hardness and brittleness might also lead to inferior toughness. This proposal is consistent with Figure 9.5 which shows that increasing the overall mean hardness is also harmful to toughness. The current estimated results in relation to carbon are consistent with Bhadeshia's report (1995) on submerged and manual metal arc welds.

Manganese is a strong deoxidising element. Zhang and Farrar (1997) carried out a systematic investigation of the microstructure and toughness of C-Mn-Ni low alloy

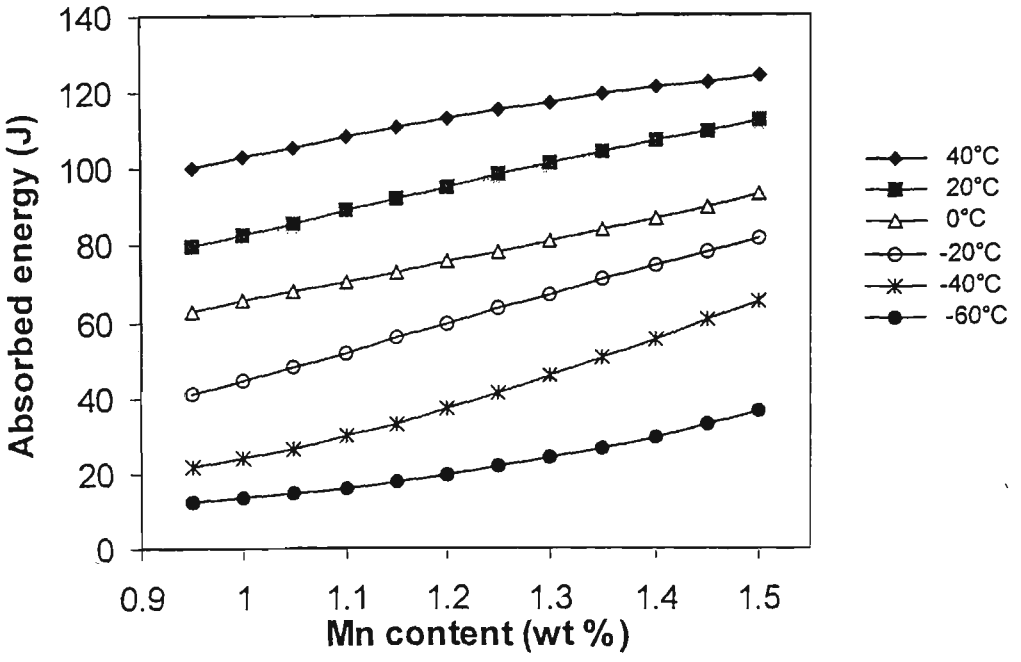

Figure 9.7: Relationship between estimated toughness and manganese content with different test temperatures.

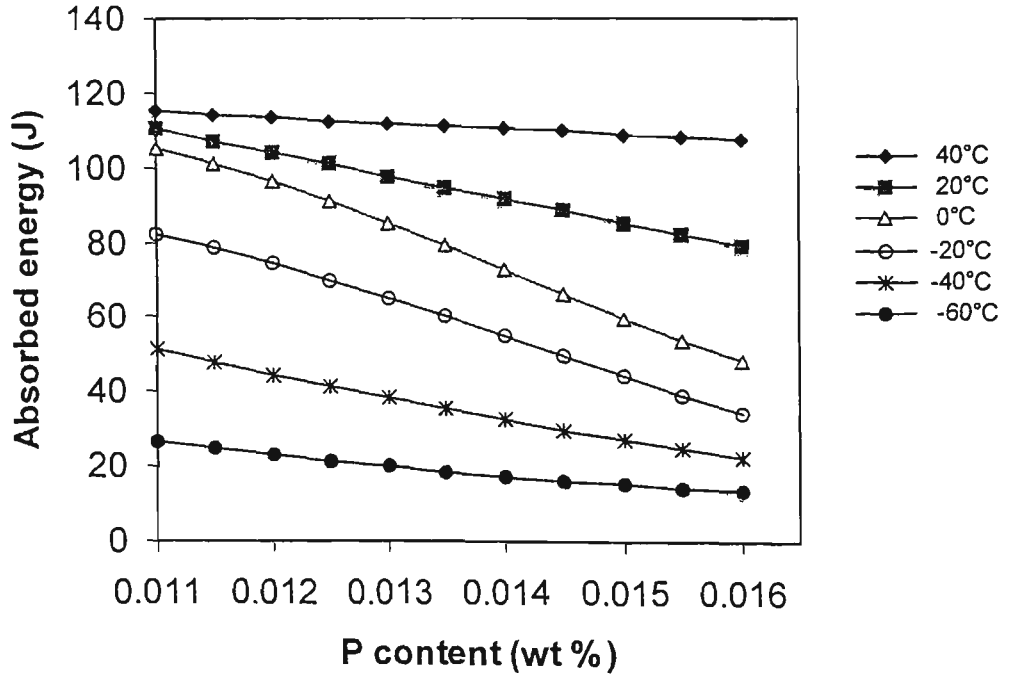

Figure 9.8: Relationship between estimated toughness and phosphorus content with different test temperatures.

weld metals. It was found that Mn promoted acicular ferrite at the expense of grain boundary ferrite and ferrite with a second phase. Evans (1978) also reported that increasing manganese refined the acicular ferrite, refined the coarse grained region and reduced the grain size of the equiaxed fine grained zone. The optimum impact properties of the weld metals were attained at 1.5 % manganese, due to the competitive influence of yield strength and microstructure. The estimated toughness from the current neural network model resulting from increased manganese is shown in Figure 9.7. The analysis indicates that increasing manganese leads to better toughness, consistent with Evans' report for the input range 0.94 - 1.5 wt % Mn.

Bhadeshia et al. (1995) found that the elements silicon and manganese do not individually have a substantial effect on toughness, presumably because they exert their effect through the microstructure. However, in the analysis undertaken in the present work Mn and Si show strong effects on toughness (Figure 9.5). Silicon and to a lesser extent Mn are strong deoxidising elements which therefore form inclusions capable of nucleating AF. In this way, silicon can contribute to toughness, like manganese. The beneficial effect of silicon over the range examined is shown in the sensitivity analysis of the neural network model (Figure 9.5).

Sulphur can combine with manganese to form manganese-sulphide non-metallic inclusions. The adverse effect on transverse impact energy values of elongated manganese sulphide stringer inclusions is well known. If MnS is present in significant amounts and/or as elongated stringers, it can adversely affect the toughness (Yeomans 1994). Ferrous sulphide also induces brittleness in steel. Therefore, the sulphur content should be kept as low as possible as suggested by Dennis (1963). In agreement with

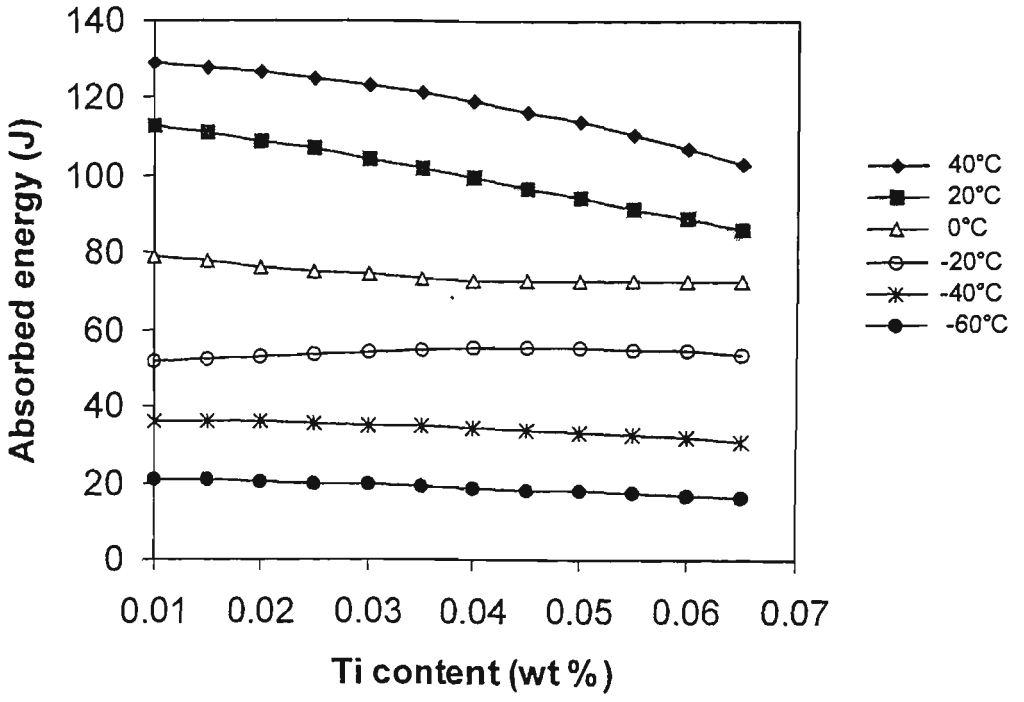

Figure 9.9: Relationship between estimated toughness and titanium content with different test temperatures.

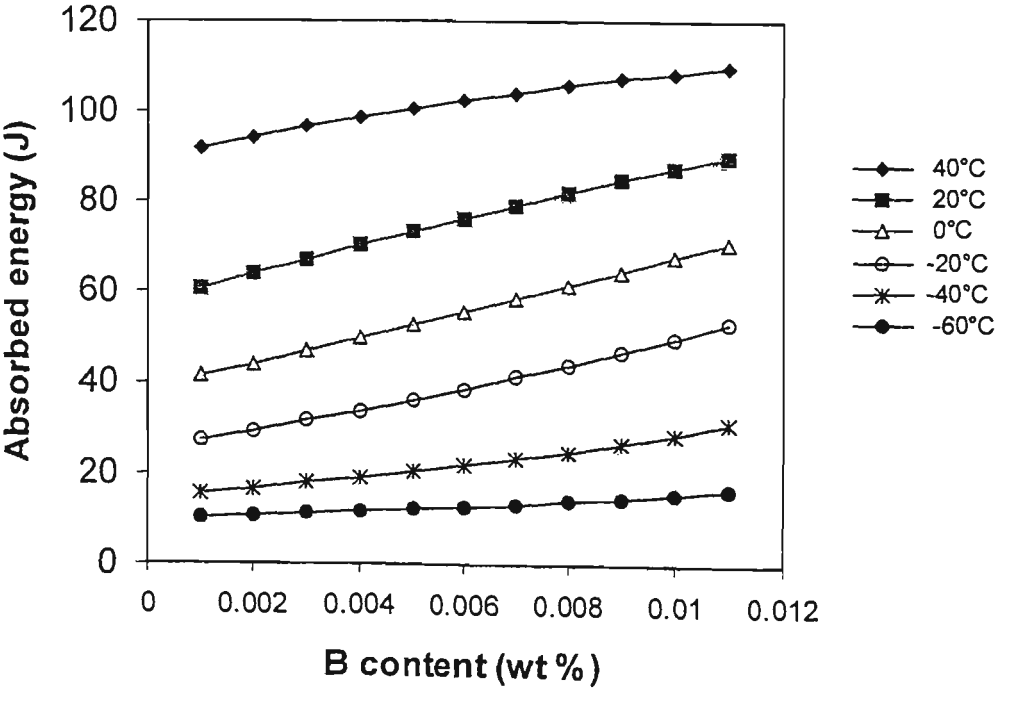

Figure 9.10: Relationship between estimated toughness and boron content with different test temperatures.

these observations, a harmful effect on toughness is shown in the sensitivity analysis of the neural network model (Figure 9.5).

Phosphorus has a large harmful influence on impact toughness according to the sensitivity analysis of the neural network model (Figure 9.5). Figure 9.8 shows the relationship between estimated toughness and phosphorus content. A significantly harmful effect of increasing phosphorus content on toughness was observed. This predicted result is consistent with Yeomans' report (1994).

Figure 9.9 shows the relationship between estimated toughness and titanium content. Surprisingly, Figure 9.9 predicts that Ti will have a deleterious effect, despite the fact that Ti additions are regarded as favourable for formating acicular ferrite and improving toughness. The direct influence of Ti on toughness is unknown, but its influence on the microstructure of low carbon steel has been reported by many researchers (McCutcheon et al. 1983, George and Irani 1968, George et al. 1971, Edwards et al. 1986, Apps and Andrade 1985, Uwer et al. 1990). It has been demonstrated that a small addition of Ti, produces austenite grain size control for the reheating cycle experienced in welding (Yeomans 1994). Because of the marked grain-refining effect of titanium, it might also be expected that the use of this element in small quantities would improve the low temperature impact resistance of steel. However, as was indicated by Comstock (1955), this is not always true. The current result for the effect of Ti is very similar to Comstock's report (1955), in which a comparison of the effects of aluminum, titanium and zirconium on the low temperature impact resistance of steel is provided. Comstock (1955) claimed that although grain refinement is generally considered to improve impact resistance, Ti has the opposite effect. Comstock concluded that the adverse

effect of Ti at low temperatures is due to the presence of this element in the steel, despite the grain refinement.

The effect of Ti in weld metal is not necessarily the same as in the HAZ of welded steel, because Ti forms oxides which are present as non-metallic inclusions. The favourable effect of TiO in nucleating acicular ferrite is well acknowledged and part of the positive effect of AF on toughness (Figure 9.5) may be attributable indirectly to Ti. Moreover, the use of the total weld Ti contents from Table 4.5 in the neural network analysis may not be justified as Ti reacts first with N to form main refining particles of TiN. The neural network predictions of the effect of Ti on impact toughness should therefore be viewed with caution and only the excess Ti is available to form oxide (see Section 5.2.2).

In order to improve the current model, appropriate physical factors should be considered and the input data should be preprocessed and linked by using physical fundamentals before training and prediction. For instance, Ti preferentially combines with N, and Ti present in excess of the stoichiometric composition for TiN, will form TiO. Unreacted oxygen will then form SiO_2 and MnO which are also strong oxide factors (Bhadeshia et al. 1993). This approach may allow a more accurate linking of various interactions of input factors as well as the prediction of the multiple effect of these factors.

Evans (1991) reported that for a balanced basic low-hydrogen electrode, of a specific slag base type, the following occurred on increasing the amount of aluminum from zero: the hardness and tensile properties of as-deposited metal tended to increase; but the optimum notch toughness characteristics were exhibited at the zero aluminum level.

The calculated harmful effect of aluminum in the sensitivity analysis of the neural network model (Figure 9.5) is consistent with this report.

Boron can be successfully utilized to improve the toughness of welded joints in Ti-containing steels, because boron segregates to the prior austenite grain boundaries and suppresses the formation of grain boundary nucleated ferrite. This effect facilitates the intragranular nucleation of AF on oxide inclusions. Therefore, a beneficial effect of B is shown in the sensitivity analysis of the neural network model (Figure 9.5) and in predictions of Figure 9.10. Figure 9.10 shows increasing boron content from 0.001 % to 0.011% may lead to better toughness and the influence is very large. However, it has been reported that for an excess of soluble boron combination with carbon to form boron carbides can occur which is detrimental to toughness (Habu 1978, Dan and Gunji 1984).

In the sensitivity analysis of the neural network model (Figure 9.5), molybdenum shows a medium harmful effect. The physical basis of such a prediction is not clear, but Mo does increase hardenability and therefore hardness, properties which could be linked to reduced notch toughness.

Oxygen appears to have a significant effect on toughness of weld metals deposited by different arc welding processes. Some contradictions exist as to the exact mechanism by which oxygen affects the weld metal transformation and the oxygen content that is considered optimum for toughness. For example, Nakanishi and Komizo (1982) observed that 200-300 ppm was optimum for good toughness in GMA welding. Terashima and Tsuboi (1982) found that 300 ppm is optimum and Devillers et al. found that 400-500 ppm is an optimum in SA welding. However, Lathabai and Stout (1985) reported extensive work on FCA welding and claimed that there was no optimum

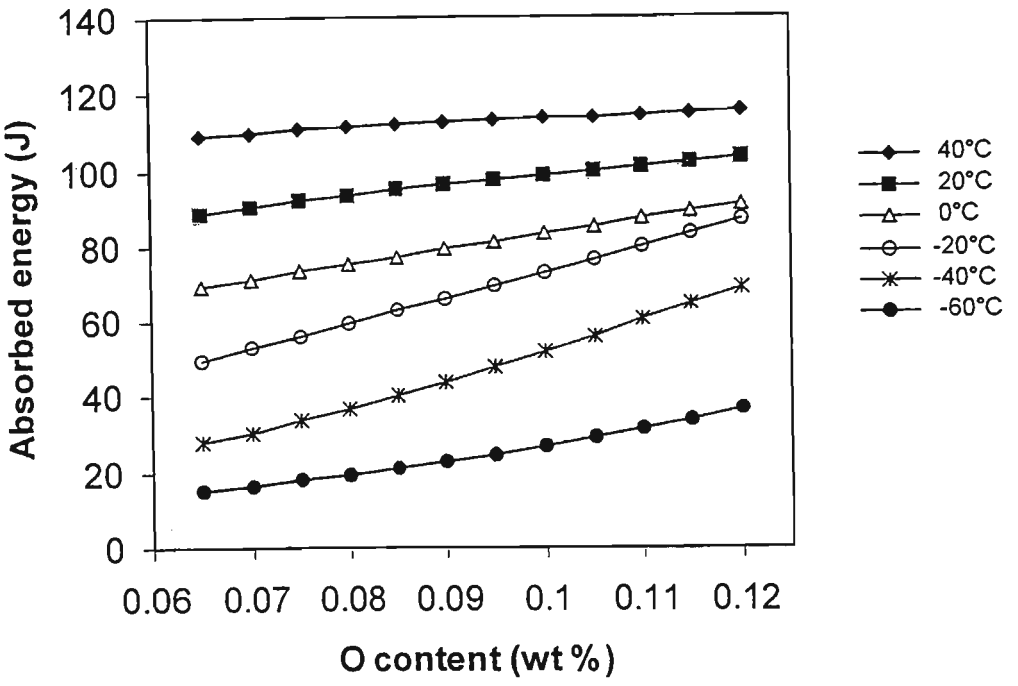

Figure 9.11: Relationship between estimated toughness and oxygen content with different test temperatures.

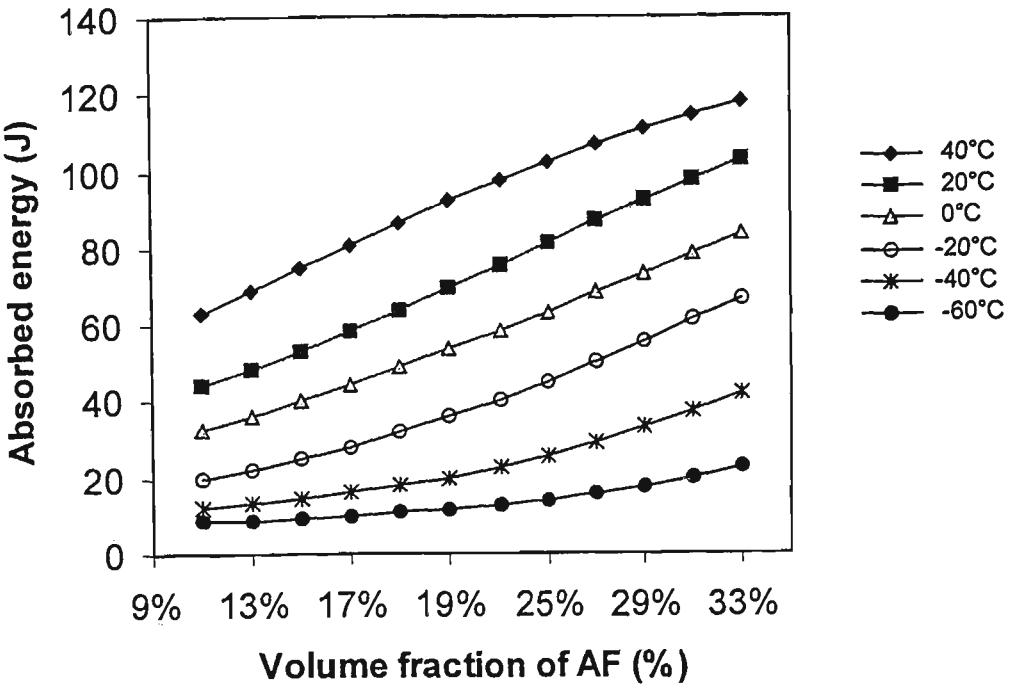

Figure 9.12: Relationship between estimated toughness and the overall volume fraction of acicular ferrite (AF) in the weld metal with different test temperatures.

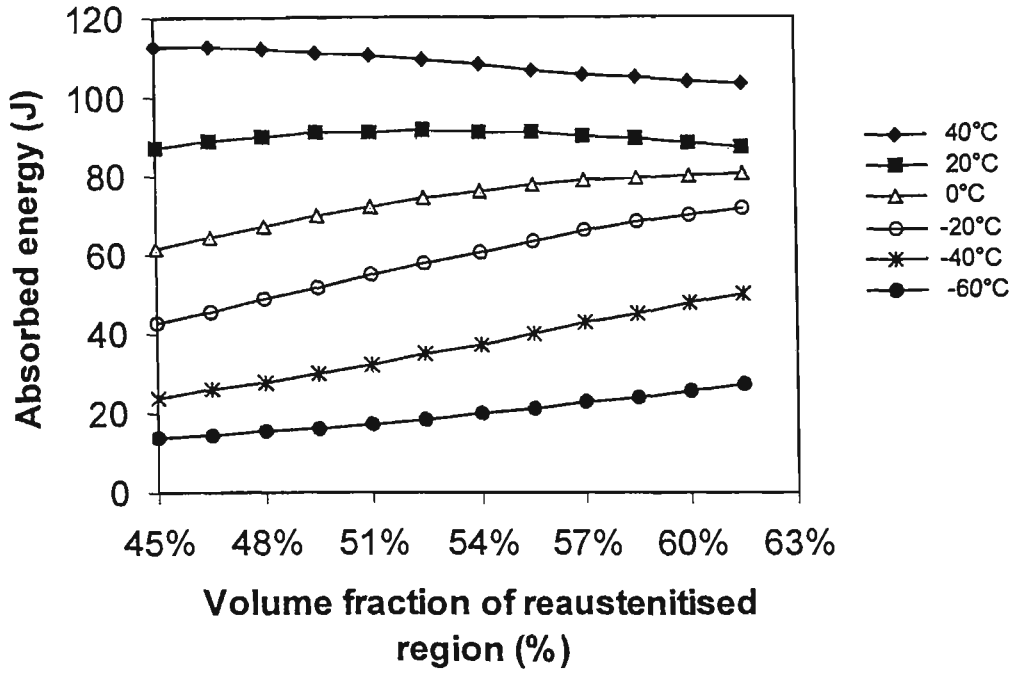

Figure 9.13: Relationship between estimated toughness and the volume fraction of reaustenitised region with different test temperatures.

oxygen level for FCA weld metals. It is also reported that the optimum level of oxygen content for intragranular acicular ferrite formation varies depending on the aluminum content in the weld metal (Koseki et al. 1997 and Horii et al. 1986). Figure 9.11 shows the results of the current neural network model. The slightly beneficial effect of increasing oxygen content is probably through the contribution to the intragranular nucleation of AF in the weld metal, thus imparting better toughness. The influence of AF content on toughness is discussed in the next section and the current result is consistent with results reported by Lathabai and Stout (1985) for FCA welding at a lower heat input (1.6 kJ/mm). However, it should be noted that the oxygen contents were high in the present case and outside the range found to be optimum for GMA welding.

Nitrogen is known to have a potent detrimental effect on the toughness of the weld, as has been reported experimentally (Svensson 1994, Lau et al. 1987, Oldland 1985, Ahlblom et al. 1986, Grong 1988). The mechanism of embrittlement is believed to be associated with strain age-hardening. This, combined with solid-solution hardening causes an increase in the yield stress of the weld without modifying the microstructure causing a decrease in the toughness (Bhadeshia and Sevensson 1993). A detrimental influence was calculated and shown in the sensitivity analysis of the neural network model (Figure 9.5), consistent with these other research findings.

9.6.2 Microstructure

Beside test temperature, the sensitivity analysis of the neural network model (Figure 9.5) shows that the second most significant factor is the volume fraction of acicular ferrite (AF). The beneficial influence of increasing volume fraction of AF is shown in Figure 9.12. It is apparent that AF consisting predominantly of fine, interlocking laths

of ferrite is the most desirable structure from a toughness point of view. Pargeter and Dolby (1984) reported that the lath form and the fine grain size are responsible for the good toughness. In contrast, a structure made up of large proportions of grain boundary ferrite PF(G) and ferrite with a second phase (FS) would have low toughness. French (1998) explained that AF, with its fine interlocking grains, results in more difficult cleavage crack propagation than the PF(G) and FS, which offer a larger effective grain size, and thus easier cleavage propagation. This detrimental influence of PF(G), PF(I) and FS is reflected in the sensitivity analysis of the neural network model (Figure 9.5).

It should be noted that the range of volume fractions of AF reported in Figure 9.12 is based on the data measured in the SW region (Table 5.1) and AF in the GC sub-zone is not included. However, AF formation takes up more than 50 % of the GC sub-zone and the volume fraction of GC sub-zone is typically near 20 % of the weld metal (Figures 6.1 to 6.3 and Table 6.1). Therefore, the actual overall % AF should be about 10 % larger than the values used in the neural network model.

There has been some discussion recently of the importance of reaustenitised regions in determining mechanical properties. Burget et al (1988) reported that the toughness properties are lower for solidified weld metal compared to reaustenitised regions. On the other hand, Chen et al. (1993) suggested that the weakest region for fracture would be reaustenitised structure.

The current predictions are interesting, Figure 9.13, in that a detrimental trend is found above room temperature (20 °C) and a beneficial trend is established below room temperature. The influence at room temperature is not significant. At lower temperature, it appears that the reheated microstructures become a stronger link in determining the weld metal's impact behaviour. A possible interpretation is that the

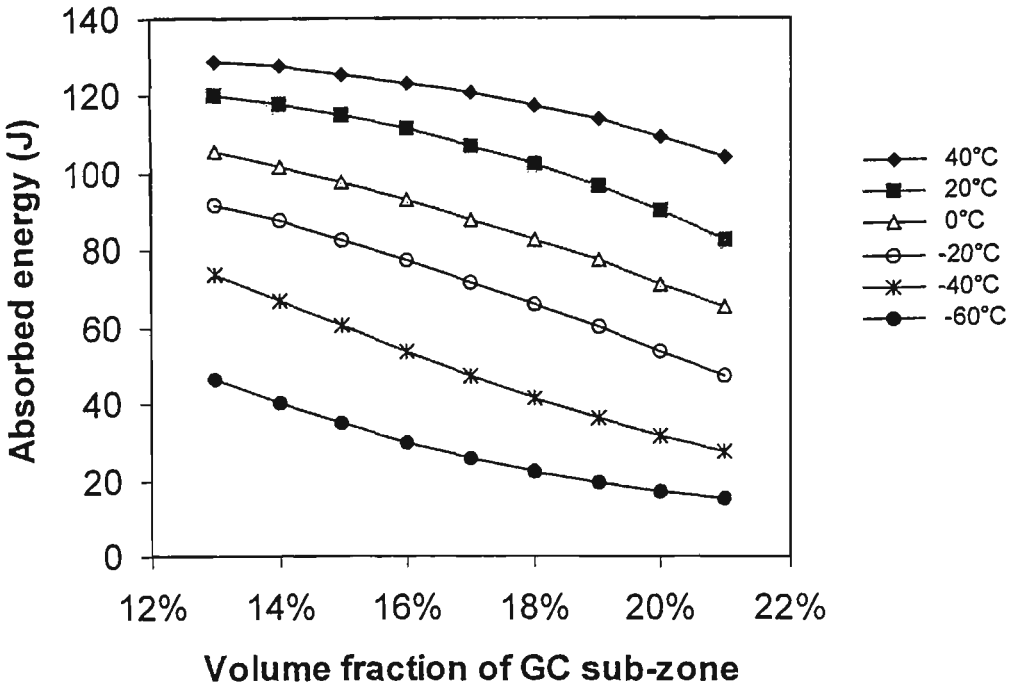

Figure 9.14: Relationship between estimated toughness and the volume fraction of grain coarsened (GC) sub-zone with different test temperatures.

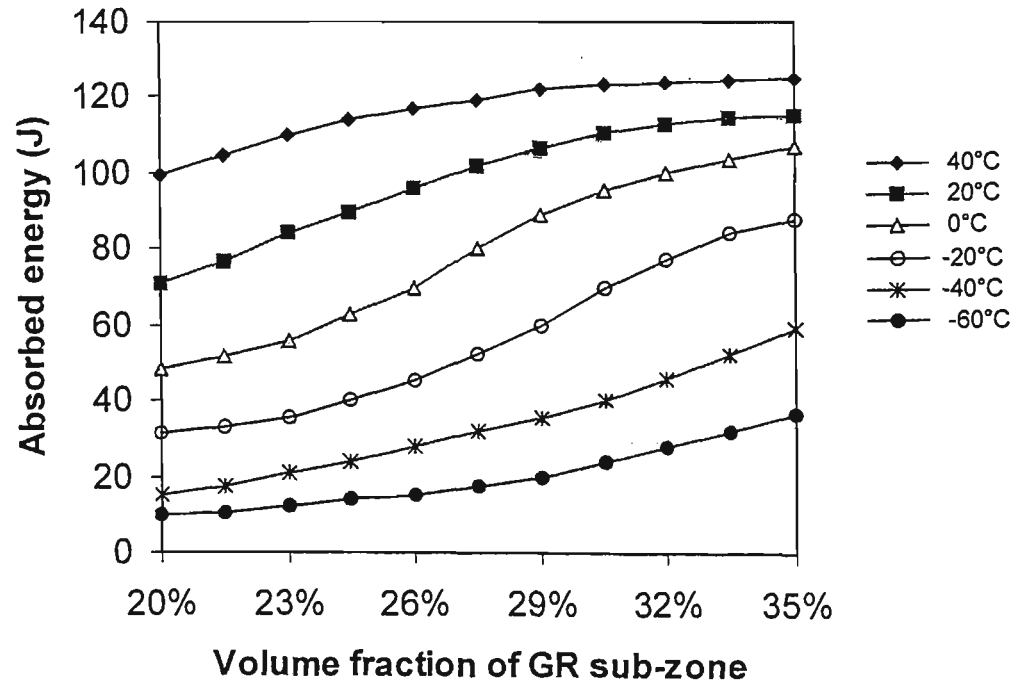

Figure 9.15: Relationship between estimated toughness and the volume fraction of grain refined (GR) sub-zone with different test temperatures.

fracture transition for reaustenitised weld metal is delayed to lower temperatures compared with the unreaustenitised regions so that absorbed energy moves to higher values with increasing volume fraction of reaustenitised region. At higher temperatures ($\geq$20°C) the effect is minimal.

Both % AF and % reaustenitised region appear to favour increased toughness. However, these two microstructural factors are competitive in that the higher the % reaustenitised the smaller will be the % AF. Some optimum combination may therefore produce maximum toughness.

It should be noted that Figure 9.5 indicate that whereas the volume fraction of reheated region has a favourable effect on toughness, the volume fraction of double-reheated region has a strong negative effect. This latter result is probably biased by the fact that the weave welds which showed no double reheated region, had relatively high toughness values.

The interactivity among the proportions of each HAZ sub-zone (GC, GR and IC) in the reheated region also contribute to the effect of the reheated region on toughness. The estimated toughness also shows large influence from the sub-zones of reheated regions. Figure 9.14, Figure 9.15 and the sensitivity analysis of the neural network model (Figure 9.5) show that the proportion of GC sub-zone has a large harmful effect while the GR and IC sub-zones have beneficial effects. The GC sub-zone consists of similar constituents to the solidified weld metal (SW), ie PF(G), FS and AF. The resistance to cleavage crack propagation offered by this sub-zone should be similar to, or higher than that offered by SW region since propagating cracks will at least as frequently encounter grain boundaries (French 1998). In contrast, the GR sub-zone will almost always exhibit a satisfactory low-temperature toughness (Grong and Akselsen 1986). The GR sub-zone is highly resistant to cleavage crack propagation, because this sub-zone

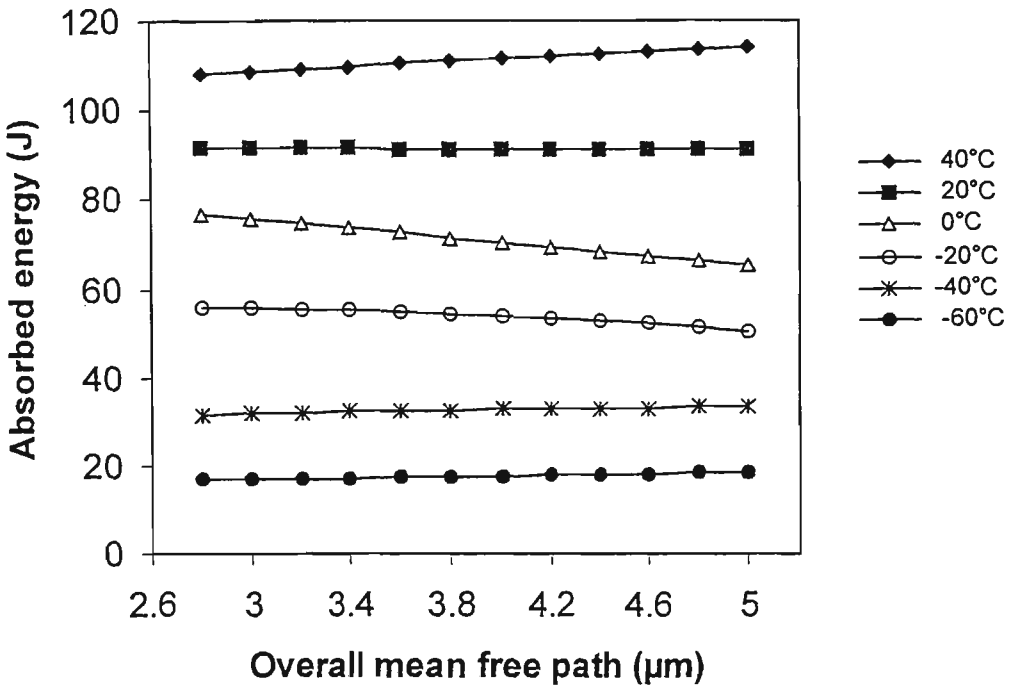

Figure 9.16: Relationship between estimated toughness and overall mean free path with different test temperatures.

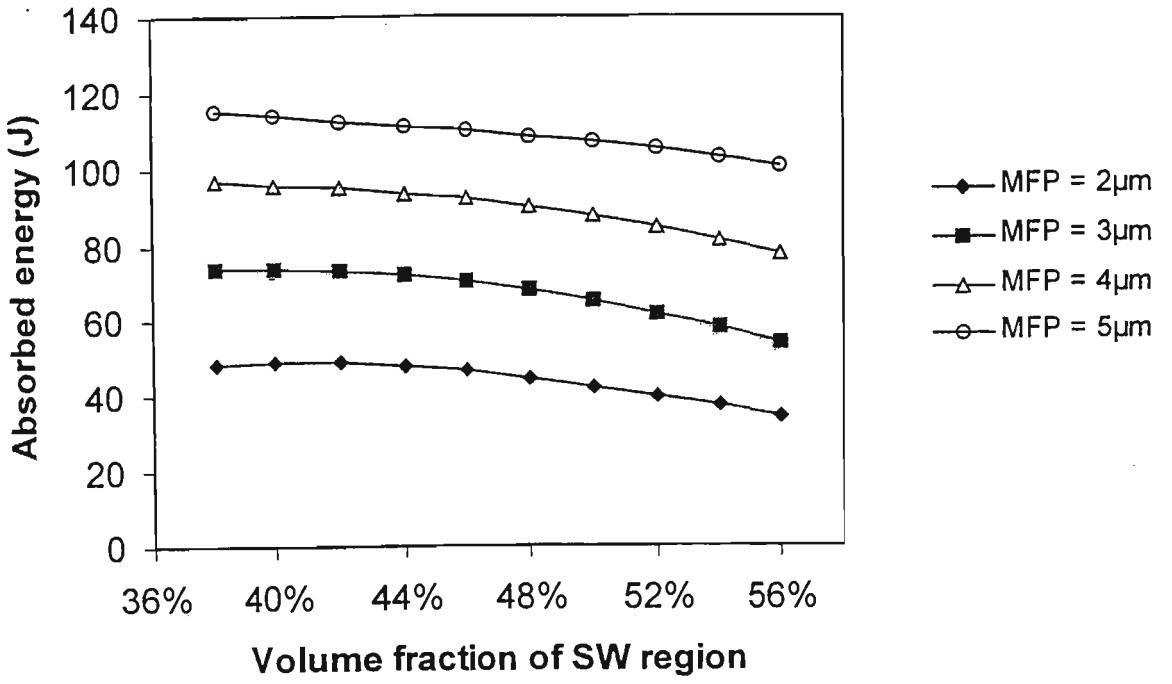

Figure 9.17: Relationship between estimated toughness and the volume fraction of solidified weld metal (SW) with different values of mean free path (MFP) at 0°C.

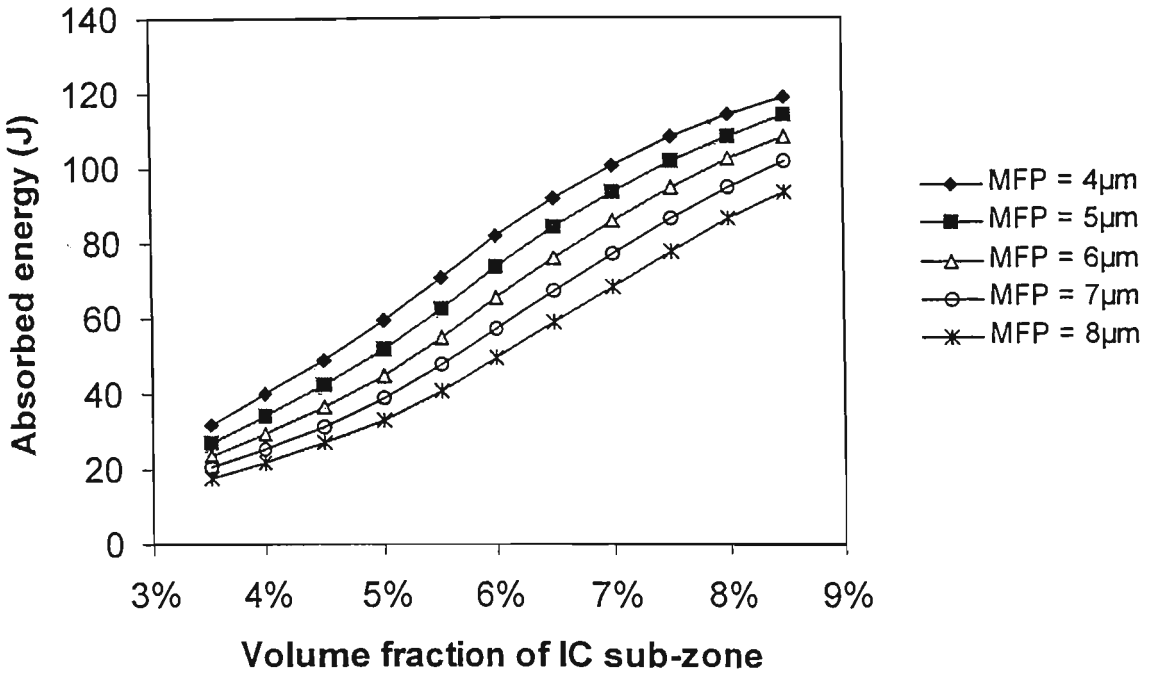

Figure 9.18: Relationship between estimated toughness and the volume fraction of intercritical (IC) sub-zone with different values of mean mean free path (MFP) at 0°C.

consists of characteristic fine polygonal grains separated by high angle boundaries, in which the thermal cycles are only sufficient to recrystallise the austenite to subsequently form a fine equiaxed ferritic structure (French 1998).

The relationship between overall mean free path ($\bar{L}_o^w$) and estimated toughness of the current neural network model is shown in Figure 9.16. Like prior experimental results (Figure 8.6), this figure shows a very small correlation with toughness. The sensitivity analysis of the neural network model (Figure 9.5) also demonstrated that the influence of mean free path is via each sub-zone, particularly for the SW region and the IC sub-zone, in that $\bar{L}_{SW}$ has a large beneficial effect and $\bar{L}_{IC}$ has a large detrimental effect. Munning Schmidt-Van Derr Burg et al. (1985), and Svensson and Gretoft (1990) reported that a fine microstructure may not always be beneficial to weld metal toughness. Support for this hypothesis is also shown in Figures 9.17 and 9.18. Figure 9.17 demonstrates that although increasing the volume fraction of SW region slightly decreases the predicted toughness, an increase in $\bar{L}_{SW}$ at a constant volume fraction of SW may actually give a better toughness. A possible explanation is that despite minor microstructural coarsening (increased $\bar{L}_{SW}$) the decrease in hardness of the weld metal may have a counteractive beneficial effect on toughness. In contrast, Figure 9.18 shows that increasing $\bar{L}_{IC}$ may have a detrimental influence, although increasing the volume fraction of IC sub-zone overall is beneficial to toughness. This result is surprising since MA islands present in the IC sub-zone are generally considered to produce local embrittlement. However, CTOD testing is used to detect this embrittlement and the Charpy testing used in this work may be insensitive to this effect, particularly since the IC sub-zone is small. The positive effect of increasing volume fraction of IC sub-zone shown by the neural network analysis may be due to a complementary effect of another variable, such as decreasing hardness.

9.6.3 Non-metallic inclusions

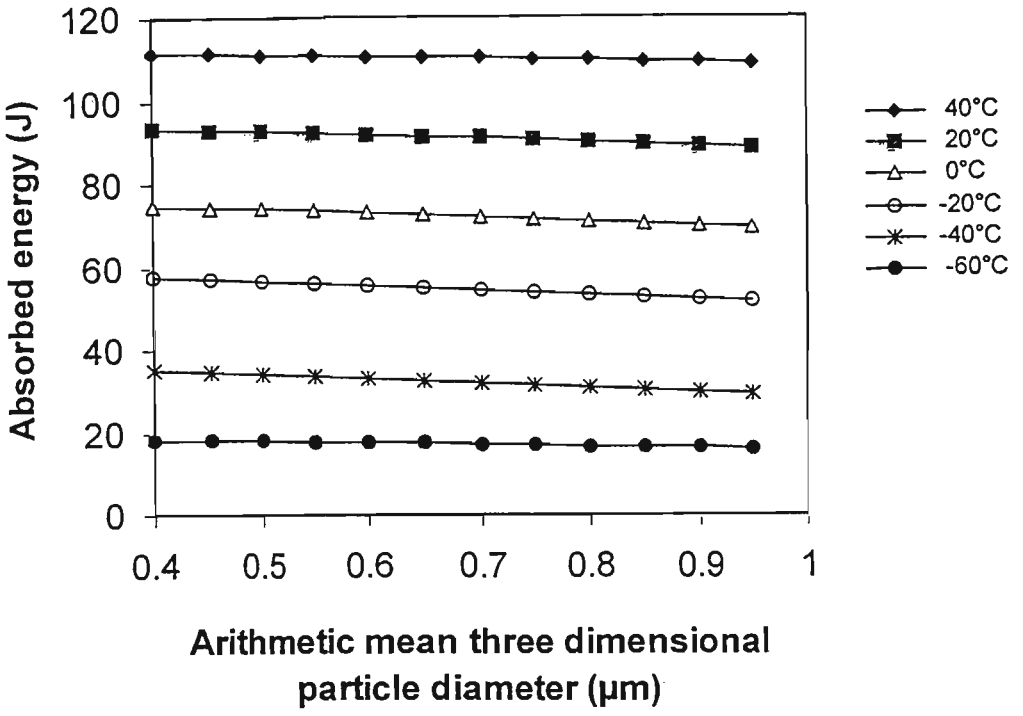

Figure 9.19: Relationship between estimated toughness and arithmetic mean three dimensional particle diameter with different test temperatures.

Non-metallic inclusions are generally not homogeneous and can consist of mixtures of both glassy and crystalline phases. Inclusions in structural steel welds commonly contain oxides of manganese, silicon, aluminium and titanium as well as sulphides of manganese and possibly copper. A high density of relatively small inclusions are known to favour AF formation (Liu and Olson 1986) and significant numbers of inclusions larger than about 1 μm directly influence cleavage fracture resistance because these inclusions can act as initiation points for cleavage cracks. However, inclusion size is not necessarily the only factor (French 1998).

While it is obvious that non-metallic inclusions have some influence on microstructural development, it should also be noted that they might have a direct influence on toughness, especially in the upper shelf region, because of the role they play in the micro-mechanisms of ductile fracture. Ductile fracture is controlled by the nucleation, growth and coalescence of voids around non-metallic inclusions. The effect of the inclusions on transition temperatures is not clear, though it has been reported that they might have a role in nucleating cleavage cracks (Tweed and Knott 1982).

The current results indicate only a small direct influence of the characteristic parameters of the non-metallic inclusions on toughness (Figure 9.5). The relationship between estimated toughness and arithmetic mean three dimensional particle diameter of the current neural network model is shown in Figure 9.19. This figure shows a very small correlation with toughness and the other characteristic factors of non-metallic inclusions give similar results. However, it should be remembered that the significant influence of non-metallic inclusions is to modify the nucleation and growth structures, particularly AF, which have been identified by the current model as very important variables in determining toughness. More detailed study of the effect of non-metallic inclusions on the nucleation of the microconstituents is needed in order to develop a clearer understanding of their indirect influence on impact toughness.

9.7 Neural Predict Analysis of Welding Conditions

Changing an input factor in the neural network model will result in a change in predicted impact toughness. Some changes are beneficial and some are detrimental. The following discussion involves the original welding conditions e.g. consumable, heat input, shielding gas, welding technique and welding position to see how they influence impact toughness through changes in chemical composition, microstructure and non-metallic inclusion characteristics. Then finally, these concepts are used to predict how an increased toughness can be obtained.

9.7.1 Training of Predict Model

To achieve this aim many individual models were trained by using the Neural Predict software package, referred to in this thesis as the "Predict Model", which involves welding conditions as input variables and individual chemical compositions, microstructures and toughness as output variables for each model.

The Neural Predict software package uses two types of learning rules: an adaptive gradient learning rule which is a form of back-propagation and is widely applicable, and a Kalman learning rule which is applicable to regression type problems. In the present cases the adaptive gradient learning rule was selected. Neural Predict software uses a constructive method for determining a suitable number of hidden nodes. This constructive method is referred to as "Cascade Learning". This method is characterised by the following features (NeuralWorks Predict 1996):

1. Hidden PEs are added one or a few at a time.

2. New hidden PEs have connections from both the input buffer and the previously established hidden nodes.

3. Construction is stopped when performance on an independent test set shows no further improvement.

It is also common for Cascade Learning architectures to have direct connections from the input buffer to the output nodes. By using these concepts, Predict software specifies a list of five transfer functions (linear, sigmoid, hyperbolic tangent, gaussian and sine) to test and create a hidden node. When the end of the list is reached, training cycles back to the beginning. It continues this process until all of the hidden node have been trained using the selected transfer functions.

The input variables for the Predict Model were consumable type, heat input, shielding gas, welding technique and welding position. Table 4.4 shows all the welding conditions which have been involved in the models and most of them are non-quantitative. There are several methods for handling non-quantitative data such as continuous encoding, binary encoding, and one-of-N coding. In the present case, a linear or continuous encoding was used to simply scale the raw data into the range 0 to +1 and to accord with other numerical input variables such as heat input and shielding gas. The value of impact toughness of room temperature (20 °C) was selected to train the Predict Model. All the information for 17 samples (Table 4.4) has been involved in the data base. 75% of the data base was selected randomly as a training data set to fit the parameters of the model. The remaining 25% of the data base was held back to work as a testing data set to measure how well the model interpolates. It is used as part of the model building process to prevent overfitting.

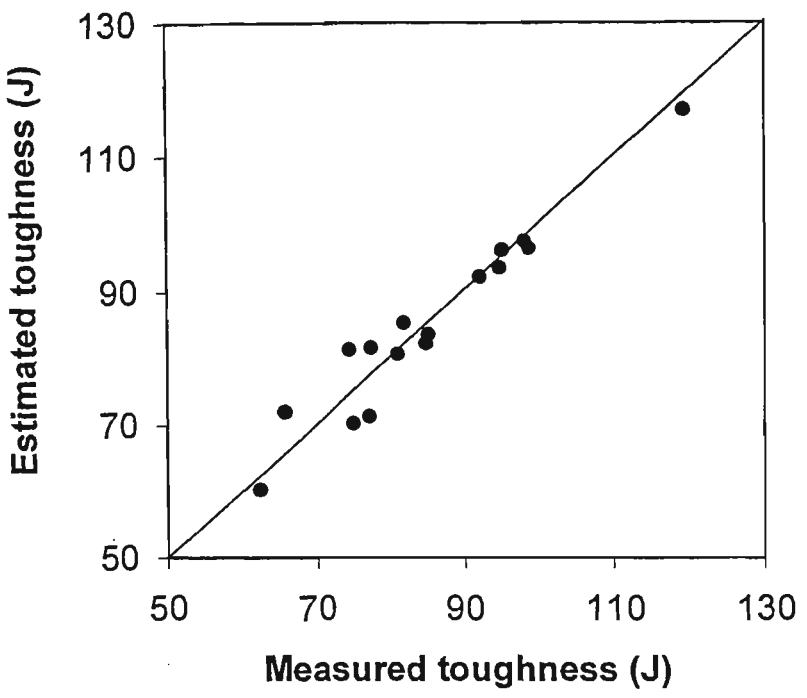

Figure 9.20: Comparison of estimated and measured toughness for the data base of current Predict model. Both training and testing data are included.

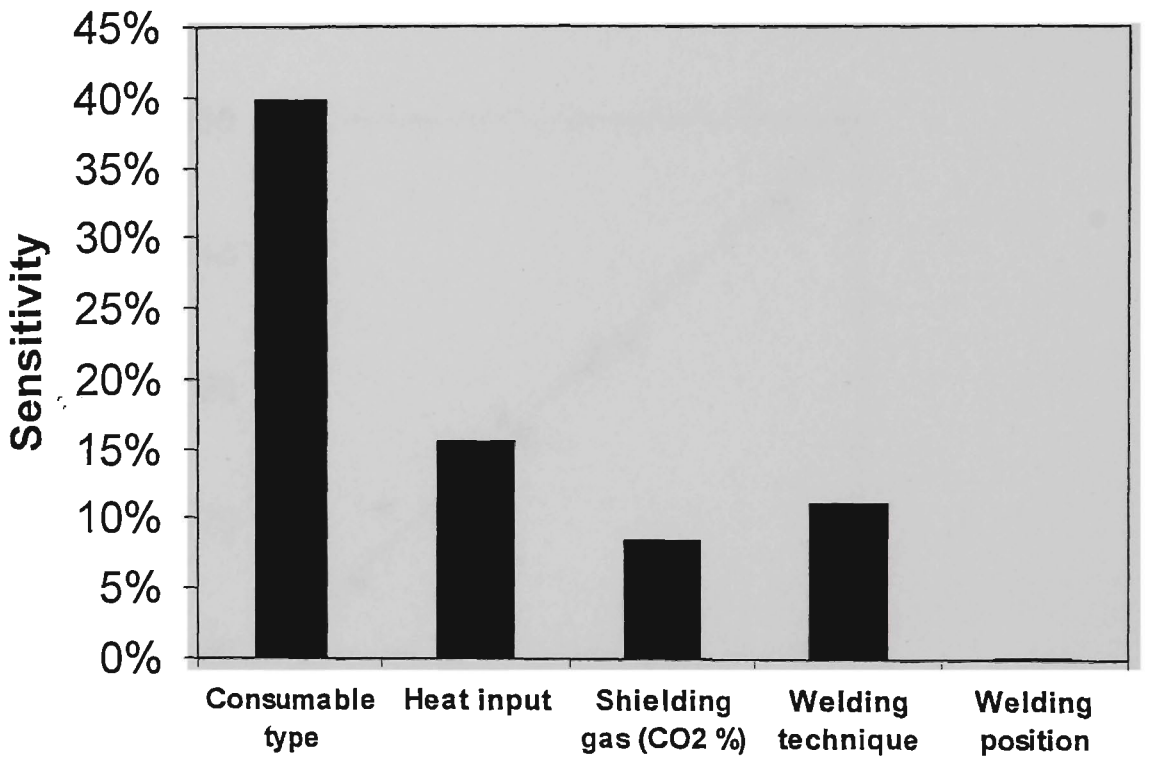

Figure 9.21: Sensitivity of welding variables calculated by the Predict Model for toughness.

9.7.2 Neural Predict analysis

The RMS errors for the training data set and the testing data set are shown in Table 9.2. Both results for RMS errors show this network has good accuracy. The level of agreement for the data base is shown in Figure 9.20. Good predictions occur for both the training and testing data.

Table 9.2: RMS error for the current Predict Model.

Data	RMS Error
Training Data Set	0.034
Testing Data Set	0.037

The sensitivity of each welding condition on toughness is shown in Figure 9.21. This sensitivity analysis shows that consumable type has a very large influence on impact toughness. Heat input, CO_2 shielding gas and welding technique have a certain amount of influence while only a very small influence was attributed to the change of welding position.

9.8 Influences of Welding Conditions

9.8.1 Consumable type

As shown in the sensitivity analysis of the Predict Model (Figure 9.21), of all the welding conditions, the consumable type is considered to be the most important in respect of toughness. Figure 9.5 provides a good reference for choosing the consumable

type such as higher Mn and B contents which may result in improved toughness. Lower P and S contents may also have the same effect.

Table 9.3 shows the predicted toughness with some predicted weld metal chemical contents and microstructures for the three different consumables. Beside consumable type, the other welding conditions remained unchanged in this prediction: the average welding conditions were 1.8 kJ/mm of heat input, 25% CO_2 in shielding gas, stringer welding technique and horizontal welding position and all the results are based on a test temperature of 20 °C.

Table 9.3: Predicted toughness and corresponding compositional and microstructural factors for the different consumables.

Consumable Types	RB Wire	MC Wire	R Wire
Toughness (J)	83	80	84.5
Manganese (wt %)	1.12	1.48	1.34
Phosphorus (wt %)	0.0146	0.0136	0.0129
Boron (wt %)	0.00774	0.0001	0.0001
Oxygen (wt %)	0.071	0.119	0.074
Volume Fraction of Reaustenitised Region (%)	51.01	48.18	47.38
Volume Fraction of Double-reheated Zone (%)	13.13	13.13	13.13
$\overline{L}_{sw}$ (μm)	3.85	3.85	3.85
$\overline{L}_{(IC)}$ (μm)	6.28	4.99	5.59
Overall Volume Fraction of AF (%)	28.86	25.84	19.58
Volume Fraction of GC Sub-zone (%)	18.60	17.19	16.94
Volume Fraction of IC Sub-zone (%)	5.87	4.21	5.77

This table shows that although boron content, proportion of AF and reaustenitised region, which are beneficial to impact toughness, are higher in RB wire welds, the toughness for RB wire welds was not generally superior for the selected welding conditions. This prediction arises because of the detrimental influences of some other factors such as lower manganese content and higher phosphorus content, MFP of IC sub-zone and volume fraction of GC sub-zone.

9.8.2 Heat input

Heat input has a significant effect on toughness according to the sensitivity of Predict Model (Figure 9.21). The effect of heat input on toughness depends on the cooling rate that is produced. Increasing heat input may generally decrease the cooling rate and can prevent the formation of susceptible microstructures containing low temperature transformation products. Thus a high heat input can lead to reduction in susceptibility to cold cracking. On the other hand, very slow cooling rate will result in a longer time spent above the grain coarsening temperature, leading to a large grain coarsened zone in the HAZ and a coarse low toughness transformed structure. It is therefore necessary to seek a heat input that gives the optimum combination of grain size and cooling rate.

According to the prediction of Predict Model, the optimum heat input for each consumable type will vary depending on the case. There is no generalized rule to specify the optimum heat input if different wires are used for fabrication because heat input is highly dependent on the consumable types. Therefore, an optimum heat input for a specific process and consumable type is needed in order to obtain a better impact property. In the present analysis, increasing heat input can potentially result in better toughness for the R and MC wires, but for the RB wire the optimum value occurred at lower heat inputs.

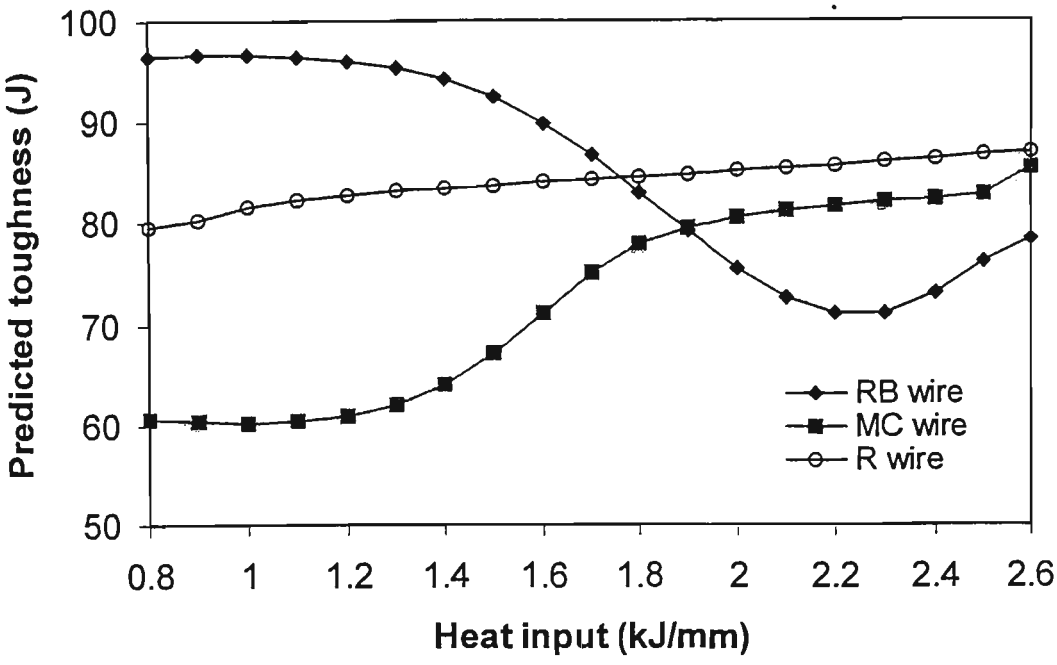

Figure 9.22: The relationship between predicted toughness and heat input for the different consumable types.

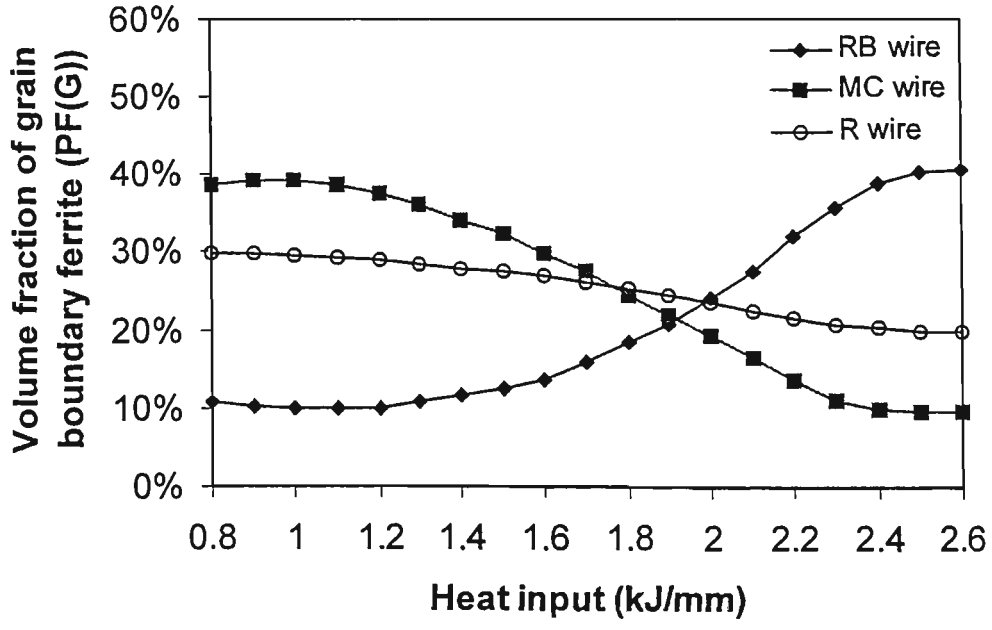

Figure 9.23: The relationship between volume fraction of grain boundary ferrite (PF(G)) and heat input for the different consumable types.

Through the Predict Model, the optimum heat inputs for the three experimental consumable types were predicted based the test temperature of 20 °C, 25% CO_2 in shielding gas, stringer welding technique and flat welding position. The estimated results are shown in Figure 9.22. Better toughness is achieved at a heat input of 2.6 kJ/mm for the metal-cored (MC) and rutile flux-cored (R) wires. However, for B containing rutile flux-cored (RB) wire, the best toughness occurs in the range 0.8 - 1.2 kJ/mm and this is consistent with the suggestion reported by Schumann and French (1995), that the heat input should be limited for the B containing rutile flux-cored (RB) wire. In addition, Grong (1994) stated that embrittlement can normally be avoided by decreasing the cooling rate, but there is an exception for boron-containing weld metals.

According to the experimental results of Chapter 6, an increase in heat input had a limited effect on the percentage of reaustenitised region. However, it led to a large decrease in volume fraction of GC sub-zone which has a large detrimental influence on toughness according to the neural network model. In contrast, the increase in heat input also led to a decrease in the volume fraction of IC sub-zone which is beneficial to toughness. Increasing heat input also coarsened the microstructure considerably. According the discussion in Chapter 8, this may cause $\bar{L}_{SW}$ and $\bar{L}_{IC}$ to increase, although the rate of increase also depends on the consumable type. Increasing $\bar{L}_{SW}$ is predicted to have a large beneficial effect and $\bar{L}_{IC}$ has a large harmful effect on toughness according to the neural network model.

A tendency existed for composition changes with increasing heat input, such as an increase in phosphorus and boron. Like microstructure, some of these change are beneficial and some are harmful to toughness, as indicated by the sensitivity analysis of the neural network model (Figure 9.5).

From the above discussion on the influence of heat input, it can be concluded that there is no certainty that a decrease or increase in heat input will lead to a better (or worse) weld in terms of toughness because of contradictory effects such as chemical content, microstructure and non-metallic inclusions and their interactivity. Some of the factors may be increased by higher heat input and some of them may be decreased and different trends may occur in different consumable types. However, the volume fraction of grain boundary ferrite (PF(G)) seems to contribute more to toughness than other factors on changing the heat input. The relationship between estimated proportion of PF(G) and heat input is shown in Figure 9.23. An increased trend is found for RB wire with increasing heat input while a decreased trend is evident for MC wire and a slight decrease for R wire. The decrease in predicted PF(G) with increasing heat input is consistent with the data in Table 5.1, but it is not evident why PF(G) should decrease for a slower cooling rate. An increase in the proportion of PF(G) has been reported to be detrimental to toughness because these structures provide preferential easy crack propagation paths during weld metal cleavage fracture (French 1998, Abson and Pargeter 1986, Grong and Matlock 1986, Farrar and Harrison 1987). The corresponding trends in toughness with heat input for the three consumables (Figure 9.22) are consistent with the trends in PF(G) in Figure 9.23 in that increasing PF(G) is consistent with decreasing toughness. Therefore, the different trends of toughness with changing heat input in the present research are likely to be caused mainly on the different trends in proportion of PF(G).

9.8.3 Volume fraction of CO_2 in shielding gas

Shielding gases play an important role in the arc welding process. They have the dual purpose of protecting the arc and weld pool from contamination by air and providing a

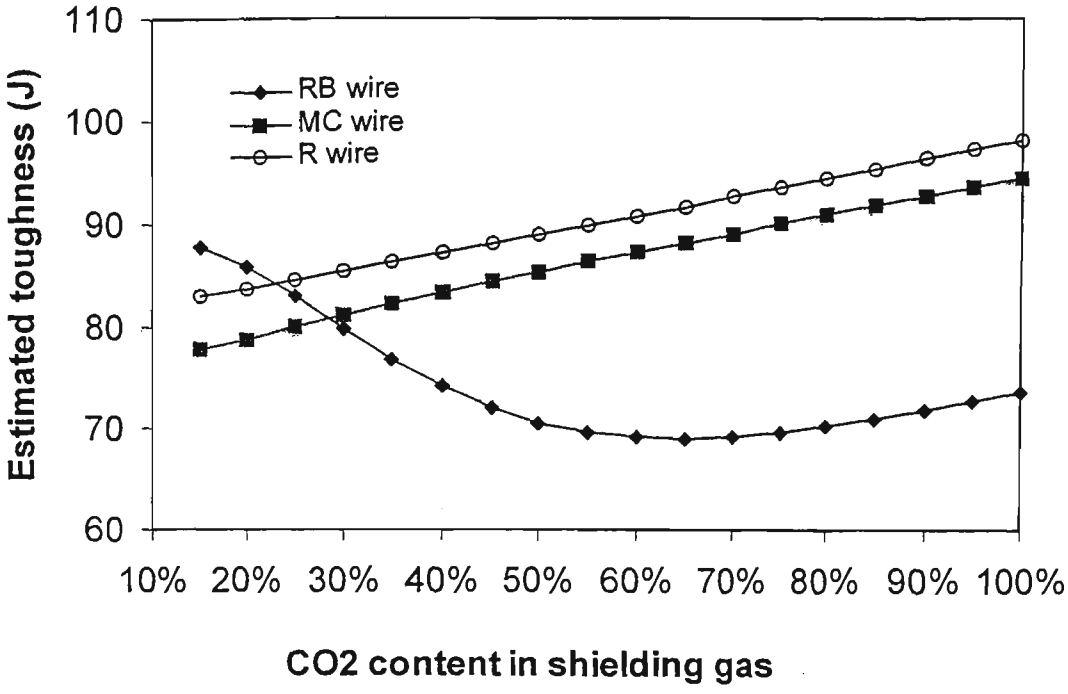

Figure 9.24: The relationship between predicted toughness and CO_2 content in shielding gas.

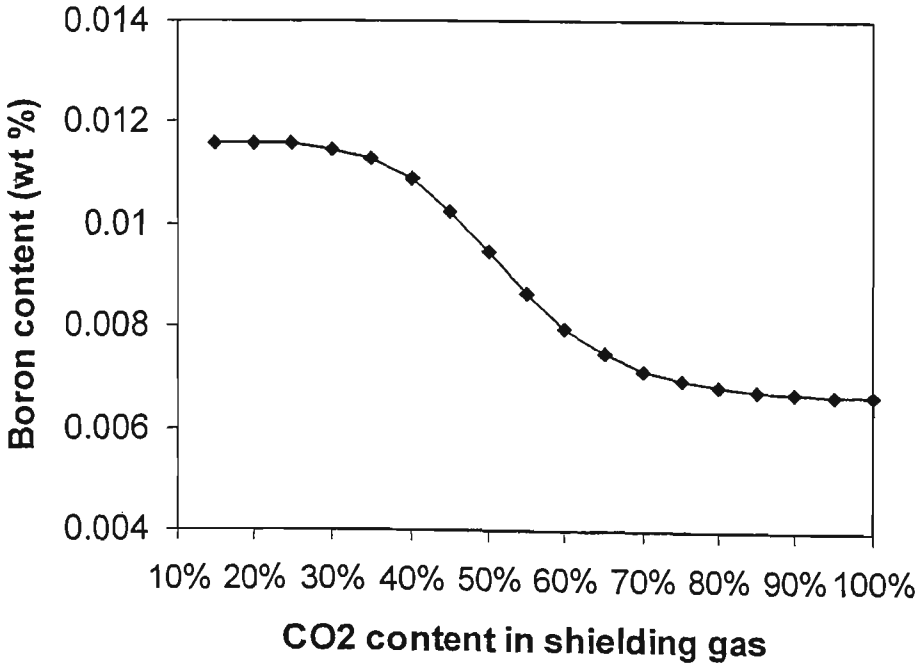

Figure 9.25: The relationship between predicted boron content and the proportion of CO_2 content in shielding gas.

suitable medium for the stable operation of a sustained low-voltage arc. The toughness of the weld is influenced by the interaction of the shielding gas with the base metal and with the filler materials.

Varying the percentage of CO_2 in the shielding gas composition affects the oxygen content of the weld metal and influences the recovery of individual elements. This effect has been verified by Grong and Christensen (1983) in a detailed study of factors controlling GMAW weld metal composition. They claimed that for a given filler metal and heat input, an increase of the CO_2 content of the shielding gas generally produced higher oxygen content in the weld metal and lowered the manganese and silicon contents. It also made the arc harsher and increased the spatter levels, the bead convexity and the weld penetration in the high current globular drop transfer range.

An increase of the CO_2 content of the shielding gas also led to a change of microstructure. According to the discussion in Chapter 6, the volume fractions of reaustenitised region and GC sub-zone were both lower. Reaustenitisation is generally beneficial and the formation of GC is harmful to toughness. According to the discussion in Chapter 8, the MFP of the SW region, and the GC, GR and IC sub-zones all became larger when CO_2 was used. Some of these factors are beneficial and some are harmful to toughness, as indicated by the sensitivity analysis of the neural network model (Figure 9.5). However, these changes are mainly because of the arc efficiency resulting from the use of CO_2 shielding gas. As reported by Grong (1994), CO_2 shielding generally gives a higher arc efficiency so that the effective heat input is higher than for welds produced by Ar gas mixtures. The relationship between predicted toughness and CO_2 content in the shielding gas is shown in Figure 9.24. For MC and R wires, an increase of the percentage of CO_2 in the shielding gas leads to better

toughness. For the RB wire, a smaller proportion of CO_2 in shielding may give a better toughness.

An increase of the CO_2 content of the shielding gas generally produced higher effective heat input. Therefore, similar trends to heat input occurred for changing CO_2 content in the shielding gas. Another possible explanation for the differing trends for the different wires is that the presence of boron in the RB wire is important to structure development and toughness. Figure 9.25 gives the relationship between boron content in the weld metal and CO_2 content in the shielding gas for RB samples. A decreased trend for boron content was shown with increasing CO_2 content in the shielding gas because of loss of boron due to oxidation.

It has been reported that increasing boron content can successfully improve the toughness of HAZ in Ti-containing steels. As discussed in Chapter 5, the addition of a combination of titanium and boron to the weld metal produces a fine acicular microstructure that displays good low temperature toughness (Chen et al. 1993). Several authors have reported that the formation of grain boundary nucleated ferrite, PF(G) and FS, can nearly be eliminated by balanced alloying with boron and titanium (Tsuboi and Terashima 1983, Mori et al. 1982, Watanabe and Kojima 1983, Kohno et al. 1982, Davis et al. 1983, Watanabe et al. 1980). The mechanism for the hardenability contribution of boron was discussed earlier and is based on the fact that boron segregates extensively to the prior austenite grain boundaries, where it suppresses the formation of grain boundary nucleated ferrite and facilitates the intragranular nucleation of AF on oxide inclusions (Widgery 1974). Therefore, different tendencies in toughness were shown with boron containing wire and non-boron containing wires with increasing CO_2 content in shielding gas (Figure 9.24).

9.8.4 Welding techniques and welding positions

The sensitivity of the Predict Model (Figure 9.21) shows that changing welding technique between stringer and weave might also influence the toughness. According to the current experimental results and the Predict Model, the changes are mostly through microstructure. As indicated by Schumann and French (1995) the microstructures of the welds made with the weave technique could not directly be compared with those made with the stringer technique, as the use of the weave technique changed the thermal cycle of the welds.

According to the discussion in Chapter 6, it is evident that although the volume fraction of AF is lower for weave-bead welds than stringer-bead welds, using weave-bead welding increased the volume fraction of the reaustenitised region relative to the stringer-bead welds. This increased trend is generally beneficial for toughness. Table 9.4 shows the predicted values for toughness for the three consumable types. All the predictions in Table 9.4 are based on a heat input of 1.8 kJ/mm, 25% CO_2 in shielding gas, horizontal welding position and a test temperature of 20 °C. This table shows that better impact properties are predicted by using the weave-bead welding technique. A very significant influence was shown for the RB wire.

Table 9.4: Prediction of toughness with change in welding technique.

Consumable Types	Toughness (J) (Stringer Technique)	Toughness (J) (Weave Technique)
RB Wire	82.9	115.5
MC Wire	79.9	90.5
R Wire	82.4	84.5

As indicated by Evans (1980) changing welding position from flat to vertical resulted in increases in carbon, manganese, silicon and oxygen contents in the weld metal and also reduced the volume fraction of reaustenitised region (see discussion in Chapter 6). However, these changes in chemical contents and microstructures were too small in the present case to substantially influence the toughness. Therefore, similar values of toughness are predicted by the Predict Model for the two main welding positions. The predicted results are shown in Table 9.5. All the predictions in Table 9.5 are based on a heat input of 1.8 kJ/mm, 25% CO_2 in shielding gas, stringer welding technique and a test temperature of 20 °C.

Table 9.5: Prediction of toughness with change of welding position.

Consumable Types	Toughness (J) (Flat Position)	Toughness (J) (Vertical Position)
RB Wire	82.9	82.8
MC Wire	79.9	79.7
R Wire	84.5	84.9

All three types of consumables followed the same trend that almost the same toughness values are predicted for the two welding positions. These results are also a reflection of the sensitivity analysis of the Predict Model (Figure 9.21) in that there is a very small influence on toughness.

9.9 General Discussion (How to Improve Toughness)

Assessment and understanding of the impact properties of welds is central to the avoidance of catastrophic failure of welded steel structures (French 1998). This section addresses the factors that are important to the low temperature impact properties of

steel welds with the aim of identifying these factors, clarifying their influence and giving practical guidance on how impact properties might be improved in real welding.

Figure 9.5 and Figure 9.21 both give a very clear idea on how to improve toughness for FCA weld metals. Changing each factor in the 31 input variables of the current neural network model will result in different values for toughness. Some factors are beneficial and some are detrimental. Some have a large effect and some have a small effect. However, each field of the input variables (chemical contents, microstructures and non-metallic inclusions) is essentially controlled by welding conditions such as base material, wire composition, shielding gas, heat input, welding technique and welding position. Therefore, the welding conditions are also important factors in determining impact toughness.

Figure 9.21 shows that, above all, the choice of consumable type is the most important welding condition, because it directly affects the chemical composition and indirectly affects microstructure and the non-metallic inclusions. Higher contents of manganese, silicon and boron and lower contents of sulphur and phosphorus are suggested by Figure 9.5 to be favourable trends.

Optimum heat input and shielding gas are also important in determining toughness. However, there is no single rule which can explain the trend on changing these factors. Complexity arises from the combined effect of the increase or decrease on the 31 input factors for the current neural network model. Therefore, the prediction of optimum heat input and shielding gas should be on the basis of consumable type. The use of a range of consumable types is likely to result in a more comprehensive understanding of the effect on impact properties, because of the complex interaction of the influential variables.

Changing welding technique also changed the thermal cycle of the welds, leading to a change in microstructure. The impact toughness is relatively high for all three consumable types, especially for the RB wire. Even though the use of weave-bead technique is likely to improve impact properties, inconvenience may result if the weaving technique is chosen for both automatic and manual welding and the technique is usually restricted to higher heat input welding (Evans 1980).

Heat flows during welding were different between the flat and vertical welding positions. Different weld pool shapes and sizes were noted by Evans (1980). However, the influence on chemical composition and microstructure were small in the current work and in the predictions of the Predict Model. Therefore, the influence on impact toughness was also small. In general, the choice of welding position will not affect the quality of the welds and the welding position is determined by the selection of the welding process (Welding Handbook 1983).

Neural network analysis has its own restrictions, in that any attempt to extrapolate beyond the training data range can make the prediction far less useful. For example, Evans (1978) claimed that the optimum impact properties for multipass weld metal were attained at 1.5 % manganese content. This optimum manganese content value was not included in the range of the training data set. However, an increasing trend of toughness was predicted with increasing manganese content by the current neural network model.

In order to improve the current trained models, more information about FCA welding beyond the range of the current training data range are needed. The wider the range of the training data the better the prediction of the model and the current neural network model can simply be retrained if a wider range of input variables is supplied. Therefore,

a more generalized model can be achieved if the data base is sufficient to include the practical range of input variables and all of the welding processes. In many cases, the final selection of appropriate welding conditions results from a compromise of diverging influences. By relying on this pre-assessment, welding trials can be significantly reduced.

9.10 Conclusions

1. The significant influence of chemical composition on toughness characterised by the current neural network model is summarized below. For the composition ranges investigated, the elements Mn, Si, B and O have beneficial effects whereas C, S, P, Ti, Al, Mo and N have detrimental effects.

2. The significant influence of microstructure on toughness characterised by the current neural network model is summarized below: increasing the values of $\bar{L}_{SW}$ and the volume fractions of AF, reaustenitised region and IC sub-zone have beneficial effects while increasing the values for PF(G), PF(I), FS, double-reheated sub-zones, GC sub-zone, $\bar{L}_{GC}$ and $\bar{L}_{IC}$ show detrimental effects. These trends arise because some of the microstructures provide easy paths for crack propagation and the others result in more difficult crack propagation.

3. The characteristic of the non-metallic inclusion distribution have only small direct influence on toughness according to the current neural network model. However, it should be noted that the significant influence of non-metallic inclusions is to modify the nucleation and growth structures, particularly AF, which has been identified by the current model as a very important variable in determining toughness.

4. There is no simple trend to be expected for the influence of heat input on toughness. Complexity arises from the combined effect resulting from heat input, such as changes in chemical composition and microstructure which are also highly dependent on the consumable type. Through the current Predict Model, the optimum heat input was found to occur at a higher heat input (2.6 kJ/mm) for metal-cored (MC) and rutile flux-cored (R) wires, but for B containing rutile flux-cored (RB) wire, the best toughness was achieved for the range 0.8 to 1.2 kJ/mm. These trends may be physically related to the proportion of PF(G) with varying heat input, which seems to contribute more to toughness than other microstructural factors.

5. An increase of CO_2 content in the shielding gas can lead to better toughness for metal-cored (MC) and rutile flux-cored (R) wires. However, for B containing rutile flux-cored (RB) wire, a smaller proportion of CO_2 may give a better toughness, because the CO_2 content of the shielding gas also varies the effective heat input. In addition, the boron in the RB samples shows a decreased concentration with increasing CO_2 content reducing the beneficial effect of B on AF formation. Boron indirectly affects AF formation through retarding PF(G) formation. This retardation causes the super-cooled condition intragranually and enhances AF formation.

6. Better impact properties were predicted by using a weave-bead technique than stringer-bead, particularly for B containing rutile flux-cored (RB) wire. The changes are mostly through microstructure such as a greater proportion of reaustenitised region, which is generally characterised to be beneficial for toughness.

7. Changing welding position from horizontal to vertical might influence the heat flow, but the changes in the chemical composition and microstructure were too small to influence the toughness. Therefore, similar values of toughness for the two main welding positions are predicted by the current Predict Model.

8. In order to improve the current trained models, more information about FCA welding beyond the range of the current training data range is needed. A more generalized model can be achieved if a wider range of input variables is supplied. In many cases, the final selection of appropriate welding conditions results from a compromise of diverging influences. By relying on this pre-assessment, welding trials can be significantly reduced.

9. Although the neural network approach can be valuable, its limitations should be appreciated. For example, the adverse effect on toughness predicted for Ti content should be viewed with caution since the chemical reactions of Ti in formation of nitride and oxide are not taken into account. Further, the adverse effect of double-reheated sub-zones on toughness is unrealistic since the prediction is biased by the absence of double-reheated sub-zone in the weave welds.

CHAPTER 10

OVERALL CONCLUSIONS

Five different aspects of the research program are presented in Chapters 5 to 9 and have been discussed and relevant conclusions have been drawn. Chapter 10 summarises the main overall conclusions of this study of factors affecting the mechanical properties, especially the toughness, of three types of flux-cored arc welds.

1. All three groups of test plates followed essentially the same trend: the mean free path values for each sub-zone and the overall mean free path ($\bar{L}_o^w$) increased linearly with increasing heat input due to the decrease in cooling rate which allowed transformation of austenite at higher temperatures to coarser ferritic products.

2. Weld metal tensile and yield strengths for all three wires decreased by approximately 70 to 80 MPa when heat input was increased from 1 to 2.5 kJ/mm. The decreases in tensile strength properties with heat input correlate well with the increase in the overall mean path ($\bar{L}_o^w$) of the weld metal microstructure which can be expected at the lower cooling rates associated with higher heat inputs.

3. All three groups of test plates followed essentially the same trend that the volume fraction of reaustenitised region was reduced by using of 100 % CO_2 as the shielding gas because the increased arc efficiency reduced the cooling rate compared to Ar CO_2 mixtures used at the same nominal heat input.

4. The volume fraction of reaustenitised region was also decreased by changing from flat to vertical welding. In contrast, using weave welding increased the volume fraction of the reaustenitised region relative to the stringer welding technique.

5. The volume fraction of grain coarsened (GC) sub-zone in the HAZ decreased linearly with increasing heat input while the volume fractions of grain refined (GR)

and intercritical (IC) sub-zone in the HAZ increased linearly with increasing heat input.

6. The total volume fraction of the double-reheated zone was largely unaffected by heat input, welding position, shielding gas, composition and the changes in consumable types examined in this investigation.

7. Examination of the microstructures of the double-reheated sub-zones did not reveal marked differences from reheated zones experiencing a single thermal cycle equivalent to the second cycle of the double-reheated sub-zone, except for the GC-IC and GR-IC sub-zones. It is inferred that the second thermal cycle dominates the final microstructure.

8. The hardness of each sub-zone in the weld metal and the overall mean hardness ($\overline{H}$) decreased with increasing heat input and was reduced for 100% CO2 shielding gas compared to an Ar rich gas mixture. This decrease is due to an increase in structural coarsening as reflected by increasing values of overall mean free path $\overline{L}_o^w$.

9. Mean free path analysis showed that MFP in the GC sub-zone of reheated weld metal was actually much lower than in GR sub-zone. So although the prior γ grain size is much coarser the efficiency of intragranular nucleation of AF results in an overall finer microstructure than the grain refined sub-zone where grain boundary nucleation of ferrite dominates.

10. The influences of chemical composition, microstructure and non-metallic inclusions on toughness characterised by the current neural network model are summarised

below: Mn, Si, B and O have beneficial effects; whereas C, S, P, Ti, Al, Mo and N have detrimental effects. In addition, increased proportions of AF, reaustenitised region, IC sub-zone and higher $\overline{L}_{SW}$ values are predicted to have beneficial effects; whereas increasing proportions of PF(G), PF(I), FS, double-reheated zone, GC sub-zone, and increased values of $\overline{L}_{GC}$ and $\overline{L}_{IC}$ have detrimental effects. The characteristics of the non-metallic inclusion distribution had only a small direct influence on toughness according to the neural network model.

11. The consumable type has a strong influence on the welding variables and the effect of the welding variables on toughness is complex and determined by their combined effect on chemical composition and microstructure. Through the current Predict Model, the optimum heat input was found to occur at higher heat input (2.6 kJ/mm) for metal-cored (MC) and rutile flux-cored (R) wires. However, for B containing rutile flux-cored (RB) wire, the best toughness was achieved in the range 0.8 to 1.2 kJ/mm.

12. According to the prediction of the Predict Model, an increase of CO2 content in shielding gas may lead to better toughness for MC and R wires, but for the RB wire a smaller proportion of CO2 may give a better toughness. This prediction is consistent with both the higher effective arc efficiency of CO2 shielding gas and the counteractive loss of B by oxidation in the case of the RB welds. Better impact properties were also predicted for the use of weave-bead technique rather than stringer-bead for all three wires; but changing welding position from flat to vertical did not affect the toughness of the welds produced by the three wires.

13. Although the neural network approach can be valuable, some unrealistic results may occur after training, such as the adverse effects on toughness of Ti content and double-reheated regions predicted by the current neural network model. However, appropriate physical factors can be considered and the input data can be preprocessed by using physical fundamentals before processing, training and prediction. Since the problem of toughness is still not solvable by a purely numerical model because of gaps in physical understanding, the neural network approach can provide a better way to link the various interactions of input factors, as well as predicting the multiple effects of these factors

14. Analysis of the relationship between toughness and type of FCAW process indicated a strong dependence on consumable selection and sensitivity to operating variables (heat input, shielding gas, stringer/weave welding) in order to optimise the toughness for a selected consumable. In terms of compositional and microstructural factors which are the result of the selected process and operating conditions, toughness is predicted to respond most favourably to increasing % AF and to a lesser extent % reaustenitised region. Elements which exert a favourable effect on toughness are Mn, Si, O and B. For tensile properties the overall MFP correlates well with the tensile strength of welds and therefore welding processes which produce highly refined microstructures should increase the weld strength.

REFERENCES

Abson D. J. and Dolby R. E. (1978). Welding Institute Research Bulletin, July, 202.

Abson D. J., Dolby R. E. and Hart P. H. M. (1978). in Proc. of Int. Conf., Trends in Steels and Consumables for Welding, London, England, 75-101.

Abson D. J. and Pargeter R. J. (1986). International Metals Reviews, 31, 141.

Ahlbom B. (1984). IIW Doc. IX - 1322-84.

Ahlblom B. et al. (1986). in Proc. Conf. Residuals and Impurities in Steels, Abington, The Welding Institute, paper 49.

Ahmed N. U. and Yellup J. .M. (1988). Materials Forum, 12, 62.

Akselsen O. M., Solberg J. K. and Grong O. (1988). Scandinavian Journal of Metallurgy, 17 (5), 194.

Akselsen O. M. and Grong O. (1992). Mater. Sci. Eng., A159, 187-192.

Alberry P. J., Brunnstrom R. R. L. and Jones K. E. (1983). Metals Technology, 10 (1), 28.

Alberry P. J., Chew B. and Jones W. K. C. (1977). Metals Technology, 4 (6), 317.

Aleksander I. and Morton H. (1995). An Introduction to Neural Computing, International Thomson Computer Press (ITP), London, 134-149.

American Welding Society, ANSI/AWS A5.20 (1979). Specification for Carbon Steel Electrodes for Flux Cored Arc Welding.

Amano K. et al. (1986). in Proc. 5th Int. Symp. On Offshore Mechanics and Arctic Engineering (OMAE), Tokyo, vol. 2, 338.

Anderson J. A. (1972). Mathematical Biosciences, vol. 14, 197-200.

Apps R. L. and Andrade A.M.V.P.D. (1985). in Roads to Recovery, Proc. 33rd Ann. Conf. of Australian Welding Institute, AWI, Brisbane, 327.

Ashby M. F. and Ebeling R. (1966). Trans. TMS-AIME, 236, 1396-1404.

ASTM Standards, E23-96 (1996). Standard Test Methods for Notched Bar Impact Testing of Metallic Materials, ASTM Committee, 137-156.

Australian Standard, AS 1391, Methods for Tensile Testing of Metals, Standards Association of Australia.

Australian Standard, AS 1544.2 (1989). Methods for Impact Tests on Metals, Part 2, Charpy V-Notch, Standards Association of Australia.

Australian Standard, AS 1815, Method for Rockwell Hardness Test, Standards Association of Australia.

Australian Standard, AS 1816, Method for Brinell Hardness Test, Standards Association of Australia.

Australian Standard, AS 1817, Method for Vickers Hardness Test, Standards Association of Australia.

Australian Standard, AS 2203-1 (1990). Cored Electrodes for Arc Welding Part 1 Ferritic Steel Electrodes, Standards Association of Australia.

Australian Standard, AS 2205, Method for Destructive Testing of Welds in Metals, Standards Association of Australia.

Australian Standard AS 3678 (1990). Structural Steel-hot-rolled Plates, Floor Plates and Slats, Standards Association of Australia.

Bailey N. (1972). Welding Journal Research Supplement, 51(4), 169s.

Bain E. C. and Paxton W. H. (1961). Alloying Elements in Steel, 2nd edition, ASM.

Batchelor B. G. (1974). Practical Approach to Pattern Recognition, Plenum Press, New York.

Baumgardt H. and Strassburger C. (1985). in Thyssen Techn. Berichte H. 1, 42-49.

Beckert M and Hoz R. (1973). Schwesis Technik ,Berlin, (8) 334, 23

Bhadeshia H. K. D. H., Sevensson L. -E. and Gretoft B. (1985). Acta Metalllurgica, 33(7), 1271-1283.

Bhadeshia H. K. D. H., Sevensson L. -E. and Gretoft B. (1986). In Proc. of the 3rd Int. Conf. Welding and Performance of Pipelines, London, 12-21.

Bhadeshia H. K. D. H. and Sevensson L. -E. (1989a). Effect of Alloying Additions on Microstructure and Properties of Vertical-up MMA Welds. 1. Method of Theoretical Assessment, Joining and Materials, 182R-187R.

Bhadeshia H. K. D. H. and Sevensson L. -E. (1989b). Effect of Alloying Additions on Microstructure and Properties of Vertical-up MMA Welds. 2. Results and discussion, Joining and Materials, 236R-238R.

Bhadeshia H. K. D. H. and Svensson L. -E. (1993). in Mathematical Modelling of Weld Phenomena, eds H. Cerjak and K. E. Easterling, The Institute of Materials, London, 109-180.

Bhadeshia H. K. D. H., Mackay D. J. C. and Svensson L. -E. (1995). Materials Science and Technology, 11, 1046.

Bhatti A. R. et al. (1984). Welding Journal, 63 (7), 224s-230s.

Blodgett O. W. (1979). Welding Journal 58, 12, 26-42.

Boothby P. J. (1985). Metal Construction,17 (6), 363-366.

Bowers R. J. and Letts M. W. (1996). IIW Doc. IX-1865-96.

British Standard 5135 (1974). Specification for Metal Arc Welding of Carbon and Carbon-Manganese Steels.

Bryhan A. J. (1981). Welding Journal Research Supplement, 50 (9), 169-s.

Buchmayr B. (1990). in Proc. Int. Conf. Computer Technology in Welding, Brighton, Paper 32.

Buchmayr B. (1990). Recent Trends in Welding Science and Technology, ASM, 237-242.

Buchmayr B. (1995a). in Mathematical Modelling of Weld Phenomena 2, eds H. Cerjak and H. K. D. H. Bhadeshia, The Institute of Materials, London, 265-277.

Buchmayr B. (1995b). in Mathematical Modelling of Weld Phenomena 2, eds H. Cerjak and H. K. D. H. Bhadeshia, The Institute of Materials, London, 119-137.

Burget W. and Blauel L. G. (1988). in Proc. Int. Conf. Weld Failures, Abington, London, 501-510.

Chaillet J. et al. (1976). ASM Int. Conf. Welding of HSLA Steels.

Chen J. H., Xia T. D. and Yan C. (1993). Welding Research Supplement, 72, 19s-27s.

Chin L. L-J. (1969). Welding Journal, 48, 290s.

Clark J. N. (1985). Materials Science and Technology, 1 (12), 1069.

Cochrane R. C. and Kirkwood P. R. (1978). ibid.

Comstock G. F. (1955). Titanium in Iron and Steel, John Wiley and Sons Inc., New York.

Cool T., Bhadeshia H. K. D. H. and MacKay D. J. C. (1996). Numerical Analysis of Weldability, Cambridge.

Cun Y. L. (1988). In Artificial Neural Networks: Concepts and Theory, eds P. Mehra and B. W. Wah, IEEE Computer Society Press, CA, 331-338.

Dan T. and Gunji K. (1984). Transactions Nat. Res. Inst. for Metals (Japan), 26, 8.

Davis M. L. E., Pargeter R. J. and Baily N. (1983). Metal Constr., 15, 338-344.

Dearden J. and O'Neill H. (1940). Transactions of the Institute of Welding, 3 (10), 203.

deMeester B. (1988). Welding in the World, 26 (11/12), 308; also in IIW Doc. 1020-88 (1988).

Dennis W. H. (1963). Metallurgy of The Ferrous Metals, Sir Isaac Pitman & Sons Ltd. London.

Desforges C. D. et al. (1976). Manganese in Ferrous Metallurgy, The Manganese Centre, Paris.

DeSieno D. (1988). IEEE Int. Conf. on Neural Networks, vol. 1.

Devillers L., Marandet L., Kaplan B., Ribes A. and Riboud P. V. (1982). Fracture and the Role of Microstructure vol. 1, Fracture and Fracture Toughness, Proc. of Conf., Leoben, Austria.

Dolby R. E. (1979). Welding Journal Research Supplement, 58 (8), 225-s.

Dolby R. E. (1983). Met. Techol., 10, 349-362.

Dowling J. M., Corbett J. M. and Kerr H. W. (1986). Met. Trans. A, 17A(9),1611-1623.

Duren C. (1985). IIW Doc. IX-1356-85.

Easterling K. E. (1983). Introduction to The Physical Metallurgy of Welding, Butterworths & Co Ltd., London.

Easterling K. E. (1990). Recent Trends in Welding Science and Technology, ASM, 177-188.

Edward R. H., Squires I. F. and Barbaro F. J. (1986). Australian Welding Journal 31 (1), 11.

Eichhorn F. and Pyrasch D. (1986). Australian Welding Journal, 31 (3), 39.

Evans G. M. (1978). Oerlikon-Schweiβmitt, 36(82), s 4-19; also IIW Doc. II-A-432-77.

Evans G. M. (1979). Oerlikon-Schweiβmitt, 37(87), s 17-31; also IIW Doc. II-A-460-78.

Evans G. M. (1980a). Oerlikon-Schweiβmitt, 38(90), s 4-17; also IIW Doc. II-A-469-79.

Evans G. M. (1980b). Oerlikon-Schweiβmitt, 38(92), s 20-35; also IIW Doc. II-A-490-79.

Evans G. M. (1981). Effect of Welding Position on The Microstructure and Properties of C-Mn All-weld Metal Deposits, Welding Industries Oerlikon Buhrle Ltd., Switzerland.

Evans G. M. (1991), Welding Research Supplement, Jan., 32-s; also Oerlikon-Schweiβmitt, 49, 18-39.

Farrar R. A. and Harrison P. L. (1987). Journal of Materials Science, 22, 239.

Farrante M. and Farrar R.A. (1982). Journal of Materials Science 17 (11), 3293-98.

Ferree S.E. (1992). in Proc. of 40th National Conf., WTIA, Darwin, Australia, paper11.

French I. and Schumann O. (1994). Welding Condition-weld Mechanical Properties-Microstructure Relationship from E70 Strength Level and Cored Wires, CSIRO report: CRC Project 93.05, Australia.

French I. (1998). Australian Welding Journal, 43(4), 27-29.

French I. (1999). Australian Welding Journal, 44 (2), 44-46.

George T. and Irani J. J. (1968). Journal Australian Institute of Metals, 13 (2), 94.

George T., Bashford G. and MacDonald J. (1971). Journal Australian Institute of Metals, 16 (1), 36.

Goldak J. et al. (1986). Advances in Welding Science and Technology, ASM, 15-27.

Graville B. A. (1976). in Proc. Conf. on Welding of HSLA Structural Steels, Rome, ASM/AIM.

Grong O. and Christensen N. (1983). Scan. J. of Met., 4, 155.

Grong O. and Akselsen (1986). Metal Constr., 18, 557-562.

Grong O. and Matlock D. K. (1986). International Metals Reviews, 31, 27.

Grong O., Kluken A. O. and Bjornbakk B. (1988). Join. Mater., 1, 164-169.

Grong O. (1994). in Metallurgical Modelling of Welding, eds H. K. D. H. Bhadeshia, The Institute of Materials, London, 27.

Grossberg S. (1976). Biological Cybernetics, vol. 23, 121-134.

Habu R. (1978). Transactions I.S.I.J., 18, 492.

Harrison P. L. and Farrar R. A. (1981), Journal of Materials Science, 16 (8), 2218-26.

Hart P. H. M. and Harrison P. L. (1987). Welding Journal Research Supplement, 66 (10), 310-s.

Heagey J.C. and Wodzinski D.M. (1991). in Proc. of 39th National Conf., WTIA, 63-77.

Hecht-Nielsen R. (1990). Neuralcomputing, Addison-Wesley Inc., USA.

Hondros E. D. and Seah M. P. (1983). in Physical Metallurgy 3rd ed., eds R. W. Cahn and P. Haasen), North Holland Physics Publiching, part 1, 855-931.

Hopfield J. J. (1982). Proc. of the National Academy of Sciences, U.S.A., vol. 79, 2554-2558.

Horii Y. et al. (1986). in Proc. Int. Trends in Welding Research, ASM.

Houldcroft P. T. (1977). Welding Process Technology, Cambridge University Press.

Hrivnak I. (1995). in Mathematical Modelling of Weld Phenomena 2, eds H. Cerjak and H. K. D. H. Bhadeshia, The Institute of Materials, London, 162-171.

IIW Doc. 475-75 (1975). International Institute of Welding; also in Welding in the World, 13 (3/4) (1995), 71.

Ikawa, H., Oshige H. and Noi S. (1977). Journal of Welding (Japan), 7, 396.

Illin V. P. and Razikov M. I. (1966). Automatic Welding, 19, 3.

Inagaki M. and Sekiguchi H. (1960). Transactions National Research Institute of Metals (Japan), 2(2), 40.

International Institute of Welding (1967). IIW Doc. IX-535-67.

International Institute of Welding (1991). Guide to Light Microscope Examination of Ferritic Steel Weld Metals, Welding in the World, 29,160.

Ito Y. and Bessyo K. (1968). IIW Doc. IX-576-68.

Ito Y. and Nakanishi M. (1976). Sumitomo Search 15, 42-62.

Ito Y., Nakanishi M. and Komizo Y. (1982). Metal Construction 14 (9), 472-478.

Ito Y., Nakanixhi M. and Komizo Y. (1985). IIW Doc. IX-1349-85.

Ito Y., Nakanishi M. and Komizo Y. (1988). Joining and Materials, 1 (4), 179.

Jackson C. E. and Goodwin W. J. (1948). Welding Journal Research Supplement, 27(5), 253-s.

Jacobs R. A. (1991). Neural Computation, 3, 79-87.

Karppi R. (1978). IIW Doc. IX-1102-78.

Kiessling R. (1989). Non-metallic Inclusions in Steel, Part V, USA.

Kihara H., Suzuki H. and Kandatani Y. (1959). NRIM Report, 1, 39.

Kluken A. O., Grong O. And Hjelen J. (1988). Mater. Sci. Tech., 4, 652-653.

Kluken A. O. and Grong O. (1989). Metall Trans A, 20A, 1335.

Kluken A. O., Grong O. and Rorvik G. (1990). Metall Trans. A, 21A, 1335-1349.

Kohno R. et al. (1982). Weld. J., 61, 373s-380s.

Kohonen T. (1988). Self-organization and associative memory, 2nd edition, Springer-Verlag, New York.

Kong L. X., Hodgson P. D. and Collinson D. C. (1998). ISIJ International, 38(10), 1121-29.

Koseki T., Ohkita S. and Yurioka N. (1997). Science and Technology of Welding and Joining, 2(2), 65-69.

Koshio T. M. et al. (1981). IIW Doc. II-955-81.

Lalan S. H., Bhadeshia H. K. D. H. and Mackay D. J. C. (2000). Australian Welding Journal, 45 (1), 33-37.

Lancaster J. F. (1993). Metallurgy of Welding, George Allen & Unwin Ltd., UK.

Lathabai S. and Stout R. D. (1985). Welding Journal, 64(11), 303s-313s.

Lau T. W. et al. (1987). in Welding Metallurgy of Structural Steels, eds Koo J. Y., 349-366, Warrendale, PA, Metall. Soc. AIME.

Lebedev Y. M., Letuchi V. N. and Tsyukh S. M. (1986). Welding Production, 33 (12), 24.

Leonard J. A., Kramer M. A. and Ungar l. H. (1992). IEEE Transactions on Neural Networks, 3(4), 624-627.

Lloyds Register of Shipping (1995). Approval of Welding Consumables, London.

Liao J., Ikeuchi K. and Matsuda F. (1996). Welding International, 10(7), 552-558.

Li H. et al. (1998). in Proc. Mat. 98, Biennial Conf. of the Inst. of Mat. Eng., Australia, 1, 301-306.

Lin M. L. and Eagar T. W. (1986). Advances in Welding Science and Technology, ASM, 47-51.

Liu S., Dallam C. B. and Olson D. L. (1982). in Proc. Conf. Oak Ridge National Laboratory, Oak Ridge, TN 37830, 445-465.

Liu S. and Olson D. L. (1986). Welding Journal, 65(6), 139s-150s.

Liu S. (1992). Key Engineering Materials, vol. 69 & 70, 1.

Lomozik M., Szaja G. and Nowak W. (1997). Welding International, 11(3), 173-178.

Lorenz K. and Duren C. (1981). in Proc. Int. Conf. on Steels for Line Pipe and Pipeline Fittings, London, The Metals Society, paper 37.

Lula R. A. (1986). Manganese Stainless Steels, The Manganese Centre, Paris.

Matsuda, S. and Okumura, N. (1978). Transactions I. S. I. J., 18, 198.

Matsunawa A. and Yokoya S. (1990). Recent Trends in Welding Science and Technology, ASM, 31-36.

McCulloch et al. (1943). Bulletin of Mathematical Biophysics, vol. 5, 115-133.

McCutcheon D. B. et al. (1983). in Proc. Conf. on Technology and Application of HSLA Steels, Philadelphia, ASM, 881.

McGlone J. C. (1982). Metal Construction, 14 (7), 378.

Mercer W. L. (1975). in Material Requirements for Pipe Line Construction. Rosenhain Centenary Conf. Proc., eds R. G. Baker and A. Kelly, Royal Society, 7.

Metals Handbook (1964). vol. 2, Heat Treating, Cleaning and Finishing, American Society for Metals.

Milner D. R. and Apps R. L. (1968). Introduction to Welding and Brazing, Pergamon Press, Oxford.

Minsky et al. (1969). Perceptrons, MIT Press, Cambridge.

Mori N. H. et al. (1981). IIW Doc. IX - 1196-81.

Mori N. H. et al. (1982). IIW Doc. IX-1229.

Munning Schmidt-Van Derr Burg M. A., Hoekstra S. and Den Ouden G. (1985). Welding Journal, 64 (3), 63s.

Nakano N. et al. (1986). in Proc. of Fifth International Offshore Mechanics and Arctic Engineering (OMAE) Symposium, Tokyo, vol. 2, 354.

Neural computing (1996). Neural Ware Inc. Technical Publications Group, Pittsburgh, U.S.A.

NeuralWorks Predict (1996). Neural Ware Inc. Technical Publications Group, Pittsburgh, U.S.A.

Neural Reference Guide (1996). Neural Ware Inc. Technical Publications Group, Pittsburgh, U.S.A.

Norrish J. (1992). Advanced Welding Processes, Institute of Physics Publishing, Bristol, Philadelphia and New York.

Oldland R. B. (1985). Australian Weld Res., Dec. 31-43.

Paju M., Grabke H. J. and Hougardy H. P. (1991). Scandinavian Journal of Metallurgy, 20 (2), 135.

Pang W. et al. (1991). in Proc. 35th Conf, of South East Asia Iron and Steel Institute, Wollongong, Australia, vol. 2, paper 25.

Pang W. (1993). The Structure and Properties of the HAZ of Structural Plate Steels Welded by High Productivity Processes, Ph D thesis, University of Wollongong.

Pargeter R. J. and Dolby R. E. (1984). IIW Doc. IX-1323.

Parker D. B. (1985). Learning-logic, report TR-47, Cambridge, MA: Massachusetts Institute of Technology, Centre for Computational Research in Economics and Management Science.

Pisarski H. G. and Pargeter R. J. (1984). Metal Construction, 16 (7), 412.

Porter D. A. and Easterling K. E. (1981). Phase Transformations in Metals and Alloys, Van Nostrand Reinhold.

Rasanen E. and Tenkula J. (1972). Scandinavian Journal of Metallurgy, 1 (2), 75.

Reed R. C. and Bhadeshia H.K.D.H. (1989). in Proc. 2nd Int. Conf., Recent Trends in Welding Science and Technology, Gatlinburg, ASM Int.

Reed R. C. and Bhadeshia H. K. D. H. (1994). A simple model for multipass steel welds, Elsevier Science Ltd., 3663-3678.

Ricks R. A., Howeel P. R. and Barrite G. S. (1982). Journal of Materials Science, 17.

Rojas R. (1996). Neural Networks: a System Introduction, Springer, Berlin.

Rosenthal D. (1946). Transactions ASME, 68 (11), 849.

Rumelhart D. E. and McClelland J. L. (1986). Parallel distributed processing: explorations in the microstructure of cognition, vol. 1, Foundations, MIT Press, Massachusetts.

Sakai Y., Nishikawa Y., Suga T. and Nakai Y. (1992). in Proc. of 40th National Conf., WTIA, paper10.

Savage W. F. (1980). Welding in the World, 18, 89.

Schumann G. O. and French I. E. (1995). in Proc. 4th Int. Conf. on Trends in Welding Research.

Siebert C. A. et al. (1977). The Hardenability of Steels, ASM.

Sim R. G. (1992). Productivity Potential of Flux Cored Wires, in Proc. of 40th National Conf., Welding Technology Institute of Australia, paper 8.

Specht D. F. (1991). IEEE Transactions on Neural Networks, 2(6), 568-576.

Stout R. D., Vasudevan and Pence A. W. (1976). Welding Journal Research Supplement, 55 (4), 89-s.

Stout R. D. (1987). Weldability of Steels, 4th ed., Welding Research Council, New York.

Sugden A. A. B. and Bhadeshia H. K. D. H. (1988). Metallurgical Transactions, 19A(6), 1597-1602.

Svensson L. -E. and Gretoft B. (1990). Welding Journal, 69 (12), 454s.

Svensson L. -E. (1994). Control of Microstructures and Properties in Steel Arc Welds, Ann Arbor, CRC Press.

Szekely J. (1986). Advances in Welding Science and Technology, ASM, 3-14.

Tanaka J. and Kitada T. (1976). IIW Doc. IX-959-76.

Taylor L. G. and Farrar R. A. (1975). Welding and Metal Fabrication 43 (4), 305-310.Thaulow C., Paauw A. J. and Guttormsen K. (1987). Welding Journal Research Supplement, 66 (9), 266-s.

Terashima H. and Tsuboi J. (1982). Metal Construction 14 (12), 648-654.

Tomita Y. et al. (1985). in Proc. Conf. on HSLA Steels - Metallurgy and Applications, Beijing, China, 641.

Tsuboi J. and Terashima H. (1983). Weld. in the World, 21, 304-317.

Tsuchida Y., Okamoto K. and Tokunaga Y. (1996). Welding International, 10(6), 454-460.

Tsuei H., Dunne D. and Li H. (1998). in Proc. Mat. 98, Biennial Conf. of the Inst. of Mat. Eng., Australia, 1, 319-324.

Tweed J. H. and Knott J. F. (1982). in Proc. Int. Conf., Fracture and Fracture Toughness, Leoben, Austria, vol. 1.

Uchino K. et al. (1986). in Proc. Of Fifth International Offshore Mechanics and Arctic Engineering (OMAE) Symposium, Tokyo, vol. II, 373.

Underwood E. E. (1970). Quantitative Stereology, Addison-Wesley, London.

Underwood E. E. (1985). Metallography and Microstructure, Metals Handbook, 9th ed, ASM.

Using NeuralWorks (1996). Neural Ware Inc., Pittsburgh, U.S.A.

Uwer D., Lotter U. and Baumgardt H. (1990). Welding Research Abroad, 36 (1), 26; also (1989) Welding and Cutting, 4.

Vandermeer R. A., Vold C. L. and King W. E. (1990). Recent Trends in Welding Science and Technology, ASM, 223-228.

Vander Voort G. F. (1984). Metallography Principles and Practice. McGraw-Hill Inc. NY, U.S.A.

Van Stone R. H. et al. (1985). International Materials Reviews, 30, 157.

Verburg S. J. (1974). Philips Welding Reporter, 3/4.

Watanabe I. and Kojima T. (1980). Report 1 - Journal of Japan Welding Society 49 (11), 772-780; Report 2 - ibid 50 (7), 702-709.

Watanabe I. and Kojima T. (1983). in Proc. Int. Conf. Effect of Residual, Impurity and Microalloying Elements on Weldability and Weld Properties, Abington, London, paper 12.

Watanabe I., Suzuki M. and Kojima T. (1980). in Proc. Int. Conf. ,p 43-48; also Welding research in the 1980's, University Welding Research Inst., Osaka, Japan.

Wedgery D. J. (1978). Weld. Res. Int., 4, 54-80.

Welding Handbook (1987). 8th ed., vol. 1 Welding Technology, eds L. P. Connor, American Welding Society, Miami.

Welding Handbook (1991). 8th ed., vol. 2 Welding Technology, eds R. L. O'Brien, American Welding Society, Miami.

Welland W. G. (1989). Welding Journal, 68 (3), 55.

Wells A. A. (1952). Welding Journal Research Supplement, 31 (5), 263-s.

Widrow, Bernard and Hoff, Marcoan (1960). 1960 IRE WESCON Convention Record, part 4, 96-104.

Widrow B. et al. (1988). in Artificial Neural Networks: Concepts and Theory, eds P. Mehra and B. W. Wah, IEEE Computer Society Press, CA, 217-244.

Wingrove A. L. (1987). Scandinavian Journal of Metallurgy, 16 (4), 174.

Yamanaka K. and Ohmori Y. (1977). Transactions of ISIJ, 17 (2), 92.

Yang Y. X. et al. (1986). Transactions of China Welding Institute, 7 (4), 174.

Yeomans S. R. (1994). Welding in Structural Engineering Steels and Aluminium Alloys, School of Civil Engineering, University college, UNSW, Canberra ACT, Australia.

Yoshikawa H., Kawashima Y. and Konno K. (1988). in Proc. Conf. on Physical Metallurgy of Thermomechanical Processing of Steels and Other Metals (THERMEC-88), Tokyo, Japan, vol. 2, 487.

Yurioka N., Oshita S. and Tamehire H. (1981). in Pipeline Welding in the 80's, Proc. Of Symp. Of Australian Welding Research Association, Melbourne; also Welding Journal Research Supplement, 62 (6), 147-s.

Yurioka N., Okumura M. and Kasuya T. (1987). Metal Construction. 217-223R.

Yurioka N. (1990). in Proc. First United States-Japan Symp. On Advances in Welding Metallurgy, Florida, American Welding Society, 79.

Zhang Z. and Farrar R. A. (1997). Welding Journal, May, 183s.

Zhu J. H. et al. (1995). Acicular Ferrite Refinement in the Weld Zone of Microalloyed Rutile Flux-cored Arc Welded C-Mn Structural Steel, CSIRO report: CRC Project 93.05, Australia.

Zimmer C. and Schmerling D. (1983). Welding Journal, 62 (4), 41-44.

Zurada J. M. (1992). Introduction to Artificial Neural Systems, West Publishing Company, St. Paul.

APPENDICES

APPENDIX 1 WELDING PARAMETERS

Wire Types	Heat Input (kJ/mm)	Welding Position	Welding Technique	Shielding Gas	Welding Current (A)	Welding Voltage (V)	Welding Speed (mm/min)
RB Wire	0.87	1G	Stringer	Ar-25%CO2	280	31	600
	1.51	1G	Stringer	Ar-25%CO2	280	31	344
	2.14	1G	Stringer	CO2	300	31	211
	1.61	1G	Stringer	Ar-25%CO2	280	31	323
	1.20	3G	Stringer	Ar-25%CO2	200	24	239
	2.44	3G	Weave	Ar-25%CO2	190	21	107
MC Wire	0.99	1G	Stringer	Ar-16%CO2-2.5%O2	280	31	526
	1.58	1G	Stringer	Ar-16%CO2-2.5%O2	280	31	326
	1.66	1G	Stringer	CO2	280	31	330
	1.99	1G	Stringer	Ar-16%CO2-2.5%O2	300	31	280
	2.58	1G	Weave	Ar-16%CO2-2.5%O2	280	31	202
R Wire	1.00	1G	Stringer	Ar-25%CO2	280	31	520
	1.43	1G	Stringer	Ar-25%CO2	280	31	362
	1.99	1G	Stringer	CO2	300	31	264
	1.44	1G	Stringer	Ar-25%CO2	280	31	366
	1.06	3G	Stringer	Ar-25%CO2	190	24	258
	2.51	3G	Weave	Ar-25%CO2	190	24	109

APPENDIX 2 EXPERIMENTAL DATA BASE FOR NEURAL NETWORK

Sample Code	C (wt %)	Mn (wt %)	Si (wt %)	S (wt %)	P (wt %)	Ti (wt %)	Al (wt %)	B (wt %)
RB-1	0.08	1.14	0.45	0.013	0.014	0.055	0.004	0.0116
RB-2	0.08	1.14	0.42	0.01	0.015	0.063	0.004	0.0074
RB-3	0.06	0.94	0.34	0.014	0.015	0.05	0.004	0.0067
Rb-4	0.08	1.1	0.42	0.01	0.016	0.065	0.005	0.0071
RB-5	0.08	1.15	0.47	0.015	0.015	0.069	0.004	0.0086
RB-6	0.09	1.14	0.47	0.012	0.012	0.066	0.006	0.0089
MC-1	0.06	1.41	0.61	0.011	0.015	0.018	0.007	0.0001
MC-2	0.06	1.5	0.66	0.011	0.014	0.018	0.005	0.0001
MC-3	0.05	1.23	0.51	0.011	0.013	0.011	0.005	0.0001
MC-4	0.06	1.48	0.64	0.011	0.014	0.019	0.006	0.0001
MC-5	0.06	1.43	0.63	0.011	0.014	0.015	0.004	0.0001
R-1	0.09	1.34	0.59	0.013	0.013	0.045	0.002	0.0001
R-2	0.09	1.33	0.58	0.012	0.011	0.049	0.002	0.0001
R-3	0.08	1.24	0.53	0.013	0.012	0.056	0.004	0.0001
R-4	0.09	1.4	0.62	0.013	0.012	0.06	0.002	0.0001
R-5	0.08	1.29	0.55	0.012	0.012	0.052	0.006	0.0001
R-6	0.09	1.41	0.62	0.011	0.014	0.055	0.002	0.0001

Sample Code	Mo (wt %)	O (wt %)	N (wt %)	% Reheated	% Double-reheated	$\bar{L}_o^w$ (μm)	$\bar{L}_{sw}$ (μm)	$\bar{L}_{GC}$ (μm)
RB-1	0.01	0.073	0.013	50.97	16.4	3.61	3.26	3.23
RB-2	0.01	0.073	0.013	50.92	13.8	2.77	2.63	2.07
RB-3	0.01	0.071	0.011	49.7	13.07	4.03	3.76	3.56
Rb-4	0.01	0.069	0.013	52.03	10.27	3.97	3.5	3.89
RB-5	0.01	0.073	0.006	47.77	11.19	2.97	2.86	2.77
RB-6	0.01	0.07	0.012	59.2	0	4.75	4.3	4.29
MC-1	0.02	0.11	0.0045	52.46	0	5.6	4.71	4.67
MC-2	0.02	0.124	0.0074	46.04	15.66	3.7	3.24	3.07
MC-3	0.01	0.107	0.0072	44.85	14.73	4.18	3.31	3.23
MC-4	0.02	0.121	0.006	46.3	14.39	3.17	2.72	2.44
MC-5	0.02	0.117	0.0054	50.85	13.1	4.66	4.18	3.69
R-1	0.02	0.07	0.005	47.29	13.64	4.28	4.09	3.61
R-2	0.01	0.074	0.0047	47.74	13.7	3.39	2.85	3.02
R-3	0.01	0.079	0.0083	46.65	10.36	3.79	3.39	3.33
R-4	0.02	0.079	0.0055	47.89	11.26	2.94	2.71	2.69
R-5	0.01	0.083	0.004	44.16	13.03	3.26	3.29	2.64
R-6	0.02	0.081	0.0047	62.28	0	5.24	4.5	4.1

Sample Code	$\bar{L}_{GR}$ (μm)	$\bar{L}_{IC}$ (μm)	% AF	% PF(G)	% PF(I)	% FS	% GC
RB-1	4.28	4.48	28.7	12.2	4.2	1.9	19.78
RB-2	3.31	3.63	33.2	5.5	6.5	0.9	20.46
RB-3	4.48	5.5	23.8	16.2	4.6	6.1	16.68
Rb-4	4.34	4.96	25.5	15.6	3.8	2.4	18.03
RB-5	3.2	3.5	30.7	12	4.7	4.7	18.14
RB-6	5.35	5.62	16.4	18.8	2.45	3.3	19.57
MC-1	6.95	8.3	9.3	0.9	33.4	2.8	15.9
MC-2	4.48	5.3	19.2	16.6	9.1	8	17.54
MC-3	6.04	6.25	19.7	23	6	6	13.41
MC-4	4.21	4.83	15.9	19.8	5.8	6.8	20.41
MC-5	5.67	7.04	15	21.3	7.3	4.9	17.6
R-1	4.96	6.11	19	15.5	8	8.3	16.69
R-2	4.18	5.56	19.9	16	3.9	10.2	18.72
R-3	4.48	5.73	22	17.5	4.4	10.8	13.84
R-4	3.29	4.52	24.6	14.4	5.7	9	19.1
R-5	3.54	4.21	24.2	16.1	5.7	10	18.39
R-6	6.47	7.22	8.3	11.5	15.9	3.6	20.3

Sample Code	% GR	% IC	V_v (%)	$\bar{D}_v$ (μm)	N_v ($1/\mu m^3$)	$F \geq 1.5$ (%)	$\bar{H}$
RB-1	27.42	5.76	0.8092	0.6587	0.05407	1.81	206.5
RB-2	25.31	8.08	0.6354	0.6063	0.05446	0.76	221
RB-3	26.62	6.08	0.689	0.6551	0.04681	1.78	197.2
Rb-4	29.4	5.38	0.612	0.5911	0.0566	0.74	200.5
RB-5	22.82	6.93	0.6566	0.6019	0.05752	1.71	218.4
RB-6	34.15	5.41	0.7605	0.5714	0.07787	0.96	193.2
MC-1	33.72	3.96	1.0353	0.897	0.0274	3.93	192.9
MC-2	25.01	4.06	0.8611	0.6198	0.06907	1.53	204.1
MC-3	26.81	4.98	1.1272	0.758	0.04944	3.67	200.2
MC-4	26.13	5.25	0.7721	0.5983	0.06886	1.79	215.8
MC-5	29.23	4.68	0.8301	0.6788	0.05069	2.12	197.7
R-1	25.59	5.41	0.7503	0.5165	0.104	1.29	202.7
R-2	25.19	6.12	0.9011	0.5751	0.09048	0.76	216.5
R-3	26.18	5.3	0.686	0.4775	0.12034	0.69	203.2
R-4	21.12	6.13	0.8921	0.5403	0.10802	1.02	222.8
R-5	21.31	4.34	0.7101	0.5052	0.10518	1.49	224.6
R-6	35.74	4.6	0.6105	0.5542	0.0685	1.3	191.5

Sample Code	Test Temperature (°C)	Impact Toughness (J)
RB-1	-60	15.5
	-40	31.5
	-20	56.3
	0	71.3
	20	92.0
RB-2	-60	57.0
	-40	76.0
	-20	99.0
	0	96.6
	20	98.6
RB-3	-40	7.0
	-20	18.3
	0	49.3
	20	77.3
	40	100.0
Rb-4	-40	20.0
	-20	38.3
	0	56.0
	20	65.6
RB-5	-60	22.5
	-40	42.5
	-20	65.3
	0	92.0
	20	95.0
RB-6	-40	14.5
	-20	59.0
	0	105.0
	20	119.3
MC-1	-40	11.5
	-20	21.3
	0	39.6
	20	74.6
	40	119.5
MC-2	-40	20.5
	-20	28.6
	0	46.0
	20	75.0
	40	113.0
MC-3	-40	16.5
	-20	33.3
	0	69.0
	20	94.7
	40	138.0

Sample Code	Test Temperature (°C)	Impact Toughness (J)
MC-4	-40	18.0
	-20	33.0
	0	46.0
	20	62.3
	40	90.0
MC-5	-40	19.5
	-20	35.3
	0	62.0
	20	81.0
	40	134
R-1	-40	18.0
	-20	33.3
	0	53.3
	20	82.0
	40	112.0
R-2	-60	13.5
	-40	27.5
	-20	42.3
	0	73.0
	20	85.3
R-3	-60	14.5
	-40	26.5
	-20	35.6
	0	68.0
	20	98.0
R-4	-60	14.5
	-40	30.0
	-20	33.3
	0	48.3
	20	77.6
R-5	-40	16.5
	-20	42.3
	0	68.0
	20	85.0
	40	84.0
R-6	-40	17.5
	-20	31.6
	0	54.6
	20	82.0
	40	117.5

APPENDIX 3 WEIGHTS FOR NEURAL NETWORK MODEL

(Data can be used to make preditions of toughness)

Description	Weight	Description	Weight
Bias to hidden PE 1	-0.1376	Bias to hidden PE 2	-1.1250
Carbon to hidden PE1	-0.1544	Carbon to hidden PE 2	0.4694
Manganese to hidden PE 1	-0.2707	Manganese to hidden PE 2	0.1512
Silicon to hidden PE 1	-0.2664	Silicon to hidden PE 2	0.2259
Sulphur to hidden PE 1	0.2382	Sulphur to hidden PE 2	0.2298
Phosphorus to hidden PE 1	0.0896	Phosphorus to hidden PE 2	-0.2658
Titanium to hidden PE 1	-0.2898	Titanium to hidden PE 2	0.3539
Aluminium to hidden PE 1	-0.9341	Aluminium to hidden PE 2	-0.2618
Boron to hidden PE 1	-0.0020	Boron to hidden PE 2	0.3288
Molybdenum to hidden PE 1	0.1915	Molybdenum to hidden PE 2	-0.3252
Oxygen to hidden PE 1	-0.3201	Oxygen to hidden PE 2	0.3059
Nitrogen to hidden PE 1	-0.0380	Nitrogen to hidden PE 2	0.2885
% Reheated to hidden PE 1	-0.1189	% Reheated to hidden PE 2	0.5153
% D-reheated to hidden PE 1	0.6960	% D-reheated to hidden PE 2	-0.7224
$\bar{L}_o^w$ to hidden PE 1	-0.0030	$\bar{L}_o^w$ to hidden PE 2	-0.1883
$\bar{L}$ sw to hidden PE 1	0.2189	$\bar{L}$ sw to hidden PE 2	-0.3237
$\bar{L}$ GC to hidden PE 1	-0.1417	$\bar{L}$ GC to hidden PE 2	-0.3715
$\bar{L}$ GR to hidden PE 1	-0.0286	$\bar{L}$ GR to hidden PE 2	-0.2926
$\bar{L}$ IC to hidden PE 1	-0.1400	$\bar{L}$ IC to hidden PE 2	-0.0467
% AF to hidden PE 1	0.2512	% AF to hidden PE 2	0.3004
% PF(G) to hidden PE 1	0.0109	% PF(G) to hidden PE 2	-0.2507
% PF(I) to hidden PE 1	-0.0042	% PF(I) to hidden PE 2	0.3984
% FS to hidden PE 1	0.2203	% FS to hidden PE 2	0.1129
% GC to hidden PE 1	-0.1663	% GC to hidden PE 2	-0.3738
% GR to hidden PE 1	-0.2210	% GR to hidden PE 2	-0.0731
% IC to hidden PE 1	0.4329	% IC to hidden PE 2	0.6113
V_v to hidden PE 1	-0.2259	V_v to hidden PE 2	0.3146
$\bar{D}_v$ to hidden PE 1	0.1007	$\bar{D}_v$ to hidden PE 2	-0.0467
N_v to hidden PE 1	-0.2599	N_v to hidden PE 2	0.5358
$F \geq 1.5$ (%) to hidden PE 1	-0.1808	$F \geq 1.5$ (%) to hidden PE 2	0.0089
$\bar{H}$ to hidden PE 1	-0.2123	$\bar{H}$ to hidden PE 2	0.4747
Temperature to hidden PE 1	1.5501	Temperature to hidden PE 2	1.5192

Description	Weight	Description	Weight
Bias to hidden PE 3	-0.0711	Bias to hidden PE 4	-0.1356
Carbon to hidden PE 3	0.2980	Carbon to hidden PE 4	0.2245
Manganese to hidden PE 3	0.4414	Manganese to hidden PE 4	-0.1092
Silicon to hidden PE 3	0.4239	Silicon to hidden PE 4	0.1665
Sulphur to hidden PE 3	-0.5187	Sulphur to hidden PE 4	-0.1546
Phosphorus to hidden PE 3	0.6287	Phosphorus to hidden PE 4	0.1494
Titanium to hidden PE 3	-0.6050	Titanium to hidden PE 4	-0.2518
Aluminium to hidden PE 3	-0.4968	Aluminium to hidden PE 4	0.0749
Boron to hidden PE 3	0.0711	Boron to hidden PE 4	-0.3024
Molybdenum to hidden PE 3	-0.1303	Molybdenum to hidden PE 4	-0.1953
Oxygen to hidden PE 3	0.2220	Oxygen to hidden PE 4	-0.0928
Nitrogen to hidden PE 3	-0.5521	Nitrogen to hidden PE 4	0.1948
% Reheated to hidden PE 3	-0.0412	% Reheated to hidden PE 4	-0.2945
% D-reheated to hidden PE 3	0.7251	% D-reheated to hidden PE 4	-0.1160
$\bar{L}_o^w$ to hidden PE 3	0.3676	$\bar{L}_o^w$ to hidden PE 4	-0.0232
$\bar{L}_{sw}$ to hidden PE 3	0.3516	$\bar{L}_{sw}$ to hidden PE 4	-0.0780
$\bar{L}_{GC}$ to hidden PE 3	-0.4495	$\bar{L}_{GC}$ to hidden PE 4	-0.0120
$\bar{L}_{GR}$ to hidden PE 3	0.8584	$\bar{L}_{GR}$ to hidden PE 4	0.2877
$\bar{L}_{IC}$ to hidden PE 3	-0.3401	$\bar{L}_{IC}$ to hidden PE 4	0.0094
% AF to hidden PE 3	0.4772	% AF to hidden PE 4	0.0624
% PF(G) to hidden PE 3	-0.3800	% PF(G) to hidden PE 4	-0.1548
% PF(I) to hidden PE 3	0.3540	% PF(I) to hidden PE 4	-0.1148
% FS to hidden PE 3	-0.9723	% FS to hidden PE 4	0.2331
% GC to hidden PE 3	-0.3616	% GC to hidden PE 4	-0.2038
% GR to hidden PE 3	-0.0501	% GR to hidden PE 4	0.0612
% IC to hidden PE 3	-0.1798	% IC to hidden PE 4	0.2560
V_v to hidden PE 3	-0.0826	V_v to hidden PE 4	-0.1086
$\bar{D}_v$ to hidden PE 3	0.0037	$\bar{D}_v$ to hidden PE 4	-0.0334
N_v to hidden PE 3	-0.2687	N_v to hidden PE 4	0.2150
$F \geq 1.5$ (%) to hidden PE 3	0.8890	$F \geq 1.5$ (%) to hidden PE 4	-0.2036
$\bar{H}$ to hidden PE 3	-0.2894	$\bar{H}$ to hidden PE 4	-0.2868
Temperature to hidden PE 3	2.2861	Temperature to hidden PE 4	0.0288

Description	Weight	Description	Weight
Bias to hidden PE 5	0.1445	Bias to hidden PE 6	0.0668
Carbon to hidden PE 5	0.0634	Carbon to hidden PE 6	0.1007
Manganese to hidden PE 5	-0.1222	Manganese to hidden PE 6	-0.0660
Silicon to hidden PE 5	0.1717	Silicon to hidden PE 6	-0.2354
Sulphur to hidden PE 5	0.1191	Sulphur to hidden PE 6	0.0502
Phosphorus to hidden PE 5	0.0832	Phosphorus to hidden PE 6	-0.1125
Titanium to hidden PE 5	-0.1725	Titanium to hidden PE 6	-0.0116
Aluminium to hidden PE 5	0.0163	Aluminium to hidden PE 6	0.2795
Boron to hidden PE 5	-0.0088	Boron to hidden PE 6	-0.0634
Molybdenum to hidden PE 5	-0.1421	Molybdenum to hidden PE 6	0.1140
Oxygen to hidden PE 5	-0.0773	Oxygen to hidden PE 6	-0.0812
Nitrogen to hidden PE 5	-0.0177	Nitrogen to hidden PE 6	-0.1096
% Reheated to hidden PE 5	-0.0906	% Reheated to hidden PE 6	-0.0419
% D-reheated to hidden PE 5	0.0336	% D-reheated to hidden PE 6	0.0419
$\bar{L}_o^w$ to hidden PE 5	-0.2194	$\bar{L}_o^w$ to hidden PE 6	0.1745
$\bar{L}_{SW}$ to hidden PE 5	-0.3187	$\bar{L}_{SW}$ to hidden PE 6	0.4746
$\bar{L}_{GC}$ to hidden PE 5	0.0124	$\bar{L}_{GC}$ to hidden PE 6	-0.1056
$\bar{L}_{GR}$ to hidden PE 5	0.0881	$\bar{L}_{GR}$ to hidden PE 6	0.0435
$\bar{L}_{IC}$ to hidden PE 5	-0.0504	$\bar{L}_{IC}$ to hidden PE 6	0.0912
% AF to hidden PE 5	-0.3519	% AF to hidden PE 6	0.0308
% PF(G) to hidden PE 5	-0.0107	% PF(G) to hidden PE 6	0.2494
% PF(I) to hidden PE 5	0.2248	% PF(I) to hidden PE 6	-0.0329
% FS to hidden PE 5	0.0559	% FS to hidden PE 6	-0.1545
% GC to hidden PE 5	-0.0523	% GC to hidden PE 6	0.1013
% GR to hidden PE 5	0.2758	% GR to hidden PE 6	-0.2988
% IC to hidden PE 5	0.1229	% IC to hidden PE 6	0.1683
V_v to hidden PE 5	0.0288	V_v to hidden PE 6	0.0744
$\bar{D}_v$ to hidden PE 5	-0.0237	$\bar{D}_v$ to hidden PE 6	0.0011
N_v to hidden PE 5	-0.0583	N_v to hidden PE 6	0.0322
$F \geq 1.5$ (%) to hidden PE 5	-0.1887	$F \geq 1.5$ (%) to hidden PE 6	0.0436
$\bar{H}$ to hidden PE 5	-0.1451	$\bar{H}$ to hidden PE 6	0.2134
Temperature to hidden PE 5	-0.0667	Temperature to hidden PE 6	-0.2264

Description	Weight	Description	Weight
Bias to hidden PE 7	-0.0701	Bias to hidden PE 8	-0.1912
Carbon to hidden PE 7	-0.1296	Carbon to hidden PE 8	-0.2493
Manganese to hidden PE 7	-0.1832	Manganese to hidden PE 8	-0.0115
Silicon to hidden PE 7	-0.1585	Silicon to hidden PE 8	-0.2402
Sulphur to hidden PE 7	-0.2032	Sulphur to hidden PE 8	0.4567
Phosphorus to hidden PE 7	-0.0339	Phosphorus to hidden PE 8	0.3061
Titanium to hidden PE 7	-0.0313	Titanium to hidden PE 8	-0.1812
Aluminium to hidden PE 7	-0.3775	Aluminium to hidden PE 8	-0.0527
Boron to hidden PE 7	-0.1045	Boron to hidden PE 8	0.0105
Molybdenum to hidden PE 7	-0.2535	Molybdenum to hidden PE 8	0.3118
Oxygen to hidden PE 7	-0.1385	Oxygen to hidden PE 8	-0.1885
Nitrogen to hidden PE 7	-0.2993	Nitrogen to hidden PE 8	0.5146
% Reheated to hidden PE 7	0.2844	% Reheated to hidden PE 8	-0.8894
% D-reheated to hidden PE 7	0.1322	% D-reheated to hidden PE 8	0.7936
$\bar{L}_o^w$ to hidden PE 7	-0.0736	$\bar{L}_o^w$ to hidden PE 8	-0.3436
$\bar{L}_{SW}$ to hidden PE 7	0.1767	$\bar{L}_{SW}$ to hidden PE 8	-0.4280
$\bar{L}_{GC}$ to hidden PE 7	0.0136	$\bar{L}_{GC}$ to hidden PE 8	0.2605
$\bar{L}_{GR}$ to hidden PE 7	-0.0999	$\bar{L}_{GR}$ to hidden PE 8	-0.2471
$\bar{L}_{IC}$ to hidden PE 7	-0.0653	$\bar{L}_{IC}$ to hidden PE 8	-0.0870
% AF to hidden PE 7	0.1675	% AF to hidden PE 8	-0.0462
% PF(G) to hidden PE 7	0.0546	% PF(G) to hidden PE 8	0.0331
% PF(I) to hidden PE 7	0.2500	% PF(I) to hidden PE 8	-0.0012
% FS to hidden PE 7	-0.0101	% FS to hidden PE 8	0.5533
% GC to hidden PE 7	0.2292	% GC to hidden PE 8	-0.4746
% GR to hidden PE 7	0.0267	% GR to hidden PE 8	-0.2858
% IC to hidden PE 7	-0.1207	% IC to hidden PE 8	-0.5133
V_v to hidden PE 7	0.0375	V_v to hidden PE 8	0.2705
$\overline{D_v}$ to hidden PE 7	0.0527	$\overline{D_v}$ to hidden PE 8	-0.1989
N_v to hidden PE 7	-0.2146	N_v to hidden PE 8	0.2012
F≥1.5 (%) to hidden PE 7	0.0139	F≥1.5 (%) to hidden PE 8	0.0270
$\bar{H}$ to hidden PE 7	0.0975	$\bar{H}$ to hidden PE 8	-0.2001
Temperature to hidden PE 7	0.2781	Temperature to hidden PE 8	-1.1245

Description	Weight
Bias to hidden PE 9	-0.1246
Carbon to hidden PE 9	-0.1696
Manganese to hidden PE 9	-0.1360
Silicon to hidden PE 9	0.0038
Sulphur to hidden PE 9	-0.0985
Phosphorus to hidden PE 9	-0.2872
Titanium to hidden PE 9	0.1479
Aluminium to hidden PE 9	-0.1935
Boron to hidden PE 9	-0.0437
Molybdenum to hidden PE 9	0.0896
Oxygen to hidden PE 9	-0.0682
Nitrogen to hidden PE 9	-0.0349
% Reheated to hidden PE 9	0.3190
% D-reheated to hidden PE 9	-0.2632
$\bar{L}_o^w$ to hidden PE 9	-0.1876
$\bar{L}_{sw}$ to hidden PE 9	-0.2531
$\bar{L}_{GC}$ to hidden PE 9	-0.0399
$\bar{L}_{GR}$ to hidden PE 9	-0.0877
$\bar{L}_{IC}$ to hidden PE 9	0.0668
% AF to hidden PE 9	0.0043
% PF(G) to hidden PE 9	-0.1392
% PF(I) to hidden PE 9	-0.1794
% FS to hidden PE 9	-0.2771
% GC to hidden PE 9	0.3882
% GR to hidden PE 9	0.0572
% IC to hidden PE 9	0.1150
V_v to hidden PE 9	0.2038
$\bar{D}_v$ to hidden PE 9	0.0359
N_v to hidden PE 9	-0.3347
$F \geq 1.5$ (%) to hidden PE 9	0.2231
$\bar{H}$ to hidden PE 9	0.2313
Temperature to hidden PE 9	0.4974

Description	Weight
Bias to output PE	-0.3015
Carbon to output PE	0.0701
Manganese to output PE	0.4130
Silicon to output PE	0.3318
Sulphur to output PE	-0.2829
Phosphorus to hidden PE1	-0.2329
Titanium to hidden PE1	-0.2721
Aluminium to hidden PE1	-0.4477
Boron to hidden PE1	0.3115
Molybdenum to hidden PE1	-0.2685
Oxygen to hidden PE1	0.2908
Nitrogen to hidden PE1	-0.1479
% Reheated to hidden PE1	0.2601
% D-reheated to hidden PE1	-0.2087
$\bar{L}_o^w$ to hidden PE1	0.0777
$\bar{L}_{sw}$ to hidden PE1	0.5658
$\bar{L}_{GC}$ to hidden PE1	-0.3008
$\bar{L}_{GR}$ to hidden PE1	0.1246
$\bar{L}_{IC}$ to hidden PE1	-0.4665
% AF to hidden PE1	0.7341
% PF(G) to hidden PE1	-0.1001
% PF(I) to hidden PE1	-0.1009
% FS to hidden PE1	-0.2812
% GC to hidden PE1	-0.5412
% GR to hidden PE1	-0.1106
% IC to hidden PE1	0.7722
V_v to hidden PE1	-0.0690
$\bar{D}_v$ to hidden PE1	-0.0142
N_v to hidden PE1	-0.0393
$F \geq 1.5$ (%) to hidden PE1	0.0660
$\bar{H}$ to hidden PE1	-0.0608
Temperature to hidden PE 1	1.9165
Hidden PE 1 to output PE	-0.4182
Hidden PE 2 to output PE	-0.5952
Hidden PE 3 to output PE	-0.4504
Hidden PE 4 to output PE	-0.0490
Hidden PE 5 to output PE	-0.0377
Hidden PE 6 to output PE	-0.0225
Hidden PE 7 to output PE	0.0278
Hidden PE 8 to output PE	0.1934
Hidden PE 9 to output PE	0.1207

APPENDIX 4 LIST OF FIGURES

Figures **Opposite page**

APPENDIX 5 LIST OF TABLES

APPENDIX 6 LIST OF SYMBOLS AND ABBREVIATIONS

1. Symbols

$Ac1$	the temperature at which the transformation of austenite starts
$Ac3$	the temperature at which the transformation of austenite finishes
$Ar3$	the temperature at which the transformation of ferrite starts
a_{pj}	the activation of jth PE for the pth training example.
$\overline{Da}$	the arithmetic mean two dimensional particle diameter
$\overline{Dv}$	the arithmetic mean three dimensional particle diameter
d_{pj}	the desired output of the jth PE for the pth training example
E	elasticity
Ep	overall output error
e_{pj}	the computed error of the jth PE for the pth training example
$F \geq 1.5$ (%)	volume fraction of particles $\geq$ 1.5 μm
$\overline{H}$	overall mean hardness
$\overline{H}(i)$	mean hardness of sub-zone i
I	welding current
$\overline{L}$	mean free path
$\overline{L}_{GC}$	mean free path of GC sub-zone
$\overline{L}_{GR}$	mean free path of GR sub-zone
$\overline{L}_{IC}$	mean free path of IC sub-zone
$\overline{L}_{SW}$	mean free path of SW region
$\overline{L}_i^w$	weighted mean free path for sub-zone i

$\bar{L}_o^w$	overall mean free path
N_a	the number of particle per unit area
N_v	the number of particle per unit volume
o_{pi}	the value of the ith incoming connection (actual output) for the pth training example
Pcm	carbon equivalent
r^2	correlation coefficient
S	welding speed
S_v	the total particle surface area per unit volume
T	temperature (°C)
T_{47J}	temperature which corresponds to 47 J impact energy
t	time
u	the value of threshold
V	voltage
vf	volume fraction
$V_v(A_A)$	volume fraction of inclusions
w_{ji}	the weight of jth PE for the ith input
α	ferrite phase
β	learning coefficient
γ	austenite phase
λ	thermal conductivity
λ_v	the mean particle center to center volume spacing
η	arc efficiency
1G	flat welding position

3G vertical-up welding position

1,1 the double-reheated sub-zone GC-GC

1,2 the double-reheated sub-zone GC-GR

1,3 the double-reheated sub-zone GC-IC

2,1 the double-reheated sub-zone GR-GC

2,2 the double-reheated sub-zone GR-GR

2,3 the double-reheated sub-zone GR-IC

3,1 the double-reheated sub-zone IC-GC

3,2 the double-reheated sub-zone IC-GR

3,3 the double-reheated sub-zone IC-IC

% Reheated volume fraction of reheated region

% D-reheated volume fraction of double-reheated region

ΔH weighted hardness

$\Delta_p w_{ji}$ the change for the weight which joins the jth PE to its ith incoming connection for the pth training example

$\Delta t_{8\text{-}5}$ cooling time between 800-500°C

2. Abbreviations

adaline	adaptive linear neuron
AF	acicular ferrite
ART	adaptive resonance theory
AS	Australian standard
ASTM	the American Society for Testing and Materials
AWS	American Welding Society
BSB	brain state in a box
CCT	continuous cooling time
CE	carbon equivalent
CVN	Charpy V notch
EDS	energy dispersive spectroscopy
ESW	electro-slag welding
FC	ferrite-carbied aggregate
FCAW	flux-cored arc welding
FS	ferrite with a second phase
GC	grain coarsened
GMA	gas metal arc
GR	grain refined
HAZ	heat affected zone
HB	Brinell hardness testing
HI	heat input
HV	Vickers or Diamond Pyramid hardness testing

HSLA	high strength low alloy
IC	intercritical
IIW	the International Institute of Welding
LVQ	learning vector quantization
M-A	martensite - austenite
madaline	multiple adaptive linear neuron
MC	metal-cored
MFP	mean free path
MMA	manual metal arc
PE	processsing element
PF(I)	intragranular polygonal ferrite
PF(G)	grain boundary ferrite
R	rutile flux-cored
RB	boron containing rutile flux-cored
RBF	Radial Basis Function
RC	Rockwell hardness testing
RMS	root mean square
SAW	submerged arc welding
SEM	scanning electron microscopy
SOM	self-organizing-maps
SW	solidified weld metal
TanH	the hyperbolic tangent function

PUBLICATIONS

1. H. Tsuei, D. Dunne and H. Li, " Analysis of weld metal structures in flux cored arc welded steel", Proceedings of the Biennial Conference of the Institute of Materials Engineering Australia, 1998, vol. 1, pp. 319-324.

2. D. Dunne, H. Tsuei and H. Li, "A study of double-reheated zones in multipass steel welds" to be published.

3. D. Dunne, H. Tsuei and H. Li, "Mean free path analysis of ferritic weld metal in flux cored arc welded steel", to be published.

4. D. Dunne, H. Tsuei and H. Li, "Neural network analysis of low temperature impact properties in flux cored arc steel welds", to be published.